BEHAVIOR OF ULTRA-HIGH PERFORMANCE CONCRETE BEAMS UNDER FIRE CONDITIONS

By

Srishti Banerji

A DISSERTATION

Submitted to
Michigan State University
in partial fulfillment of the requirements
for the degree of

Civil Engineering - Doctor of Philosophy

2021

ABSTRACT

BEHAVIOR OF ULTRA-HIGH PERFORMANCE CONCRETE BEAMS UNDER FIRE CONDITIONS

By

Srishti Banerji

Ultra-high performance concrete (UHPC) is a novel class of concrete that has superior mechanical properties and durability characteristics as compared to that of conventional concrete. When structural members made of UHPC are used in building construction, the provision of appropriate fire resistance is a key safety consideration. Since UHPC is a new construction material, there is limited information, as well as limited research on the fire performance of UHPC members. Preliminary research at the material and structural level have shown that UHPC members exhibit comparatively poor fire performance as compared to conventional concrete due to fire-induced spalling resulting from its dense microstructure as well as faster degradation of mechanical properties with temperature. At present, there is a lack of experimental data and numerical models for evaluating the fire resistance of UHPC structural members.

To overcome some of the current knowledge gaps, the behavior of UHPC under fire conditions is studied at both the material and structural levels. As part of material characterization, thermal and mechanical property tests were carried out in the 20-800°C temperature range on two types of UHPC mixes (with and without polypropylene (PP) fibers). Data from measured property tests were utilized to propose empirical relations for high-temperature material properties of UHPC. As part of structural level characterization, four UHPC beams were tested under simultaneous application of loading and fire exposure. The test variables included the presence of polypropylene fibers, load level, and type of fire exposure. As part of the numerical study, a macroscopic finite element (MFE) model, originally developed to evaluate the fire resistance of reinforced concrete

(RC) beams made of conventional concrete, was extended to predict the thermo-mechanical response of UHPC beams under fire conditions. The novelty of the developed numerical model lies in the consideration of stresses resulting from pore pressure, structural loading, and thermal gradients for evaluation of spalling, instead of evaluating spalling based on only stresses due to pore pressure as in the previous studies. Further, the fire resistance analysis model was also modified to carry out a member-level structural analysis rather than an analysis of a single critical section. In addition, an expression for variation in permeability of concrete resulting from cracking patterns across the cross-section is proposed. The program also accounts for permeability variation due to the addition of polypropylene fibers. The model was validated by comparing thermal and structural response, the extent of spalling, and fire resistance predictions against measured test data on UHPC beams.

The validated model was further applied to conduct a set of parametric studies to quantify the effect of critical parameters on the fire response of UHPC beams. Results from the studies indicate that load level, fire scenario, cover thickness, specimen shape, sectional dimensions, and dosage of steel and polypropylene fibers have a significant influence on the fire response of UHPC beams. Further, among beams of different concrete types, the fire resistance of UHPC beams was significantly lower due to higher spalling levels resulting from their lower permeability, than normal strength concrete (NSC) and high strength concrete (HSC) beams, where permeability is relatively higher. Finally, results from the studies are used to develop a set of broad guidelines for the fire design of UHPC beams. By adopting the design guidelines, spalling in UHPC beams can be minimized and fire resistance can be improved.

This dissertation is dedicated to all lives touched by fire.

ACKNOWLEDGEMENTS

I would like to express my deepest gratitude to my Ph.D. advisor, Dr. Venkatesh Kodur for his invaluable guidance, constant support, and encouragement. He has continuously supported me for my academic growth and I thank him wholeheartedly for providing me this opportunity to pursue my research. I want to sincerely thank the members of my committee Dr. Nizar Lajnef, Dr. Weiyi Lu, and Dr. Lik-Chuan Lee for their insightful comments, suggestions, guidance, and support. I would like to extend my gratitude to Dr. Parviz Soroushian for his guidance on UHPC mix design and fabrication of the test specimens.

I would like to thank my peers and friends; Roya Solhmirzaei, Ankit Agrawal, Saleh Mohammad Alogla, Pratik Bhatt, Mohannad Naser, Svetha Venkatachari, Puneet Kumar, Augusto Masiero Gil, and Derek Hibner for their help and support. I would like to express my gratefulness to Mr. Siavosh Ravanbakhsh, the manager of Civil Infrastructure Laboratory, and Mr. Charles Meddaugh for their support and kindness during the trying times in the laboratory. My warmest thanks to my colleagues in Applied Engineering Sciences; Dr. Laura Genik and Jason Smith for their constant encouragement and understanding. I would like to thank Laura Taylor, Laura Post, Margaret Conner, and Bailey Weber for their administrative assistance. I am grateful for the support from the Department of Civil and Environmental Engineering and the College of Engineering for providing several resources during my graduate studies. In addition, I acknowledge the funding from United States Agency for International Development, U.S. Airforce Research Laboratory (AFRL), and Metna Company.

I would like to thank my husband, Harshal, for years of patience, love, unwavering support, and encouragement. I would like to express my deepest gratitude to my parents for their constant support, inspiration, and motivation. Special thanks to my puppy, Jasper, for his endless affection and positivity.

TABLE OF CONTENTS

LIST OF TABLES

LIST OF FIGURES

LIST OF SYMBOLS

A = Cross-sectional area of the beam

f'_c = Compressive strength of concrete at room temperature

f'_{cT} = Compressive strength of concrete at temperature 'T'

n_y and n_z = Components of outward normal vector to the surface in the plane of the cross section

α_i = Coefficient of thermal expansion in concrete layer 'i'

ε_{cr} = Creep strain in concrete

λ = Darcy's coefficient of permeability

D = Damage variable for concrete permeability

d = Effective depth of the beam

ρ_L = Density of liquid water

ρ_V = Density of water vapor in the concrete boundaries

$\rho_{V\infty}$ = Density of water vapor in the surrounding environment

d_f = Diameter of fiber

D_0 = Diffusion coefficient of water vapor at the boundaries of the beam

s = Distance along the boundary

y = Distance from geometrical centroid of beam cross-section to the center of the element

μ_V = Dynamic viscosity of water vapor

h = Time step

E_c = Elastic modulus of concrete at room temperature

E_{cT} = Elastic modulus of concrete at temperature 'T'

ε = Emissivity factor

F_e = Equivalent nodal heat flux for elements

F = Equivalent nodal heat flux vector

T_f = Fire temperature

R = Gas constant

M = Global mass matrix

K = Global stiffness matrix

q = Heat flux

h_{con} = Heat transfer coefficient convective

h_{rad} = Heat transfer coefficient radiative

h_f = Incremental rise in permeability during melting of polypropylene fibers

Q = Internal heat source

k_D = Intrinsic permeability of concrete accounting for damage

k_0 = Initial undamaged permeability of concrete

∇ = Laplacian differential operator

l_f = Length of fiber

L = Span length of the beam

E = Mass of evaporated water

J = Mass flux of water vapor

m_{LW0} = Mass of liquid water at t=0 (initial mass of liquid water)

m_L = Mass of liquid water at any time t

m_D = Mass of liquid water formed due to dehydration

m_V = Mass of water vapor

M_e = Mass matrix for each element

γ_{MD} = Mechanical damage parameter for concrete permeability

α_T = Mechanical property degradation factor at temperature 'T'

ε_{me} = Mechanical strain in concrete

ε_{mes} = Mechanical strain in steel

σ_{me} = Mechanical stress in concrete

M-κ = Moment-curvature

I = Moment of inertia of the beam

n_V = Number of moles of water vapor

β = Parameter tracing the shape of the σ-ε curve of UHPC

k_1 = Parameter describe ascending branch of the σ-ε relation of UHPC

k_2 = Parameter describe descending branch of the σ-ε relation of UHPC

ε'_c = Peak strain (strain at peak stress) at room temperature

ε'_{cT} = Peak strain (strain at peak stress) at any temperature 'T'

k_T = Permeability of concrete at temperature, T

k_f = Permeability of fiber tunnels

k_{fm}^{P} = Permeability of fibers and concrete matrix when they are in parallel with fluid flow

k_{fm}^{NP} = Permeability of fibers and concrete matrix when they are in series with fluid flow

PPF = Polypropylene fiber content by % of volume

P_V = Pore pressure

γ_{PP} = Pore pressure variation parameter for concrete permeability

σ_P = Pore pressure stress in concrete

ν_0 = Poisson's ratio of concrete at room temperature

ν = Poisson's ratio of concrete at any temperature 'T'

p = Probability of percolation of polypropylene fiber tunnels

RH = Relative humidity in the concrete

P_{S0} = Initial saturation pressure in concrete

N = Shape functions vector

ρ_v = Shear reinforcement ratio

ρc = Specific heat

σ = Stefan-Boltzman constant = 5.67×10^{-8} ($W/m^2 . K^4$)

σ-ε = Stress-strain

K_e = Stiffness matrix for each element

ε_0 = Strain at the geometrical centroid of beam cross-section

SF = Steel fiber content by % of volume

T = Temperature

$\dot{T}$ = Temperature derivative with respect to time

T_E = Temperature of the environment depending on exposure conditions

γ_{TG} = Temperature gradient parameter for concrete permeability

ρ_t = Tensile reinforcement ratio

f'_t = Tensile strength of concrete at room temperature

f'_{tT} = Tensile strength of concrete at temperature 'T'

t = Time

k_t = Thermal conductivity

σ_{th} = Thermal stress in concrete

ε_t = Total strain in concrete

ε_{ts} = Total strain in steel

ε_{th} = Thermal strain in concrete

ε_{ths} = Thermal strain in steel

ε_{tr} = Transient strain in concrete

T_v = Transition temperature for Poisson's ratio

V_V = Volume fraction of water vapor

V_L = Volume fraction of liquid water

V_{S0} = Initial volume fraction of solid

V_D = Volume fraction of dehydrated liquid water

f_y = Yield strength of steel at room temperature

f_{yT} = Yield strength of steel at temperature 'T'

CHAPTER 1

1. Introduction

1.1. Background

Concrete is one of the most extensively used building materials in the construction industry due to its excellent properties, such as strength, versatility, durability, non-combustion properties, ease of fabrication, and readily available raw materials. In recent years, research and development in the field of concrete technology have led to the development of ultra-high performance concrete (UHPC). UHPC is characterized as an advanced cementitious material typically made with very low water to binder ratio, high fineness admixtures, steel fibers, and without any coarse aggregates. UHPC has higher compressive (above 150 MPa) and tensile strength (5 MPa or higher), enhanced toughness, and increased durability than that of conventional normal strength concrete (NSC) or high strength concrete (HSC) [1,2]. Owing to the superior mechanical properties of UHPC, it has gained popularity in structural applications such as bridges, and to a limited extent in high-rise buildings.

Fire is one of the most serious threats that buildings can be exposed to and thus, a key consideration in building design is the fire resistance of structural members. Fire resistance is the duration during which a structural member exhibits resistance with respect to insulation, integrity, and stability criteria [3]. Concrete structures exhibit excellent fire resistance, and this is attributed to the low thermal conductivity and high thermal capacity of concrete, as well as to slower degradation of its strength and modulus properties with temperature. However, few preliminary studies have indicated that UHPC structural members do not exhibit the same level of fire resistance as that of NSC and HSC members. This is mainly due to the faster degradation of strength and modulus properties of UHPC with temperature, as well as its high susceptibility to fire-induced spalling. In

addition, although most of the high-temperature material properties have been widely studied for NSC and HSC, only a scarce amount of data is available for UHPC.

Fire-induced spalling is the break-up of chunks of concrete from a concrete member under severe fire exposure. Spalling can lead to loss of cross-section, thereby increasing heat penetration to inner concrete layers and steel reinforcement, leading to a decrease in the overall fire resistance of the structural member. Therefore, it is critical to consider spalling while evaluating the capacity of fire-exposed reinforced concrete (RC) members. Only limited studies in the literature have focused on developing approaches to assess and predict spalling of concrete under fire conditions. Even where advanced analysis methods are adopted for fire resistance analysis, fire-induced spalling is often not included in calculations for evaluating fire resistance. The current lack of spalling evaluation methods is due to the complexity of the spalling phenomenon and limited test methods and equipment to generate required data for validation of associated numerical models.

The current fire design provisions in codes assign fire resistance ratings to concrete members based on their sectional dimensions and cover thickness to steel reinforcement. These ratings are based on fire tests predominantly conducted on NSC members subjected to standard fire exposure and do not specifically consider fire-induced spalling that can take place in a concrete member. Hence, they might not be directly applicable to UHPC members. Thus, a rational approach that accounts for realistic fire exposure scenarios, loading conditions, high-temperature material properties, and fire-induced spalling is needed for reliable prediction of fire resistance of UHPC structural members. RC beams function in a building as essential load-bearing structural members and the complexities involved in tracing the fire response of beams are discussed below to gain a better understanding of the problem.

1.2. Behavior of Reinforced Concrete Beams under Fire Exposure

When exposed to fire, a reinforced concrete (RC) beam experiences a rise in sectional temperatures with time due to heat transmission from the fire-exposed surfaces of the beam to the interior section. The increased sectional temperatures will influence the structural behavior of the beam and can result in loss of capacity and stiffness in the beam, which in turn can lead to failure of the beam. The behavior of a typical RC beam under fire exposure is illustrated in Figure 1.1 (a). Beams are exposed to fire from three sides as shown in Figure 1.1 (b), as typically a slab is present on the top side of the beam. The beam has a flexural capacity of M_0 at ambient conditions. With increasing fire exposure time, the temperature rises within the beam cross-section (see Figure 1.1 (c)) through the heat conduction process and depends on the variation in the thermal properties of concrete and rebars with increasing temperature. The applied moment due to external load remains constant with progression in fire exposure time. However, the increasing sectional temperatures lead to gradual degradation of strength and modulus properties (mechanical properties) in concrete as well as reinforcing steel, which in turn leads to a decrease in moment capacity (M_0 to M_3) of the beam with time (T_0 to T_3) as shown in Figure 1.1 (d). In addition, the beam experiences increasing deflection as a result of a reduction in modulus properties of constituent materials (concrete and reinforcing steel), and also due to high-temperature creep effects, which become significant in the later stages of fire exposure. When the moment due to applied structural load exceeds the decreasing moment capacity of the beam, the beam experiences failure at that time (see Figure 1.1 (e)), and the fire exposure time to attain failure is taken as the fire resistance of the beam.

In addition, concrete members can experience spalling under fire exposure. If spalling of concrete occurs in RC beams, it can lead to loss of cross-section, which in turn can accelerate temperature

propagation and result in faster degradation of properties in concrete and steel, lowering the overall fire resistance of the beam. The effect of spalling is usually neglected in the fire design of NSC beams, as they are less prone to spalling. However, spalling can be a major problem in structural members made of HSC and UHPC, due to the built-up of high pore pressure as a result of its impermeable and dense microstructure. Further, owing to its significant higher strength, UHPC members have reduced sectional size (less thermal mass) and lower cover thickness as compared to structural members made of conventional concrete (NSC or HSC). Therefore, in the fire resistance evaluation of UHPC structures, all the influencing factors, and temperature-dependent material properties must be given due consideration.

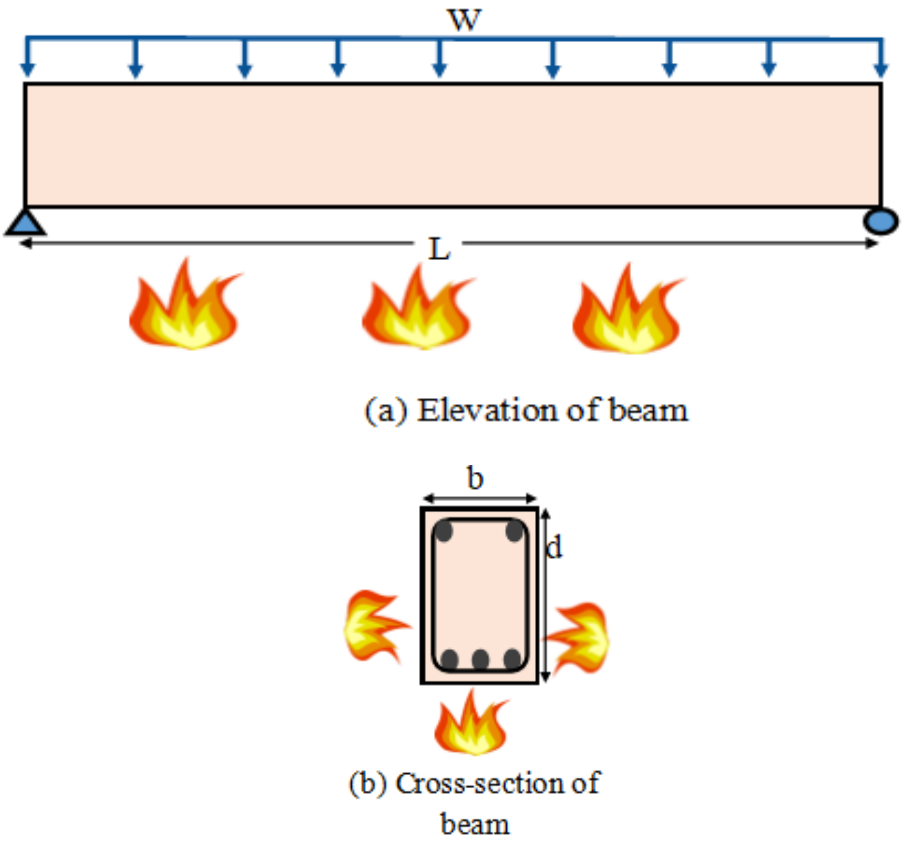

Figure 1.1. Behavior of typical RC beam under fire exposure.

Figure 1.1. (cont'd).

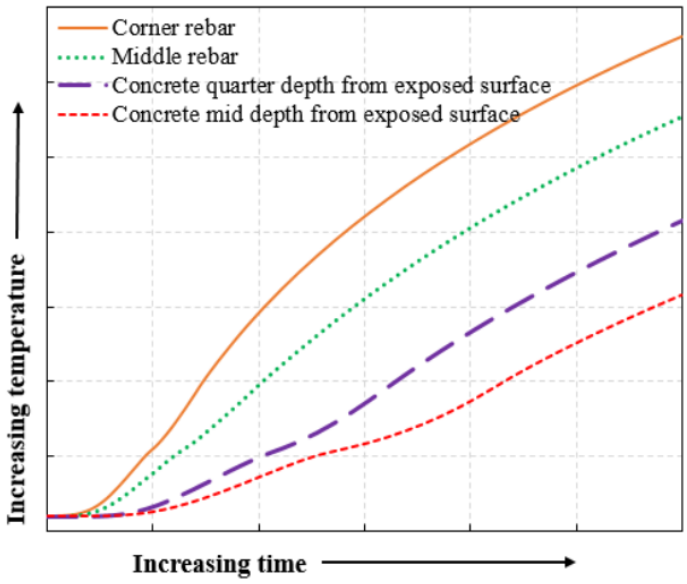

(c) Progression of sectional temperatures with fire exposure time

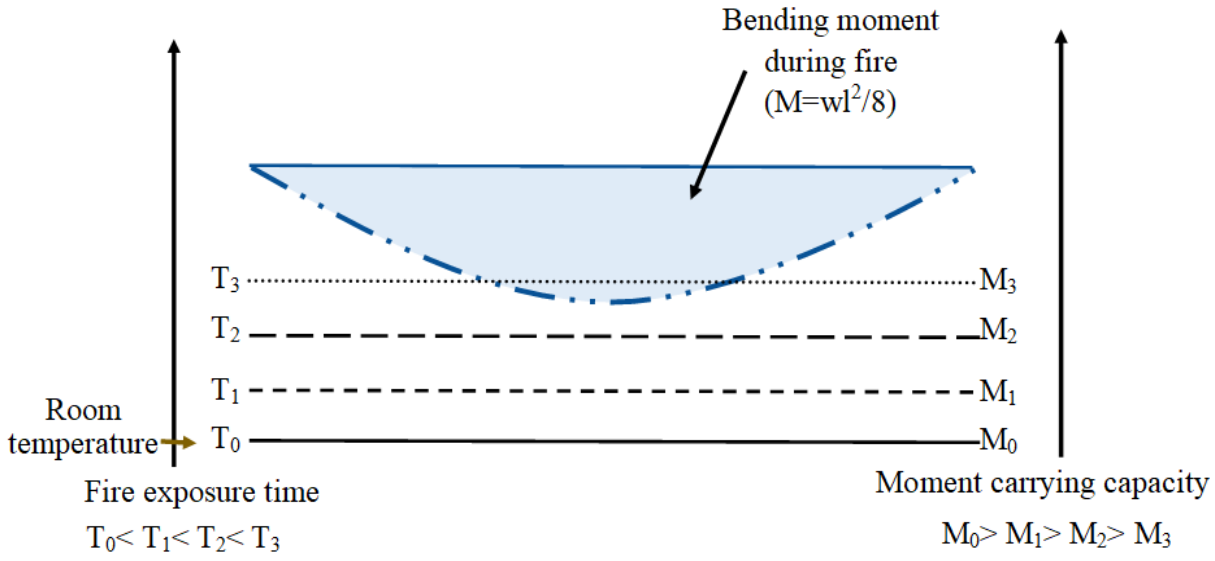

(d) Bending moment diagram and degradation in moment carrying capacity

Figure 1.1. (cont'd)

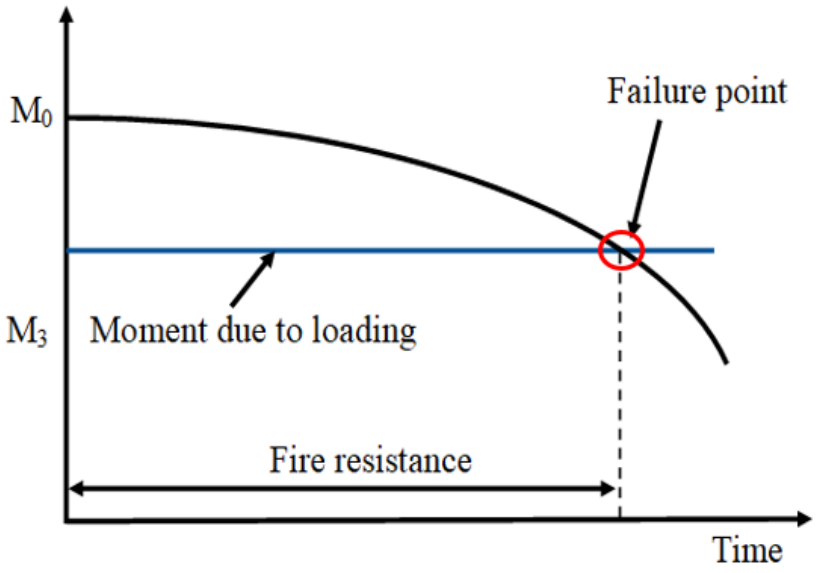

(e) Degradation of moment capacity with fire exposure time

1.3.High-Temperature Properties of UHPC

Fire resistance is defined as the duration of time during which a structural member withstands the adverse effects of fire without failure. For theoretically evaluating the fire resistance of a structural member, information on property variation of constituent materials (namely concrete, steel, etc.) at elevated temperatures is required. The properties of concrete that are needed for fire resistance analysis are thermal, mechanical, and specific properties for distinct phenomena such as fire-induced spalling. Thermal properties that include thermal conductivity, specific heat, thermal expansion, and mass loss determine the level of temperature rise in structural members, while the mechanical properties that include strength and modulus, as well as high temperature creep govern the extent of loss of sectional capacity and progression of deflections under fire exposure.

In addition, fire-induced spalling that occurs in concrete under certain conditions deteriorates the performance of a reinforced concrete member. For predicting such spalling, related properties such as permeability, moisture content, and tensile strength of concrete at high temperatures are

required. Previous research has shown that adding polypropylene (PP) and steel fibers are added to the concrete batch mix can minimize the extent of spalling. Addition of steel fibers enhances the tensile strength of concrete and helps to withstand higher tensile stress generated due to pore pressure developed at elevated temperatures, thus reducing spalling mainly in high strength concrete (HSC) members. On the other hand, polypropylene (PP) fibers melt when sectional temperatures in concrete under fire exposure reach about 160°C. This melting of PP fibers constructs channels and enhances permeability inside concrete, resulting in dissipation of high pore pressure generated within the concrete, and thus preventing the occurrence of spalling. Accordingly, the influence of fibers on the properties of concrete needs to be known to evaluate the fire response of fiber-reinforced concrete (such as UHPC) structural members. The thermal, mechanical, and special properties of concrete vary with temperature and are also influenced by the type of concrete mix (i.e. strength, aggregate type, and presence of fibers).

Establishing the behavior of UHPC at the material level and characterizing their high-temperature properties is important for quantifying the fire resistance of UHPC structural members. A good amount of data and well-established property relations are present for the high temperature thermal and mechanical properties of conventional concretes (NSC and HSC). However, a very limited amount of data is available on high-temperature material properties of UHPC. Moreover, at present, there are no standardized test methods for evaluating the properties of UHPC at elevated temperatures. Further, there is a lack of standardized testing procedures and instrumentation to measure spalling-related characteristics (such as pore pressure) and transport properties (such as porosity, permeability) at high temperatures.

1.4. Fire-induced Spalling Phenomenon in Concrete

Many experimental and numerical studies have been conducted in the last decades to gain an understanding of the driving mechanisms for spalling in concrete under fire exposure. Based on these studies, fire-induced spalling can be theorized to occur based on either of the two mechanisms, namely: (i) pore (or vapor) pressure development or, (ii) thermal stress generation. These two spalling mechanisms are schematically illustrated in Figure 1.2 for the case of a reinforced concrete (RC) slab subjected to one-dimensional heating (fire) from the bottom surface. As per the pore pressure mechanism [4,5], spalling occurs when stresses generated from temperature-induced pore pressure exceed the tensile strength of concrete. When a concrete member is subjected to high temperatures, as in the case of fire, moisture present in concrete turns into vapor and this vapor moves inwards or outwards of the member depending on temperature and pressure gradients developed in the section. Depending on the permeability of concrete, a part of the vapor escapes through the heated surface and the remaining portion of the vapor moves towards the inner cooler regions of concrete, where the vapor condenses back to liquid water. With the progression of fire exposure time, the processes of concrete drying, moisture migration, and vapor condensation result in the formation of a saturated layer at a certain distance away from the heated dry concrete surface. This saturated layer is termed as “moisture clog” and this clog prevents further migration of water vapor towards inner regions, resulting in a build-up of pore (or vapor) pressure near the heated surface as shown in Figure 1.2 (a)-(iii). At the locations where pore pressure is accumulated, tensile stresses are generated in the member. When the stress from temperature-induced pore pressure exceeds the tensile strength of concrete (which is decreasing with temperature), spalling occurs in the concrete member. The transfer and movement of moisture within a concrete section can be explained based on Darcy and Fick’s laws [6]. The development

of thermal gradients, pore pressure as well as resulting spalling in the section of the slab are schematically illustrated in Figure 1.2 (a).

As per the thermal stress mechanism [7,8], spalling is said to occur due to fracture of concrete resulting from thermal stresses. The rise of temperature in the outer layers closer to a fire exposed face of the concrete member occurs at a considerably faster rate than the inner layers (core) of the concrete member (away from the fire-exposed surface), due to high thermal inertia of concrete (i.e. low thermal conductivity and high specific heat). This variation in temperature between the outer and inner concrete layers results in the development of high thermal gradients along the cross-section of the fire exposed concrete member. The large thermal gradients cause non-uniform expansion of the hotter parts, which is restrained by the cooler inner regions. Due to this restraint to thermal expansion, significant thermal stresses are induced in the member, resulting in compressive stresses parallel to the heated surface and tensile stresses in the cooler regions as shown in Figure 1.2 (b)-(iii). The compressive stresses in the heated concrete surface induce transverse tensile stresses and when these transverse tensile stresses exceed the tensile strength, brittle fracture of concrete (pieces) occurs. This phenomenon is explained based on fracture mechanics principles [9,10]. The build-up of thermal gradients, stress, and the resulting spalling in a slab are illustrated in Figure 1.2 (b). If the concrete member is subjected to structural loading during a fire incident, the applied loading generates an additional component of stress (mechanical), and this may amplify the stress developed from thermal expansion and pore pressure, which in turn can lead to accelerated spalling. However, the effect of load-induced stress on spalling is ignored in most previous studies.

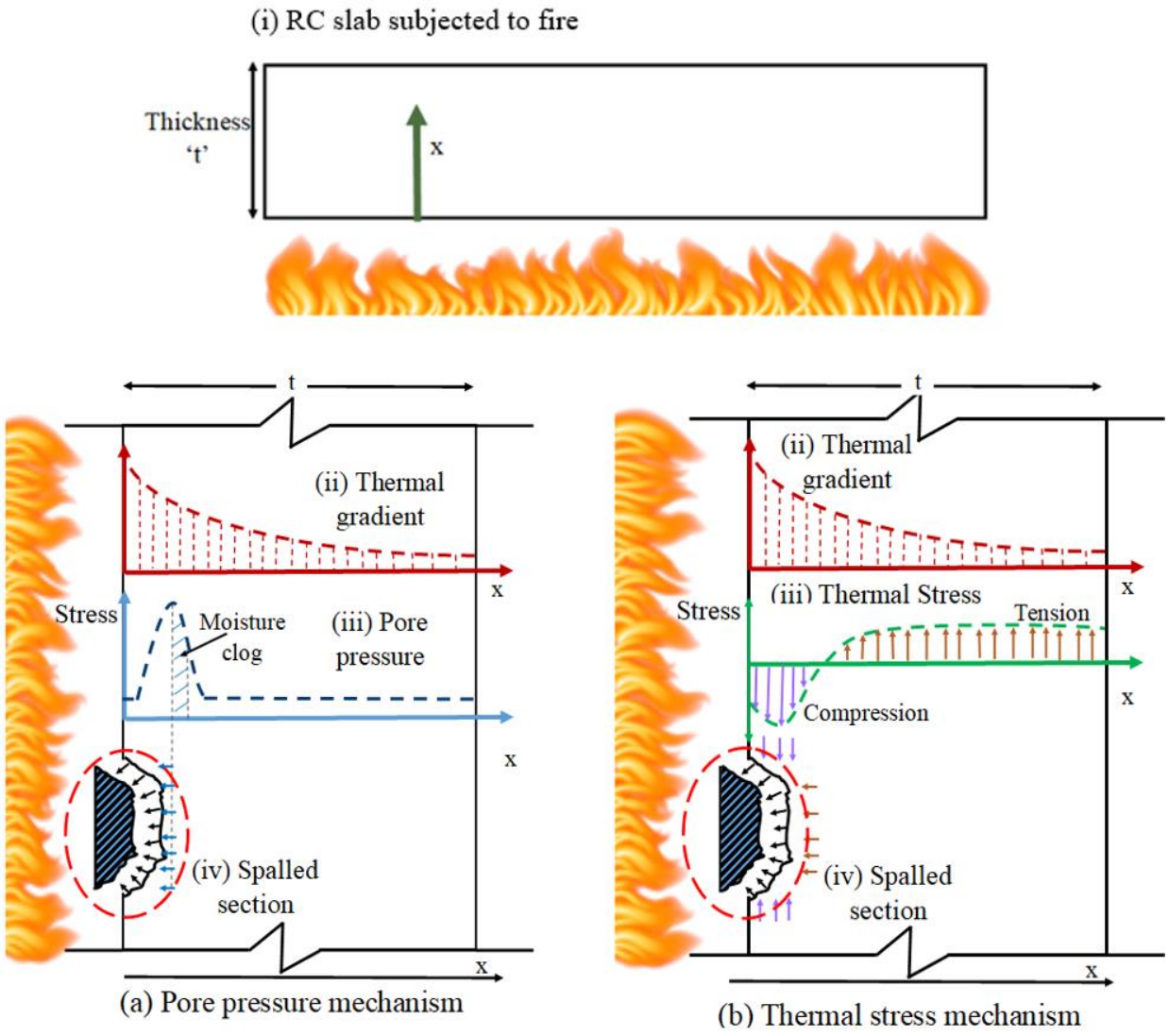

Figure 1.2. Schematic illustration of spalling mechanism in a fire exposed concrete slab: (a) Pore pressure; (b) Thermal stress.

Some research studies also indicate that spalling is a combined action of both the pore pressure and thermal stress mechanisms. Despite a number of experimental and numerical studies on fire-induced spalling in concrete members in the past three decades, there is still a lack of accurate numerical approaches for modeling spalling. Further, among the different concrete types, UHPC and HSC are more susceptible (than conventional NSC), to fire-induced spalling, specifically UHPC due to its extremely dense microstructure. Therefore, for realistic fire resistance evaluation of UHPC members, a validated spalling model is imperative.

1.5. Research Approach

1.5.1. Hypothesis

To overcome some of the current knowledge gaps and develop a better understanding of the fire behavior of UHPC beams, this research project is developed with a hypothesis stated as follows: "The response of UHPC beams under fire conditions is significantly influenced by temperature-dependent thermo-mechanical properties of constituent materials and also the occurrence of fire-induced spalling. Therefore, a realistic assessment of fire performance of UHPC beams requires proper consideration to temperature-dependent properties of UHPC and reinforcement, as well as a realistic fire-induced spalling criterion."

1.5.2. Research Objectives

This study aims to develop a comprehensive understanding of the performance of UHPC beams under fire conditions and develop a rational approach for the fire design of UHPC beams. As part of this thesis, the following specific objectives will be addressed:

- Carry out a state-of-the-art review on the behavior of UHPC structural members under fire conditions. This includes reviewing studies on the effect of temperature on material properties of UHPC, and also structural fire tests and numerical studies carried out on UHPC members.
- Undertake material level tests on UHPC specimens at elevated temperatures to quantify the effect of high temperature on the thermal and mechanical properties of UHPC.
- Conduct fire resistance experiments on UHPC beams to evaluate their fire behavior, as well as spalling progression under fire conditions.
- Extend a macroscopic finite element based numerical model to trace the response of UHPC beams under fire conditions. The model will incorporate fire-induced spalling analysis

through an improved spalling sub-model, which will consider the stresses resulting from pore pressure, thermal gradients, and structural loading in concrete members to evaluate spalling. In addition, the numerical model will account for material nonlinearities and temperature-dependent property degradation in constituent materials.

- Utilize data generated from fire resistance tests to validate the developed numerical model. The validation will be carried out by comparing thermal, structural, and spalling predictions from the model with measured results in fire tests.
- Conduct parametric studies applying the validated numerical model to quantify the influence of various critical factors influencing the behavior of UHPC beams under fire conditions.
- Develop rational design guidelines for fire resistance design of UHPC beams based on the data generated from fire tests and parametric studies.

1.5.3. Research Methodology

The above-stated research objectives will be realized through experimental and numerical studies on UHPC members under fire conditions. Experiments will be carried out on UHPC at both material and structural levels. At the material level, a comprehensive testing program will be undertaken on UHPC to generate data on high temperature thermal and mechanical properties. At the structural level, four RC beams made of UHPC will be designed, fabricated, and tested under structural loading and fire conditions.

As part of the numerical study, a macroscopic finite element based model originally developed by Dwaikat and Kodur [11] for NSC and HSC beams will be extended and upgraded to evaluate the fire-response of UHPC beams. An improved spalling sub-model will be incorporated into the macroscopic numerical model. Spalling will be based on the stresses arising from the effects of

pore pressure, thermal gradients, and structural loading generated in a concrete member during fire exposure. In addition, the numerical model will also be modified to carry out a member level analysis rather than analysis of a single critical section and accounts for spalling patterns resulting from the variation of stresses along the fire exposed length of the beam. Furthermore, the numerical model will account for high-temperature stress-strain curves (including strain hardening and softening) of concrete and steel, temperature-dependent thermal and mechanical properties, and permeability variations of concrete. Data from fire tests will be used to validate the developed numerical model for thermal, structural, and spalling analysis. The validated numerical model will be applied to conduct detailed parametric studies to quantify the effect of critical factors on the fire performance of UHPC beams. Results from parametric studies will be utilized to develop guidelines for the fire design of UHPC beams.

1.6. Layout

The research undertaken as part of this dissertation is presented in seven chapters. Chapter 1 provides a general background on the characteristics of UHPC, fire response of reinforced concrete beams, and fire-induced spalling phenomenon. Chapter 1 also lays out the research objectives and methodology of this study. Chapter 2 summarizes a state-of-the-art review of the behavior of UHPC beams exposed to fire. The review includes a summary of reported experimental and numerical studies undertaken on UHPC members, as well as presents fire design provisions for RC structural members in current codes of practice. This chapter also reviews the high-temperature material property tests undertaken on concrete needed for modeling the fire response of beams. Chapter 3 presents the fire resistance experiments conducted on UHPC beams with different types of fiber reinforcement, tested under combined effects of fire and structural loading. This chapter also presents the undertaken high-temperature material property tests on UHPC and the development

of empirical relations based on test data, for predicting high-temperature properties over a wide temperature range. Chapter 4 provides details on the macroscopic finite element based numerical model for fire resistance analysis and spalling prediction in UHPC beams. Extension of the numerical model, as well as validation of the extended numerical model, are also presented in this chapter. Chapter 5 presents the results from the parametric study on the impact of critical parameters on the fire response of UHPC beams. This chapter describes A detailed discussion on the trends along with the ranges of parameters governing the fire resistance of UHPC beams is described in this chapter. Chapter 6 provides fire design guidelines to mitigate fire-induced spalling and improve the fire resistance of UHPC beams. Finally, conclusions and recommendations for future research are summarized in Chapter 7.

CHAPTER 2

2. State-of-the-art Review

2.1. General

Fire is one of the most severe hazards to which structural members may be subjected during their lifetime and hence the provision of fire resistance to structural members is a key requirement in building design. Unlike steel structures, concrete structures possess a high level of fire resistance and this is due to the superior thermal and mechanical properties of concrete at elevated temperatures. However, preliminary studies have shown that ultra-high performance concrete (UHPC) members, unlike conventional normal strength concrete (NSC) members, do not exhibit good fire resistance due to faster degradation of thermal and mechanical properties and also due to high susceptibility of UHPC to fire-induced spalling. To mitigate such fire-induced spalling, the addition of different types of fibers, such as steel and polypropylene (PP) is often recommended for high-strength concrete mixes. At present, there is very limited data on fire resistance of UHPC members, as well as the effectiveness of fibers in mitigating spalling in UHPC members.

Fire resistance evaluation of reinforced UHPC members requires a detailed analysis of the thermal and structural response of the member, which in turn requires an input of properties of UHPC (and steel reinforcement) as a function of temperature. Thermal and mechanical properties of UHPC are probable to vary differently at elevated temperatures as compared to conventional normal strength concrete (NSC) and high strength concrete (HSC), due to microstructural differences. Currently, only limited studies have been reported on the high-temperature properties of UHPC and the fire behavior of UHPC structural members. Further, there is a lack of information on the transport properties of UHPC required for the prediction of spalling, such as porosity, permeability, and so on.

This chapter presents a state-of-the-art review of the currently available information on the high-temperature properties of UHPC at a material level. Besides, previous experimental and numerical studies on the response of UHPC structural members under fire conditions are reviewed. Also, the existing numerical models and approaches for predicting fire-induced spalling in concrete, which can be a dominating factor for the fire performance of UHPC members, are discussed. Finally, a review of design provisions in current codes and standards for fire design of concrete members is presented.

2.2. High-Temperature Properties of UHPC

Temperature-dependent thermal and mechanical properties of concrete and steel reinforcement have been extensively studied in the literature [12–14]. Further empirical relations defining the temperature dependence of these properties are specified in a few codes, standards, and manuals (such as ASCE manual [15] and Eurocode2 [16]). However, the information available regarding the temperature-dependent properties of UHPC is rather limited. A review of the information available on these properties is presented in the following sections. Typically, UHPC is made with steel fibers, which contributes to its high ductility and tensile strength properties. However, some innovative UHPC mixes do not contain steel fibers and previous tests on such mixes (plain UHPC) are also included in the literature review for the sake of completeness.

2.2.1. Thermal Properties

2.2.1.1. General

Typically, building fires can reach temperatures up to 1000°C. Thus, in typical fire scenarios, the sectional temperature in a concrete member will be in the range of 20–800°C. Therefore, for analytically evaluating the fire resistance of a structural member, the variation of material properties is to be known in the temperature range of 20–800°C. Thermal properties, namely,

thermal conductivity, specific heat, thermal expansion, and mass loss are needed for predicting the temperature profiles and subsequent thermo-mechanical analysis in concrete structures under fire exposure. The thermal properties of concrete are significantly influenced by the batch mix proportions of concrete, type of aggregate, and moisture content. The temperature-dependent thermal properties of NSC and HSC have been extensively studied by numerous test programs in the literature [17]. Data generated in the reported tests have been used to develop temperature-dependent thermal property relations of concrete and these are specified in the ASCE manual [15], Eurocode 2 [16], and other guidance documents.

To start with, thermal conductivity is the amount of heat flow under a unit temperature gradient across any material and thus, indicates the rate at which a given material transfers heat. The room temperature thermal conductivity of NSC and HSC ranges between 1.4 and 3.6 W/m K, and 2.4 and 3.6 W/m K [17–19]. Typically, the thermal conductivity of HSC is higher than that of NSC due to a low water-cement ratio (w/c) and the incorporation of different binders (such as slag and silica fume) in HSC [20,21]. Also, concretes made of siliceous aggregates have higher conductivity than those made of carbonate aggregates [22]. The thermal conductivity of concrete decreases with temperature due to loss of moisture with an increase in temperature. The second thermal property is specific heat which describes the amount of heat required to raise a unit mass of material a unit temperature. The specific heat of NSC at room temperature is in the range of 840 J/kg K and 1800 J/kg K, whereas that of HSC is in the range of 700 and 1000 J/kg K [18,20]. Similar to thermal conductivity, the specific heat is also highly influenced by moisture content, aggregate type, and mix proportions. The specific heat of carbonate aggregate concrete is higher than that of siliceous aggregate concrete in the 600-800ºC temperature range due to the substantial amount of heat needed for dissociation of dolomite in the carbonate aggregates [23]. The third property, thermal

expansion characterizes the percentage change in the length of a concrete specimen when subjected to elevated temperatures. The thermal expansion of concrete increases from zero at room temperature to about 1.3% at 700°C and then generally remains constant through 1000°C [17]. The variation in thermal expansion with temperature in HSC and NSC are similar and mainly dependent on w/c ratio, moisture content, and aggregate type [22]. Concrete made with siliceous aggregate has a higher thermal expansion than concrete made with carbonate aggregate [17]. The fourth thermal property, mass loss depicts the decrease in mass of concrete with increasing temperature resulting from loss of moisture. Mass loss can affect the enthalpy and amount of latent heat for water evaporation which directly affects all the other material properties of concrete. HSC exhibits a similar trend in the temperature-dependent mass loss as that of NSC. The mass loss is minimal for both carbonate and siliceous aggregate concretes up to about 600°C. Beyond 600°C, carbonate aggregate concrete exhibits significantly higher mass loss due to the dissociation of dolomite [17,19]. The temperature variation of thermal properties of concrete, apart from depending on the batch mix proportions, also relies on the specimen conditions and test procedure (such as the size of sample and moisture content) adopted in undertaking property tests [3,24,25]. Thus, a review of test methods and procedures specified in standards for evaluating high temperature thermal properties of concrete is presented in the following sub-section.

2.2.1.2. Test methods for high-temperature thermal properties

The thermal properties of concrete, especially at elevated temperatures, can vary significantly based on test procedures, conditioning of specimens, and equipment (instrument) used to measure these properties. Standardized test methods and procedures are required to minimize the variations in measured thermal properties arising from test methods, testing parameters, and equipment. To address this requirement, a review was undertaken to determine the suitable high-temperature test

standards for property evaluation. Test procedures provided in current test standards for measuring thermal properties are mostly focused on room temperature conditions and only limited standardized test procedures exist for evaluating thermal properties at elevated temperatures, as summarized in Table 2-1. It can be seen that there is a lack of test methods and procedures in American Society for Testing and Materials (ASTM) standards for evaluating thermal conductivity of concrete beyond the temperature of 85ºC and specific heat beyond 600ºC [25].

Table 2-1. Test standards for evaluation of thermal properties.

Thermal property	Temperature range	Test standards
Thermal conductivity	Ambient temperature to 85°C	ASTM C177, ASTM C1363 ISO 8302
	Elevated temperature (upto 1000°C)	**No ASTM standard** ISO 22007-2
Specific heat	Ambient temperature to 600°C	ASTM E1269 ISO 11357
	Elevated temperature (upto 1000°C)	ISO 22007-2
Thermal expansion	Ambient to elevated temperature (upto 1000°C)	ASTM E831 ISO 11359-2
Mass loss	Ambient to elevated temperature (upto 1000°C)	ASTM E1131 ISO 11358

The test procedure for measuring the thermal conductivity of concrete at room temperature is outlined in ASTM C177 [26] and ASTM C1363 [27] standards. ASTM C177 [26] provisions specify that thermal conductivity can be measured through guarded hot-plate apparatus. This test involves the construction of a hot plate apparatus abiding by the design requirements specified in the standard. The principle involved is to establish a temperature difference across a concrete sample of known thickness and to calculate thermal conductivity from the direct measurement of steady-state power required to maintain this temperature difference. However, the ASTM C177 test procedure is applicable only for measuring thermal conductivity at room temperature (±10ºC). ASTM C1363 [27] provisions specify design guidelines for hot box apparatus in order to measure

the thermal conductivity of building materials but it is limited to temperatures up to 85ºC. ASTM C1363 method is analogous to the ASTM C177 test procedure, except it is meant to be used for testing large specimens whose dimensions are controlled by the design of the hot box apparatus. It is noteworthy that ASTM standards do not prescribe specific test methods and procedures for measuring thermal conductivity at elevated temperatures, beyond 85ºC. Standard ISO 8302 [28] also provides provisions for thermal conductivity measurements, which are similar to ASTM C177 provisions, whereas ISO test standard 22007–2 [29] specifies transient plane heat source (TPS) or hot disc method for measuring thermal conductivity in the temperature range of 20 to 1000ºC. The TPS method is based on the principles of measuring the resistance of a transiently heated plane sensor fitted in between two test specimens.

For measuring the specific heat of concrete, ASTM E1269 [30] recommends using the differential scanning calorimetry method (DSC) in the range of room temperature to 600ºC. ISO 11357–4 [31] standard also recommends the DSC method. DSC technique is based on the principle of measuring the thermal energy necessary to establish a nearly zero temperature difference between a test specimen and a specimen of inert reference material. The accuracy of the DSC technique in determining the specific heat may not be particularly good and sometimes can range as high or as low as ±20% [17]. ISO 22007-2 [29] recommends the transient plane heat source (TPS) or hot disc method for the evaluation of specific heat up to a temperature range of 1000ºC.

For determining the thermal expansion of construction materials, a standardized test method is specified by ASTM E831–14 [32]. This method utilizes the thermo-mechanical analysis technique for room temperature as well as high-temperature measurements. The principle is based on evaluating the coefficient of linear thermal expansion by measuring the change in test specimen length as a function of temperature at a constant heating rate. This test method is similar to ISO

11359-2 [33], but is different in technical detail (such as maximum heating rate and specimen size) and focuses more on plastic materials.

For measuring the mass loss of construction materials, ASTM E1131 [34] specifies the thermo-gravimetric procedure in the temperature range up to 1000ºC. ISO 11358 [35] also recommends the thermo-gravimetric method for mass loss measurement, but ASTM E1131 is more detailed and specific. The working principle of the thermo-gravimetric method is heating a specimen of known mass to a target temperature at a constant rate and measuring its mass continuously as a function of temperature and time.

2.2.1.3. Previous studies on high-temperature thermal properties

While numerous test programs have been undertaken for characterizing the high-temperature thermal properties for normal strength concrete (NSC) and high-strength concrete (HSC), only a scarce amount of data is present on the variation of thermal properties with elevated temperature for ultra-high performance concrete (UHPC) and fiber-reinforced UHPC. From a review of literature, published test data on high-temperature thermal properties of UHPC is plotted in Figure 2.1-Figure 2.4 along with test data [20,21,25], Eurocode 2 [16] and ASCE manual [22] relations for conventional concrete types. The ASCE relations were developed for NSC only, whereas the Eurocode 2 relations were developed for both NSC and HSC [36]. The reported studies on thermal properties of UHPC at high temperatures are tabulated in Table 2-2 and it is evident that an almost negligible amount of data has been reported on thermal properties of UHPC.

Ju et al. [37] examined the effects of varying steel fiber content on the evolution of thermal conductivity, specific heat, mass loss, and thermal expansion in the 20-250ºC temperature range, which covers lower temperatures relative to those encountered in a typical fire scenario. The test data showed that specific heat and thermal expansion decrease with increasing steel fiber content,

whereas thermal conductivity and mass loss were similar for UHPCs with various fiber contents. Further, the temperature-dependent variation of thermal conductivity and thermal expansion of UHPC were found to be similar to HSC but higher than NSC. Specific heat and mass loss of UHPC were observed to be lower than NSC and HSC.

Zheng et al. [38] evaluated thermal expansion for three batches of UHPC mixes with different volume fractions of steel fibers at 20, 200, 400, 600, and 800°C. The study reported that the thermal expansion of UHPC with steel fibers was higher than that of NSC with siliceous aggregate in the 20-600°C range. Above 600°C, the thermal expansion of UHPC with steel fibers was lower than that of concretes with siliceous aggregates. In addition, the results showed that the thermal expansion of UHPC increases with an increase in steel fiber content at elevated temperatures.

Sanchayan and Foster [39] evaluated mass loss in 20-300°C and thermal expansion in 20-600°C for plain UHPC and steel-reinforced UHPC. In the study, the average mass loss was about 5% at 300°C and test specimens experienced violent explosive spalling around 300°C. The thermal strain of UHPC with steel fibers was found to be similar to that of the siliceous-aggregate NSC model in Eurocode2 [16].

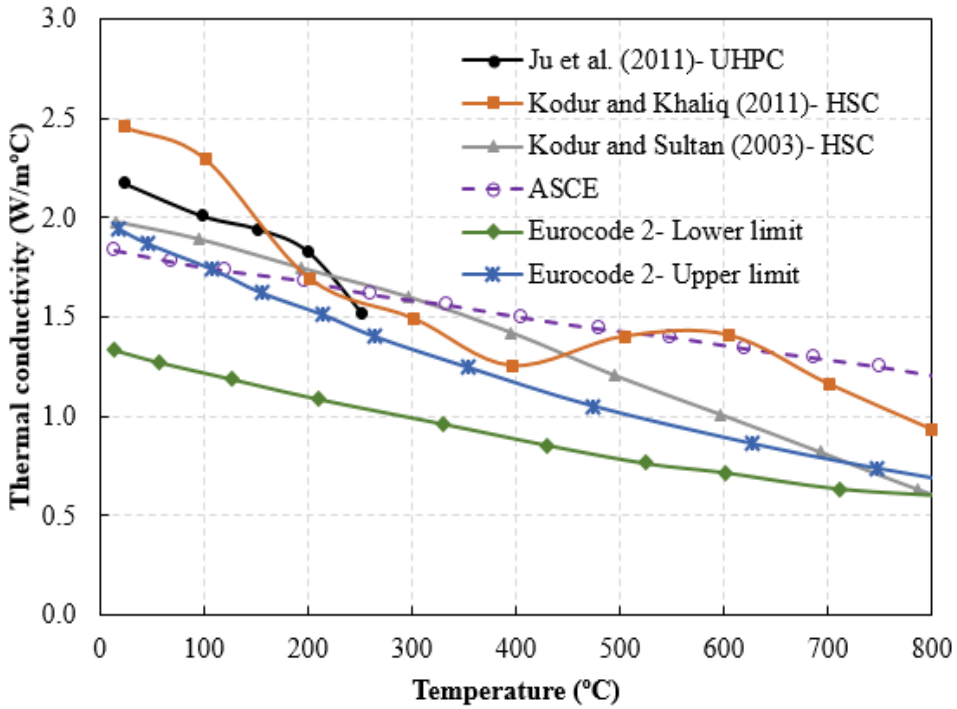

Figure 2.1. Variation of thermal conductivity in different concrete types with rise in temperature.

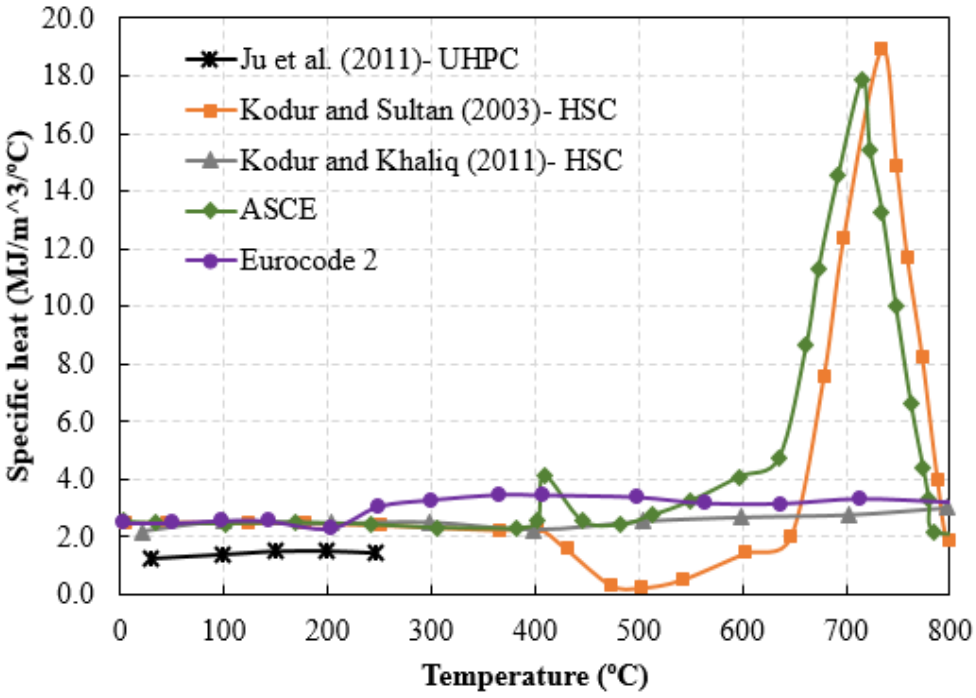

Figure 2.2. Variation of specific heat in different concrete types with rise in temperature.

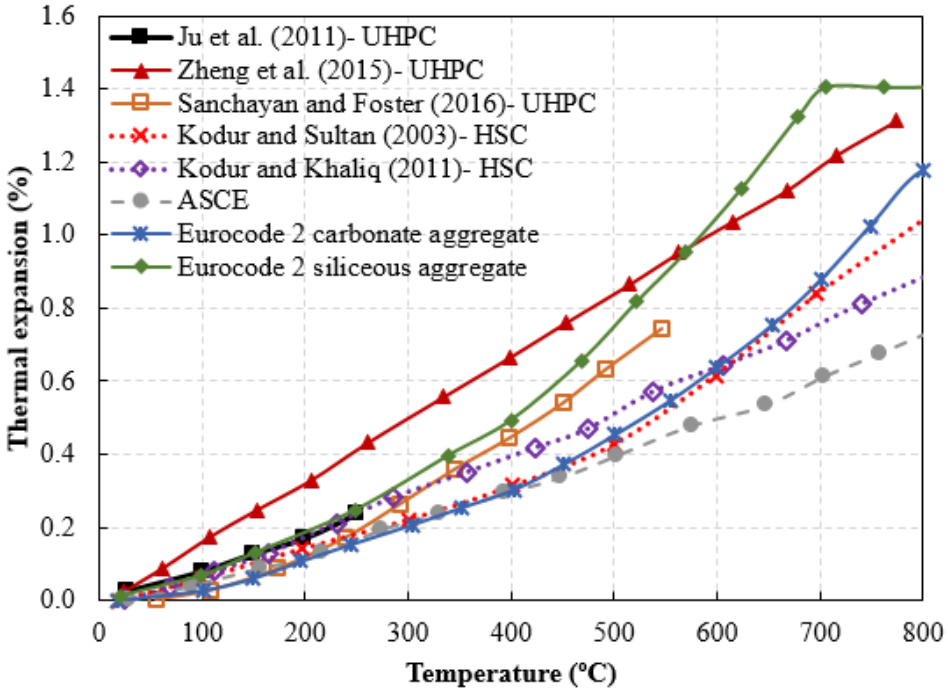

Figure 2.3. Variation of thermal expansion in different concrete types with rise in temperature.

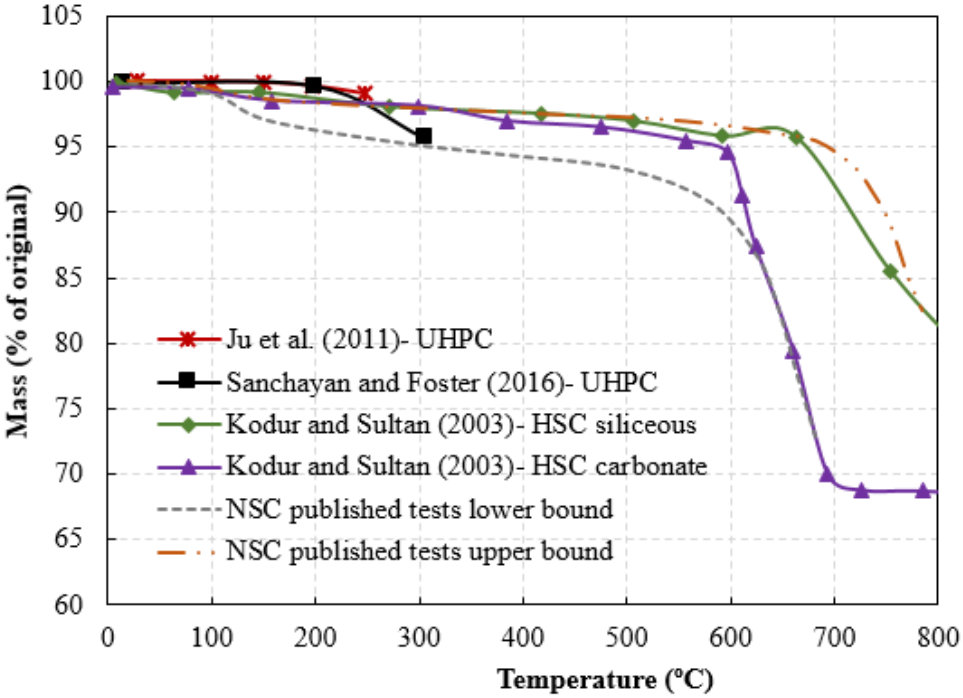

Figure 2.4. Variation of mass loss in different concrete types with rise in temperature.

Table 2-2. Reported high-temperature thermal property tests on UHPC.

Reference	Fibers (dosage %)	Compressive strength (MPa)	Temperature range	High-temperature property
Ju et al. (2011)	No fibers	157	20-250°C	Thermal conductivity
	Steel (1%)	169		Specific heat
	Steel (2%)	179		Mass loss
	Steel (3%)	191		Thermal expansion
Zheng et al. (2015)	Steel (1%)	143	20-800°C	Thermal expansion
	Steel (2%)	155		
	Steel (3%)	159		
Sanchayan and Foster (2016)	No fibers	144	20-300°C	Mass loss
	Steel (2%)	170	20-600°C	Thermal expansion

2.2.2. Mechanical Properties

2.2.2.1. General

Mechanical properties needed for fire resistance evaluation of concrete structural members include compressive strength, tensile strength, elastic modulus, creep, and stress-strain relations. The compressive (or tensile) strength is the ability of a material to resist corresponding stresses arising from compression or (tension) loading. The stress-strain response of a material captures incremental deformation (strain) under applied loading (stress). The peak stress from the stress-strain response is taken as the strength of the material and the slope of the stress-strain curve in the linear range is taken as the elastic modulus.

Generally, concrete up to a compressive strength of 70 MPa is classified as normal-strength concrete (NSC), concrete with compressive strength in the range of 70-150 MPa is referred to as HSC, while concrete with compressive strength above 150 MPa is designated as UHPC [36,40]. Mechanical properties of all types of concrete degrade with a rise in temperature due to temperature-induced microstructural changes, which are mainly influenced by the moisture content, mix proportions, and volume of admixtures in concrete. A good amount of high-temperature mechanical properties test data is available for both NSC and HSC with different types

of aggregates. The most widely adopted temperature-dependent concrete property relations are provided by ASCE Manual [22] and Eurocode 2 [16]. The ASCE material model was developed for NSC and the Eurocode model was developed for both NSC and HSC. In addition to these property relations, a widely accepted material model for HSC was developed by Kodur et al. [13,41], which is an extension to the ASCE relations for NSC.

The compressive strength of NSC gets minimally deteriorated by exposure to high temperatures up to 400°C, beyond which NSC exhibits gradual loss in compressive strength as shown in Figure 2.5. This slow degradation of strength in NSC can be attributed to the low volumes of fine supplementary cementitious materials in conventional NSC batch mix, which results in high permeability allowing easy diffusion of pore pressure developed as a result of moisture evaporation. On the contrary, HSC experiences a rapid degradation in compressive strength with temperature retaining about 60-70% of its initial compressive strength as shown in Figure 2.6. HSC batch mix utilizes admixtures, binders, and silica fume to produce a dense and superior microstructure, which results in faster degradation of strength. Additionally, the compact microstructure of HSC prevents the escape of moisture and leads to a build-up of pore pressure, thereby increasing the propensity of HSC to spall.

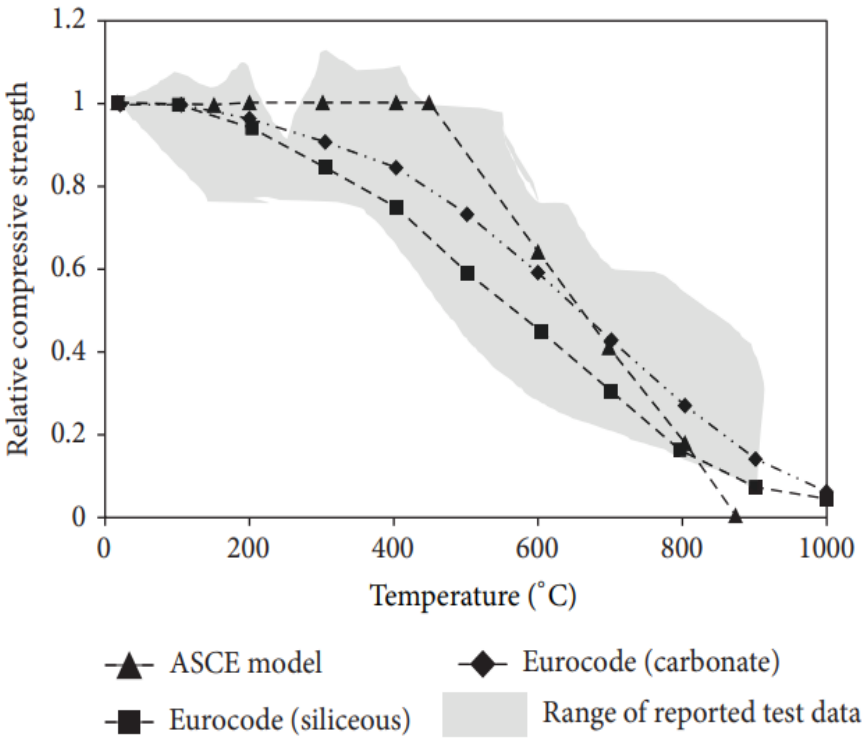

Figure 2.5. Variation of compressive strength with temperature for NSC [17].

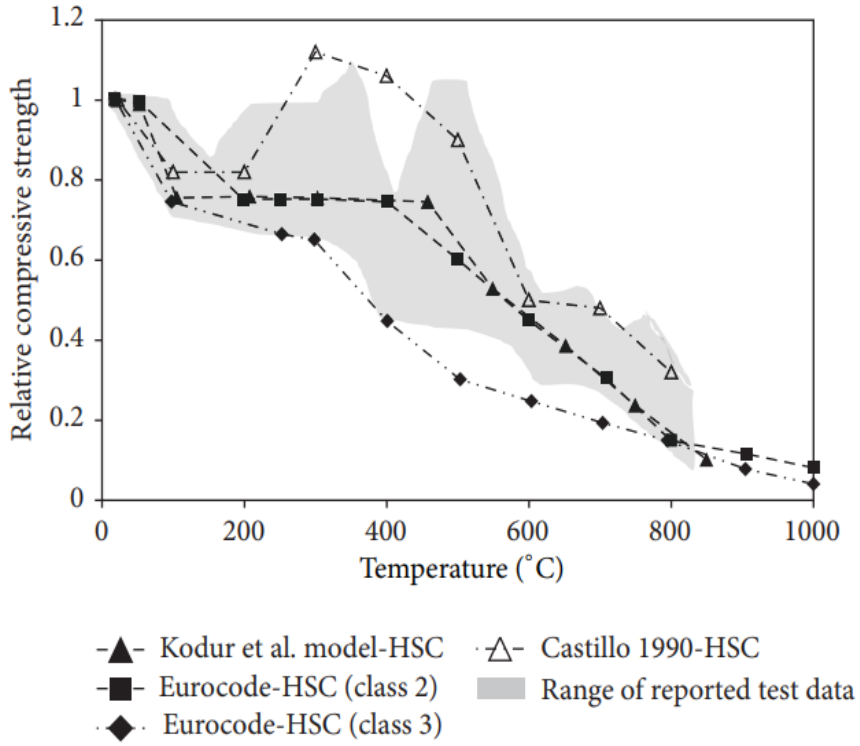

Figure 2.6. Variation of compressive strength with temperature for HSC [17].

The ambient tensile strength of concrete is much lower than the compressive strength of concrete, however, it can be crucial under fire conditions. Primarily, tensile strength is important because it resists tensile stresses and can control crack propagation in the member. In addition, higher tensile strength helps to withstand tensile stresses generated from pore pressure and can prevent fire-induced spalling in concrete. Figure 2.7 shows compiled data on the tensile strength of concrete at elevated temperatures from different codes of practice and previous studies [17]. At 300°C, NSC loses about 20% of its initial tensile strength and above 300°C, the tensile strength in NSC drops at a rapid rate due to extensive thermal damage in the form of microcracks. HSC also exhibits a similar trend in loss of tensile strength with temperature due to the development of thermal stresses and pore pressure in its dense microstructure [42]. There are relatively fewer studies on the tensile behavior of concrete at elevated temperature, as compared to compressive strength.

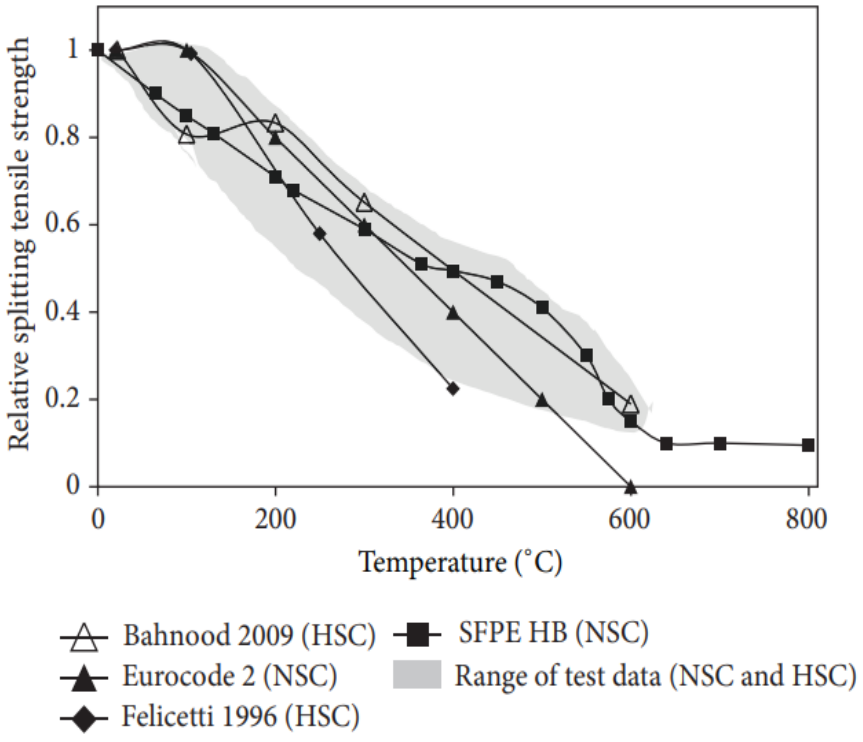

Figure 2.7. Variation of tensile strength with temperature [17].

The modulus of elasticity of concretes at room temperature varies over a wide range of 5–35 GPa and degrades rapidly with a rise in temperature. As shown in Figure 2.8, the degradation of elastic modulus with temperature of HSC is similar to that of NSC, with a majority of the degradation in elastic modulus occurring beyond 400°C. At around 600°C, elastic modulus losses about 80% of its room temperature value for both NSC and HSC. Beyond 600°C, concrete softens significantly, and elastic modulus is marginal as reported by test data. The loss of elastic modulus in both NSC and HSC can be attributed to the disintegration of hydrated cement products and the breakage of chemical bonds in the cement paste in the concrete microstructure.

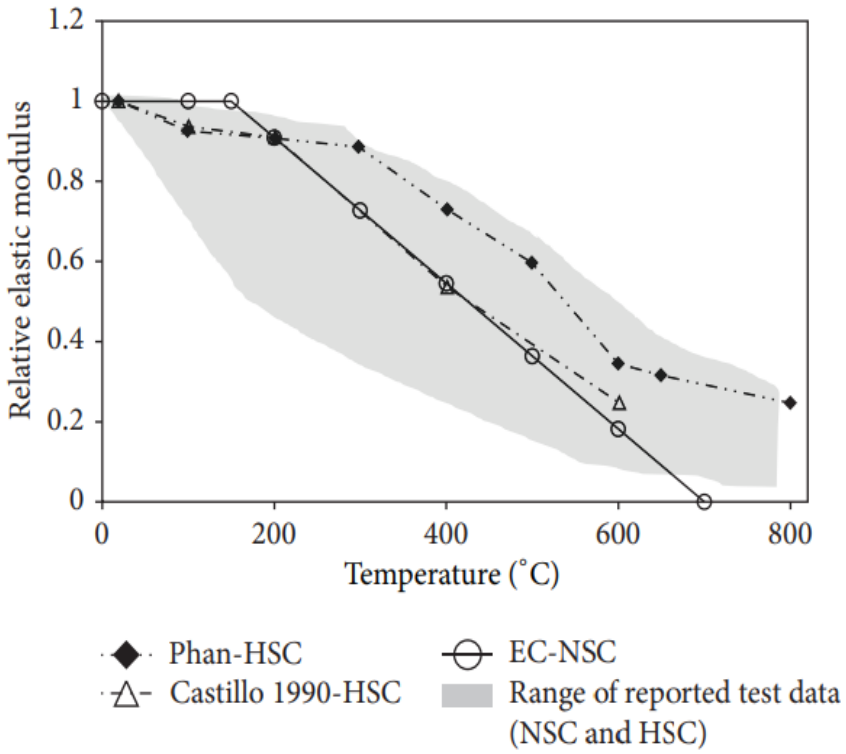

Figure 2.8. Variation of elastic modulus with temperature [17].

The high temperature compressive stress-strain behavior of concrete is of significant importance in the fire resistance analysis of RC structural members as they are helpful to trace the structural response. The stress-strain curve of concrete becomes flatter with increasing temperature, due to a

decrease in compressive strength and elastic modulus, and an increase in ductility of concrete. As elastic modulus decreases, strain at a given stress level increases at high temperatures. The stress-strain curves at elevated temperatures of NSC and HSC are shown in Figure 2.9 and Figure 2.10 respectively. Previous studies have pointed out that HSC has steeper and more linear stress-strain curves in comparison to NSC in the 20ºC -800°C temperature range. The descending branch of the stress-strain curve of concrete also softens due to temperature-induced plastic deformations, and result in higher ultimate strain values with increasing temperature. HSC specimens exhibit brittle post peak response at low temperatures (100ºC -300ºC).

Although a large number of data points have been reported for mechanical properties of concrete at high temperatures, there exists significant variability in the reported data. Much of this variation is due to the differences in test procedures, specimen conditions, test equipment used, and instrumentation adopted for undertaking the property tests by researchers. This is mainly due to the lack of standardized test methods for high-temperature property evaluation, as well as awareness of the significant influence of test conditions and procedures on the high-temperature properties of concrete, specifically HSC and UHPC. For reliable evaluation of high-temperature mechanical properties of concrete, standardized test methods and procedures are required.

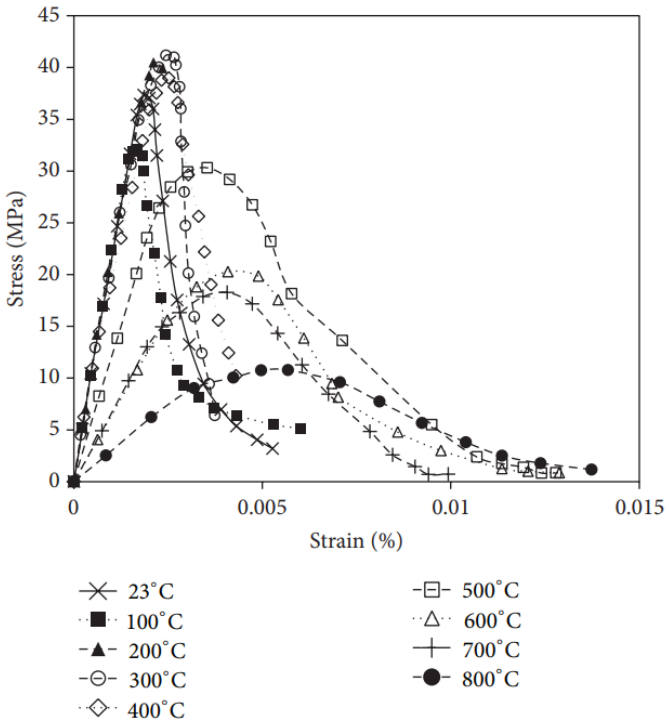

Figure 2.9. Stress-strain response of NSC at elevated temperatures [17].

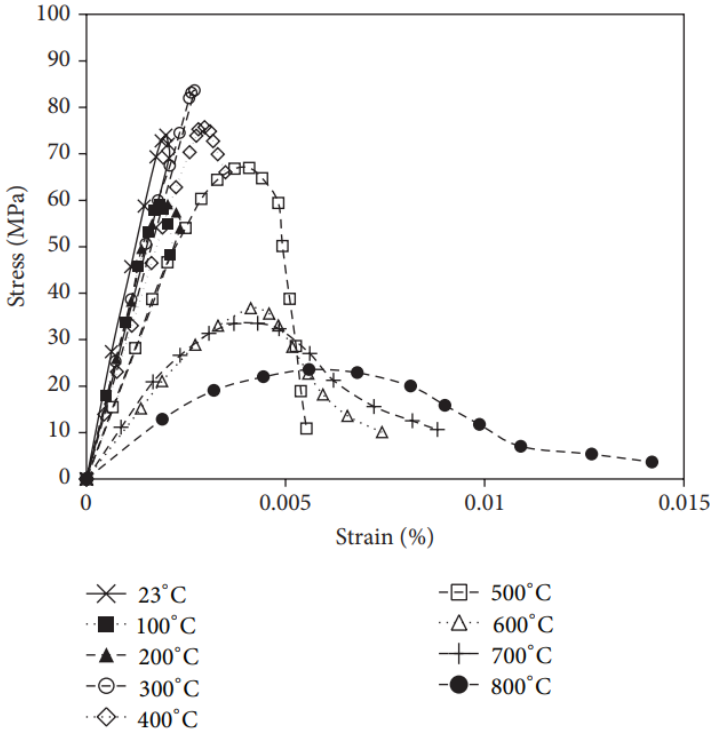

Figure 2.10. Stress-strain response of HSC at elevated temperatures [17].

2.2.2.2. Test methods for high-temperature mechanical properties

There are three testing regimes to determine high-temperature mechanical properties: unstressed, stressed, and residual. The procedures for these three test regimes are schematically shown in Figure 2.11 and are illustrated graphically in Figure 2.12 [3,25]. In the unstressed testing regime, the specimen is heated to a target temperature without the application of any preload. Once the uniform temperature is reached throughout the specimen, the load is applied on the specimen till failure. In the stressed regime, the specimen is preloaded before initiation of heating, and that preload is sustained during the entire heating phase. Once the specimen reaches thermal equilibrium, it is further loaded to failure. In the residual test regime, the specimen is subjected to heating, (with or without any preload) to a desired temperature until attaining a steady state. The specimen is cooled down to ambient temperature upon stabilization of temperature in the specimen and thereafter, it is loaded till failure. While the stressed and unstressed test conditions represent the behavior of heated concrete during fire, the residual test method is representative of the behavior of concrete following cool down after fire exposure.

For mechanical property measurements at room temperature, specific test procedures are given in test standards [43,44]. However, test standards do not provide any guidance for evaluating the mechanical properties of concrete at elevated temperatures. Only RILEM recommendations provide procedures for evaluating the mechanical properties of concrete at high temperatures in the range of 20–750°C [45]. The specific test standards for mechanical property evaluation are tabulated in Table 2-3.

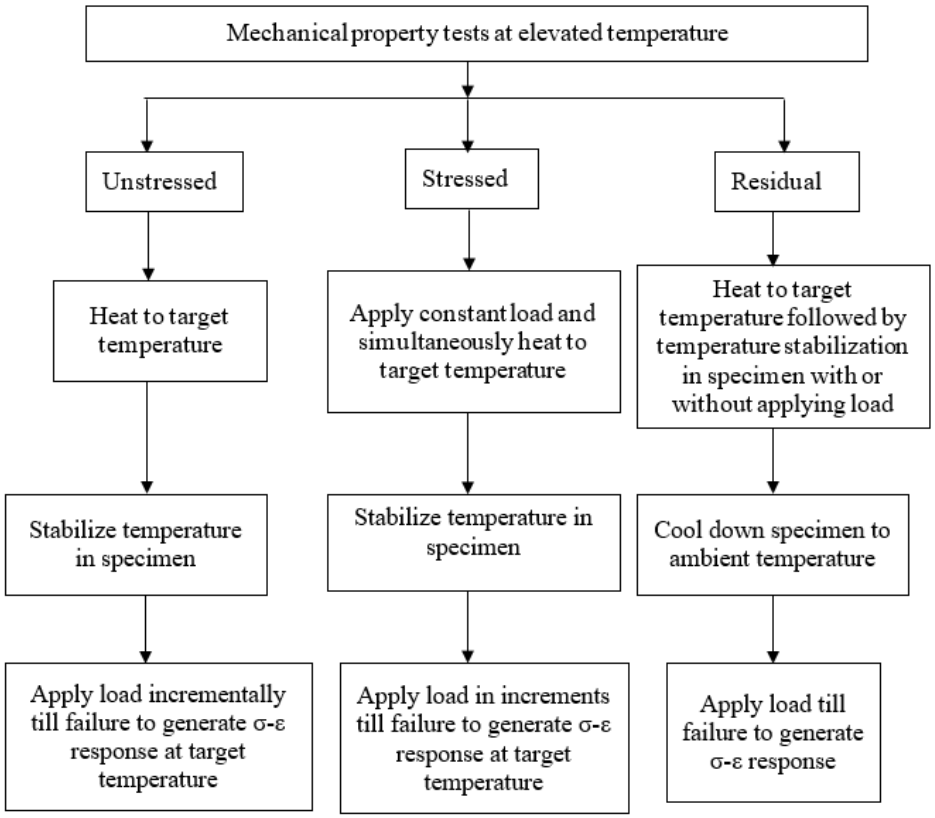

Figure 2.11. Schematic of testing regime for mechanical property evaluation at elevated temperature.

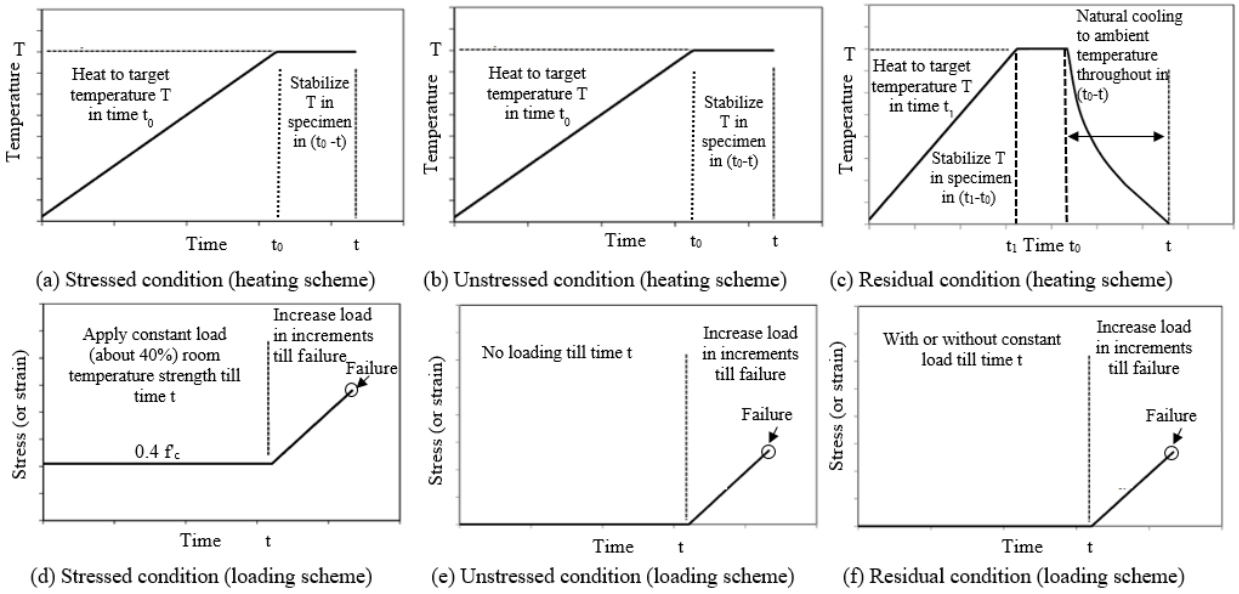

Figure 2.12. Testing regimes for evaluating mechanical properties of concrete at high temperature.

Table 2-3. Test standards for evaluation of mechanical properties.

Mechanical property	Temperature range	Test standards
Compressive strength	Ambient temperature	ASTM C39
	Elevated temperature (upto 750°C)	**No ASTM standard** RILEM 200-HTC
Tensile strength	Ambient temperature	ASTM C78 (Flexural) ASTM C1583 (Direct) ASTM C496 (Splitting)
	Elevated temperature (upto 750°C)	**No ASTM standard** RILEM 200-HTC

In the literature, researchers have evaluated the compressive strength of concrete at elevated temperature as per the procedure outlined in RILEM recommendations or by extending the room temperature procedure laid out in ASTM C39 [43]. But ASTM C39 does not provide guidance on heating rate, and so heating of specimen to target temperature is to be carried out as per RILEM testing procedure. However, these high-temperature test procedures specified in RILEM are developed based on property tests on conventional concretes, and hence, they may not be practicable and fully applicable for higher strength concretes, such as UHPC.

For evaluating compressive strength, after following the heating scheme as per the selected testing regime, a compressive load is to be applied in the direction of the central axis of the specimen at a constant rate till failure occurs. The load at failure of the specimen is to be recorded and the average failure load divided by the area of specimen is the resulting compressive strength at that temperature. The recorded incremental load and displacement data at each temperature can be used to plot the stress-strain response of concrete at the tested temperature. The temperature-dependent modulus can be evaluated as the slope of the linear part of the stress-strain curve plotted at any given temperature. The modulus at each temperature can be extracted from the stress-strain relation as per ASTM-C469/C469M [46] guidance.

The tensile strength of concrete at ambient temperatures is measured in three forms as flexural, direct, and splitting tensile strength. Flexural tensile strength can be obtained as per ASTM C78 [47] procedure through subjecting a small concrete beam to third-point flexural loading. The direct tensile strength can be measured as per ASTMC1583 [48] procedure through testing cylinder or prism specimens by applying axial tensile load in a suitable test machine until specimen breaks in direct tension. Direct tension test is less reliable as the specimen holding devices (grips) introduce secondary stresses leading to unreliable strength data. Splitting tensile strength is evaluated as per ASTM C496 [44] by applying a diametrical compressive load on a cylindrical concrete specimen along its length till failure occurs through the splitting of the specimen along the vertical diameter. For conventional concretes, splitting tensile strength at ambient temperature is usually 1.2 times of direct tension strength, whereas it is 0.6 times of flexure tensile strength. There is very limited guidance for tensile strength tests at elevated temperature since it is often neglected in the design and analysis.

Tensile strength tests at elevated temperatures can be carried out by extending room temperature test procedures. But since ASTM does not have any guidance on heating conditions, RILEM heating procedure recommendations for compressive strength tests can be adopted. However, most of the studies on high-temperature properties continue to adopt non-standardized conditions (such as specimen size, moisture content, heating rate, load level) without any consideration to limited specifications present in RILEM. Due to the application of different test procedures, there is significant variation in measured test data from the previous studies as shown in Figure 2.5-Figure 2.8. To this end, there is a dire need for standardized test procedures for generating reliable data for the characterization of mechanical properties of concrete at elevated temperatures.

2.2.2.3. Previous studies on high-temperature mechanical properties

A review of the literature indicates that high-temperature mechanical properties of UHPC have been studied somewhat more widely than the thermal properties of UHPC and the details of the reported studies are summarized in Table 2-4. The published test data on high-temperature mechanical properties of UHPC is plotted in Figure 2.13- Figure 2.15 along with Eurocode 2 [16] and ASCE manual [22] relations for NSC and HSC.

Tai et al. [49] evaluated the residual compressive strength, elastic modulus, and stress-strain response of UHPC cylinders made with different volume fractions of steel fibers. Experimental results indicated that the residual compressive strength of UHPC after heating from 20–200°C increased slightly (about 15%) than that at room temperature and beyond 300°C, the compressive strength decreased significantly. The reduction in residual compressive strength of UHPC was found to be lower than NSC till 500°C and UHPC followed a similar trend in strength loss as NSC beyond 500°C. The elastic modulus decreased with increasing temperature with 70% of modulus loss at 500°C. The stress-strain response of UHPC with steel fiber content 2% by volume, reported by Tai et al. [49] is plotted in Figure 2.16. The peak stress decreased while the peak strain increased with increasing temperatures, and the UHPC specimens with higher steel fiber content exhibited higher peak strain.

Zheng et al. [50–52] evaluated high-temperature mechanical properties of UHPC extensively, following unstressed and residual test regimes. Their study shows that compressive strength decreases at 100°C, increases at temperatures from 200 to 400°C, and decreases at temperatures above 400°C. The study shows that below 300°C, the compressive strength of UHPC increased as the steel fiber content increased, but decreased between 400 to 800°C with an increase in steel fiber content. The compressive strength of UHPC lowered with higher PP fiber dosage below

200°C but increased between 300 to 800°C as the PP fiber content increased. The elastic modulus of UHPC initially increased till 200°C and then decreased with a further rise in temperature. The tensile strength of UHPC decreases at temperatures from 20 to 200°C, remains constant at temperatures ranging from 200 to 300°C, and decreases at temperatures above 300°C. The tensile strength of UHPC increased as steel fiber content increased at temperatures below 600°C, but above 600°C, tensile strength decreased as steel fiber content increased. The stress-strain response of UHPC with steel fiber content 2% by volume, reported by Zheng et al.[52] is plotted in Figure 2.17. The evolution of stress-strain response with increasing temperature for UHPC with different steel fiber contents is similar. The stress-strain response of UHPC in the 20-300°C range is almost identical and above 300°C, the stress-strain curves become flatter with an increase in peak strain and ultimate strain values.

Sanchayan and Foster [39] evaluated compressive strength and elastic modulus of plain and steel fiber reinforced UHPC at elevated temperature. In this study, an initial increase in compressive strength was observed up to a temperature of 200°C, followed by a drastic drop with a further rise in temperature. No considerable change in modulus of elasticity was reported until 300°C; thereafter, elastic modulus decreased to 50% of the room temperature value at 400°C and to 20% at 600°C. In these reported experimental studies [39,49–52], the increase in compressive strength of UHPC upon heating till 200°C is attributed to the completion of pozzolanic reactions and hydration of the unhydrated cement products in the microstructure.

Table 2-4. Reported high-temperature mechanical property tests on UHPC.

Reference	Specimen dimensions	Fibers (dosage %)	Compressive strength (MPa)	Test procedure	High-temperature property
Tai et al. (2011)	50 x 100 mm Cylinder	Steel (1%) Steel (2%) Steel (3%)	150 168 156	Oven dried Heating at 2°C/min Temp. range: 20-800°C Residual test regime	Compressive strength Stress-strain response Elastic modulus
Zheng et al. (2012, 2013)	70.7 x 70.7 x 228 mm Prism	Steel (1%) Steel (2%) Steel (3%)	143 155 159	Oven dried Heating at 4°C/min Temp. range: 20-900°C Residual test regime	Compressive strength Stress-strain response Elastic modulus
	70.7 x 70.7 x 70.7 mm Cube	Steel (2%) + PP(0.1%) Steel (2%) + PP(0.2%) Steel (1%) + PP(0.2%)	Not mentioned	Oven dried Heating at 4°C/min Temp. range: 20-900°C Residual test regime	Compressive strength
	150 x 75 mm Dogbone	Steel (1%) Steel (2%) Steel (3%)	143 155 159	Oven dried Heating at 5°C/min Temp. range: 20-800°C Unstressed test regime	Tensile strength
Sanchayan and Foster (2016)	100 x 200 mm Cylinder	No fibers Steel (2%)	144 170	Oven dried Heating at 5°C/min Temp. range: 20-700°C Residual test regime	Compressive strength Elastic modulus
Li and Liu (2016)	40 x 40 x 160 mm Prism for flexure 150 x 75 mm Dogbone for tension	Steel (2%) + PP(0.1%) Steel (2%) + PP(0.2%) Steel (1%) + PP(0.2%)	Not mentioned	Oven dried Heating at 4°C/min Temp. range: 20-900°C Residual test regime	Flexural strength Tensile strength
Abid et al. (2019)	70.7 x 70.7 x 70.7 mm Cube	Steel (2%) PP(0.3%) Steel (2%) + PP(0.2%)	154 117 151	Oven dried Heating at 5°C/min Temp. range: 20-900°C Unstressed test regime	Compressive strength Stress-strain response Elastic modulus Tensile strength Flexural strength

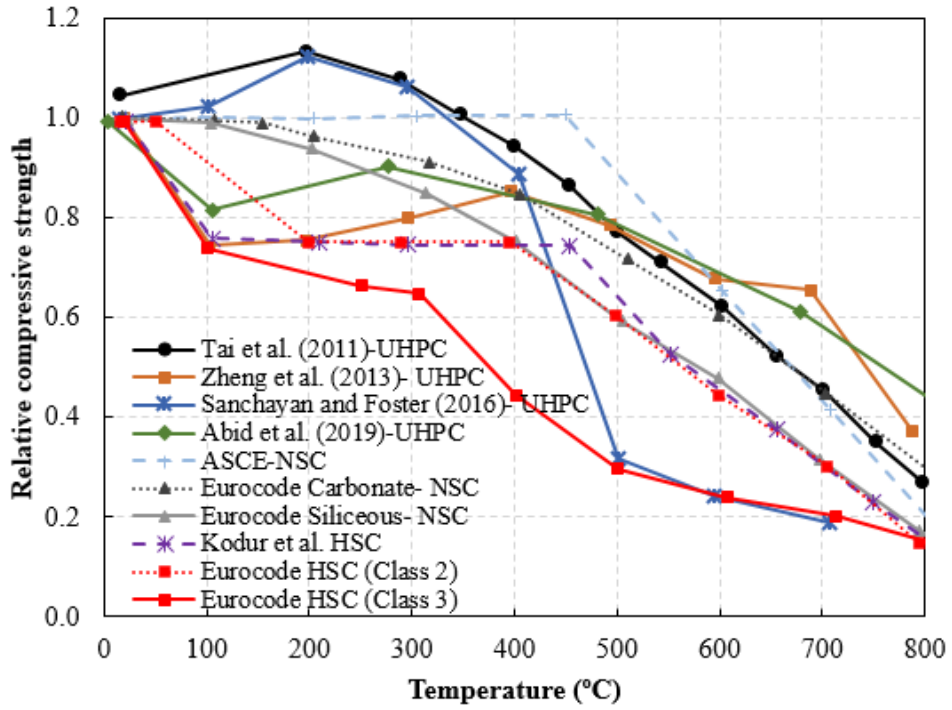

Figure 2.13. Compiled data on variation in compressive strength of UHPC with temperature.

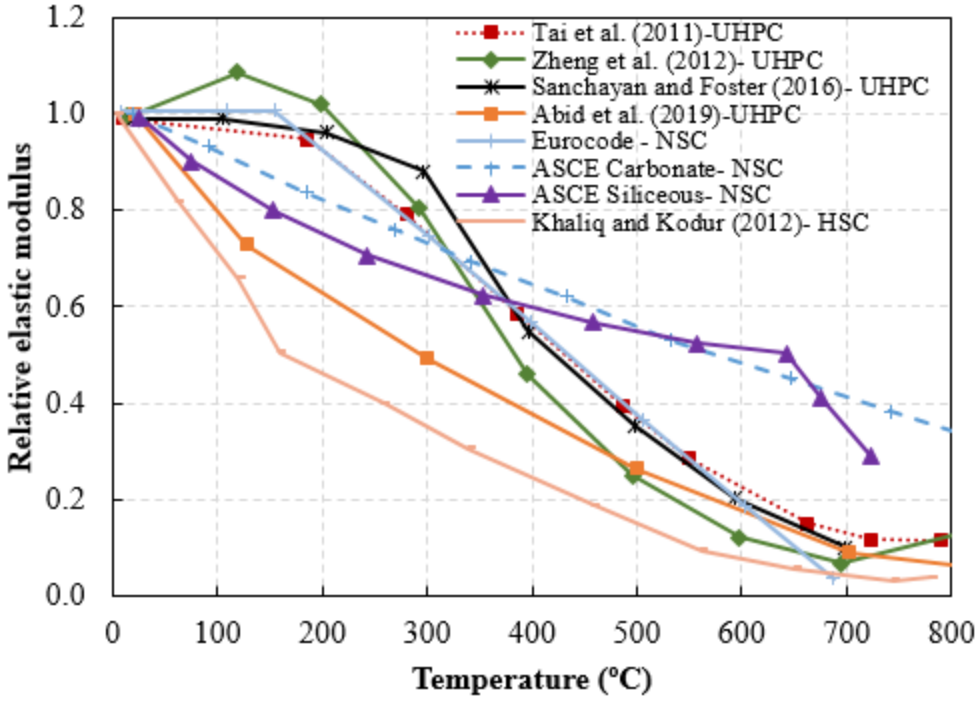

Figure 2.14. Compiled data on variation in elastic modulus of UHPC with temperature.

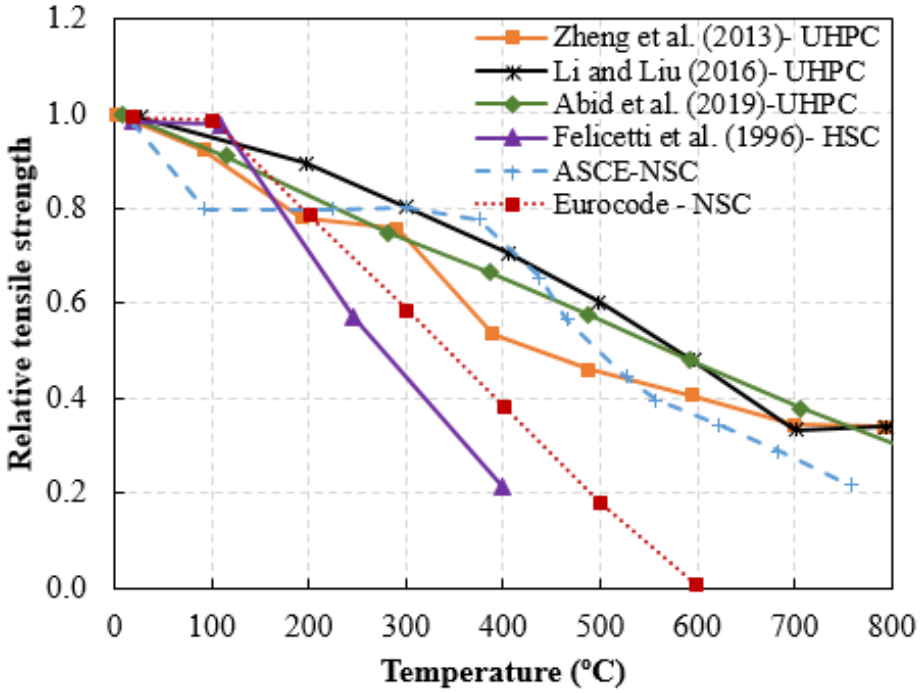

Figure 2.15. Compiled data on variation in tensile strength of UHPC with temperature.

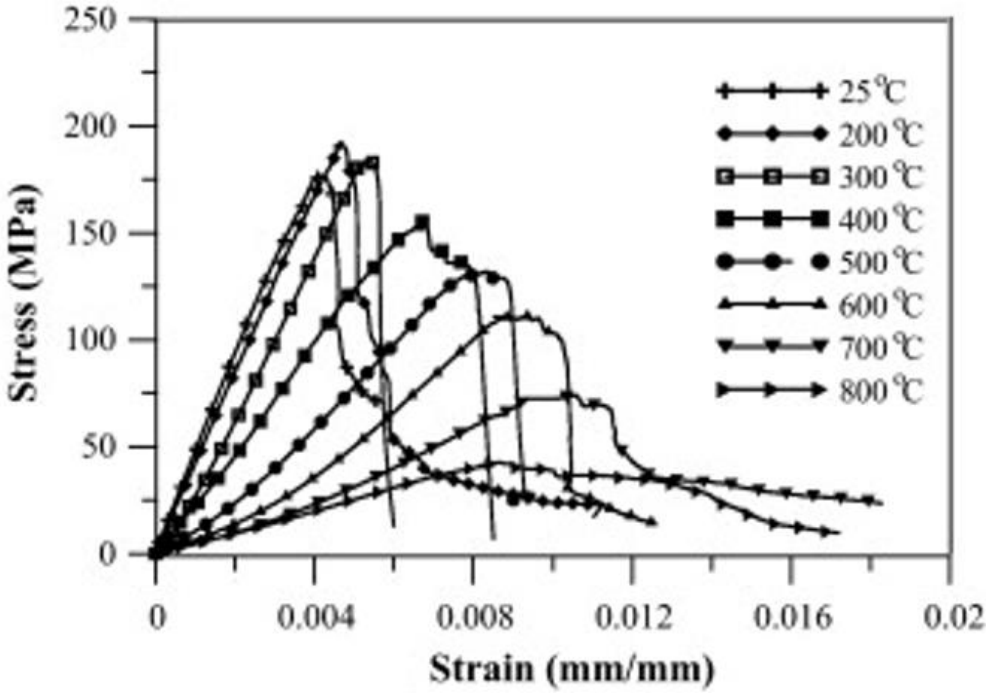

Figure 2.16. Residual stress-strain curves of UHPC with 2% steel fibers as a function of temperature [49].

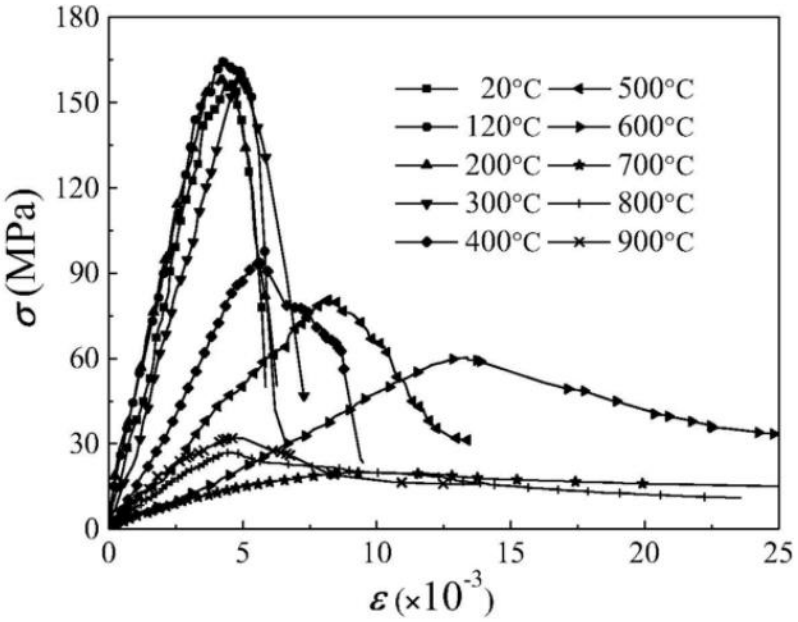

Figure 2.17. Residual stress-strain curves of UHPC with 2% steel fibers as a function of temperature [52].

Li and Liu [53] measured the direct and flexural (bending) tensile strength of UHPC made with hybrid (steel and polypropylene) fibers. The results indicated that steel fibers can improve the tensile performance of hybrid fiber-reinforced UHPC, whereas polypropylene (PP) fibers did not exhibit any evident effect on the tensile performance. This study also concluded that both direct and flexural tensile strengths of UHPC significantly linearly decreased with increasing temperature. Abid et al. [54] evaluated the effect of steel, polypropylene (PP), and hybrid (steel + PP) fibers on high-temperature mechanical properties of UHPC. The high-temperature compressive strength of all UHPCs started to decrease till 120°C; recovered slightly up to 300°C and gradually decreased above 300°C. The split-tensile strength, flexural strength, and elastic modulus gradually decreased with increasing temperature without any effect of various fibers in the different mixes. The stress-strain response of UHPC with steel and hybrid fibers was found to be ductile, whereas the stress-strain response of UHPC with only PP fibers was brittle as can be

observed in Figure 2.18. Further, the compressive strength of UHPC mix with only PP fibers and no steel fibers was very low, around 100 MPa.

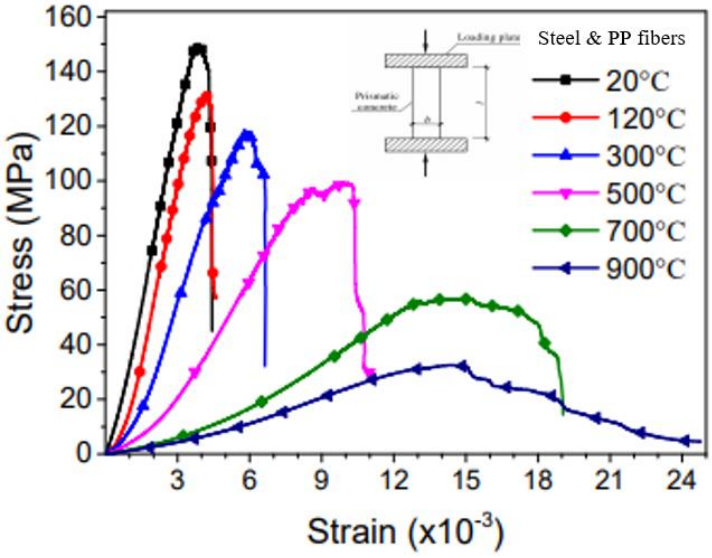

(a)

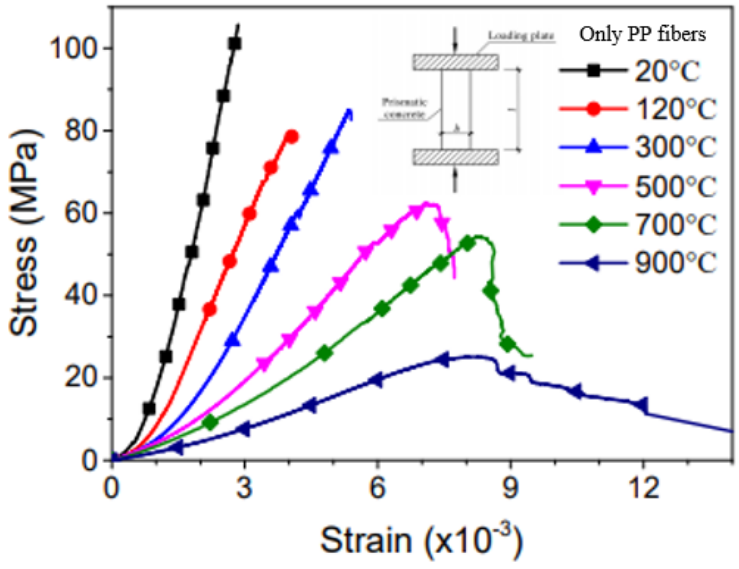

(b)

Figure 2.18. Stress-strain curves of UHPC with (a) steel and PP fibers (b) only PP fibers, as a function of temperature [54].

The literature review shows that only a limited amount of test data with a notable range of variation is available on high-temperature material properties of UHPC. Currently, there is a lack of procedures in test standards for measuring mechanical properties of concrete at elevated

temperatures [25]. As a result, there is significant variation in the test setup and test procedures including specimen size, heating rate, concrete mix proportions adopted in the reported studies to measure properties of UHPC at elevated temperatures. Moreover, UHPC is highly susceptible to fire-induced spalling even at lower heating rates due to its dense microstructure and low permeability. Hence, all of the reported strength tests were conducted after oven drying the specimens at 105°C to minimize spalling by avoiding pressure build-up resulting from the moisture. However, oven-drying does not reflect practical situations and might not be appropriate for evaluating realistic properties of UHPC. Further research is needed to address the aforementioned variations and scarcity of data.

2.2.3. Transport Properties

2.2.3.1. General

In addition to thermal and mechanical properties, transport properties are required for fire resistance analysis as transport properties determine moisture migration, which results in pore pressure build-up and fire-induced spalling. Spalling results in faster transmission of high temperatures to inner layers of concrete and steel reinforcement, thereby leading to a faster decrease in capacity of the structural member. Fire-induced spalling is dependent on a number of material properties including permeability, porosity, moisture content, and tensile strength of concrete.

The pore volume is characterized by porosity and the connectivity of pores is denoted by permeability. Thus, the ability of a material to transfer fluids (gas and liquid) under pressure gradient can be evaluated mainly by measuring porosity and permeability. Various experimental and numerical studies have indicated that modern concretes with low permeability or porosity due to their dense microstructure, such as UHPC and HSC are more susceptible to spalling than

traditional NSC. Previous studies mainly focused on the effect of high temperature on porosity and permeability of NSC and HSC, with few studies on UHPC [55–58]. Further, very limited studies have been carried out on heated specimens at elevated temperatures (hot state) due to a lack of instrumentation and guidance. Majority of the previous studies measured porosity and permeability in the residual state, i.e. after cooling the specimens to room temperature. However, residual values are different and usually higher than porosity or permeability measured at elevated temperatures [59].

2.2.3.2. Test methods for high-temperature transport properties

There are very few standardized procedures for evaluating the transport properties of concrete at room temperature. ASTM standards do not provide any guidance for measuring gas permeability. For measuring chloride diffusivity of concrete, which can be indicative of concrete permeability, ASTM C1202 [60] provides rapid chloride ion penetration test procedures. According to ASTM C1202 test procedures, the concrete specimens should be initially water-saturated and then injected with NaCl and NaOH solutions separately into positive and negative terminals respectively. The total charge passing through the specimens is recorded and converted to the effective chloride diffusion coefficient of concrete through empirical relation. However, the ASTM C1202 test procedure may not be suitable for concrete that contains electrically conductive material such as steel fibers in UHPC. It is because the presence of conductive material in concrete, in the case of steel fiber, can allow more current to pass through the specimen leading to incorrectly high diffusivity values [61].

Another representative metric for permeability is concrete sorptivity, which quantifies the tendency of a material to absorb, desorb, and transfer liquid. ASTM C1585 [62] provides procedures for measuring sorptivity of concrete. All but one surface of the concrete specimen is to

be sealed to prevent moisture ingress and the remaining unsealed surface is kept in contact with water for penetration. The change in weight after the certain intervals should be recorded and the coefficient of sorptivity can be calculated based on the readings. Higher sorptivity indicates higher permeability and vice versa. A similar procedure is recommended by RILEM TC 116-PCD [63] for measuring capillary absorption for concrete.

RILEM TC 116-PCD [63] provides recommendations for measuring gas permeability of concrete using the Cembureau method. This method involves the measurement of permeability through a Cembureau permeameter with nitrogen or oxygen as the infiltrating gas. Concrete specimens are to be subjected to constant upstream pressure. Gas is to be injected at the bottom surface of the specimen. The applied injection pressure should be maintained till the stabilization of gas flow through the concrete specimen. The pressure and flow rate are to be recorded and the downstream pressure will be the atmospheric pressure. The pressures at the front and back of the specimen can be measured using thermal mass flow meters. This mass flow rate can then be converted to an equivalent volumetric flow rate. Applying the principle of mass conservation to Darcy's law for the isothermal flow of gas, the apparent permeability can be calculated. The intrinsic gas permeability of concrete can be calculated from the apparent permeability by utilizing the Klinkenberg method [64].

For measuring the porosity of concrete, test procedures are provided by ASTM C642 [65]. First, the specimen has to be dried at a temperature of 110 °C in a hot air oven until its mass is constant. Then the dry mass of the specimen is to be weighed. Followed by dry weighing, the specimen is to be immersed in water at 21°C for 48 h and mass is to be recorded. Then, the specimen is to be boiled in hot water for 5 h, followed by cooling for 14 h to a final temperature of 25°C. Finally, the specimen is to be suspended into water and the apparent mass in water is determined by

hydrostatic weighing. Substituting the values of mass in different conditions in a mathematical formula, the volume of voids can be determined. Porosity measurement procedure is also given by RILEM-049-TFR draft recommendations [66], wherein the only variation from ASTM C642 is in the saturation mode. RILEM recommends subjecting to vacuum for 4 h instead of boiling. All the above-discussed standardized procedures for evaluating permeability and porosity were developed for ambient conditions. There is absolutely no guidance for undertaking tests to characterize spalling-related transport properties of concrete at elevated temperatures.

2.2.3.3. Previous studies on high-temperature transport properties

Only one study in the literature undertaken by Li et al. [67], measured permeability of UHPC at elevated temperatures in the 20-300°C range. The experimental setup was developed by extending the room temperature test guidelines in RILEM-CEMBUREAU [63], wherein the gas flow through a specimen is measured under steady air pressures. In the reported study, the entire device was placed inside an electric furnace and the specimen was heated to target temperatures at a low heating rate of 1°C/min to avoid the formation of micro-cracks by thermal gradients. The permeability of UHPC at room temperature was in the range between 1.2×10^{-18} and 2.6×10^{-18} m^2, which is lower than that of NSC and HSC (10^{-17} to 10^{-16} m^2) reported in other studies [55,56]. The general trend in permeability remained unchanged from ambient temperature to 105°C, beyond which permeability increased gradually to three orders of magnitude from 105 to 300°C. The increase in permeability with temperature rise is due to the formation of micro-cracks and the dehydration of hydrated products which makes the microstructure more porous. This study also investigated the influence of aggregate size and inclusion of PP and steel fibers on the permeability of UHPC. Results presented in Figure 2.19 reveal that the inclusion of PP fibers

or larger aggregates increased the permeability while the addition of steel fiber did not contribute to the enhancement of permeability of UHPC at elevated temperature.

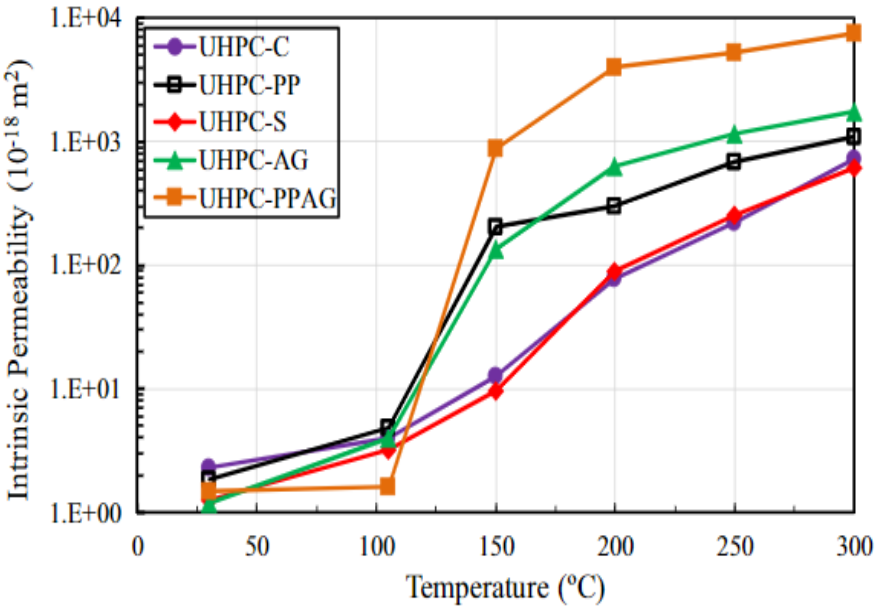

Figure 2.19. Permeability of UHPCs as a function of temperature [67].

Similar to permeability, one study by Abid et al. [54] has been reported in the literature on porosity measurement of UHPC, carried out in residual state. Porosity was measured through mercury intrusion porosimetry (MIP), wherein the volume of mercury that intrudes into the material with each pressure change is utilized to determine the volume of pores. The porosity of UHPC as a function of temperature is plotted in Figure 2.20 and compared with that of NSC and HSC as reported in the literature [68,69]. At room temperature, porosity of NSC, HSC, and UHPC is 15%, 10%, and 5% respectively. Porosity of all concretes increases with increasing temperature primarily due to moisture evaporation, decomposition of hydration products, and micro-cracks resulting from the thermal expansion mismatch between cement paste and aggregate.

Spalling is theorized to occur primarily by the build-up of pore pressure during heating. However, till date, there is no relevant testing procedure and instrumentation in test standards to measure pore pressure in concrete at high temperatures. Only two research groups at CSTB, France [70]

and Politecnico di Milano, Italy [71] have developed their own experimental set-up for measuring pore pressure in concrete specimens. The experimental set-up comprised of installing stainless steel pipes filled with silicon oil and connected to a pressure transducer, in the concrete specimen for measuring pore pressure. Thus, from the literature review, it is apparent that there is a serious lack of test data for temperature-dependent transport properties for spalling evaluation.

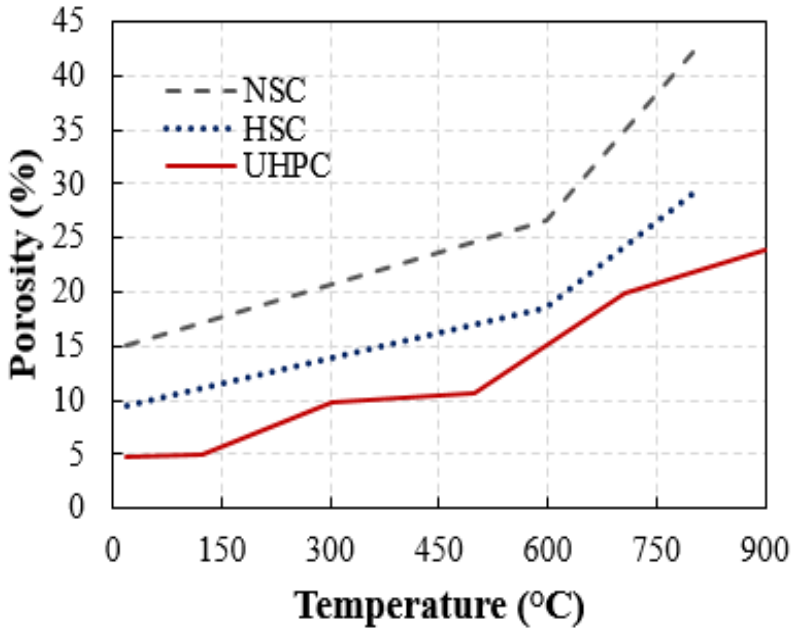

Figure 2.20. Porosity of different concrete types as a function of temperature.

2.3. Experimental Studies on UHPC Members

During the last four decades, several researchers have conducted fire resistance experimental studies on NSC members and to a lesser extent on HSC members [72,73]. Majority of these studies were focused on RC columns, with a fewer number of fire tests on RC beams [74]. Results from past fire tests show that the main factors which influence fire resistance of a structural member include section dimensions of RC beams and columns, concrete cover thickness, fire exposure, applied load level, concrete moisture content, concrete strength, aggregate type, concrete mix, fiber (steel, PP, jute, nylon) reinforcement, and yield strength of reinforcing steel [11,75–77]. In the

previous studies, minor or no spalling was reported in fire tests on NSC members. Moreover, this minor spalling was mostly in the form of flaking after completion of the fire tests.

For the case of HSC, the occurrence of spalling was observed in a number of studies and was found to be affected by a number of factors, such as load level, fire scenario, moisture content, fiber reinforcement, type of aggregate, specimen dimensions, and lateral reinforcement [10,11,73]. The studies showed that the addition of polypropylene (PP) and steel fibers minimizes spalling in HSC members under fire conditions. The extent of spalling was lesser in HSC columns with bent ties at 135° and with closer tie spacing (at 0.75 times that required for NSC columns). Further, a higher rate of temperature rise and HSC members made with siliceous aggregate concrete in lieu of carbonate aggregate concrete were found to increase spalling and reduce fire resistance.

While a considerable amount of literature is available on fire resistance experiments on NSC and HSC, a review of the literature (shown in Table 2-5) indicates that there has been very limited experimental work on the evaluation of fire behavior of UHPC members. The state-of-the-art of experimental studies is discussed herein. Lee et al. [78] tested two UHPC columns under ISO-834 standard fire exposure for 3 hours. The square section columns (500 × 500 mm) were 3428 mm in length. The columns were fabricated with a UHPC mix comprising of hybrid fibers; steel (0.5% by volume), nylon (0.2% by volume), and PP fibers (0.2% by volume). Both columns experienced only minor spalling and attained fire resistance of 3 hours and this good performance (minor spalling) was attributed to the presence of hybrid fibers in the UHPC mix.

Kahanji et al. [79] conducted fire tests on seven UHPC beams of rectangular cross-section (100 × 200 mm) with a span length of 2000 mm. Six of these beams were made of UHPC batch mix that had steel fibers; three beams with 2% (by volume) of steel fibers, and another three with 4% (by volume) of steel fibers. The seventh beam was made of a UHPC mix having a combination

of steel fibers (2% by volume) and PP fibers (4 kg/m^3). The beams were exposed to standard ISO-834 fire exposure for 60 min, but the exposure was only on the bottom half of the beam (cross-section). All six UHPC beams, with only steel fibers (but without PP fibers), experienced severe explosive spalling. The seventh UHPC beam (with a high dosage of PP fibers) did not experience spalling. However, the addition of PP fibers in the seventh beam led to a significant reduction in compressive strength of the UHPC mix to 100 MPa (from 163 MPa in the case of UHPC with steel fibers only).

Table 2-5. Reported fire tests on UHPC members.

Authors	Specimen details	Fiber type and dosage	Compressive strength (MPa)	Test parameters	Main findings
Lee et al. (2012)	2 columns: 500 x 500 x 3428 mm	Steel (0.5%) + PP (0.2%) + Nylon(0.2%) Steel (0.5%) + PP (0.2%) + Nylon(0.2%)	204 205	-ISO 834 standard fire exposure for 3 h. -Constant axial load of 9500 kN.	-Both columns attained fire resistance of 3 h with minor spalling.
Kahanji et al. (2016)	7 beams: 100 x 200 x 2000 mm	Steel (2%) Steel (2%) Steel (2%) Steel (4%) Steel (4%) Steel (4%) Steel (2%) + PP (0.4%)	157 163 178 162 166 173 100	-ISO 834 standard fire exposure to bottom half of the beams for 1 h. -Three load levels: 20, 40 and 60% of ultimate capacity at room temperature.	-No spalling in beam containing hybrid fibers. -Lower extent of spalling was reported under higher load level. -Beams containing 4% steel fibers spalled less than the beams with 2% steel fibers.
Hou et al. (2019)	4 beams: 200 x 400 x 4900 mm	Steel (2%) + PP (0.2%) Steel (2%) + PP (0.2%) Steel (2%) + PP (0.2%) Steel (2%) + PP (0.2%)	127 127 127 127	-ISO 834 till failure of beam. -Two load levels: 30 and 50% of ultimate capacity at room temperature. -Varying cover thickness: 25mm, 35mm.	-Minor spalling in all beams. -Fire resistance increases with an increase in concrete cover thickness.

Hou et al. [80] tested four UHPC beams of rectangular cross-section (200 × 400 mm) with a span length of 4900 mm exposed to ISO-834. The beams were made of a UHPC batch mix containing 2% steel fibers and 0.2% PP fibers. The test results indicated that the fire resistance of the UHPC beams increased by 40% when the cover thickness was increased from 25 mm to 35 mm. Additionally, a higher load level decreased the fire resistance of the beams. Only minor spalling in the form of peeling-off was observed in the tested beams due to the presence of PP fibers. However, the strength of the UHPC mix was 127 MPa, which is lower than the characteristic strength of UHPC mix (150 MPa).

The above review clearly indicates that there are only limited fire resistance studies on UHPC beams. Thus, there is a lack of data, including detailed observations and recordings of spalling, and response of UHPC beams under fire exposure. Further, it can be seen that the previous experimental studies used a high dosage of PP fibers for the mitigation of spalling. The high PP dosage resulted in reduced compressive strength of the concrete mixes in previous studies to levels below that of optimum desired strength of 150 MPa in UHPC. Unlike previously published works, this study seeks the incorporation of a balanced dosage of PP fibers in UHPC mix to achieve spalling mitigation, without impacting on compressive strength and workability. Moreover, the reported tests in the literature were carried out by subjecting UHPC members to standard fire exposure only, without any due consideration to realistic fire scenarios; that encompass a cooling phase. In addition, the previous fire tests on UHPC members were carried out using concrete batch mixes without any coarse aggregates. Such UHPC mixes, made with fine aggregates and high superplasticizer and silica fume, incur higher costs and require special mixing equipment that is not commonly available in many concrete batch mix plants.

2.4. Numerical Studies on UHPC members

Numerical studies on simulating the fire behavior of concrete structures can be undertaken at the microscopic or macroscopic level through finite-element based method. In the microscopic method, computer packages such as ABAQUS, ANSYS, and SAFIR can be utilized, wherein a structural member is discretized into a meshed model and coupled or uncoupled thermal and structural analyses are carried out to evaluate fire response. In the macroscopic method, sectional analysis is carried out at a critical cross-section, or a number of cross-sections along the length of the member to predict the fire response of the structural member. Both microscopic and macroscopic numerical studies have been undertaken for NSC and HSC structural members in previously published studies. Conversely, there have been only a handful of numerical studies on the fire behavior of UHPC members.

Mai et al. [81] analyzed a three-story two-bay UHPC frame structure subjected to standard ISO-834 fire for 2 h using commercial software ABAQUS. The numerical simulation compared the thermal and structural response of a UHPC frame structure with that of a HSC frame structure. However, the validation of the numerical model by comparing predicted parameters with test data was not undertaken. Hou et al. [80,82] developed a sequentially coupled thermal stress model in ABAQUS to simulate the response of the hybrid fiber reinforced UHPC beams tested by them, as discussed in section 2.3. Fire-induced spalling was entirely neglected in both the numerical analyses, which can be an influencing factor in tracing the fire response of UHPC structures due to the high susceptibility of UHPC to spalling.

In fire-resistance analyses of concrete structures, generally spalling is not considered, mainly due to the complexity involved in modeling the spalling phenomenon, as well as due to limited property data available to undertake analysis. Further, there are conflicting theories through which spalling

occurs in a fire-exposed member [83]. Anyhow, the two widely accepted mechanisms for spalling are pore-pressure build-up and thermal stress (discussed in section 1.4). The proposed numerical approaches in the literature for evaluating spalling can be broadly grouped into three categories based on the mechanism driving spalling in concrete: (i) hydro-thermal models, which assume spalling, based on pore pressure mechanism; (ii) thermo-mechanical model based on thermal stress mechanism; and (iii) hydro-thermo-mechanical model based on a combination of both the mechanisms (i) and (ii). Some of the major studies are summarized in Table 2-6 and discussed in the following paragraphs.

In addition to the afore-mentioned three types of models, a simplified approach was proposed by Kodur et al. [13] to account for spalling based on detailed experimental studies on high strength concrete (HSC) columns. This basic model was developed in order to minimize the complexity of spalling calculations and for easy usage of numerical models for fire resistance analysis. This crude model involved the following a set of rules to determine the extent of spalling:

(i) Spalling occurs when the temperatures in an element reach above 350°C.

(ii) In HSC column, spalling occurs only outside the reinforcement cage when the ties are bent at 135º into the concrete core. When ties are bent in a conventional pattern, spalling occurs throughout the cross-section.

(iii) No spalling occurs inside reinforcement core when tie spacing is 0.7 times of standard spacing.

(iv) The extent of spalling is higher (100%) in the siliceous aggregate HSC than that for carbonate aggregate HSC (40%).

(v) The extent of spalling in HSC columns with polypropylene fibers 0.1% to 0.15% by volume is 0% and with steel fibers is 50%.

(vi) A higher relative humidity in HSC column (90% or higher) leads to higher spalling.

Table 2-6. Reported numerical studies on fire-induced spalling.

Authors	Model	Main findings
Kodur et al. [13]	Simplified	-A set of guidelines were proposed based on observations from detailed experimental studies on HSC columns for determining the extent of spalling.
Bazant and Thonguthai [7]	Hydro-thermal	- Spalling is due to a sudden unstable release of the potential energy of thermal stresses stored in the structure and vapor pressure is not the main reason of spalling.
Dwaikat and Kodur [84]	Hydro-thermal	- Spalling is predicted to occur when the pore pressure exceeds the tensile strength of concrete. - Fire scenario, tensile strength, and concrete permeability largely influence the extent of fire-induced spalling in concrete beams.
Ichikawa and England [85]	Hydro-thermal	- Developed one-dimensional model to predict spalling by vapor pressure mechanism.
Ulm et al. [9]	Thermo-mechanical	-Simulated spalling through restrained thermal expansion in "Chunnel" Tunnel. -Proposed a thermo-chemo-plastic constitutive model taking into account the hardening and softening using plastic mechanics theory and dehydration of concrete at high temperature.
Msaad and Bonnet [86]	Thermo-mechanical	- "Chunnel" tunnel fire is modeled by a thermo-chemo-plastic constitutive model, wherein mechanical stresses and strains near the heated surface (the concrete wall) are calculated. -Spalling is due to chemical decohesion (strength degradation) and not to chemical softening (rigidity reduction).
Gawin et al. [87]	Hydro-thermo-mechanical	- The proposed model considered the multi-phase change of concrete at high temperatures and considered mass transport processes, mechanical behavior and phase changes. - Contribution of the stored elastic energy and vapor pressure build-up to the kinetic energy of spalled concrete pieces is estimated. -An expression for permeability variation due to hydrothermal damage is proposed.
Zhang and Davie [88]	Hydro-thermo-mechanical	- The model utilizes an isotropic damage model formulated using a modified von Mises definition adopting strain tensors. - Concrete was modeled as a multi-phase system consisting of solid, liquid, and gas phases. - Numerical analysis of one-dimensional concrete members indicated that thermal stresses play the primary role in driving spalling.
Zhao et al. [89]	Hydro-thermo-mechanical	- The high temperature behavior of HPC cubic specimens is numerically modeled and the spalling mechanism is investigated at a meso-level. - The dominant role of vapor pressure or temperature gradient-induced thermal stress on spalling is studied under two heating conditions.

Table 2-6. (cont'd)

Tenchev and Purnell [90]	Hydro-thermo-mechanical	- The model, derived based on the principles of mechanics and thermodynamics, accounts for coupling between stress analysis and pore pressure calculations. - Concrete permeability tensor, diffusion coefficients and material stiffness tensor are required to predict spalling.

One of the preliminary hydro-thermal analysis for predicting fire-induced spalling in concrete was developed by Bazant and Thonguthai [5,7]. The finite element based model was developed based on coupled differential equations of heat and moisture transfer in concrete. In this model, the mass balance equations were derived by assuming the different phases of water (water vapor and liquid water) as a single-phase, namely capillary water. The variation in permeability was considered to increase by two orders of magnitude beyond 100°C, which was an overestimate, causing numerical convergence issues under rapid heating conditions. The study analyzed a concrete wall section and inferred that pore pressure is only a triggering point for spalling and the brittle fracture (spalling) of concrete is due to a sudden release of high potential energy generated from thermal stresses. However, the authors did not evaluate mechanical stresses and strains.

Another widely cited hydro-thermal model was developed by Dwaikat and Kodur [84,91,92] where spalling was assumed to occur in a concrete section when the accumulated vapor pressure exceeded the degraded tensile strength of concrete at elevated temperatures. This model incorporated the different phase changes (liquid and vapor) of moisture. Pore pressure was calculated considering the ideal gas equation and utilizing conservation equations of mass, momentum, and energy. The model was validated by comparing spalling predictions with test data in walls, beams, and columns. In this analysis, the variation in permeability due to pressure and temperature was considered using the expression developed by Gawin et al. [93] based on experimental results. Additionally, initial permeability (at room temperature) included the effects

of cracking and curing conditions of the concrete member through empirical relations. A similar hydro-thermal model was proposed by Ichikawa and England [85] to predict fire-induced spalling in concrete walls. In this study, concrete permeability and tensile strength were assumed constant with temperature.

The second category of spalling models is thermo-mechanical models, which primarily incorporate plastic or damage constitutive equations to compute stresses due to thermal restraint and then resulting spalling. Ulm et al. [9] developed a thermo-mechanical model utilizing chemo-plasticity mechanics theory to evaluate fire-induced spalling of concrete tunnel rings in the "Chunnel tunnel" using plastic strain as an indicator for evaluation of the spalling depth. To account for the effects of elevated temperatures in concrete, a thermo-chemo-plastic constitutive model with chemo-plastic softening was proposed in this study. A similar thermo-mechanical spalling model was proposed by Msaad and Bonnet [86], wherein spalling was evaluated using stresses developed due to restrained thermal dilatation.

In the third category of spalling models, i.e. hydro-thermo-mechanical models, the coupled effect of pore pressure and restrained thermal expansion is considered. Gawin et al. [87,93] developed such a hydro-thermo-mechanical model applying the governing equations of conservation of mass, momentum, and energy principles for pore pressure calculations in heated concrete. The model considered concrete as a multiphase porous media and accounted for the phase changes in water. One of the notable contributions by Gawin et al. [93] was the proposal of an expression for permeability variation incorporating the effect of pore pressure and temperature rise. For accounting thermal spalling, constrained elastic energy was compared against the fracture energy in concrete, however, properties for determining fracture energy at elevated temperatures are not yet well established for concrete. Their hydro-thermo-mechanical model was utilized for

evaluating spalling in NSC and HSC slabs and wall sections without any structural loading to be present [94].

Zhang and Davie [88] developed a hydro-thermo-mechanical finite element model utilizing an isotropic damage model formulated using a modified von Mises definition adopting strain tensors. It should be noted that although this study attempted to model the physical processes, the critical inputs for the model such as strain tensors are not defined at high temperatures. Concrete was modeled by the authors as a multi-phase system consisting of solid, liquid, and gas phases. The solid phase represented the concrete skeleton undergoing deformations. The liquid phase comprised of free, adsorbed, and chemically bound water. The gas phase included water vapor and dry air, assumed to behave as ideal gases. Theoretical concrete wall and square column sections were analyzed with constant permeability were presented. The results showed that thermal induced stresses are the primary factor in causing spalling and the effect of stresses due to pore pressure is secondary.

Zhao et al. [89] proposed a hydro-thermo-mechanical meso-level numerical model for investigating spalling mechanism in a high performance concrete (HPC) cube. Effective first principal stresses due to thermal gradients and vapor pressure were calculated, and HPC was assimilated as a two-phase material with assumed properties for each phase, that is cement paste and aggregates. The study concluded that spalling mechanisms are dependent on heating conditions. For fast heating, as under ISO standard fire, thermal stress mechanism is dominant, whereas under slower heating of 5ºC/min, pore pressure mechanism governs spalling.

Tenchev and Purnell [90] proposed a hydro-thermo-mechanical finite element model to simulate fire-induced spalling in concrete wall sections without loading. Concrete was considered as a two-phase material comprising of mortar and coarse aggregate having constant volume fractions with

temperature. Material properties were defined using tensors and the effect of concrete damage due to stresses from constrained thermal expansion was included in the model. The coupling between pore pressure and stress analysis was through the application of pore pressure as a body force in the stress analysis.

Recently, Shen et al. [95] developed a three-dimensional hydro-thermal model coupled with the Lattice Discrete Particle Model (LDPM) for simulating spalling depth in fire exposed concrete. LDPM captures the concrete meso-structure by simulating the interaction of coarse aggregate pieces. This numerical study concluded that spalling occurred due to a combined action of thermal stress and pore pressure, with thermal stress being dominant at the early stages of fire (within 25 min) and pore pressure being more pronounced with increase in heating time. The effect of load-induced stress was not considered in evaluating spalling.

In the above discussed review of literature, most studies carried out spalling analysis at a section and spalling was assumed to remain uniform throughout the length of the member. Fire tests and field observations have shown that spalling in concrete members occurs in a non-uniform pattern, which implies that the spalled cross-section is not constant along the longitudinal dimension of the member [92,96,97]. Therefore, evaluating spalling at a section (level) might not yield realistic spalling predictions in structural members. In addition, the reported numerical studies in literature did not account for the effect of mechanical stress arising from structural load on the member into spalling calculations.

Further, it is well known that the permeability of concrete largely influences the extent of fire-induced spalling in concrete members. Yet majority of the previous numerical studies assume concrete permeability to be uniform over the concrete cross-section (and at room temperature values), without taking into consideration the progression of cracking due to increasing

temperature, pore pressure, and load level. Moreover, among the different concrete types, UHPC and HSC are more susceptible (than conventional NSC) to fire-induced spalling, specifically UHPC due to its extremely dense microstructure. The previously reported numerical analyses simulate spalling in structural members made of either NSC or HSC. There is a lack of validated numerical models for predicting spalling in UHPC members under fire exposure.

2.5. Provisions in Standards and Codes on Fire Resistance of Concrete Members

The specifications for fire resistance ratings of concrete structural members are provided in building codes and national standards. In the USA, ACI 216.1 (2014) [98] standard provides prescriptive provisions for fire design of concrete and masonry structures. The specifications for fire resistance ratings of concrete members provided in ACI 216.1 are derived based on results of ASTM E119 standard fire tests [99]. As per ACI 216.1 provisions, failure is considered to occur when steel reinforcement attains a critical temperature (593°C), without any consideration to strength or deflection failure conditions. The critical temperature is defined as the temperature at which the reinforcement loses so much of its strength that it can no longer support the applied load. ACI 216.1 specifies minimum sectional dimensions (width) and concrete cover thickness requirements for achieving a required fire resistance rating in an RC beam. Additionally, separate fire ratings are specified for beams with restrained and unrestrained support conditions. ACI 216.1 provisions are applicable for conventional NSC (<83 MPa) beams only and no clear guidelines are laid down for beams made using new types of concrete such as HSC or UHPC. ACI 216.1 also provides minimum sectional dimensions for RC columns made with NSC to attain the required fire resistance rating, giving consideration to three aggregate types: carbonate, silicate, and semi-lightweight. For HSC columns, ACI 216.1 provides additional guidance for preventing fire-

induced spalling by the provision of rectangular ties with 135° bends, and circular ties with 90° bends.

In Europe, Eurocode 2, Part 1-2: Structural fire design [16] provides a choice of tabulated data, simplified, or advanced methods for determining the fire resistance of concrete members. The data in tabulated format provides minimum dimensions and cover thickness to attain desired fire ratings for concrete members based on fire tests carried out as per ISO 834 [100] standard. For RC beams, the tabulated data is applicable to NSC made with siliceous aggregates. The same tabular data can be applied for carbonate aggregate concrete and high strength concrete through alteration of the required minimum sectional dimensions by modification factors. For RC columns, Eurocode 2 specifies two tabulated methods: Method A and Method B. Method A utilizes an empirical equation, whereas Method B is based on tabulated values. Both the methods provide minimum dimensions and axis distance to the main reinforcement to achieve the specified fire rating in the column.

The simplified method in Eurocode 2 is based on evaluating reduced sectional capacity at a critical section, considering reduced strength of constituent materials due to temperature. The simplified calculation method is applicable only to concrete members subjected to standard fire exposure. The advanced method in Eurocode 2 involves detailed thermal and structural analysis and requires the use of sophisticated numerical models. Even by following advanced fire resistance calculations, fire-induced spalling cannot be easily accounted for due to complexities in the analysis.

For addressing spalling, Eurocode 2 states that spalling is unlikely to occur when the moisture content in concrete is lower than 3%. Some general provisions in Eurocode 2 for mitigating spalling in concrete elements are: (i) use of secondary reinforcement mesh with a nominal cover

of 15 mm; (ii) use of concrete that does not have a tendency to spall; (iii) limit the maximum content of silica fume to less than 6% by weight of cement; (iv) use protective thermal layers; and (v) addition of at least 2kg/m^3 polypropylene fibers in the concrete batch mix. The guidelines in Eurocode 2 are qualitative and without due consideration to critical factors that influence the phenomenon, such as permeability and tensile strength of concrete, heating conditions, and level of loading.

Based on the above review, it can be summarized that the fire resistance provisions in current codes and standards do not fully account for realistic fire and loading conditions, as well as spalling, encountered by structural members under fire conditions. Additionally, the fire performance of structural members made using new concrete types such as UHPC can be significantly different and lower than that of conventional concrete members. Therefore, current prescriptive methods specified for conventional NSC members cannot be directly applied for the advanced concretes.

Currently, there are limited guidelines and design recommendations for the structural design of UHPC members at room temperature only, including FHWA [101], AFGC-SETRA[40], JSCE [1], and KCI [102] developed by the US, France, Japan, and South Korea respectively. Although there is limited guidance on structural design at ambient temperature conditions, as the literature review indicates there are absolutely no design provisions for UHPC members under fire conditions. This is primarily due to a lack of fire-related research on UHPC members. Further research, including detailed experimental and numerical studies, is needed to quantify the fire performance of UHPC members for the development of fire resistance design guidelines.

2.6. Cost of UHPC

UHPC exhibits enhanced mechanical and durability properties as compared to conventional concrete. However, one of the limitations to the widespread use of UHPC in construction projects is its high initial cost due to the incorporation of high volumes of fineness materials and steel fibers. In North America, the cost of UHPC is around $2000 per cubic yard, whereas the cost of conventional NSC is $100 per cubic yard [103]. For wider adoption of UHPC by the infrastructure market, ongoing research studies are aimed at developing economic UHPC mixes by optimizing raw materials and production techniques while retaining the same level of mechanical performance [104,105]. Such studies have led to the development of cost-effective UHPC mixes in comparison to the cost of typical UHPC mixes formulated decades ago. Moreover, despite the initial cost of UHPC being higher than that of conventional concrete, UHPC structures can be cost-effective in terms of other performance factors. Due to the superior mechanical properties of UHPC, members with smaller cross-sections and lower reinforcement can be designed for carrying the same level of load as compared to conventional concrete members. This leads to lower costs owing to a reduction in quantities of concrete, reinforcement, formwork, and associated labor and transport costs required for fabrication. In addition, due to high durability properties, UHPC exhibits high permeability resistance to water and chemicals, resulting in lower susceptibility to corrosion in rebars, which in turn lowers maintenance and repair costs in the long run. Consequently, lower life-cycle costs for UHPC structures have been assessed by studies in the literature in terms of costs incurred during production, repair, maintenance, and demolition [104,106,107].

2.7. Knowledge Gaps

The state-of-the-art review presented in this chapter clearly shows that there is a lack of data on the behavior of UHPC at high temperatures. Very limited data is available on the material

properties of UHPC at elevated temperatures. Likewise, limited fire tests and numerical studies have been carried out to evaluate the fire resistance of the UHPC members. Most of the reported numerical studies on RC members did not incorporate the effect of fire-induced spalling. Further, there is a lack of validated numerical models that can evaluate spalling in concrete members. In addition, the available codes and standards do not provide any guidelines for the fire resistance design of UHPC members. The current provisions in design codes for evaluating fire resistance of concrete structural members are only for NSC members, and to a limited extent for HSC members. Moreover, the fire resistance ratings in the design codes are based on prescriptive approaches without specifically accounting for spalling, which is a serious concern for UHPC. The following are major knowledge gaps on the behavior of UHPC at the material level and structural level:

- There is a lack of high-temperature property relations of UHPC for fire resistance modeling of UHPC structural members. Further, there are no standardized testing procedures for measuring high-temperature material properties of UHPC.
- There is absolutely no guidance for undertaking tests to characterize special properties in new concretes, such as temperature-induced spalling, permeability, and pore pressure variations at elevated temperatures.
- There is a lack of experimental data on the fire response of UHPC members. Such data from fire experiments is critical for validating numerical models to trace the response of structural members under fire conditions.
- Most of the available numerical models for fire resistance analysis of RC members are for NSC and HSC, and do not account for fire-induced spalling. In particular, there are no numerical models for evaluating the fire response of UHPC beams.

- The current spalling models do not fully account for the effects of structural loading and assume the same spalling level as in the analyzed critical cross-section, instead of member level. There are no numerical studies on the prediction of spalling in UHPC members.
- There are no design approaches and guidance in codes and standards on fire resistance design of UHPC members.

CHAPTER 3

3. Experimental studies

3.1. General

As summarized in the literature review in Chapter 2, there have been a number of experimental studies on the fire performance of NSC beams, and to a lesser extent on HSC beams. These studies investigated the effect of various parameters, such as fire scenario, the extent of spalling, cross-sectional size, concrete strength, load intensity, reinforcement ratio, etc., on the fire response of RC beams. However, the review shows that there has been only very limited research on large-scale UHPC beams under fire exposure. Thus, there is a lack of data, including detailed observations and recordings of spalling, and response of UHPC beams under fire exposure. Moreover, there is very limited information on the fire response of beams made of UHPC with polypropylene fiber reinforcement. Additionally, it is remarkable to note that the previous experimental studies used a high dosage of polypropylene (PP) fibers (4 kg/m^3) for mitigation of spalling, which resulted in reduced compressive strength of the concrete mixes to levels below that of optimum desired strength of 150 MPa in UHPC. Unlike previously published works, this study seeks the incorporation of a balanced dosage of PP fibers in the UHPC mix to achieve spalling mitigation, without impacting on compressive strength and workability. Furthermore, the reported tests in the literature were carried out by subjecting UHPC members to standard fire exposure only, without any due consideration to realistic fire scenarios that encompass a cooling phase.

For evaluating the fire response of UHPC members, high temperature-dependent material properties of UHPC are required. However, there is a lack of data on the properties of UHPC and polypropylene fiber reinforced UHPC at elevated temperatures. Even in these limited studies, there is substantial variance associated with the experimental setup and test procedures including

varying specimen size, heating rate, moisture content, concrete mix proportions adopted in the reported studies. This wide disparity is owing to the lack of standardized testing procedures and limitation in testing equipment for measuring material properties of concrete at high temperatures. Furthermore, UHPC is highly prone to fire-induced spalling at lower heating rates due to its dense microstructure and low permeability, which further adds to the complexities in characterizing its high-temperature property variation.

To address the aforementioned knowledge gaps, a detailed experimental program was designed as a part of this study. The experimental program consisted of undertaking a set of thermal and mechanical property tests on UHPC specimens in the temperature range of 20-800°C. In addition, fire resistance tests on four ultra-high performance concrete (UHPC) beams were carried out under simultaneous application of structural loading and fire exposure. Full details on the fabrication of test specimens, instrumentation, test procedures together with measured properties and response parameters are presented in this chapter.

3.2. Mix Design of UHPC

The batch mix proportions in conventional UHPC mixes mainly comprise of specially graded fine aggregates, high volume of silica fume, and superplasticizers, and do not usually contain coarse aggregates. Such conventional UHPC mixes require considerably high mixing energy and the use of specialized mixing equipment. The mixing procedure is complex, and the specialized equipment is not readily available in most concrete production plants at the current time [105]. Therefore, in the present study, a relatively new mix design for UHPC was adopted in which a controlled amount of coarse aggregates (as in conventional concrete mixes) were also included in the batch mix in order to facilitate ease of preparation and to reduce the dosage of cementitious material and thus

the cost of UHPC. The specialized UHPC mix design was developed by Metna Co. (Prof. Soroushian) as part of a larger ongoing project on Ultra-High Performance Concrete [108].

Four batch mixes, namely UHPC plain (without any fibers), UHPC-S1 (steel fibers), UHPC-S2 (steel fibers), and UHPC-H (with hybrid i.e. steel and polypropylene fibers) were prepared. The batch mix proportions are given in Table 3-1. All the batches comprised of binder (including cement-type I, silica fume, slag, and limestone powder) and calcareous (carbonate based) coarse aggregates with a maximum size of 12.7 mm, and fine aggregates (natural sand and silica sand). The desired workability of UHPC was obtained by adding a high-range water reducer (HRWR), which is a polycarboxylate-based superplasticizer (Chryso 150) [109].

Table 3-1. Mix proportions in UHPC batch mixes.

Ingredient	UHPC plain (Kg/m^3)	UHPC-S1 (Kg/m^3)	UHPC-S2 (Kg/m^3)	UHPC-H (Kg/m^3)
Coarse Aggregate	517	478	517	517
Natural sand	544	504	544	544
Silica sand	299	277	299	299
Cement	510	472	510	510
Silica fume	224	208	224	224
Slag	102	94	102	102
Limestone powder	184	170	184	184
Water	121	136	121	121
Superplasticizer	48	43	48	48
Steel fibers (1.5% vol.)	-	118	127	127
PP fibers (0.11% vol.)	-	-	-	1.6
Water to binder ratio	0.14	0.15	0.14	0.14
Beams casted	-	U-B1, U-B2	-	U-B10, U-B11
High temperature property test specimens	Thermal	-	Thermal, mechanical	Thermal, mechanical
Comp. strength- 28^{th} day	151	145	168	160
Comp. strength- 90^{th} day	164	167	178	173
Split tensile strength- 28^{th} day	6	14	15	14
Split tensile strength- 90^{th} day	7	15	16.5	15
Casting date	April 2018	July 2015	April 2018	April 2018

The batch mixes were prepared by a local ready-mix concrete plant and were supplied to the site for fabrication of beams, prisms, and cylinders. Batch UHPC-S1 was cast at a field site on Michigan State University campus in July 2015. Batches UHPC plain, UHPC-S2, and UHPC-H were poured at the Civil Infrastructure Laboratory of Michigan State University in April 2018. The UHPC mixing sequence is crucial for attaining a uniform and workable mix without fiber balling. For the batch poured earlier in July 2015, cement and coarse aggregate were added using the automated system in the plant. Then, 80% of total water was added to the mix truck followed by the addition of superplasticizer. After that, silica sand, silica fume, slag, and limestone powder were loaded into the truck. Then, the rest of the water and steel fibers were added. All the ingredients were mixed at a rate of 70 revolutions within 5–7 min and transported to the field site approximately 10 miles away. However, cement balling and fiber balling were observed in this batch (UHPC-S1). Therefore, a new mixing procedure was adopted for the next batch. The mix UHPC-S1 was poured into two beams (U-B1 and U-B2) and specimens for strength tests.

For the concrete batches cast in April 2018, the coarse and fine aggregates were first dry mixed, followed by dry mixing of the binders in the following order: silica fume, slag, limestone powder, and cement. Then, one-third amount of the total water was added to the mix in the form of ice, for slowing down the reaction time. Pre-mixed remaining water (two-third of total) and superplasticizer were added and mixed at high speed (1 revolution per 4 seconds) for 5 minutes, followed by reversing the mixing bowl of the truck in order to bring the settled ingredients from the bottom to the top, to ensure uniformity in the mix. At this point, the plain UHPC mix was poured into specimens for thermal property and strength tests. Following this, the remaining mix was used for batches UHPC-S2 and UHPC-H, wherein steel fibers were added and mixed for another 5 min with bowl reversal to attain a homogenous mixture. Polypropylene fibers are added

in UHPC-H and mixed for another 5 min. UHPC-H was poured into two beams (U-B10 and U-B11), and both UHPC-S2 and UHPC-H were poured into specimens for thermal and mechanical property tests.

Steel fibers, 1.5% by volume fraction was added to all batch mixes, except batch UHPC plain. Based on the literature review, steel fibers with an aspect ratio higher than 65 did not significantly improve the strength and ductility properties and also instituted problems of poor flowability, fiber balling, and uneven distribution of fibers in UHPC [110,111]. Thus, the steel fibers with an aspect ratio of 65 (0.2 mm diameter and 13 mm length) were incorporated. The steel fibers were of straight type (without hooks) and had tensile strength in the range of 690 to 1000 MPa. In addition to steel fibers, polypropylene (PP) fibers, 0.11% by volume fraction, were added to UHPC-H mix. The optimal amount of polypropylene fibers recommended to mitigate spalling ranges from 1 to 3 kg/m^3 and this is mostly based on studies for HSC members [112]. The dosage of PP fibers was selected prudently as 1.6 kg/m^3, to attain the desired high strength and workability of the UHPC mix. Monofilament PP fibers with a length of 13 mm and a melting point of 160°C were used. The tensile strength of the PP fibers is in the range of 570–660 MPa. The steel and polypropylene fibers utilized in this study are shown in Figure 3.1 and their property details are presented in Table 3-2.

Table 3-2. Properties of steel and polypropylene fibers used in UHPC batch mix.

Type of fiber	Diameter d_f (mm)	Length l_f (mm)	Aspect ratio (l_f /d_f)	Tensile strength (MPa)	Density (kg/m^3)	Melting temperature (°C)
Steel	0.2	13	65	960	7850	-
Polypropylene	0.018	13	722	570-660	910	170

a)  b) 

Figure 3.1. Fibers: (a) Steel (b) Polypropylene (PP).

3.3. Design and Fabrication of UHPC Specimens and Beams

The UHPC beams were designed based on the available best practice recommendations as no specific design provisions for UHPC members are currently available [110,113–115]. Four UHPC beams, designated as U-B1, U-B2, U-B10, and U-B11, were designed and fabricated. Beams U-B1 and U-B2 were fabricated from UHPC mix reinforced with steel fibers only (UHPC-S1), while beams U-B10 and U-B11 were fabricated from UHPC mix with steel and polypropylene fibers (UHPC-H). All the UHPC beams were of rectangular cross section with dimensions of 180 mm in width and 270 mm in depth. The length of the beams was 4000 mm and dictated by the size of the furnace and loading equipment at MSU civil infrastructure laboratory.

This experimental study is a part of an ongoing larger research project to develop information on the performance of UHPC beams at ambient and elevated temperatures. As a part of this larger research project, the effect of removing compression and shear reinforcement (stirrups) in beams, to take advantage of high compressive and high tensile strength offered by UHPC, is being explored. Hence, beams U-B1, U-B2, and U-B10 had only three reinforcing bars (no compression rebars or stirrups) of 13 mm diameter as tensile reinforcement (ρ_t), whereas beam U-B11, in addition to tensile reinforcement, had shear reinforcement (ρ_v).

The shear reinforcement in beam U-B11 is comprised of close looped stirrups spaced at 100 mm and made from 10 mm diameter steel rebar. All beams are provided with a nominal concrete cover of 35 mm to tensile reinforcing bars. The rebars spacing, arrangement, and shear reinforcement were designed as per ACI-318 requirements for NSC beams [116]. Geometric characteristics of the tested UHPC beams are tabulated in Table 3-3 and their detailed cross-sectional configurations are shown in Figure 3.2.

Table 3-3. Sectional dimensions and reinforcement details in UHPC beams.

Beam Designation	Width (mm)	Depth (mm)	Span length (mm)	Fiber	Tensile Reinforcement	ρ_t (%)	ρ_v (%)
U-B1	180	270	3658	Steel	3-Ø13mm	0.90	-
U-B2	180	270	3658	Steel	3-Ø13mm	0.90	-
U-B10	180	270	3658	PP*+Steel	3-Ø13mm	0.90	-
U-B11	180	270	3658	PP*+Steel	3-Ø13mm	0.90	0.79

PP*: Polypropylene fibers, ρ_t: Tensile reinforcement ratio, ρ_v: Shear reinforcement ratio

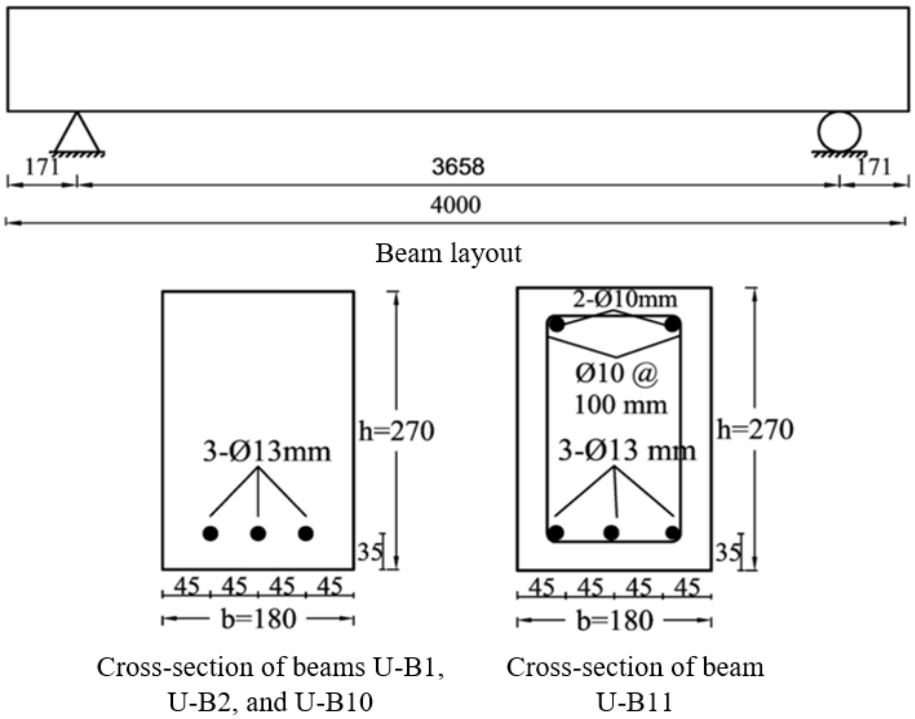

Figure 3.2. Layout and cross section of UHPC beams (All units are in mm).

In addition to beams, for measuring high-temperature material properties, small specimens including 75 x 150 mm cylinders, 100 x 100 mm cubes, and 100 x 100 x 300 mm prisms were prepared. Thermal property tests were undertaken on specimens fabricated using UHPC plain, UHPC-S2, and UHPC-H, whereas mechanical property tests were carried out on specimens made using UHPC-S2 and UHPC-H. Details of specimens utilized for high-temperature property tests are shown in Table 3-4. Mechanical property tests were carried out on 75 x 150 mm cylinders. For thermal property tests, specimens were cut from cured concrete prisms and the size of the test specimens was different for different thermal property tests.

Table 3-4. Test matrix of specimens utilized for high temperature material property tests.

Property	Concrete type	Specimen shape	Specimen dimensions	Test temperature (°C)	Heating rate (°C/min)	Number of specimens (property x concrete type x temperature x heating rate x repetitions)
Thermal conductivity Specific heat	UHPC plain UHPC-S2 UHPC-H	Prism	50x50x25 mm	20-700	N/A	2x3x1x1x3=18
Thermal expansion	UHPC plain UHPC-S2 UHPC-H	Prism	10x10x18 mm	20-900	3	1x3x1x1x3=9
Mass loss	UHPC plain UHPC-S2 UHPC-H	Prism	50x50x25 mm	20	N/A	1x3x5x1x2=30
				200 400 500 600 750	0.5	
Compression Tension	UHPC-S2 UHPC-H	Cylinder	75x150 mm	20	N/A	2x2x1x1x3=12
				200 400 600 750	0.5 2	2x2x4x2x1=32

As part of the fabrication of the beams, plywood forms were assembled to achieve the required internal dimensions in the beams. Thermal curing is essential for the development of a denser microstructure of UHPC with the completion of pozzolanic reactions for increased formation of

calcium silica hydrate (C-S-H) [117]. To attain in-situ high-temperature curing, from the heat of hydration of high cementitious binder contents in UHPC, adequate insulation was provided in the formwork of the beams using rigid Styrofoam. Rigid Styrofoam insulation of 50 mm thickness was installed on two interior sides of the framework and the bottom side of the framework was provided with rigid Styrofoam of 100 mm thickness (Figure 3.3(a)). In the fabrication of UHPC structures, the heat of hydration with surface cooling effects can generate high temperature gradients with higher temperatures developing in the concrete core (due to heat of hydration of cementitious components) as compared to regions closer to the external surface of the beams. Such non-uniform temperature distribution can disrupt the hydration process and cause cracking in concrete from thermal stresses. Besides assisting in thermal curing, the insulation provided in the formwork also helps to prevent such early age cracking by maintaining relatively uniform temperatures within the casted beams.

The beams were fabricated using a UHPC mix supplied in a ready-mix truck (Figure 3.3(b)). Following casting, insulating blankets were used to cover the casted beams (Figure 3.3(c)), and a wet muslin cloth to cover the small specimens for preventing heat loss, generated during hydration of the binder in UHPC. The temperatures developed while curing of UHPC beams, from the heat of hydration of the cementitious matrix, were monitored. A sustained rise in temperature was observed in the first 25 h of curing time with peak temperatures reaching about 75°C. During the fabrication of UHPC beams, cylinders and prisms were also cast, as mentioned above. The cylinders and prisms were steam cured for 48 h and subsequently stored in controlled conditions of air maintained at 25°C temperature and 60% relative humidity. Compression and splitting tensile strength tests were carried out on three specimens of each UHPC mix for repeatability and reliability. The average compressive and tensile strength of concrete cylinders measured at 28 and

90 days are plotted in Figure 3.4 and Figure 3.5 respectively with the standard deviation in measurements as error bars, as well as tabulated in Table 3-1.

Figure 3.3. (a) Formwork for UHPC beams, (b) Casting of beams, (c) Curing of beams using insulation blankets and lining.

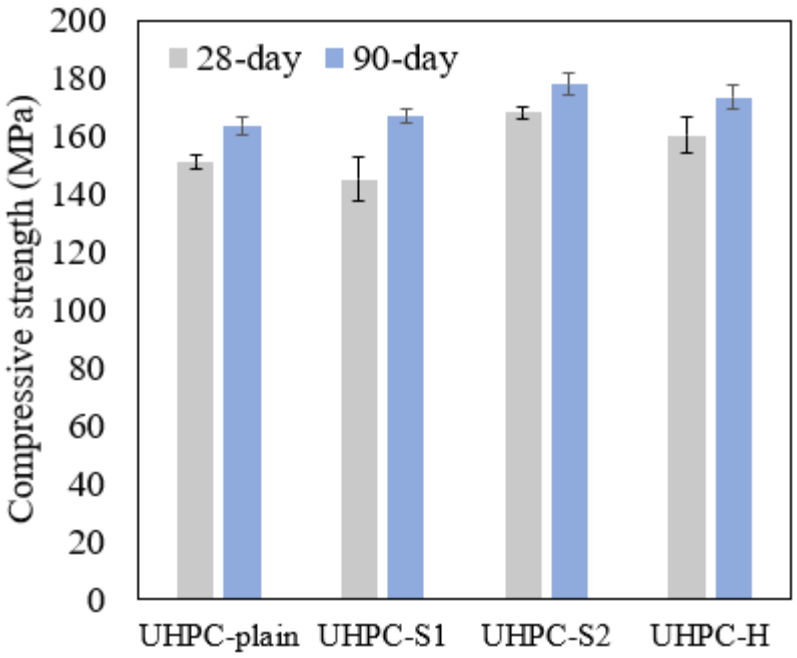

Figure 3.4. Compression strength test results for each UHPC mix.

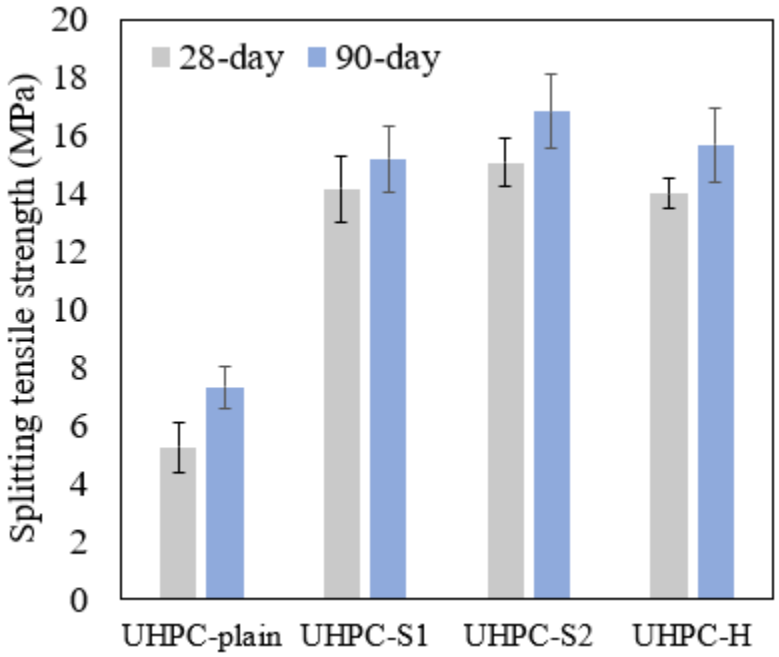

Figure 3.5. Tension strength test results for each UHPC mix.

3.4. Instrumentation

For mechanical property tests, cylinders were instrumented with three type K chromelalumel thermocouples, 0.91 mm thick, to measure temperature in the furnace, at the surface, and mid-

depth of the specimen. The instrumentation mounted in the beams included thermocouples, displacement transducers, and strain gauges. Type-K chromelalumel thermocouples, 0.91 mm thick, were installed at two different cross sections (mid-span and quarter span) in each beam for measuring concrete and rebar temperatures. The deflection of each beam is measured at mid-span as well as at the location of the two-point loads using linear variable differential transformers (LVDTs). These LVDTs were placed outside the furnace (on the top of the beam) since they cannot survive high-temperature exposure within the furnace. LVDTs are connected to a well-insulated stiff threaded steel rod attached to mid span and two load points in the beam. The steel rod extends vertically to pass through a special opening in the furnace lid. The strain gauges were mounted on two main longitudinal reinforcements and one compression reinforcement for beam U-B11 with an adhesive (glue) application. These strain gauges were of the high-temperature foil strain gauge type, which usually is able to provide reliable strain readings in the temperature range of 20-350°C. These high-temperature strain gauges were used to obtain strain data at rebar level to supplement the data obtained externally through LVDTs. The location and numbering of the thermocouples and strain gauges are shown in Figure 3.6.

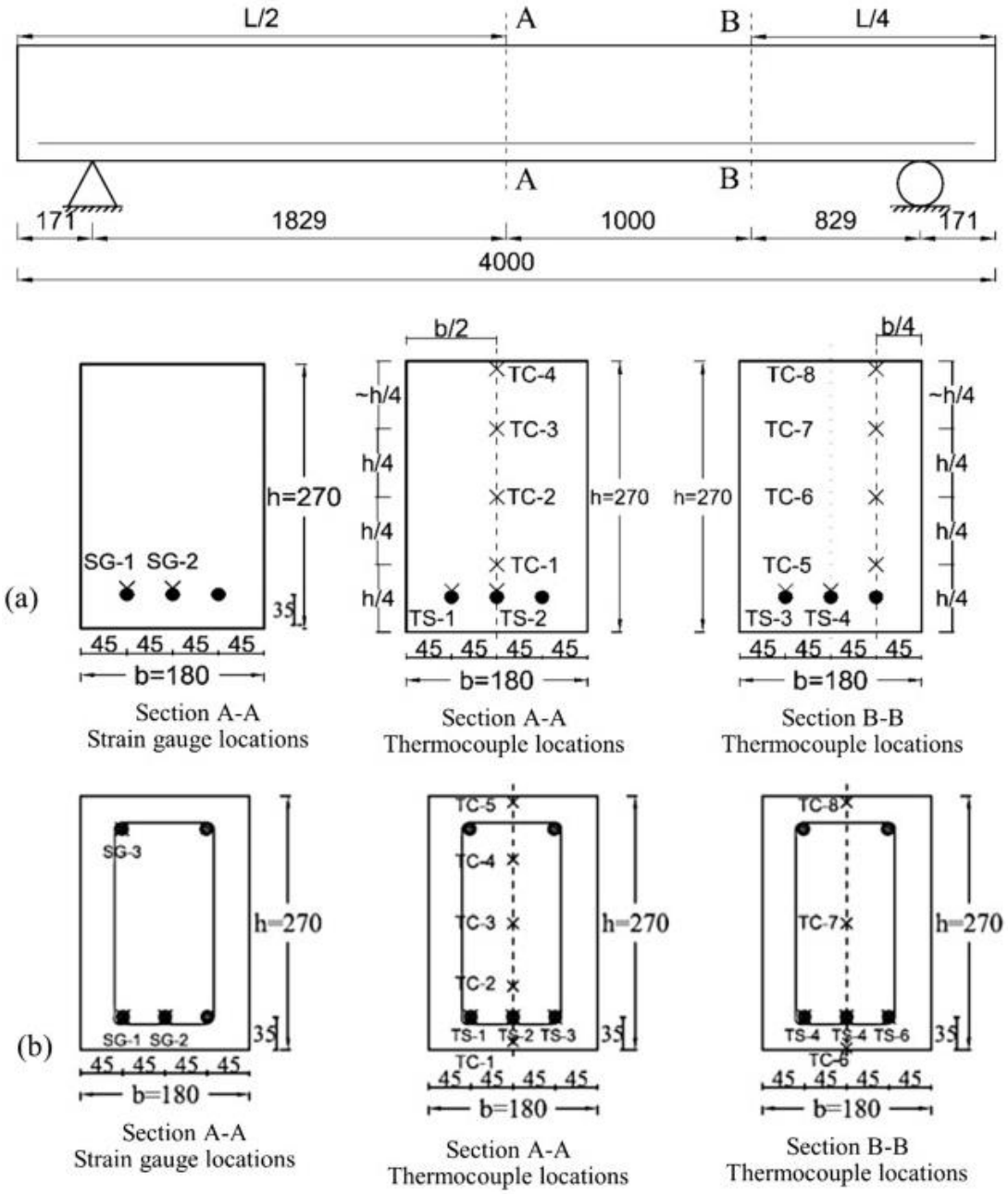

Figure 3.6. Location of strain gauges and thermocouples at various cross-sections in (a) beams U-B1, U-B2, and U-B10, (b) beam B-11 (All units are in mm).

3.5. High Temperature Property Tests on UHPC

To develop high temperature thermal and mechanical properties for UHPC, a comprehensive test program was undertaken on different types of UHPC namely, UHPC plain (no fibers), UHPC with steel (UHPC-S2), and hybrid fibers (UHPC-H).

3.5.1. Thermal Properties

3.5.1.1. Test Specimens

For thermal property tests, specimens were cut from concrete prisms using a power saw and perfectly ground at the ends for accurate measurements. For thermal conductivity, specific heat, and mass loss measurements, specimens had dimensions 50 × 50 × 25 mm (Figure 3.7(a)), whereas for thermal expansion measurements, specimens of size 10 × 10 × 18 mm were cut from the prisms (Figure 3.7(b)). The thermal properties of UHPCs were measured using relevant test procedures and equipment [25].

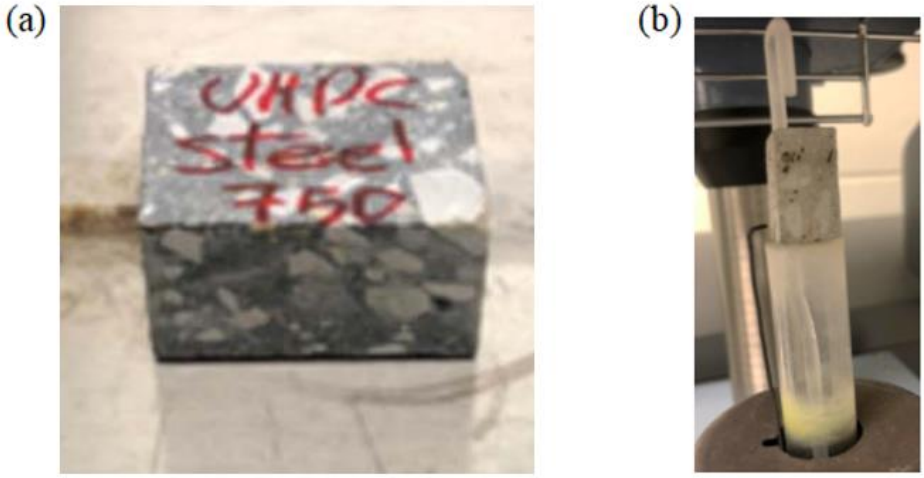

Figure 3.7. Specimens for thermal property tests: (a) 50×50×25 mm; (b) 10×10×18 mm.

3.5.1.2. Test Procedure

Thermal expansion measurements were carried out as per the procedure laid out in ASTM E831 [32]. A thermomechanical analyzer (TMA) was used for thermal expansion measurements in the temperature range of 20–900°C. The TMA utilized a movable LVDT, which generates an output signal corresponding to the dimensional change of the test specimen. A flat-tipped expansion probe was placed on the concrete specimen and a small static force was applied to the probe, so that the probe remained in contact with the specimen throughout the test. The heating rate in the TMA was

set to 3°C/min and the linear dimension changes (expansion or contraction) of the specimen were recorded at various target temperatures. During the thermal expansion test, one of the UHPC-S2 specimens spalled at around 200°C as shown in Figure 3.8 (a), which severely damaged the TMA (Figure 3.8 (b)). The thermal expansion tests were repeated on three specimens from each concrete batch and the variability was within 5%, indicating good reliability of the measurements as shown in Figure 3.9. The error bars could not be plotted for thermal expansion curves as they are measured as a continuous function of temperature through TMA.

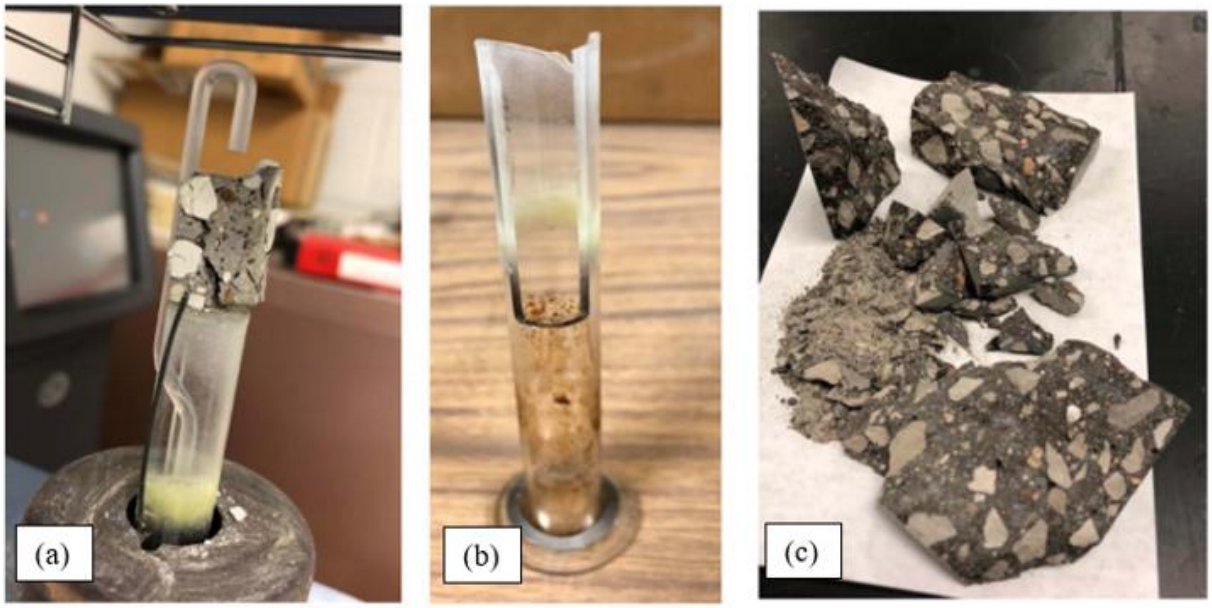

Figure 3.8. Exploded specimen during (a) TMA test; and (b) damaged glass specimen holder from TMA test; and (c) mass loss test.

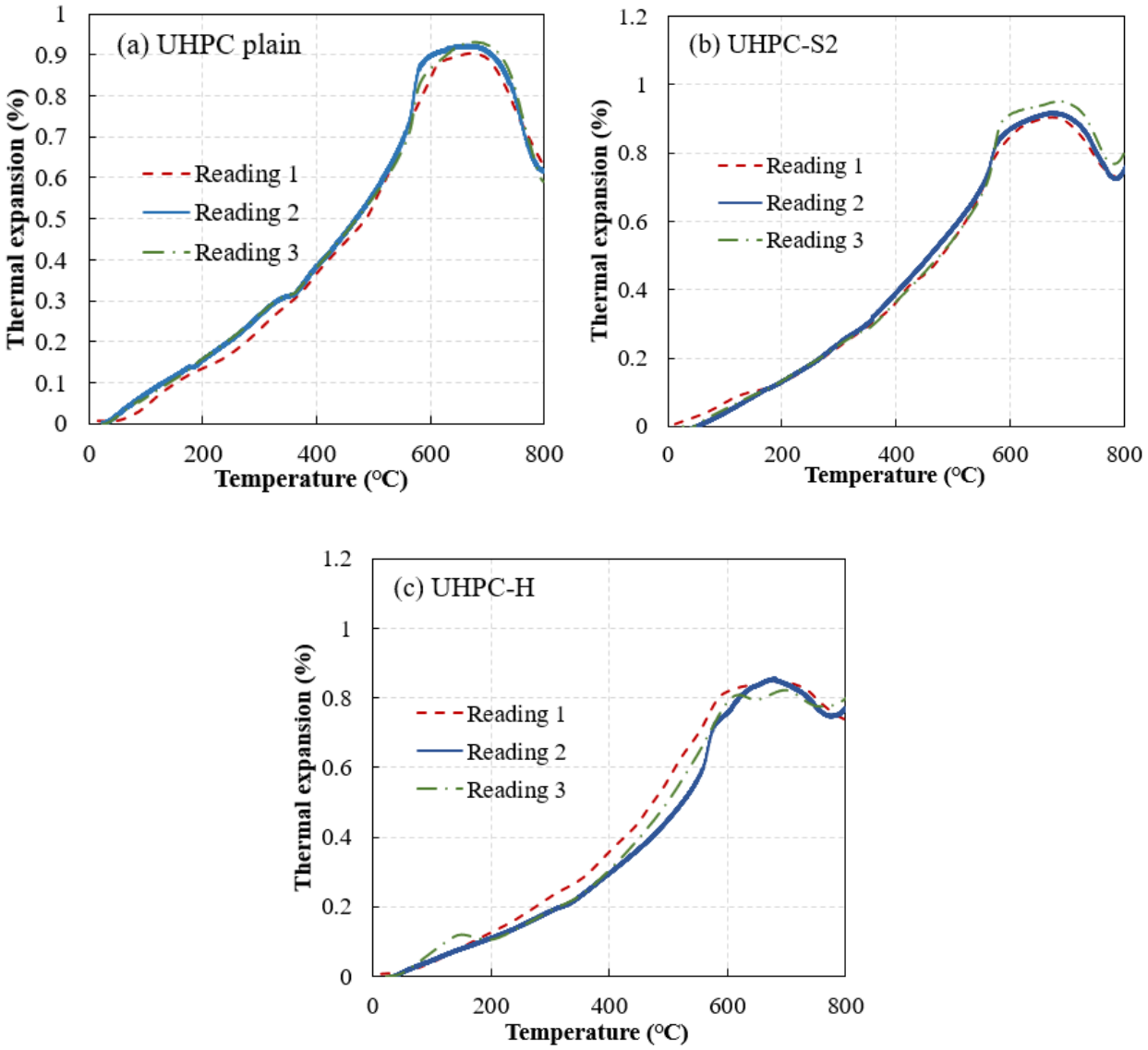

Figure 3.9. Measured thermal expansion for each UHPC mix.

Thermal conductivity and specific heat measurements were carried out using the Hot Disk TPS 2500S thermal constant analyzer, as per the procedure laid out in ISO 22007-2 [29]. The specimens were exposed to elevated temperatures in a furnace connected to the Hot Disk apparatus. Hot Disk utilizes a transient plane source (TPS) technique to measure thermal conductivity and specific heat. A flat sensor, which is a spiral nickel wire probe insulated between layers of mica was placed between two specimens. The Hot Disk test regime was set up to record thermal property measurements at eight different target temperatures of 20°C, 100°C, 200°C, 300°C, 400°C, 500°C,

600°C, and 700°C. At each target temperature, upon attainment of equilibrium conditions in the specimen, the sensor simultaneously measured thermal conductivity and thermal diffusivity, and then specific heat was computed internally.

Mass loss measurements were carried out by recording the mass of the test specimen before and after exposure to a target elevated temperature in an enclosed electric furnace. Mass loss of the test specimens at different target temperatures of 20°C, 200°C, 400°C, 500°C, 600°C, and 750°C was measured. Test specimens from the plain UHPC and UHPC-S2 (without PP fibers) batch mix suffered explosive spalling at around 200°C when subjected to heating rates of more than 0.5°C/min as shown in Figure 3.8 (c). Therefore, all mass loss test specimens were heated at a consistent low heating rate of 0.5°C/min to target temperatures. To ensure the reliability of the measurements, thermal conductivity, specific heat, and mass loss measurements were conducted on two repeat specimens at each target temperature and the measured values were within 5% as plotted in Figure 3.10 with standard deviations of the measurements as error bars.

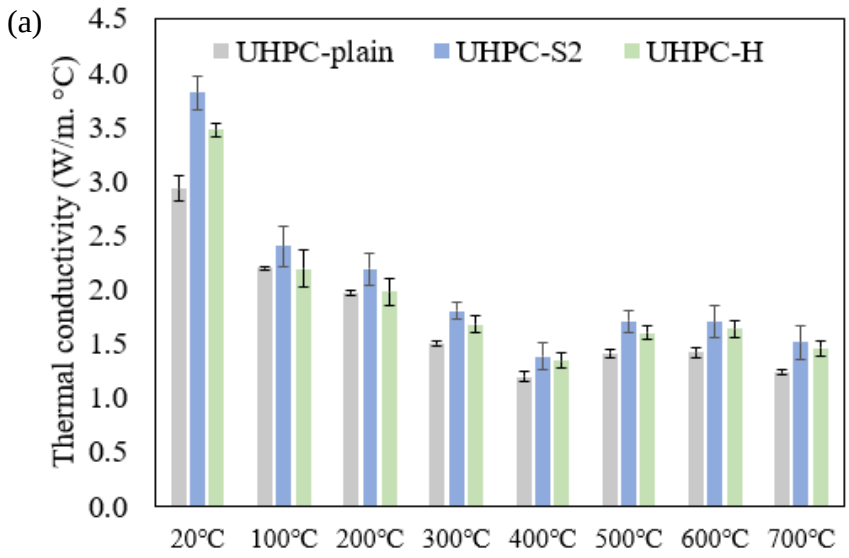

Figure 3.10. Measured thermal properties for each UHPC mix: (a) Thermal conductivity; (b) Specific heat; and (c) Mass loss.

Figure 3.10. (cont'd)

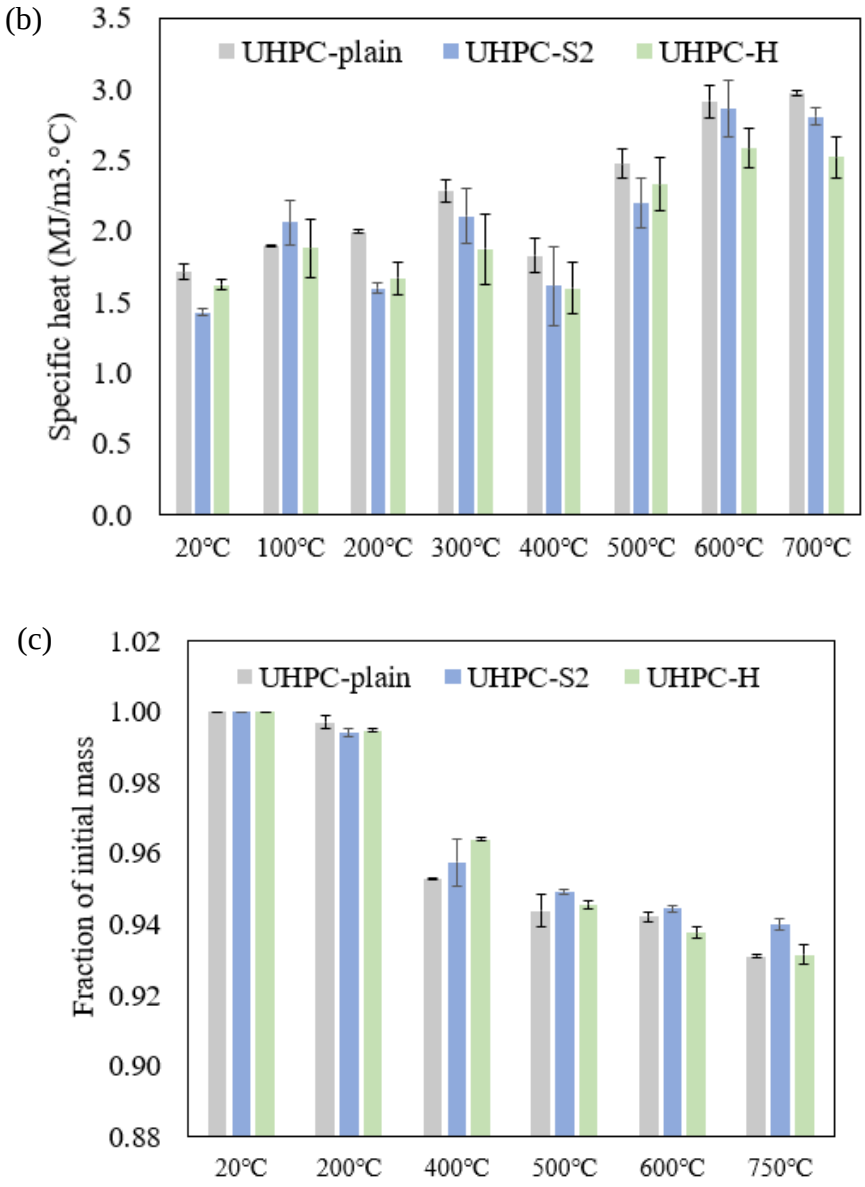

3.5.1.3. Results

The variation of thermal conductivity, specific heat, mass loss, and thermal expansion of UHPC (plain), UHPC-S2, and UHPC-H as a function of temperature is plotted in Figure 3.11. These variations with temperature follow a similar trend in all three UHPCs and can be grouped into four stages. The variation of thermal properties in concrete with temperature is mainly governed by the change in moisture levels occurring with temperature increase. Moisture is present in concrete in

different forms and the variation in the moisture level is influenced by microstructural changes that take place in concrete under high-temperature exposure as summarized in Table 3-5. At temperatures above 100°C, the free water starts to evaporate, and when the concrete temperature reaches about 300°C, adsorbed water, interlayer water from calcium silicate hydrate (C-S-H) gel and a portion of the chemically bonded water start to evaporate. Further increase in concrete temperature to 400°C causes decomposition of calcium hydroxide, $Ca(OH)_2$ into CaO and H_2O, leading to more evaporation of moisture. Further temperature rise beyond 500°C leads to decomposition of C-S-H and further deterioration of concrete and aggregate.

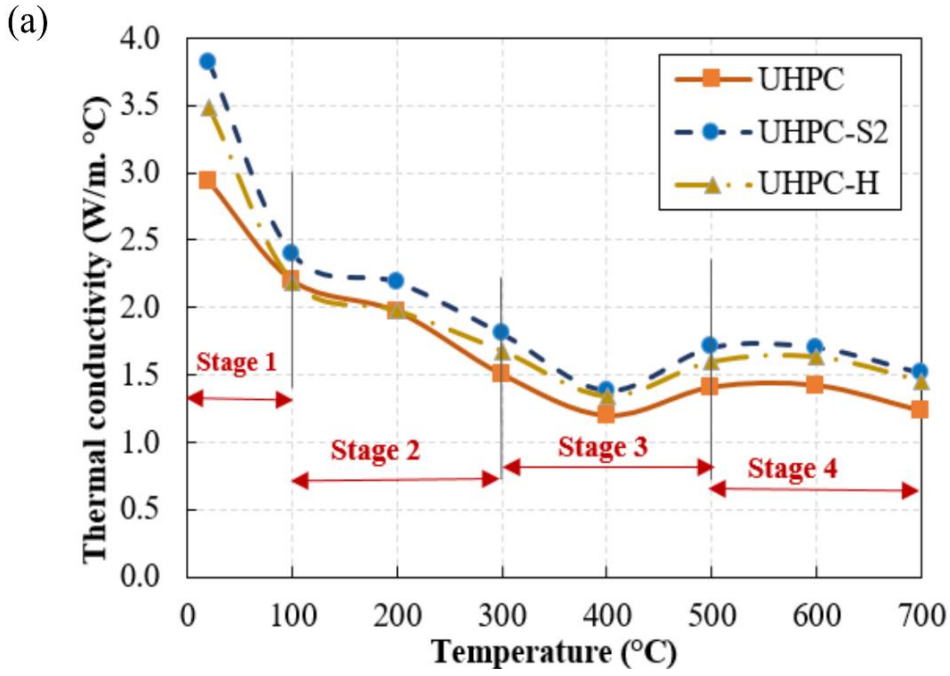

Figure 3.11. Measured thermal properties as a function of temperature for three UHPC types: (a) Thermal conductivity; (b) Specific heat; (c) Mass loss; and (d) Thermal expansion.

Figure 3.11. (cont'd)

(b)

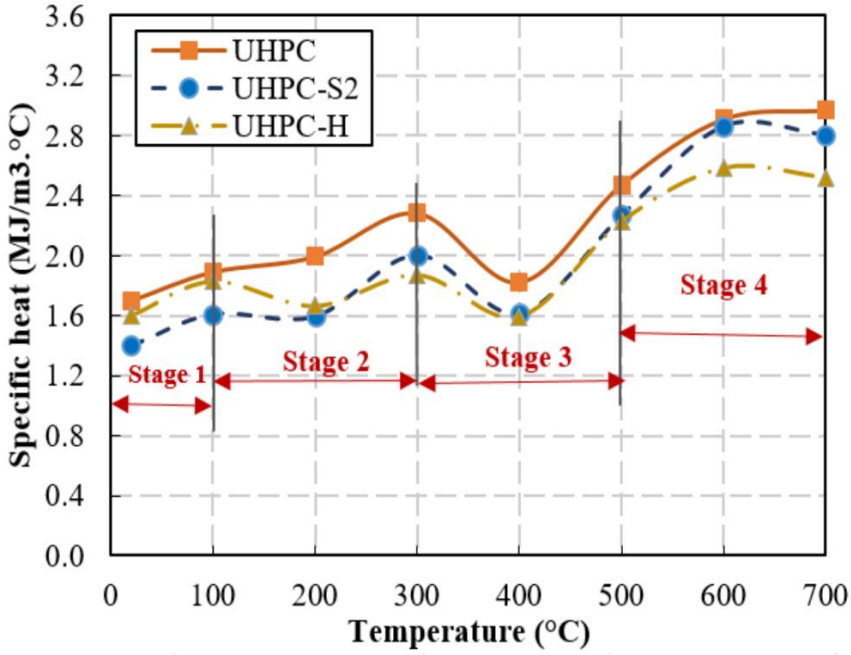

(c)

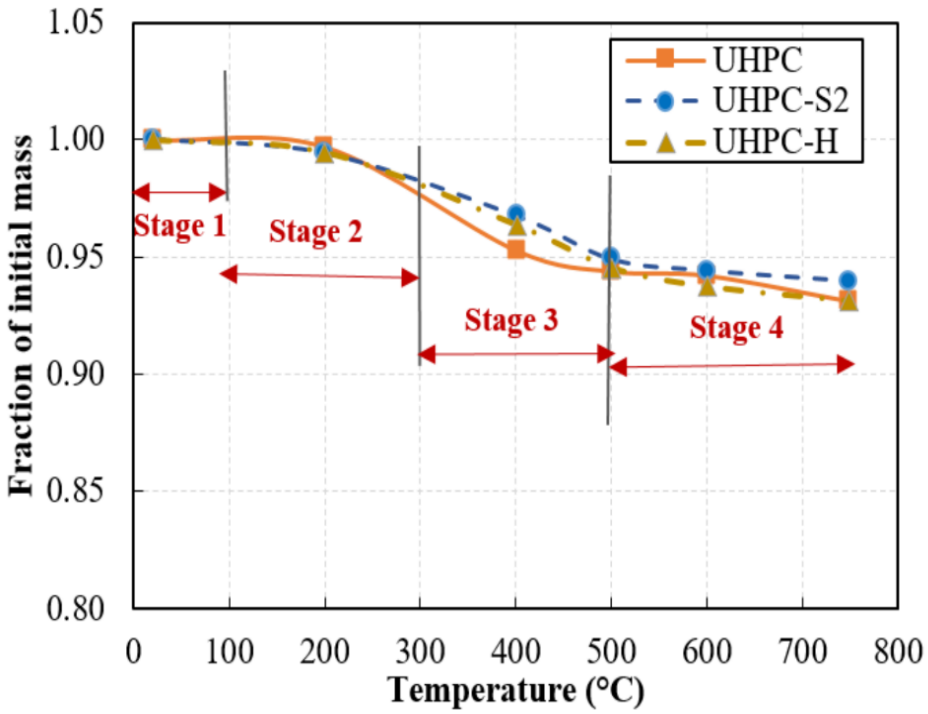

Figure 3.11. (cont'd)

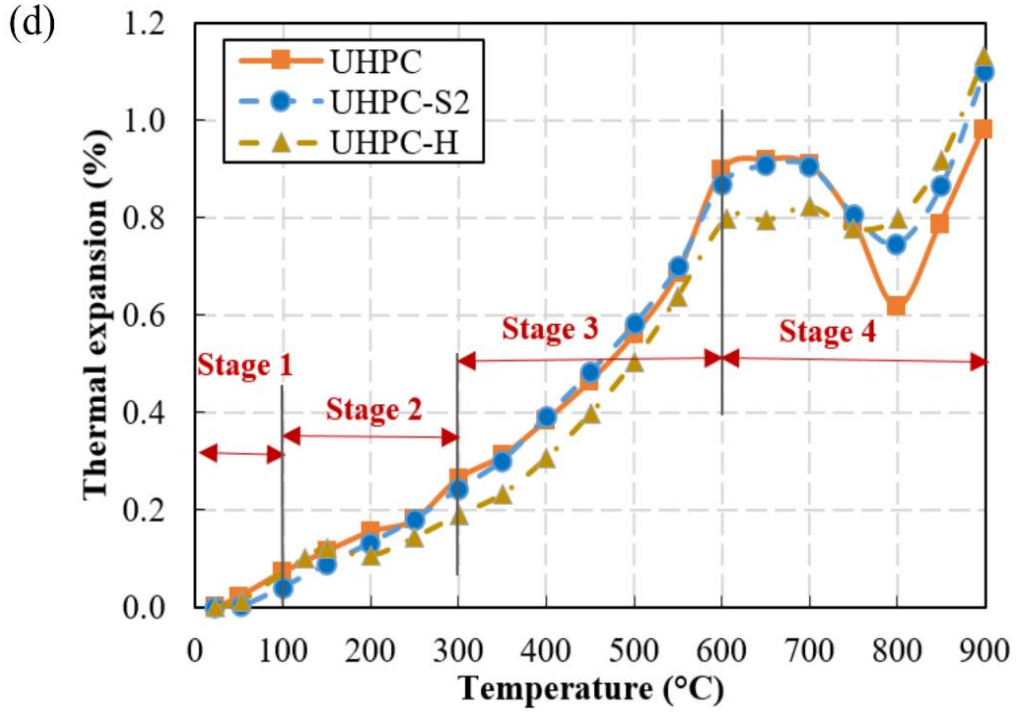

Table 3-5. Changes in concrete's microstructure with rise in temperature.

Temperature (°C)	Changes in microstructure
100	Evaporation of free water out of concrete
200	Meltdown of polypropylene fibers (if present)
300	Loss of adsorbed, interlayer C-S-H water and chemically bounded water
400	Dissociation of $Ca(OH)_2$ into CaO and H_2O
500	Decomposition of C-S-H
600	Quartz phase transformation in some aggregate (siliceous) types
700	Dissociation of dolomite in some aggregate (carbonate) types (endothermic reaction)
900	Complete decomposition of C-S-H

Thermal Conductivity

The variation of thermal conductivity of plain UHPC, UHPC-S2, and UHPC-H with temperature is plotted in Figure 3.11 (a). The thermal conductivity of these three types of UHPC at room temperature is in the range of 2.9 and 3.8 W/m°C. In general, the variation of thermal conductivity

with temperature follows a similar trend for all three UHPCs and can be grouped into four stages. For all three types of UHPC, thermal conductivity sharply decreases initially up to a temperature of 100°C in stage 1. This can be attributed to moisture loss resulting from the evaporation of free water present in concrete. In stage 2, i.e. 100-300°C, the remaining free water, together with the adsorbed water, as well as interlayer water from calcium silicate hydrate (C-S-H) gel and a portion of the chemically bonded water evaporate resulting in a steady decrease of thermal conductivity. Thermal conductivity for all UHPCs varies marginally from 300 to 500°C in stage 3, owing mainly to the decomposition of $Ca(OH)_2$ into CaO and H_2O, moisture increases, resulting in a small increase in thermal conductivity. This is followed by stage 4, beyond 500°C and up to 700°C, where a slight decrease in thermal conductivity occurs due to the second phase of C-S-H decomposition involving release of a small amount of strongly held moisture left within calcium silicate hydrate (C-S-H) layers.

Figure 3.11 (a) also shows the effect of fibers on the thermal conductivity of UHPC as a function of temperature. At room temperature, the fiber-reinforced UHPC mixes (UHPC-S2 and UHPC-H) exhibit slightly higher thermal conductivity than plain UHPC (without any fibers) and this can be attributed to the presence of steel fibers which have high thermal conductivity in the range of 50 W/m°C. Upon heating beyond 100°C, thermal conductivity of UHPC-H is lower than UHPC-S2 and follows closely to that of UHPC, due to the presence of polypropylene (PP) fibers. PP fibers have inherent low thermal conductivity values (0.1-0.2 W/m°C) and melting point of around 160°C, which create pores in concrete matrix upon melting and lower the thermal conductivity further. However, upon complete melting of all the PP fibers at high temperatures beyond 400°C, the thermal conductivity values of UHPC-S2 and UHPC-H are close to each other, and slightly

higher than UHPC without any fibers. Overall, the trends indicate that there is no significant effect of fibers in thermal conductivity values of UHPC throughout the temperature (20-700°C) range.

Specific Heat

The measured specific heat of three types of UHPC is plotted in Figure 3.11 (b) as a function of temperature. The room temperature specific heat of the three types of UHPC lies around 1.4-2 $MJ/m^3°C$. Similar to thermal conductivity, the specific heat variation in all three types of UHPC is influenced by microstructural changes due to variation of moisture and can be broadly grouped into four stages. Specific heat is also governed by the physicochemical changes that occur in the cement paste and the aggregates at temperatures exceeding 600°C. Specific heat around 100°C (in stage 1), increases due to evaporation of moisture present in the form of free water. In stage 2, i.e. 100-300°C range, specific heat increases further due to evaporation of moisture present in the remaining free water, along with adsorbed and bonded water. Specific heat in stage 3, i.e. 300-500°C range, remains almost constant due to counteracting effects of decrease in moisture owing to complete evaporation of all the water present in concrete and increase in moisture due to the release of chemically bound water in concrete from the decomposition of $Ca(OH)_2$. Finally, specific heat increases followed by stabilization in stage 4, i.e. 500-700°C range, due to release of moisture from C-S-H gel decomposition and significant deterioration of microstructure within concrete. The micro and macro crack development beyond 600°C increases the porosity of UHPC resulting in lower specific heat at elevated temperature.

All three types of UHPC (plain, with steel fiber, steel, and with hybrid fibers) exhibit similar variation in specific heat with increasing temperature. Overall, the specific heat of UHPC-H and UHPC-S2 are lower than UHPC throughout the temperature range. The lower specific heat of fiber-reinforced UHPC can be attributed to the increase in porosity due to the addition of fibers.

Moreover, the specific heat of UHPC-H (with steel and PP fibers) is slightly lower than that of UHPC-S2 (with steel fibers only) in 200-700°C range. In the case of UHPC-H, polypropylene fibers decompose (after burning), leading to an increase in the porosity of concrete. As a result, UHPC-H becomes more pervious, and less amount of heat is required to raise its temperature.

Mass Loss

The mass of concrete decreases with temperature rise due to loss of moisture. In addition, mass loss in carbonate aggregate concrete is higher due to the dissociation of dolomite in carbonate aggregate at around 600°C. The mass loss in UHPC (plain), UHPC-S2, and UHPC-H, is plotted in Figure 3.11 (c) and can be grouped into four stages based on the observed trends. In stage 1, i.e. 20-100°C range, initial mass loss in all the three types of UHPC is very small, and this loss is attributed to evaporation of free water present in concrete. Since, UHPC has a very dense microstructure due to low water-cement ratio, the free water in UHPC is considerably less. Hence, the rate of mass loss due to the evaporation of free water is marginal. In comparison with stage 1, mass loss is slightly higher in stage 2, i.e. 100-300°C range and this can be attributed to the evaporation of the left-over free water, as well as adsorbed and bounded water. In stage 3, i.e. 300-500°C range, rapid mass loss takes place due to increase in available water in the concrete microstructure from the decomposition of $Ca(OH)_2$ into CaO and H_2O. Finally, in stage 4, between 500-750°C range, mass loss stabilizes owing to complete evaporation of the water present in concrete. Only a slight increase in the extent of mass loss can be observed in this stage due to dissociation of dolomite in carbonate aggregate present in concrete. Overall, the mass loss in all types of UHPCs is within 8% in 200-750°C temperatures owing to less amount of available moisture in UHPC. Further, the effect of fibers on mass loss of UHPC is minimal due to very small amount of fibers (1.5% for steel and 0.11% for PP fibers) present in UHPC.

Thermal Expansion

The variation of measured thermal expansion of UHPC, UHPC-S2, and UHPC-H, is presented as a function of temperature in Figure 3.11 (d). For all UHPC types, thermal expansion is taken to be zero at room temperature. The thermal expansion increases steadily in 20-600°C range, becomes invariant between 600-700°C, decreases in 700-800°C and then, increases sharply in 800-900°C range. The variation of thermal strain of concrete with temperature is linked to changes in moisture content, cement paste, and aggregates and can be grouped under four stages as in the case of other thermal properties. In stage 1, i.e. 20-100°C range, thermal expansion increases at a substantial rate due to high thermal expansion of cement paste and constituent aggregates of concrete. The thermal expansion increases at a slightly lower rate in stage 2, i.e. 100-300°C range, and this is attributed to the evaporation of free, adsorbed, and combined water from the cement matrix. Loss of water due to heating contributes to thermal shrinkage rather than expansion of concrete. Thermal expansion of UHPC continues to increase with temperature in stage 3 comprising of 300-600°C range. The rate of increase is slower between 400-500°C due to evaporation of remaining water in C-S-H layers and water liberated from the dissociation of $Ca(OH)_2$. Above 500°C, thermal expansion increases steeply due to the quartz transformation in natural sand present in UHPC, along with an expansion of the cement paste. The expansion rate initially subsides but is followed by an increasing trend in stage 4, between 600 and 900°C for UHPC. The initial decrease in thermal change indicates negative volume change or shrinkage, and can be attributed to the release of chemically bound water in hydrates present in the concrete. Beyond 800°C, in stage 4, thermal expansion increases again, along with softening of concrete and development of macro-crack in the specimen. This substantial increase in expansion is due to decarbonation of limestone-based

(carbonate) aggregate. Severe cracking was observed in all the three UHPC types (plain UHPC, UHPC-S2, and UHPC-H) beyond 800°C.

As can be seen in Figure 3.11 (d), the presence of fiber has only a moderate influence on thermal expansion between 20-160°C. It can be seen that the hybrid-fiber (steel and PP) reinforced UHPC has a slightly lower thermal expansion than that of plain UHPC and UHPC-S2 types beyond 160°C. The decrease in the rate of thermal expansion beyond 160°C can be attributed to the ease of dehydration of comparatively porous UHPC-H specimen, resulting from empty channels formed after melting of polypropylene fibers. However, beyond 750°C, the effect of burning of polypropylene fibers in UHPC-H diminishes, and the rise in thermal expansion is similar to that of UHPC-S2. The addition of steel fibers does not have a pronounced effect on thermal expansion, due to counteracting effects of steel expansion and crack control effect facilitated by steel fibers. Above 800°C, the thermal expansion of steel fiber reinforced concrete increases slightly more, with temperature as compared to plain UHPC. This slight increase with temperature can be attributed to the presence of steel fibers in UHPC-S2, which continue to expand at elevated temperatures.

From the measured data, it can be clearly seen that the addition of fibers does not significantly influence the thermal properties of UHPC. However, the effect of addition of fibers is in the form of minimizing spalling in fiber-reinforced specimens as compared to plain UHPC specimens. Specimens fabricated with plain UHPC and steel-reinforced UHPC experienced spalling during thermal property tests. On the other hand, UHPC-H specimens, fabricated with a combination of steel and polypropylene (PP) fibers, did not experience any spalling in the entire 20-800°C temperature range. This can be attributed to the fact that the polypropylene fibers present in UHPC-H melt at about 160ºC creating pores and microcracks in concrete that are sufficient for relieving

vapor pressure developed in the concrete. The presence of steel fibers in UHPC-H has also some influence in minimizing spalling since steel fibers enhance the tensile strength of UHPC-H, which in turn helps in withstanding tensile stresses exerted by high pore pressure generated in concrete. However, it is evident from the undertaken tests that the sole incorporation of steel fibers is less efficient than hybrid fibers (steel and PP) in UHPC for mitigating fire-induced spalling.

3.5.1.4. Property Relations

Data generated from the thermal property measurements were utilized to develop property relations for different UHPC types as a function of temperature [118]. The correlations were developed using linear and polynomial regression analysis. Because the test data indicate that fibers have no significant effect on the thermal properties of UHPC, the developed relations are applicable for plain and fiber-reinforced UHPC (UHPC-S2 and UHPC-H). The developed empirical relations are shown in Table 3-6 over temperature ranges of 20–700°C for thermal conductivity and specific heat, 20–750°C for mass loss, and 20–900°C for thermal expansion.

Table 3-6. Thermal property relations of UHPCs generated utilizing data from tests.

Thermal property	UHPC property relation	Temperature range
Thermal conductivity (W/m °C)	k_t= -0.0092T+3.1136,	20°C ≤ *T* ≤ 100°C
	k_t= -0.0035T+2.5802,	100°C ≤ *T* ≤ 400°C
	k_t= 0.0021T+0.3481,	400°C ≤ *T* ≤ 500°C
	k_t= -10^{-5} T^2 +0.0111T-1.6565,	500°C ≤ *T* ≤ 700°C.
Specific heat (MJ/m^3 °C)	ρc= $2x10^{-6}$ T^2 +0.0013T+1.6918,	20°C ≤ *T* ≤ 300°C
	ρc= -0.0046T+3.6677,	300°C ≤ *T* ≤ 400°C
	ρc= 0.0054T-0.3217,	400°C ≤ *T* ≤ 600°C
	ρc= 0.0006T+2.5588,	600°C ≤ *T* ≤ 700°C.
Thermal expansion (%)	ε_{th} = $2x10^{-6}T^2$ +0.0002T +0.0014,	20°C ≤ *T* ≤ 600°C
	ε_{th} = $-1.443x10^{-5}T^2$ +0.0188T -5.2031,	600°C ≤ *T* ≤ 800°C
	ε_{th} = 0.0037T-2.342,	800°C ≤ *T* ≤ 900°C.
Mass loss (%)	M/Mo= 1.0005- $3x10^{-5}$T,	20°C ≤ *T* ≤ 200°C
	M/Mo= 1.0451 +$2x10^{-7}T^2$-0.0003T,	200°C ≤ *T* ≤ 750°C.

The thermal property relations were developed using the least squares method of regression analysis for a set of data points corresponding to the high temperature experimental trends. This was carried out using the analysis package available in Microsoft Excel. Microsoft Excel is selected due to the unified ease of performing regression analysis and plotting fitted data with the trends generated in thermal property tests. The regression analysis is carried out with specific thermal property as a response parameter (dependent variable) and temperature as their predictor parameter (independent variable). The accuracy of the regression analysis or the curve fitting of the relation is represented by the coefficient of determination, R^2. The value of R^2 always lies between 0 and 1, and the closer its value is to 1, the more accurate is the data fit. The relations obtained through regression analysis show R^2 values ranging from 0.97 to 1, which represents a reasonably high confidence level in fitting the equations with the measured thermal property of UHPC.

3.5.1.5. Comparison between thermal properties of UHPC and conventional concrete

The temperature-dependent thermal conductivity variation of UHPC is compared in Figure 3.12 (a) with that of conventional NSC and HSC, taken from published literature [21,119,120]. There exists notable variation in the available reported data on thermal conductivity of NSC and HSC, which can be mainly attributed to varying moisture content, test conditions, and measurement techniques used in previous set of experiments. The thermal conductivity for all concrete types decreases with temperature, and this decrease is dependent on the concrete mix properties, specifically moisture content and permeability. At ambient temperature, the thermal conductivity of NSC and HSC, ranges between 1.3 to 2.5 W/m°C (with HSC being on the higher side of this range). The thermal conductivity of UHPC is relatively higher than the thermal conductivity of conventional NSC and HSC at elevated temperatures. The higher thermal conductivity of UHPC

can be attributed to the inherent less amount of water present in UHPC. Moreover, the dense microstructure of UHPC with less porosity as compared to other types of concrete, further limits dehydration in concrete and thus maintains higher thermal conductivity than that of NSC and HSC. The specific heat of UHPC is compared in Figure 3.12 (b) with that of conventional NSC and HSC made of carbonate aggregate as reported from various studies [21,119,121]. UHPC exhibits similar values of specific heat as that of NSC and HSC in 20-400°C range. Specific heat of UHPC is relatively higher than that of NSC and HSC in 400-600°C range, which can be attributed to the lower permeability and dense microstructure of UHPC that requires more heat for evaporation of water. In the temperature range of 600-800°C, the specific heat of NSC and HSC, made of carbonate aggregates is very high due to the substantial amount of heat utilized (i.e. endothermic reaction) for dissociation of dolomite in carbonate aggregate. However, this high range of specific heat at temperatures above 600°C is not that apparent in UHPC due to the controlled (lower) amount of coarse aggregates present in the UHPC mix, so as to obtain a dense microstructure using fine constituent materials.

The measured mass loss for UHPC is compared with mass loss in NSC and HSC [20,120,122] in Figure 3.12 (c). The mass loss is not significant until 600°C in all concrete types. In the temperature range of 600-800°C, extent of mass loss in UHPC is significantly less compared with that in NSC and HSC. Mass loss in the temperature range of 600-800°C occurs in carbonate aggregate concrete mainly due to the dissociation of dolomite which results in evaporation of hidden moisture present in the carbonate aggregate [17]. The lower mass loss in UHPC than in NSC and HSC can be attributed to the lower (or none) amount of coarse aggregate present in UHPC, as opposed to a larger proportion of coarse (carbonate) aggregate present in conventional concrete mixes (NSC and HSC).

The measured thermal expansion for UHPC, along with compiled data for NSC and HSC from published test results [20,21,120] is plotted in Figure 3.12 (d) as a function of temperature. The thermal expansion of all concretes (including UHPC) varies in a similar manner in 20-500°C range. UHPC exhibits higher thermal expansion in the 500-700°C range as compared to conventional NSC and HSC. The expansion rate for concretes in this temperature range is due to the expansion of cement paste. UHPC has a higher proportion of cement paste (and a lower proportion of coarse aggregates) for a dense impermeable microstructure, which results in higher thermal expansion. The rate of thermal expansion for all concrete types slows down between 700-800°C range. The subsiding trend in thermal expansion of concrete in 700-800°C range is attributed to the loss of water present in hydrates. To achieve the desired concrete strength properties, a higher dosage of mineral admixtures, such as silica fume and slag is present in the mix for UHPC as compared to the other two concrete types (NSC and HSC). These mineral admixtures present in UHPC, react with the hydration products to form additional C-S-H gel (hydrate), the part of cement paste responsible for strength in concrete. Thus, shrinkage is observed in UHPC between 700 and 800°C, as opposed to a slower increase in thermal expansion in NSC and HSC because of loss of water from higher volume of hydrates in UHPC. Beyond 800°C, the increase in thermal expansion is owing to microstructural changes in coarse aggregate present in concrete. UHPC has relatively lower thermal expansion values than other concretes beyond 800°C, which is attributable to the limited proportion of coarse aggregates in UHPC as opposed to a substantial amount of coarse aggregate in NSC and HSC.

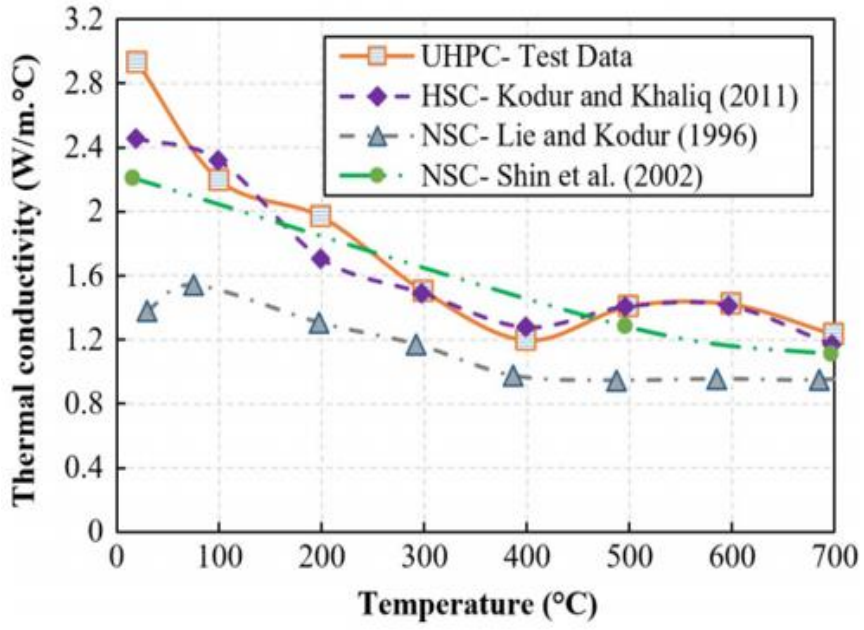

(a) Thermal Conductivity

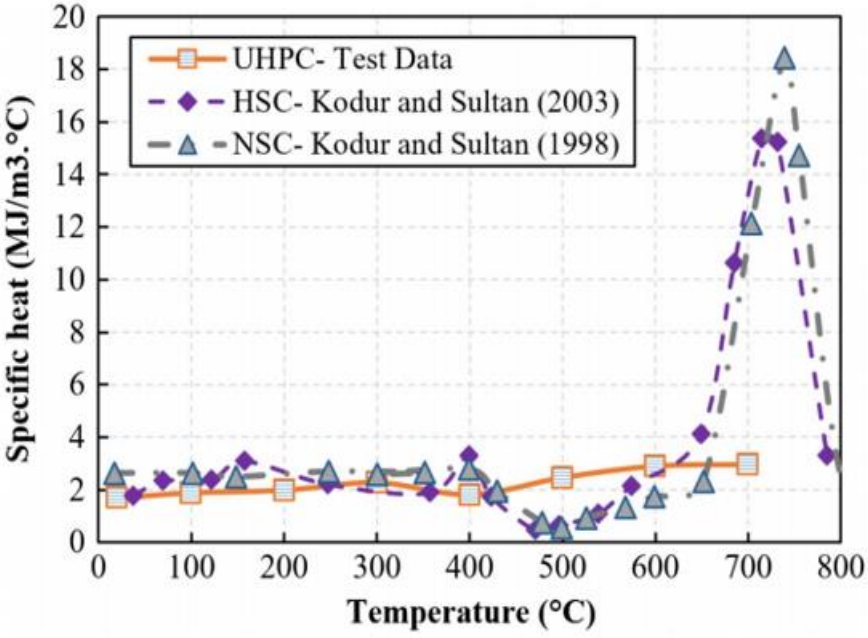

(b) Specific Heat

Figure 3.12. Comparison between thermal properties of UHPC with NSC and HSC.

Figure 3.12. (cont'd)

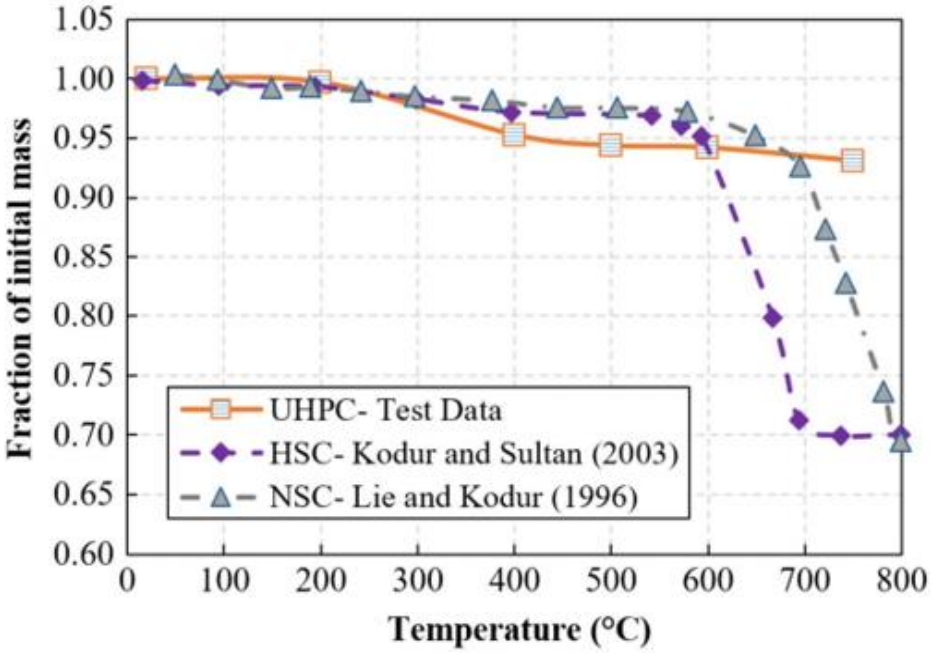

(c) Mass Loss

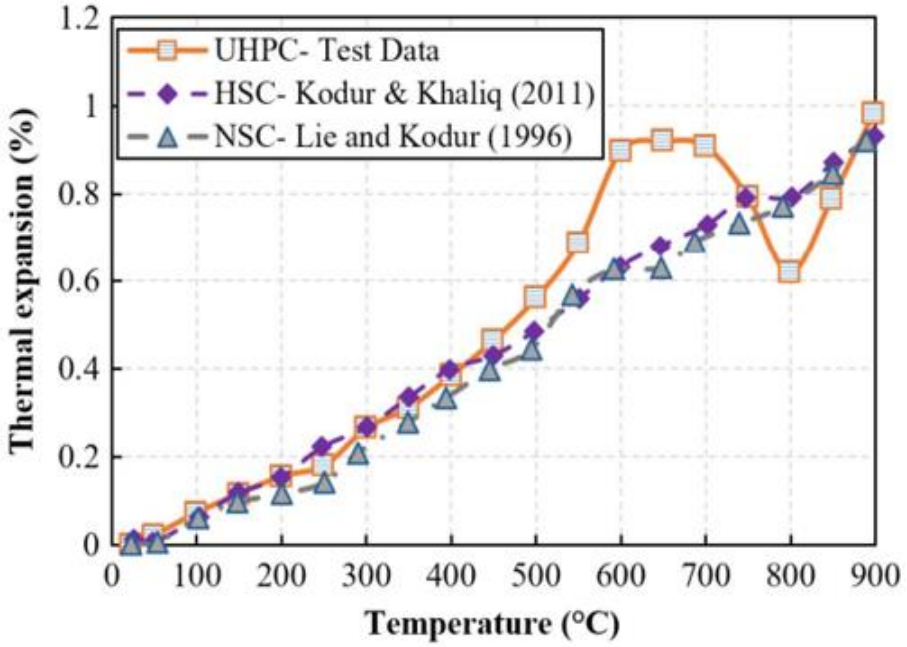

(d) Thermal Expansion

3.5.2. Mechanical Properties

3.5.2.1. Test Specimens

Mechanical property tests were carried out on two types of UHPC, namely UHPC reinforced with steel fibers (UHPC-S2) and UHPC reinforced with hybrid (steel and polypropylene) fibers (UHPC-H). From each batch, 75 x 150 mm cylindrical specimens were utilized for undertaking mechanical property tests on each type of concrete.

3.5.2.2. Test Procedure

Unstressed testing regime was followed, wherein the test specimen is heated to a certain temperature without any loading, and following the attainment of the target temperature, the specimen is loaded in increments until failure. The test equipment for evaluating temperature-dependent mechanical properties of UHPC consisted of a heating device and a loading device. The heating device used to heat the concrete specimens is an electric furnace (shown in Figure 3.13(a)). The electric furnace has internal dimensions of 100 x 200 mm and can simulate a maximum temperature of 750°C. It is internally fitted with electric heating elements, and is capable of implementing various heating rates, and can maintain a target temperature for a specified duration. The loading device utilized to undertake the strength tests is Forney strength test machine; displayed in Figure 3.13(b). This Forney strength test equipment is a 2670 kN load-controlled compressive test machine, with a digital interface for controlling the test parameters such as loading rate, failure point, etc. and is capable of capturing the stress-strain response of test specimens.

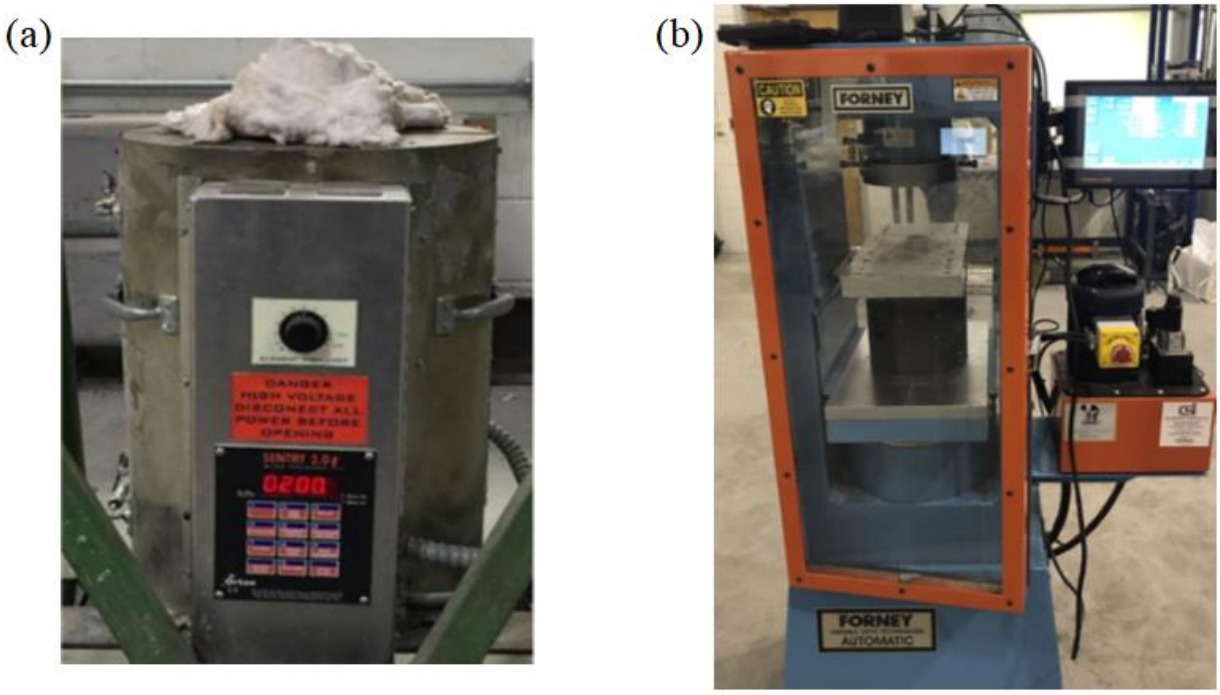

Figure 3.13. Test equipment for evaluating high-temperature mechanical properties: (a) Electric furnace; (b) Forney strength test machine.

For mechanical property measurements at room temperature, specific test procedures are given in test standards [43,44]. However, test standards do not provide any guidance for evaluating the mechanical properties of concrete at elevated temperatures. Only RILEM recommendations provide procedures for evaluating the mechanical properties of concrete at high temperatures in the range of 20–750°C [45]. However, these high-temperature test procedures specified in RILEM are developed based on property tests on conventional concretes, and hence, they may not be practicable and fully applicable for higher strength concretes, such as UHPC. For instance, RILEM recommends a heating rate of 2°C/min for a concrete cylinder of 75 mm in diameter, as utilized in this study. When UHPC-S cylinders (without PP fibers) were subjected to any heating rate greater than 0.5°C/min, the specimens suffered explosive spalling as shown in Figure 3.14, at temperatures around 200°C. It is worth noting that the UHPC-H cylinders did not encounter major spalling during heating at a rate of 2°C/min as in the case of UHPC-S, due to the decrease of pore pressure by melting of PP fibers present in the UHPC-H mix.

Currently, there is no guidance on a critical limit of moisture content for limiting fire-induced spalling in UHPC. For conventional concretes (below the strength of 80 MPa), Eurocode2 [16] states that spalling is unlikely to occur, when the moisture content (by weight) is less than 3%. Such explosive spalling at low heating rates was reported in studies by other researchers. The literature review in Chapter 2 revealed that previous high-temperature studies on UHPC dried the test specimens in the oven, prior to heating them in the furnace. Oven drying the specimens eliminates moisture and reduces the risk of spalling. However, pre-oven-drying is not a standardized test procedure and more importantly, it is not reflective of realistic situations in-built infrastructure. Therefore, to generate test data on UHPC while investigating the influence of heating rates and oven drying on the mechanical properties of UHPC, two heating regimes were adopted in this study: (i) heating the cylinder at a low heating rate of 0.5°C/min; (ii) oven-drying followed by heating the cylinder at a rate of 2°C/min, as shown schematically in Figure 3.15. As part of the drying treatment, the specimens were exposed to 105°C temperature in the oven (Figure 3.16) for 7 days. Following oven drying, the dried specimens were kept in sealed bags to prevent moisture absorption until the day of testing.

Figure 3.14. Spalled UHPC-S2 specimen during heating for mechanical property test.

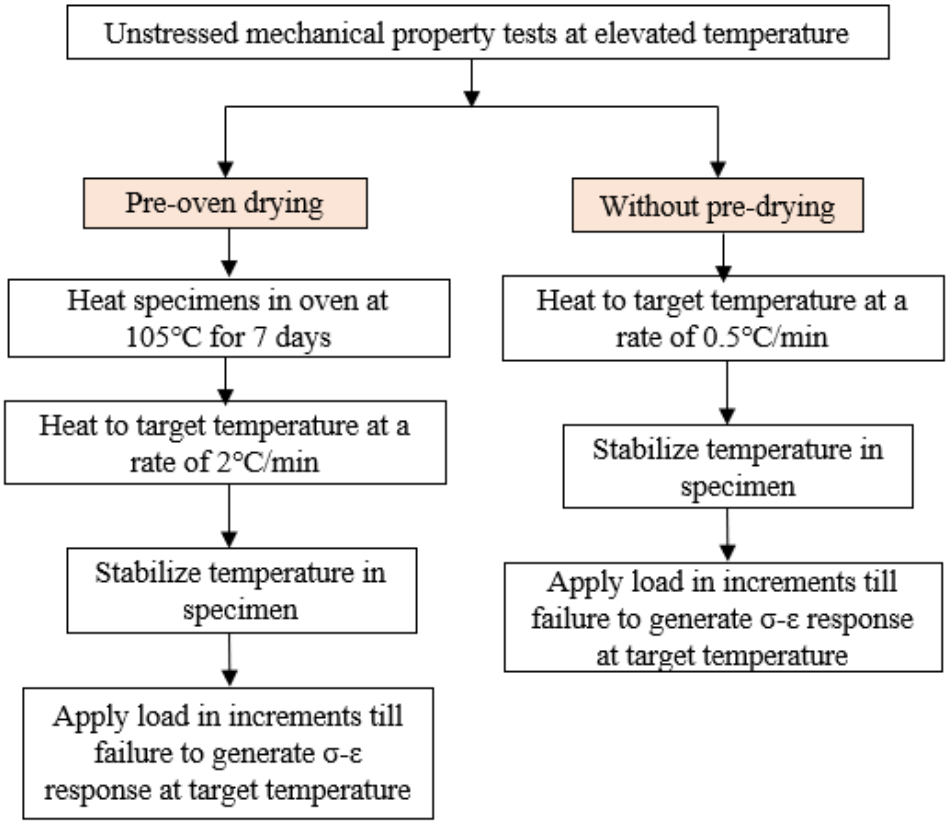

Figure 3.15. Schematic of testing procedure followed for mechanical property evaluation of UHPC at elevated temperature.

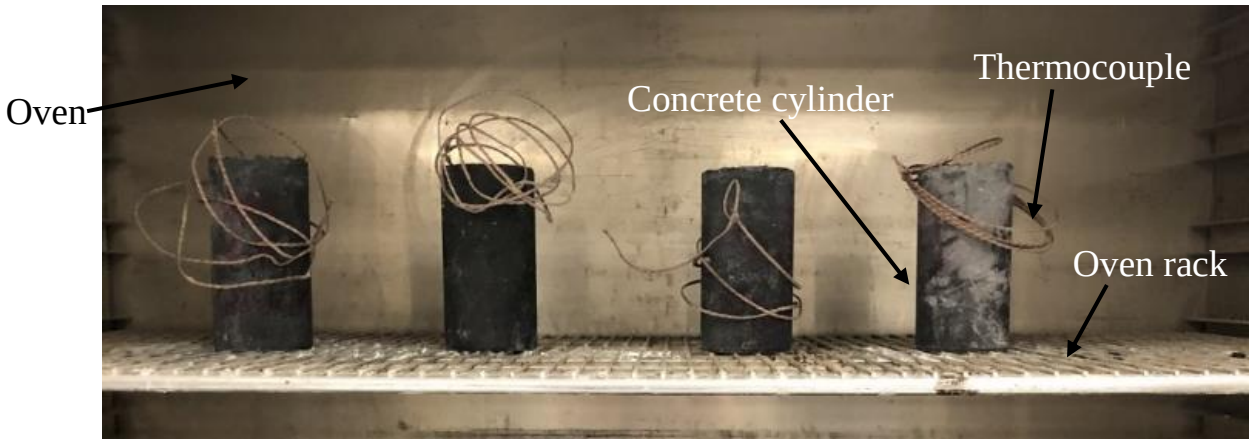

Figure 3.16. Oven drying of UHPC specimens.

To evaluate the high-temperature mechanical properties of UHPC, the test specimens were heated to target test temperatures of 200, 400, 600, and 750°C according to the selected heating regime in the electric furnace (Figure 3.13 (a)). For monitoring temperatures, two Type K thermocouples were installed at the surface and center at mid-height of the cylinder, and another one was placed

inside the electric furnace for measuring the increase in temperature with time. The temperature development inside the furnace, on the surface, and at the center of UHPC-S2 cylinder heated at two different rates for attaining 750°C target temperature is shown in Figure 3.17. It can be observed that lower thermal gradients developed in the specimen upon heating at 0.5°C/min, which could lead to uniform drying and lower build-up of pore pressure. When heated at 2°C/min, larger thermal gradients developed resulting in larger pressure gradients and higher accumulation of pore pressure, along with higher thermal stresses due to differential thermal gradients. The combined stresses imposed by pore pressure and thermal stresses could accelerate spalling phenomenon in UHPC specimens.

When the temperature in the furnace reached the aimed temperature, the cylinder continued to remain in the furnace at this temperature for 2 hours to attain thermal equilibrium (steady state) conditions. After steady state conditions are reached throughout the cylinder specimen, the hot cylinder was taken out and moved to the strength testing machine. For minimizing heat loss while transferring the heated specimen to the loading device, a thermal insulating cover was utilized for compressive strength test, and a steel bracket frame was used for splitting tensile strength test[25]. Previous studies have reported a maximum heat loss of approximately 10°C in the specimen from the time of the end of heating to the end of the strength test [123].

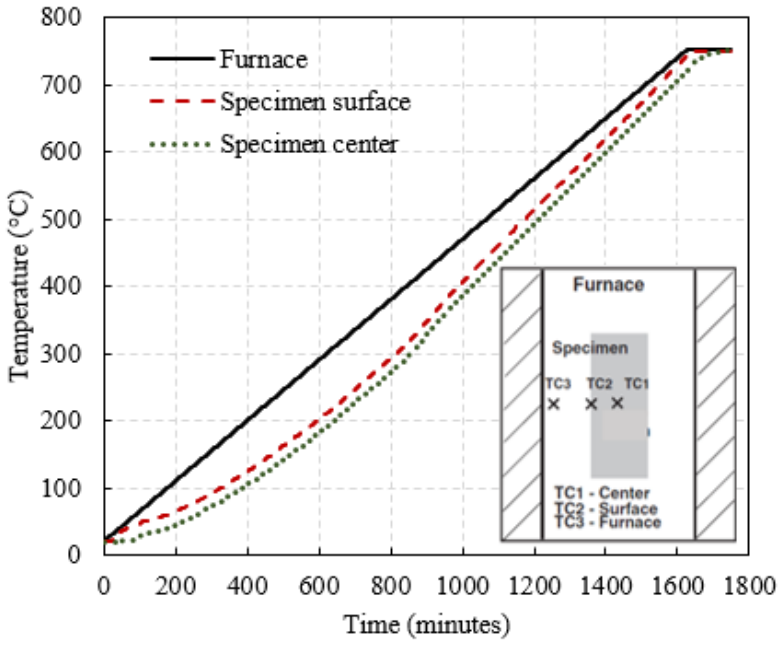

(a)

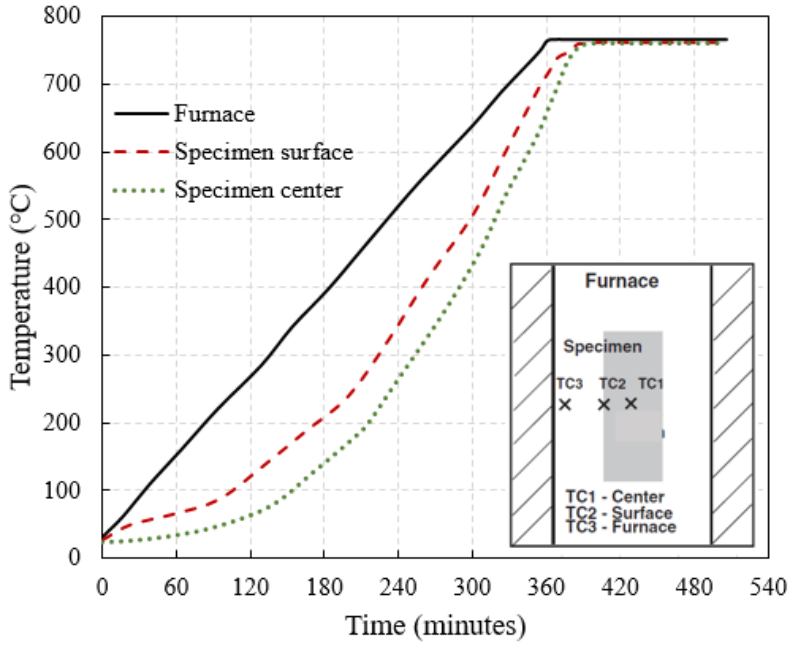

(b)

Figure 3.17. Temperature progression in UHPC-S2 specimen for target temperature of 750°C at a heating rate of: (a) 0.5°C/min; (b) 2°C/min.

For the compression test, the specimen was loaded axially (Figure 3.18 (a)) at a uniform rate of 0.25 MPa/sec till failure, as per ASTM C39 [43]. The load-displacement values measured at each load increment were utilized to generate the stress-strain curves, from which the peak failure load

was obtained. The load and displacement were recorded through the built-in load cell and linear variable displacement transducers (LVDTs) connected to the embedded data acquisition system in Forney strength test equipment. Prior to the test, exact dimensions of the test specimen were measured using a Vernier caliper and inputted in the strength test machine through its digital interface. The load and displacement were recorded at a frequency of 32 readings per second. At each time step, stress is computed internally by dividing the load by cross-sectional area of the test specimen.

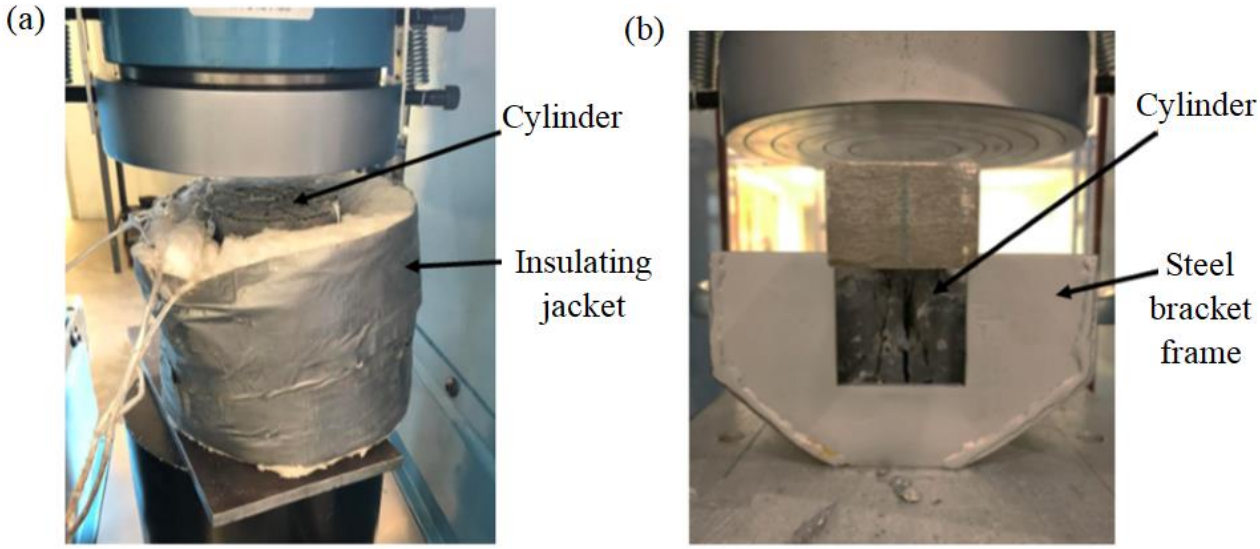

Figure 3.18. Testing of the heated specimen: (a) Compression; (b) Tension.

For measuring displacement, two LVDTs pre-attached to the top and bottom plates of the compression loading device were utilized as it is extremely difficult to connect LVDTs to hot cylinders. The strain is calculated by taking the average of the measured change in displacements at each time increment. The accuracy of displacement measurement is ±3%. Modulus of elasticity was computed utilizing the compression stress-strain curves, following ASTM C469 test standard [46]. The high-temperature splitting tensile strength test was conducted by applying a diametrical load at a rate of 0.013 MPa/sec as specified in ASTM C496 test standard [44], till the splitting failure occurred in concrete cylinder (Figure 3.18 (b)). The time taken for moving out the hot

specimen from the furnace to application of the ultimate load took around 10 minutes, depending upon the temperature-degraded strength.

3.5.2.3.Results

Compressive Strength

The peak loading point at which the heated cylinder attained failure in compression was taken as the ultimate failure load. This peak load is divided by the cross-sectional area of the cylinder to obtain the compressive strength of concrete at that particular temperature. At room temperature, UHPC-H has a slightly (4%) lower compressive strength of 171 MPa, as compared to that of UHPC-S2 (177 MPa), which can be attributed to the slight reduction in its density due to the addition of PP fibers in UHPC-H. The inclusion of polypropylene fibers leads to a reduction in density because of the lower bond strength of PP fibers, which forms a relatively weaker bond with the cement matrix and initiates micro-cracking [124]. The compressive strength (f'_{cT}) and the relative compressive strength (i.e. ratio of compressive strength at target temperature 'T' to that at room temperature, f'_{cT}/f'_{c}) are plotted in Figure 3.19 (a) and Figure 3.19 (b) respectively as a function of temperature for both types of UHPC. Both types of UHPCs experienced a steady loss in compressive strength with temperature rise throughout 20-750°C and this is due to microstructural changes that take place in concrete when exposed to elevated temperatures.

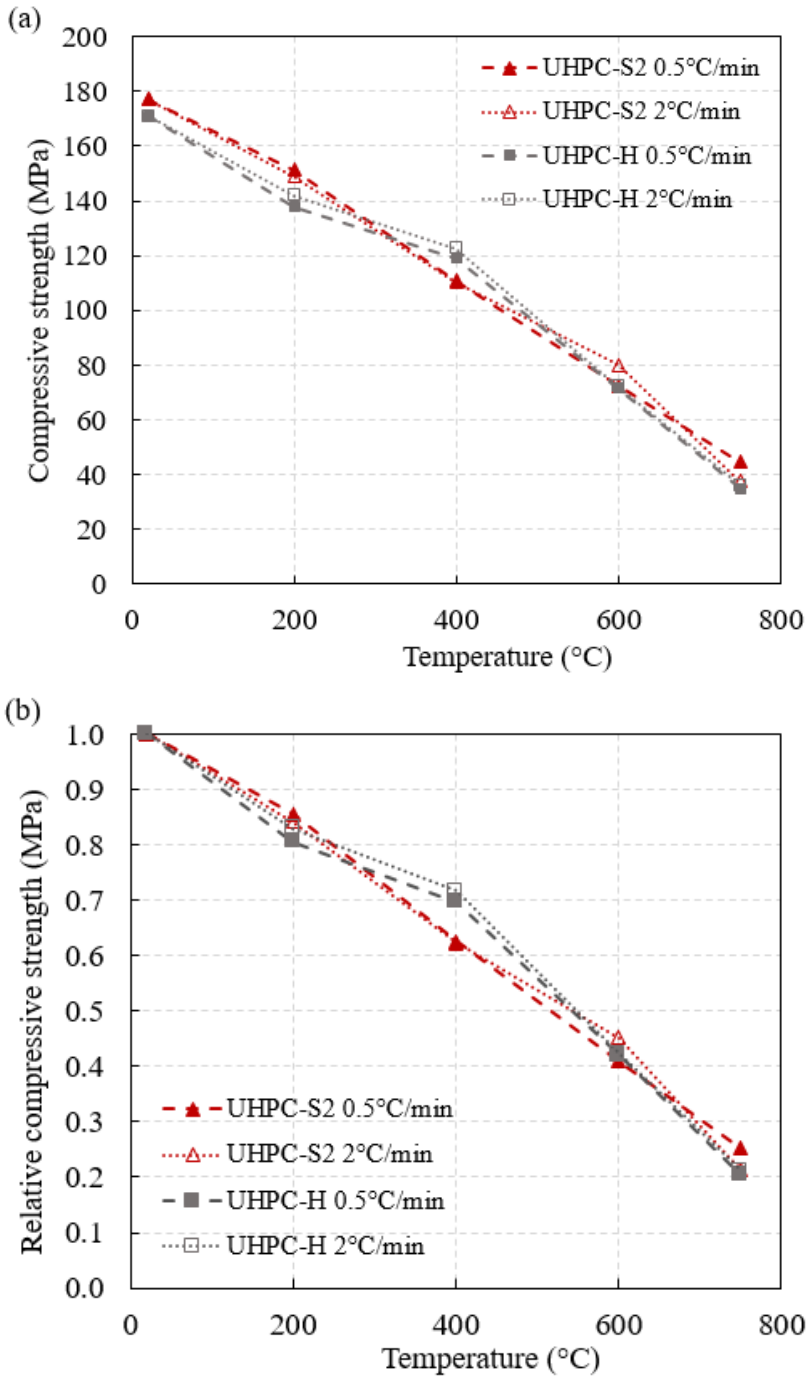

Figure 3.19. Variation in compressive strength as a function of temperature: (a) Absolute; (b) Relative.

During heating from room temperature to 200°C, the reduction in compressive strength is owing to the evaporation of most of the free water present in capillary pores and to some extent, adsorbed water between layers of cement paste in concrete. The compressive strength of UHPC-S2 remained

to be slightly higher than UHPC-H until 200°C. Upon further increase in temperature, UHPC-H retains higher strength as compared to UHPC-S2 in 200-400°C. This improved strength retention in UHPC-H can be attributed to the dissipation of pore pressure facilitated by the melting of PP fibers at about 170°C, resulting in lower degradation of the microstructure.

Beyond 400°C, compressive strength values of both the UHPCs continued to degrade and follow a similar trend up to 750°C. At temperatures higher than 400°C, chemically bound water gets released from concrete through the disintegration of calcium hydroxide ($Ca(OH)_2$) and calcium silicate hydrate (C–S–H) gel resulting in further reduction in strength. Moreover, when the temperature is above 600°C, decarbonation of calcium carbonate present in limestone (calcareous) aggregates, also reduces compressive strength. At about 750°C, excessive micro-cracking and deterioration in concrete microstructure led to significant strength loss, and only about 23% of the original compressive strength is retained in both UHPCs. There is no variation in the reduction in compressive strength under two heating rates.

Elastic Modulus

The elastic modulus was evaluated as the secant modulus at 40% of the peak stress from the respective compressive stress-strain curve at each target temperature. The elastic modulus at room temperature for both UHPC-S2 and UHPC-H is 43 GPa. Figure 3.20 (a) presents the variation in elastic modulus for specimens from either of the UHPC mixes at both heating rates. The variation in relative elastic modulus, defined as the proportion of the elastic modulus at a target temperature to that at ambient temperature (E_{cT}/E_c) is shown in Figure 3.20 (b). The plotted trends reveal that the effect of exposure to high temperatures on the loss of modulus of elasticity is nearly identical for the two types of UHPC measured at different heating rates, with less than 10% deviation.

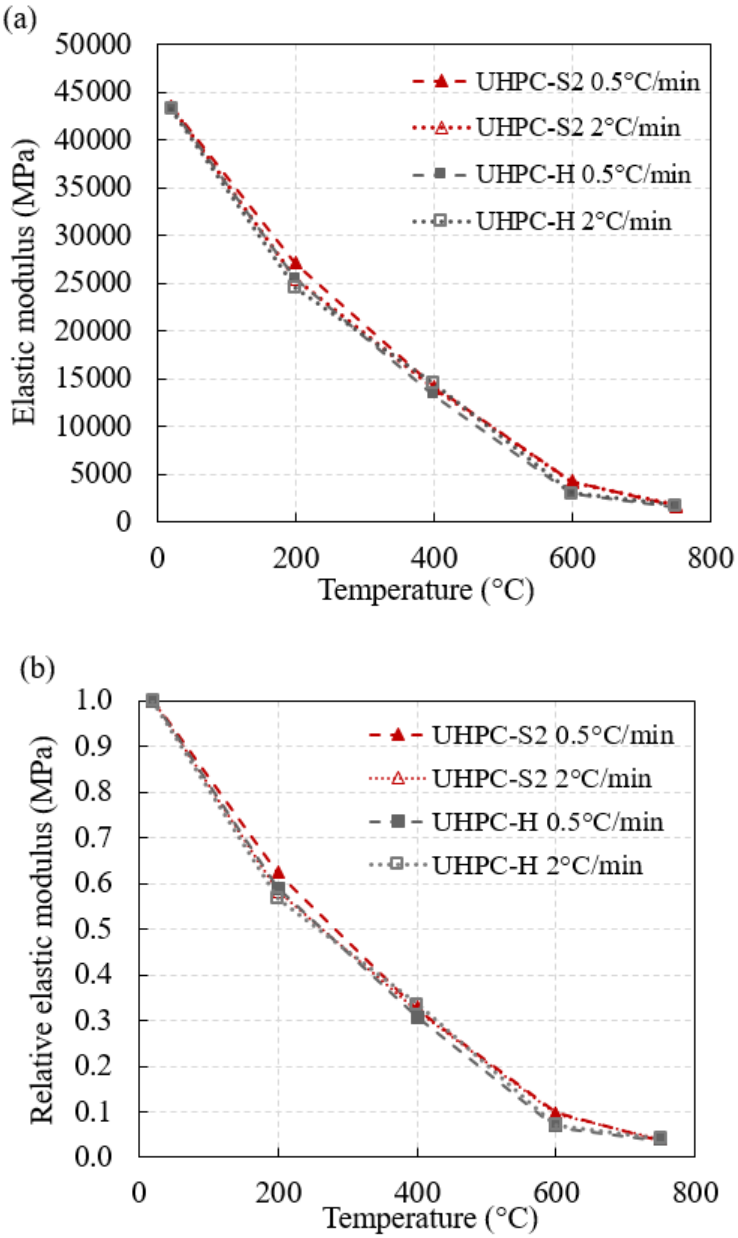

Figure 3.20. Variation in elastic modulus as a function of temperature: (a) Absolute; (b) Relative.

The deterioration in elastic modulus with temperature is mainly associated with the moisture content and the microstructure of hydrated cement products within concrete. The average values of elastic modulus at 200, 400, 600, and 750°C are 58%, 32%, 8%, and 4% to that of room temperature respectively. The degradation of modulus up to 400°C is due to micro-cracking and microstructural alterations in concrete resulting from moisture loss and shrinkage of cement paste.

In the 400 to 750°C temperature range, the deterioration of aggregate-paste bond because of thermal mismatch and onset of disintegration of $Ca(OH)_2$ and C-S-H causes degradation of elastic modulus [17,39]. Comparison of loss in elastic modulus shows that there is no significant difference in the behavior of UHPC-S and UHPC-H at elevated temperatures.

Tensile Strength

Tensile strength of conventional normal strength concrete is considerably lower than compressive strength and thus, is often neglected in strength calculations at room temperature. Conversely, the tensile strength of UHPC is much higher (in comparison to NSC) and can be efficiently utilized in achieving higher capacity in concrete in different ways. Further, under fire conditions, tensile strength is an important property because tensile strength resists crack propagation in concrete. Moreover, in higher strength concretes, tensile strength is a critical property as it helps to overcome fire-induced spalling to some extent [42,125]. Tensile strength is mostly measured as the splitting tensile strength due to its ease of execution and comparatively lower scattering in test results [126]. At each temperature, the failure load at which the heated cylinder diametrically splits in tension is used to evaluate splitting tensile strength. The trends of absolute and relative strength degradation for UHPC-S2 and UHPC-H at each heating rate (0.5°C/min and 2°C/min) are shown as a function of temperature in Figure 3.21. The inclusion of steel fibers in UHPC helps in slowing down the strength loss with increasing temperature [120].

At room temperature, the tensile strength of UHPC-H is 15 MPa, which is marginally lower than that of UHPC-S2, 16.5 MPa. This significantly high tensile strength in both UHPCs is attributed to the presence of steel fibers in UHPC. It should be pointed out that NSC possesses tensile strength in the range of 2-3 MPa. The results show that with respect to the adopted heating rates, there are no considerable differences in the individual trends of loss in tensile strength for both UHPCs in

the entire 20 to 750°C temperature range. The reduction in tensile strength of UHPC is associated with the coalescence of internal cracks formed by moisture evaporation and aggregate-paste debonding [127].

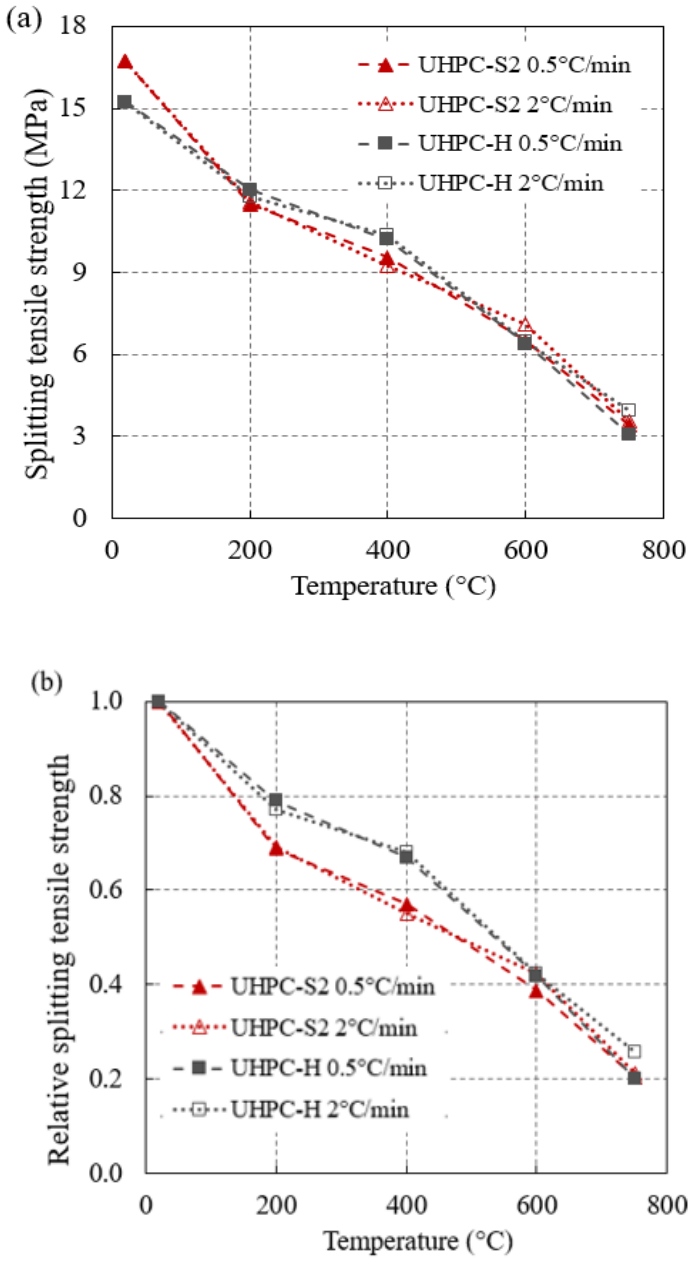

Figure 3.21. Variation in splitting tensile strength as a function of temperature: (a) Absolute; (b) Relative.

The test data indicates the average splitting tensile strength retention in UHPCs at 200, 400, 600, and 750°C to be 70%, 55%, 40%, and 20% respectively, of that at room temperature. In 20 to

600°C temperature range, the relative tensile strength retention of UHPC-H is better than that of UHPC-S2 as the melting of polypropylene fibers in UHPC-H helps to reduce the crack growth by lowering the internal pressure developed in the concrete matrix. Beyond 600°C, the trend of strength degradation in UHPC-S2 and UHPC-H is similar and both the UHPCs suffered a major loss in tensile strength. The higher decrease in tensile strength in 600-750°C was accompanied by severe cracking resulting from physical and chemical deterioration of their microstructure, and thermal incompatibility between fibers, aggregates, and cement paste [123].

Stress-strain Response

The compressive stress-strain response of UHPC-S2 and UHPC-H in the temperature range of 20-750°C was recorded at each target temperature and plotted in Figure 3.22. The stress-strain curves at each temperature comprises an elastic region followed by a parabolic section leading to peak stress and finally a descending section until the concrete specimen attains failure. The stress-strain curve can be characterized through three major parameters: (i) peak compressive stress (or strength); (ii) corresponding strain at peak stress; and (iii) modulus of elasticity. In order to compare the effect of varying heating rates, the stress-strain response recorded by following both the heating rates, 0.5°C/min and 2°C/min, are plotted concurrently in Figure 3.22 for each UHPC type. It can be seen from Figure 3.22 that the stress-strain curves obtained by complying with the two different heating rates follow closely, with less than 10% variation in the three main parameters, at all the target test temperatures for both the UHPCs.

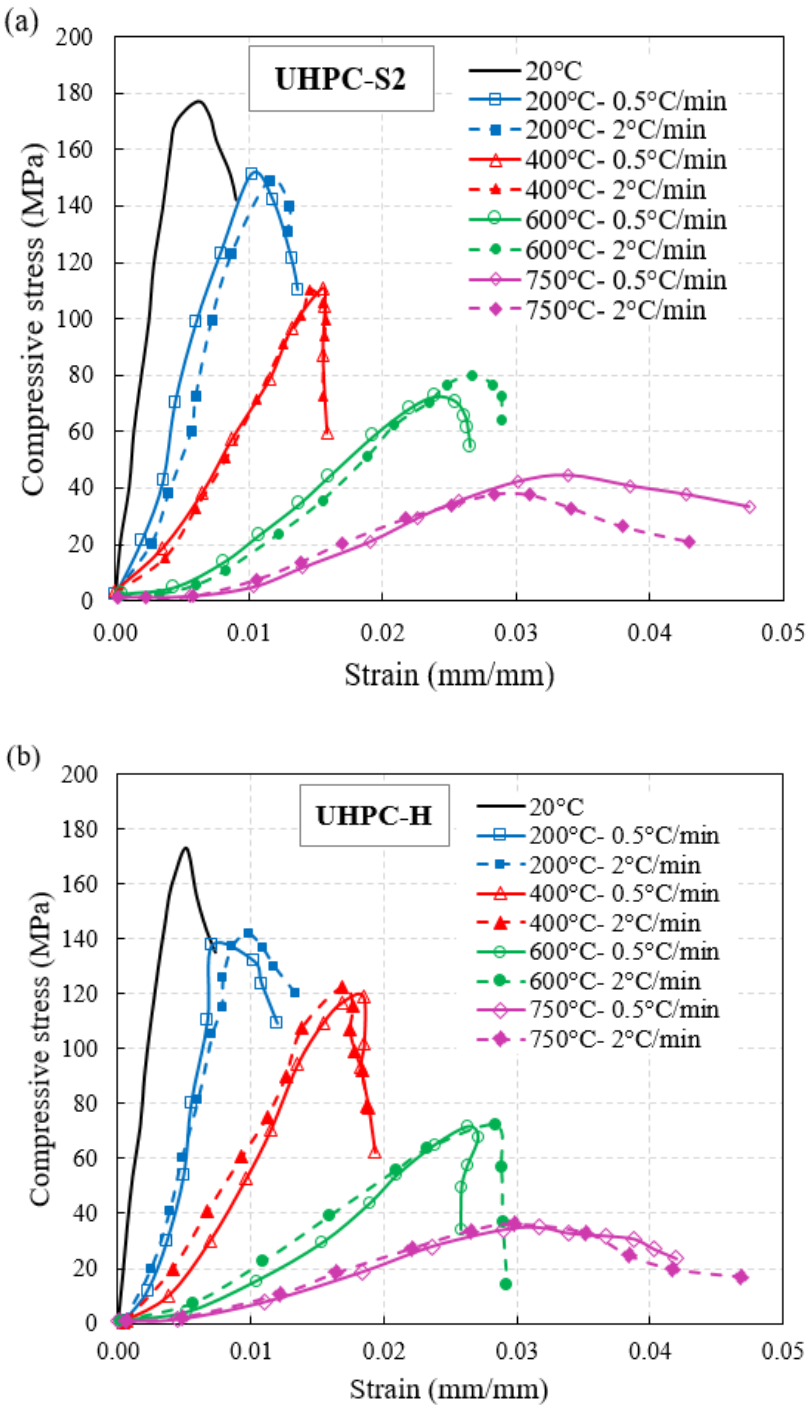

Figure 3.22. High temperature stress-strain response of: (a) UHPC-S2; (b) UHPC-H.

The main purpose of Figure 3.23 is to compare the influence of polypropylene fibers on temperature-dependent stress-strain response of UHPC at two different heating rates of 0.5°C/min and 2°C/min. At 20°C and 200°C, UHPC-H retains slightly lower stress (strength) than UHPC-S2,

and this can be attributed to the slight reduction in density and formation of weaker zones due to addition of PP fibers in UHPC-H [130]. At 400℃, higher strength is retained in UHPC-H as compared to UHPC-S2, since melting of PP fibers increases permeability and reduces deterioration in concrete microstructure. Additionally, above 400°C, the stress-strain response becomes increasingly flatter with the increasing temperatures in both the UHPCs. The enhanced ductility is a consequence of the presence of steel fibers, as well as softening that occurs at elevated temperatures. At 600℃ and 750℃, when heated at 2℃/min, the response of UHPC with and without PP fiber is almost identical, whereas when heated at 0.5℃/min, UHPC-H retains slightly lower stress and higher ductility due to increased micro cracking by complete melting of PP fibers. The average strains corresponding to peak stress in UHPC-S2 at 200, 400, 600, and 750°C are 1.7, 2.4, 4.1, and 5 times the strains at room temperature. Likewise, for UHPC-H, at 200, 400, 600, and 750°C, the peak strains are 2.4, 5, 7.6, and 8.6 times the strains at room temperature. The peak strains show that the addition of PP fibers slightly increased the ductility in UHPC-H through micro-cracking and additional strain during micro diffusion of pore water [18].

Based on the obtained test results, it can be concluded that there is no significant influence of the rate of heating on mechanical property degradation in UHPC for the two heating rates adopted in this study. This implies that an alternative testing procedure utilizing a lower heating rate of 0.5°C/min can be adopted for the measurement of mechanical properties, omitting the step of pre-drying in the oven. Further, it can be inferred that the addition of 0.11% polypropylene fibers did not deteriorate the high-temperature mechanical properties of UHPC and assisted in preventing fire-induced spalling in UHPC-H specimens as compared to UHPC-S2 specimens.

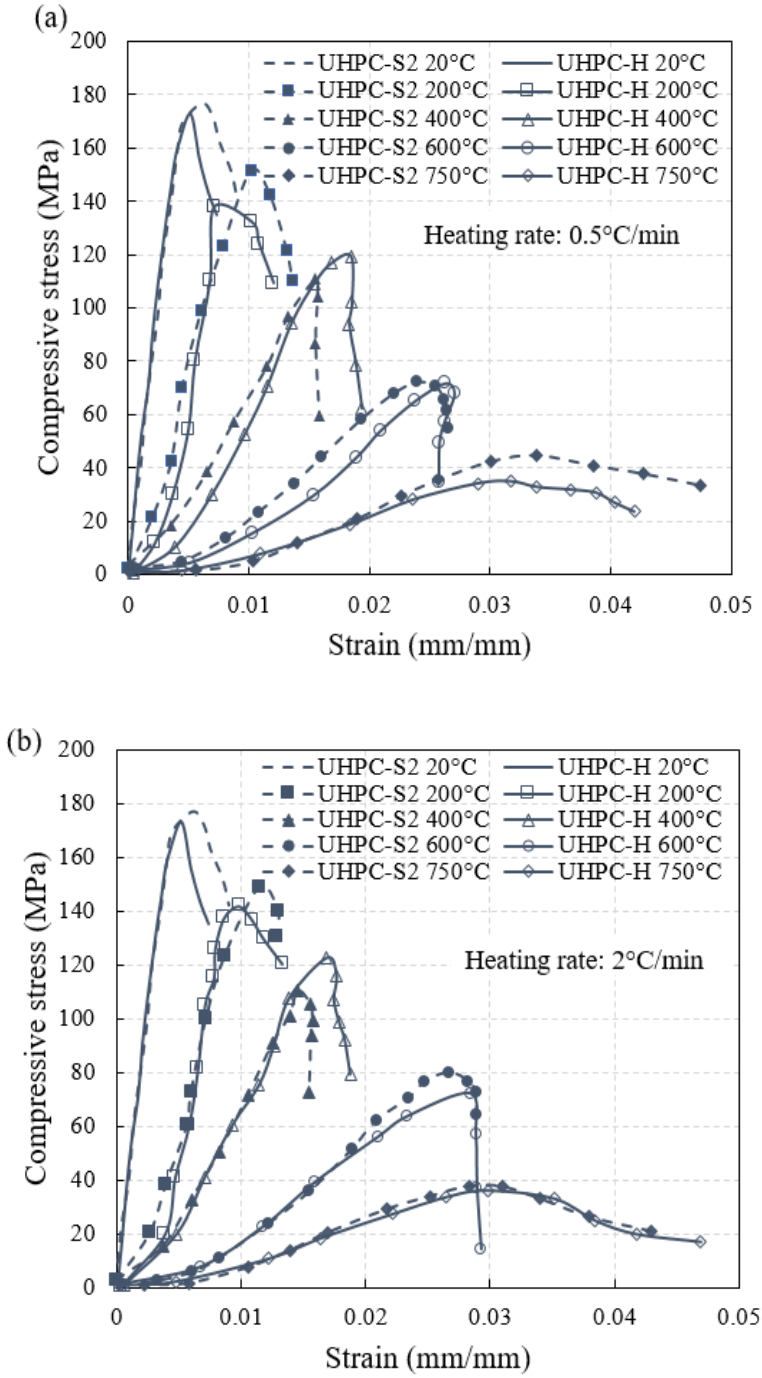

Figure 3.23. Comparison of stress-strain response of UHPC-S2 and UHPC-H following heating rates: (a) 0.5°C/min; (b) 2°C/min.

3.5.2.4.Property Relations

Data obtained from the aforementioned mechanical property measurements are applied to develop high-temperature property relations which can be used for fire resistance analysis on structural

members made of UHPC. Each property is expressed as an empirical relation over the temperature range of 20-750°C for tensile strength, compressive strength, elastic modulus, and stress-strain response. Since the test data revealed that PP fibers do not exhibit significant influence on mechanical properties of UHPC, a single set of developed relations is applicable for both types of UHPC (UHPC-S2 and UHPC-H). These empirical relations are derived through least squares regression analysis in MATLAB on mechanical properties data obtained from test results in this study. For regression analysis, the line of best fit was calculated considering temperature as an independent variable and the measured material properties as dependent variables. The coefficient of determination, R^2 is the ratio of the sum of the square of error about their independent variable and denotes the accuracy of an empirical mathematical relation developed through regression analysis. The evaluated values of R^2 for the developed high-temperature mechanical property equations for UHPC lie between 0.97 and 1, indicating that the proposed equations effectively capture the measured data. The variation of compressive strength (f'_{cT}), tensile strength (f'_{tT}), and elastic modulus (E_{cT}) with temperature in terms of a coefficient α_T representing the ratio of measured value at targeted temperature to that at room temperature (f'_c, f'_t, and E_c). The values of α_T derived for respective mechanical properties at elevated temperatures are given in the form of equations in Table 3-7 for UHPC.

Table 3-7. Mechanical property relations of UHPC generated utilizing data from tests.

Property	Relation	Temperature range
Compressive strength	$\alpha_{T,compression} = - 1.02*10^{-3}*T + 1.02$	$20°C \leq T \leq 750°C$
Splitting tensile strength	$\alpha_{T,tensile} = -1.8*10^{-3}*T+1.04$	$20°C \leq T \leq 200°C$
	$= -7*10^{-4}*T+0.82$	$200°C < T \leq 600°C$
	$= -1.4*10^{-3}*T+1.26$	$600°C < T \leq 750°C$
Elastic modulus	$\alpha_{T,modulus} = 1.42*10^{-6}*T^2 - 2.4*10^{-3}*T+1.05$	$20°C \leq T \leq 750°C$
Peak strain	$\alpha_{T,peak-strain} = 2.7*10^{-8}*T^3-2*10^{-5}*T^2+8.1*10^{-3}*T+ 0.85$	$20°C \leq T \leq 750°C$

For capturing the compressive stress-strain (σ-ε) curve at each target temperature, an analytical expression is proposed for generating the two portions of the curve: an ascending pre-peak portion and a descending post-peak portion. The basic form of the proposed σ-ε equation for UHPC is based on the room temperature stress-strain relation developed by Carreira and Chu [131] and Wu et al. [132] for uniaxial compression of fiber-reinforced concrete. The derived expressions for the ascending and descending parts of the σ-ε curve are given by Eqns. 3-1 and 3-2 respectively. Modification factors k_1 and k_2 are established to describe the path of ascending and descending branches of the σ-ε relation, respectively in Eqns. 3-4 and 3-5. The descending branch is utilized to deduce the stress-strain curve for fire-resistance analysis of UHPC structures as currently there is almost no information. However, it should be noted that the nature of the test was load-controlled, and hence, the captured softening response is not perfectly precise.

$$\text{Ascending part: } \frac{\sigma}{f'_{cT}} = \frac{k_1 \beta \left(\frac{\varepsilon}{\varepsilon'_{cT}}\right)}{k_1 \beta - 1 + \left(\frac{\varepsilon}{\varepsilon'_{cT}}\right)^{k_1 \beta}} \tag{3-1}$$

$$\text{Descending part: } \frac{\sigma}{f'_{cT}} = \frac{k_2 \beta \left(\frac{\varepsilon}{\varepsilon'_{cT}}\right)}{k_2 \beta - 1 + \left(\frac{\varepsilon}{\varepsilon'_{cT}}\right)^{k_2 \beta}} \tag{3-2}$$

$$\beta = \frac{1}{1 - \frac{f'_{cT}}{\varepsilon'_{cT} E_T}} \tag{3-3}$$

$$k_1 = 4.11 * 10^{-8} * T^3 - 4.19 * 10^{-5} * T^2 + 0.017 * T + 0.038 \tag{3-4}$$

$$k_2 = 3.24 * 10^{-8} * T^3 - 3.67 * 10^{-5} * T^2 + 0.013 * T + 0.48 \tag{3-5}$$

where β = material parameter tracing the shape of the stress-strain curve; E_{cT}= elastic modulus; f'_{cT}= peak stress (compressive strength); and ε'_{cT}= peak strain (strain at peak stress) at any

temperature ‘T’. The fitted relation for elastic modulus, peak stress, and peak strain as a function of temperature is given in Table 3-7.

3.5.2.5. Comparison between mechanical properties of UHPC and conventional concrete

The temperature-dependent property relations specified in literature such as Eurocode [16], SFPE manual [23,133], and Kodur and Naser [3] are for traditional concrete types (such as NSC) and hence, these relations might not be applicable for representing temperature-induced property variation in advanced concrete types (such as UHPC). This is mainly due to the fundamental difference in the concrete microstructure, resulting from excessive use of fillers and additives in modern concretes as compared to conventional concretes, as well as differences in fabrication and curing procedures followed during the production of modern concretes. Moreover, the newer concretes are more susceptible to fire-induced spalling, which further complicates the fire resistance evaluation procedure. The variation in material models can result in discrepancies in fire resistance calculations leading to inadequate fire design of structural members. To examine these variations, a comparison between fitted test data and property relations specified in the literature (ACI 216.1 [134], Eurocode [16], ASCE manual [22], Kodur et al. [13]) is compiled herein. The property variation expressions in Eurocode [16] are pertinent to NSC and HSC, whereas the relations in ACI 216.1 [134] and ASCE manual [22] are for NSC. The property relations by Kodur et al. [13] are for HSC, which were formulated by extending the ASCE relations for NSC. Utilizing the relations proposed in this study for UHPC and material models of NSC and HSC, the variations in relative compressive strength, elastic modulus, tensile strength, and peak strain with temperature are plotted in Figure 3.24 (a-d). There is some variation in the plotted material models for the same concrete type, mainly due to adoption of different test conditions and

procedures (such as loading and heating rate) because of a deficit of standardized test methods for conducting concrete property tests.

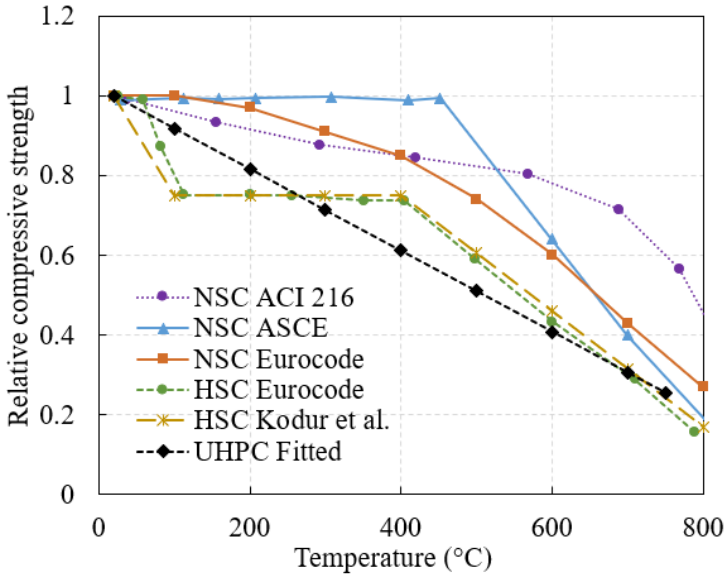

(a) Relative compressive strength

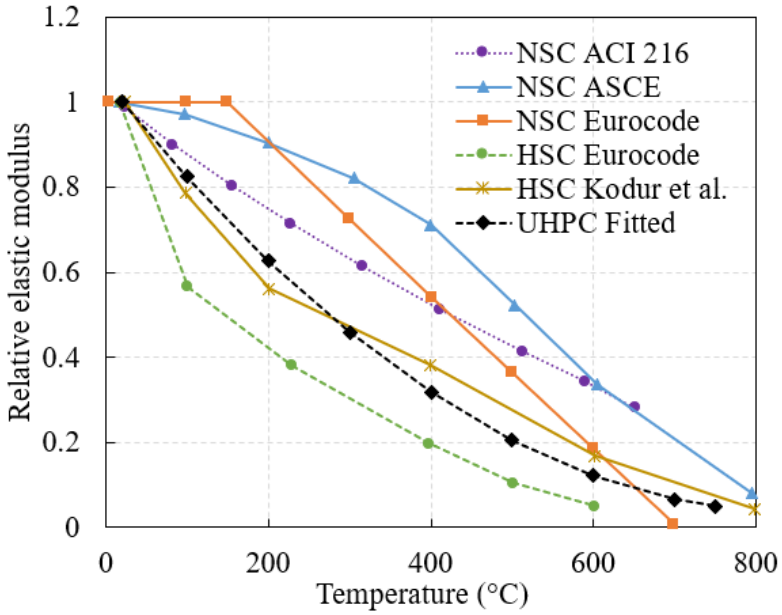

(b) Relative elastic modulus

Figure 3.24. Comparison between mechanical properties from design codes and fitted test data.

Figure 3.24. (cont'd)

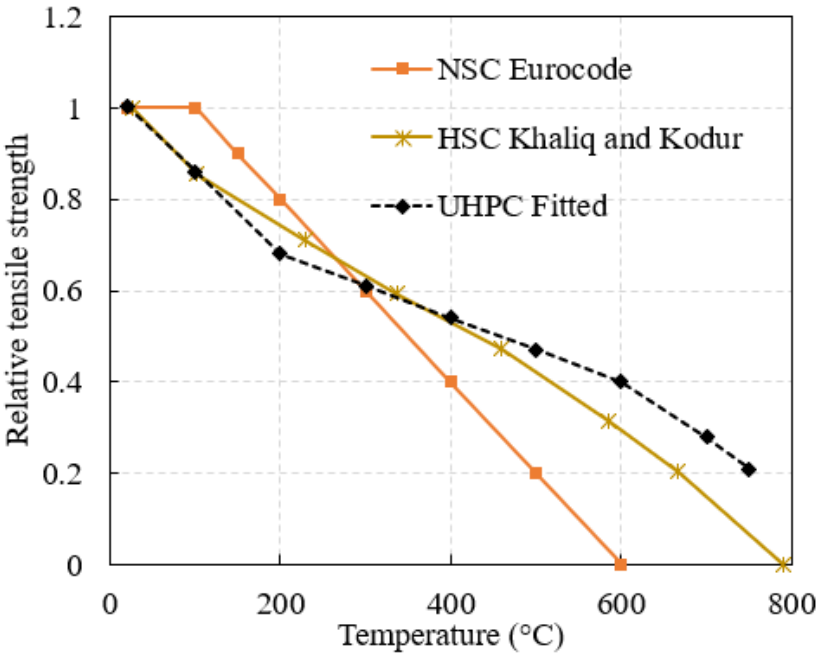

(c) Relative tensile strength

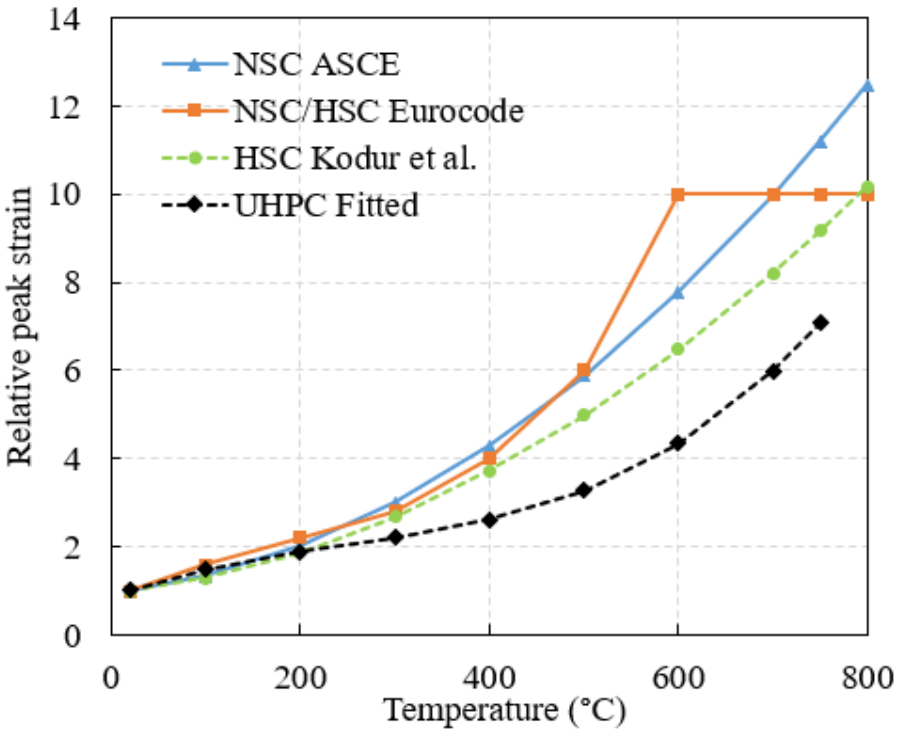

(d) Relative peak strain

A closer look at the figures reveals that HSC and UHPC have faster degradation of strength and modulus with increasing temperature as compared to NSC. With temperature rise in concrete, the cement paste undergoes shrinkage due to moisture removal, and the aggregates tend to expand. This paste shrinkage and aggregate expansion result in loss of strength and micro-cracking due to thermal mismatch of paste-aggregate and reduction in paste-aggregate bond. This degradation is more pronounced in higher strength concretes (HSC, UHPC) due to their higher cement/aggregate ratio resulting in faster loss of properties. Moreover, when the accumulation of temperature-induced pore pressure occurs in concrete, the pressure augments the internal stress and initiates further micro-cracking. In addition, as opposed to NSC, a major proportion of the water in higher strength concretes is present in the form of adsorbed moisture in cement paste layers and lesser content of free water is present in the capillary pores. Therefore, under exposure to elevated temperatures, a higher amount of adsorbed water is evaporated from HSC and UHPC as compared to the evaporation of a higher amount of available free water from NSC. The removal of adsorbed water from cement particles significantly damages the concrete microstructure and result in higher strength loss [123,135].

A comparison of trends in Figure 3.24 (a-b), between HSC and UHPC shows that UHPC exhibits somewhat better retention of compressive strength and modulus up to 300°C. This is mainly owing to the reduced volume of coarse aggregates in UHPC causing a lower paste-aggregate thermal mismatch. The loss of strength and modulus beyond 300°C is almost similar in UHPC and HSC. As compared to compressive strength and elastic modulus, fewer data points are present for tensile strength variation in Figure 3.24 (c). This is because of limited relations for loss of tensile strength of concrete at elevated temperatures in design codes. Till 300°C, UHPC and HSC exhibit a faster reduction in tensile strength with temperature due to cracks developing from high thermal stresses

and thermal incompatibilities within the concrete matrix. Beyond 300°C, the retention in tensile strength is higher in UHPC as compared to NSC and HSC and this can be accredited to the delaying of crack propagation along with effective bridging of cracks under tensile load facilitated by steel fibers in UHPC as shown in Figure 3.25. Due to the crack-bridging effect of fibers, the tensile behavior of UHPC becomes ductile, in contrast to brittle cracking in NSC and HSC. The comparison in Figure 3.24 (d) shows that relative peak strain increases with an increase in temperature for NSC, HSC, and UHPC in a comparable manner till 300°C. After temperatures exceed 300°C, the increase in peak strain of NSC and HSC is at a much rapid pace than UHPC, increasing to about twice the peak strain of UHPC at 750°C. The lower peak strain of UHPC in 300-750°C is possibly due to loss in toughness from damaged microstructure, along with weakened steel fibers above 600°C.

Figure 3.25. Bridging effects from steel fiber in UHPC specimen subjected to splitting tensile strength test.

Based on the comparison of UHPC relations from property tests and codal relations, it is evident that there is a distinct variation in the temperature dependency of the mechanical properties of

UHPC. The relative retention in properties of UHPC is much lower than that in NSC and it will be un-conservative to use NSC relations from design codes for evaluating fire resistance of UHPC structures. The variation of relative strength and modulus properties with temperature for UHPC is similar to the upper bounds of the data for HSC.

3.6. Fire Resistance Tests on UHPC Beams

The experimental program at member level consisted of conducting fire resistance tests on four UHPC beams. All the beams were subjected to a combination of structural and thermal loading to evaluate their behavior under fire conditions. The test variables included the presence of polypropylene fibers, load level, and fire exposure scenario. The test procedure followed, response parameters measured, and test results are discussed below.

3.6.1. Test Set-Up and Procedure

The fire resistance tests on UHPC beams were conducted using fire test furnace at Michigan State University (MSU) Civil Infrastructure Laboratory. This furnace is designed to generate typical conditions, such as temperature, structural loading, and heat transfer, to which a structural member might be exposed during an actual fire incident. The furnace details are illustrated in Figure 3.26(a). The fire test furnace comprises of a steel framework supported by four steel columns and a fire chamber of 3.05 m in length, 2.44 m in width, and 1.78 m in height. A loading frame comprising of steel beams and columns to apply real-time support and load conditions encloses the test furnace. The furnace is equipped with six gas burners placed on four walls of the furnace, which are capable of producing maximum heat power of 2.5 MW. Six type-K chromel–alumel thermocouples, are also placed on four walls of the furnace to monitor furnace temperature during fire tests. The input gas and ventilation are controlled manually to maintain the average furnace temperature consistent with a specified fire curve (standard or design fire exposure). All

thermocouple, LVDT, and load cell channels are connected to a data acquisition system, which displays and records temperatures, strains, and displacements in real-time. There are two viewports on two opposite walls of the furnace for taking visual observations during a fire test as shown in Figure 3.26(b).

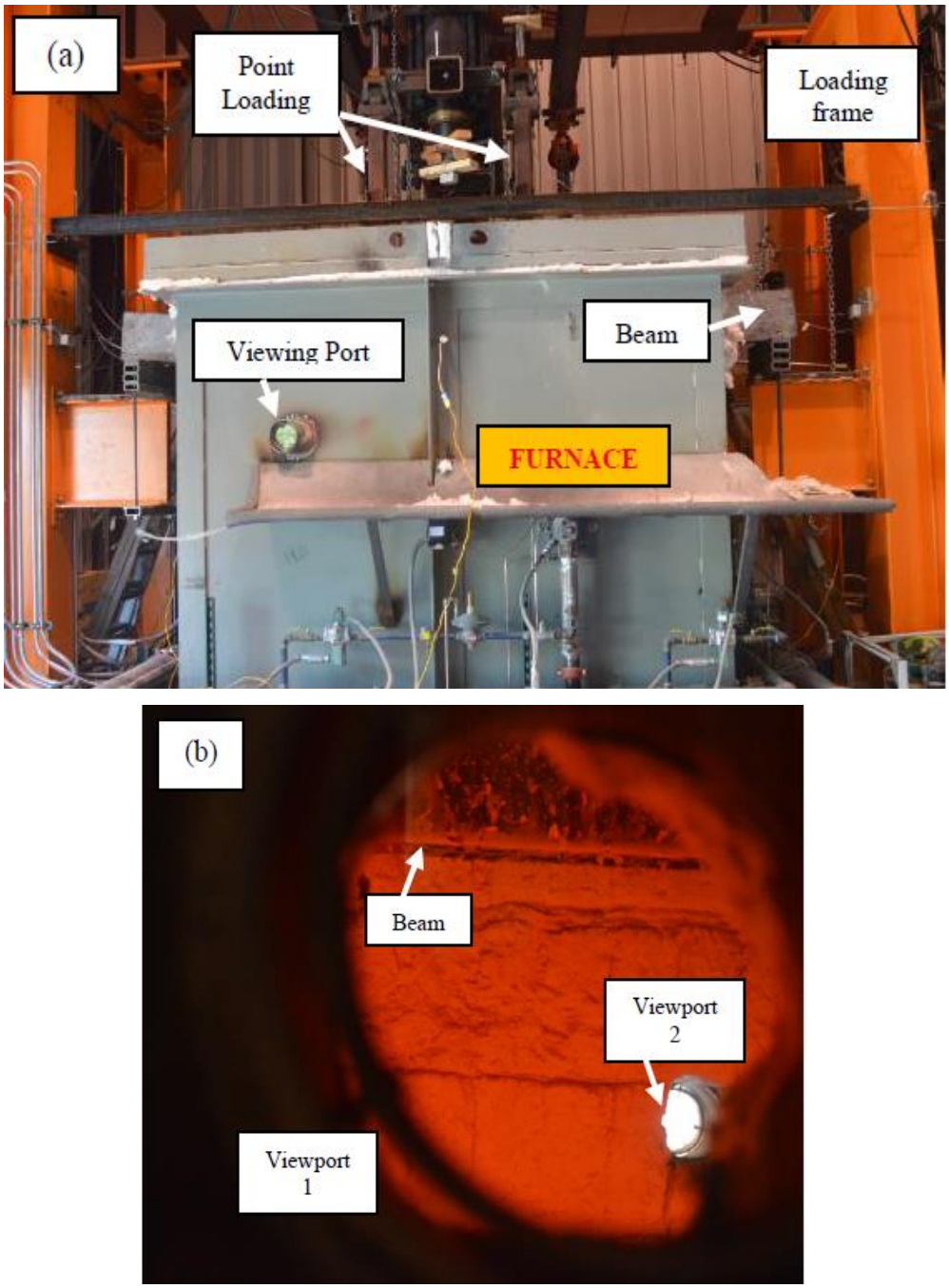

Figure 3.26. Structural fire test setup at MSU: (a) Furnace (b) Observation viewport.

The fire resistance tests were carried out by placing each UHPC beam in the furnace under simply-supported conditions and exposing them to a desired fire exposure. Only three sides (bottom and two sides) were exposed to fire, while the top surface of the beam was insulated with a 50-mm layer of insulation (ceramic fiberfrax material) to prevent heat penetration from the top. This is similar to the conditions encountered in practice where a concrete slab is present on the top side of the beam. Three out of the four tested UHPC beams (U-B1, U-B2, U-B10, and U-B11) were tested under design fire 1 (DF1) to simulate a typical office fire without a decay phase, till failure. To investigate the effect of fire scenario on the fire response of UHPC beam, beam U-B11 was exposed to design fire 2 (DF2) comprising of heating phase of 90 min followed by a cooling phase of approximately 10°C/min to represent natural cooling in typical fires encountered in real life as shown in Figure 3.27. The rate of heating in both the design fire scenarios is slightly less severe than that recommended by ASTM E119 to represent typical ventilation-controlled conditions encountered in buildings.

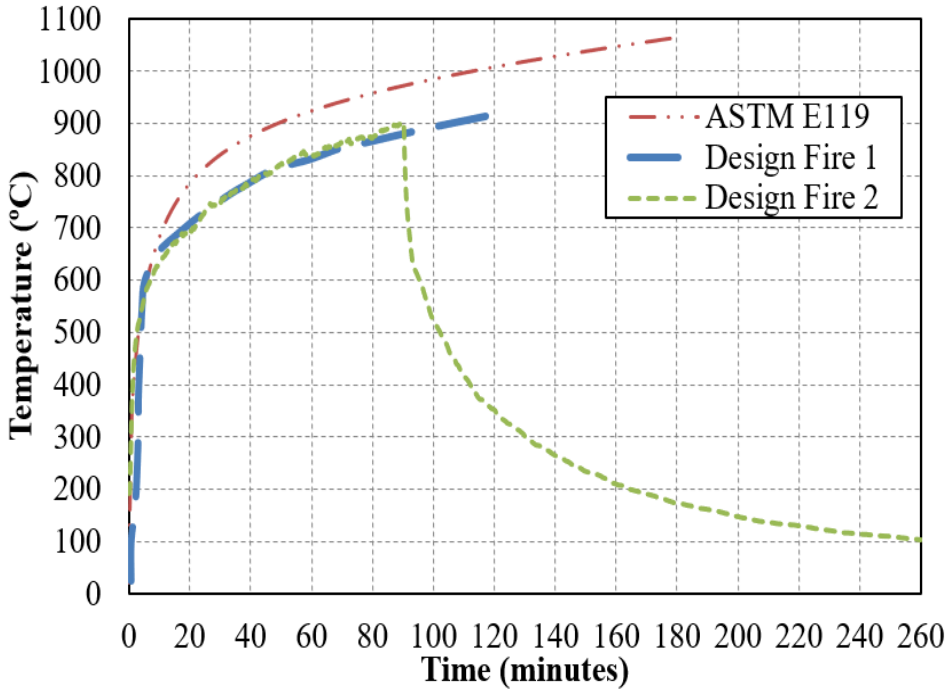

Figure 3.27. Time-temperature curves for fire scenarios used in the fire tests.

All beams were tested under two-point loads, each of which was placed at 1.4 m from the end supports as shown in Figure 3.28. This setup ensured that the critical span (mid-span) was subjected to pure flexure and no shear. The test parameters are summarized in Table 3-8. The beams tested under fire conditions were subjected to different load levels within the range of 40 to 60% of the ultimate flexural capacity of the control beam, evaluated at room temperature, 97 kN [108]. For the fire resistance tests, the loading was applied 30 min prior to the start of the fire and this loading was stabilized till no further increase in beam deformation could be measured. The applied load was then maintained constant throughout the duration of fire exposure.

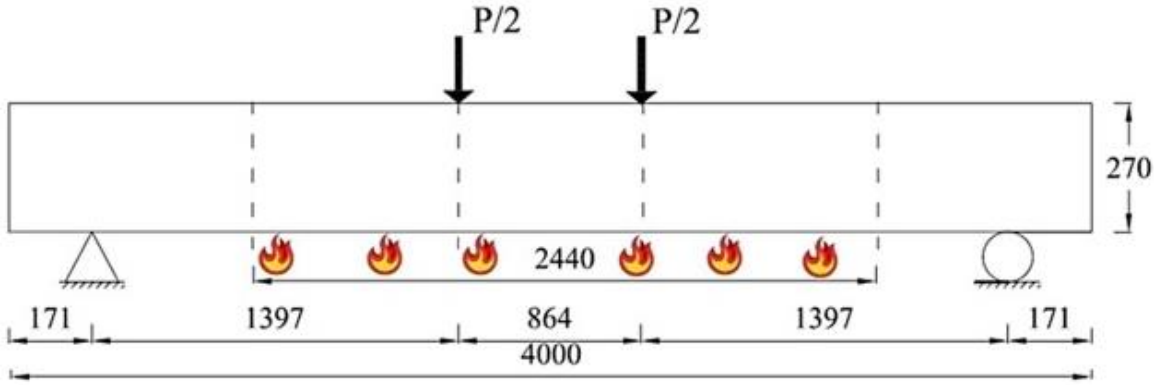

Figure 3.28. Loading set up during tests on UHPC beams (All units are in mm).

Table 3-8. Variables in tested UHPC beams.

Beam designation	Fiber	Fire exposure	Applied load kN, (% of capacity)	Relative humidity (%)	Concrete strength (MPa)		Age of specimen (months)
					28-day	Test day	
U-B1	Steel	Design Fire 1	38 (40%)	68.52	160	173	35
U-B2	Steel	Design Fire 1	60(60%)	61.51	160	173	37
U-B10	PP*+Steel	Design Fire 1	43(45%)	32.18	145	176	8
U-B11	PP*+Steel	Design Fire 2	50(50%)	32.65	145	176	10

PP*: Polypropylene fibers

Observations were made every 5 min through the view ports in the furnace to record any major changes in the specimen including occurrence of fire-induced spalling. Following the completion of fire resistance test and after complete cool down of each beam to ambient temperature (around 25°C), detailed observations on cracking and extent of spalling were made. In addition, to gauge

the extent of spalling, volumetric and weight measurements were taken on each beam after the completion of fire resistance test.

3.6.2. Results and Discussion

Data and observations generated during the above tests are utilized to trace the comparative response of UHPC beams. Relative fire performance of these beams is evaluated by comparing thermal response, structural response, spalling progression, and failure times.

Thermal Response

The measured rebar and concrete temperatures at mid-span in beams U-B1, U-B2, U-10, and U-B11 are plotted in Figure 3.29 as a function of fire exposure time. In the beams subjected to design fire DF1 (U-B1, U-B2, and U-B10), the temperatures in rebar and concrete increase with fire exposure time, whereas, in the beam subjected to design fire DF2 (U-B11), the measured temperatures increase to a peak value and then starts to decrease as per the targeted heating-cooling cycle applied on this beam. Since the initial portion of the DF2, prior to the decay phase, followed the same time temperature curve as DF1, all four beams had the same fire exposure up to 90 minutes and thus the rebar and concrete temperature rise can be compared directly. The temperature measured at the quarter depth (h/4) from the top surface in beam U-B2 is aberrant due to malfunctioning of the thermocouple.

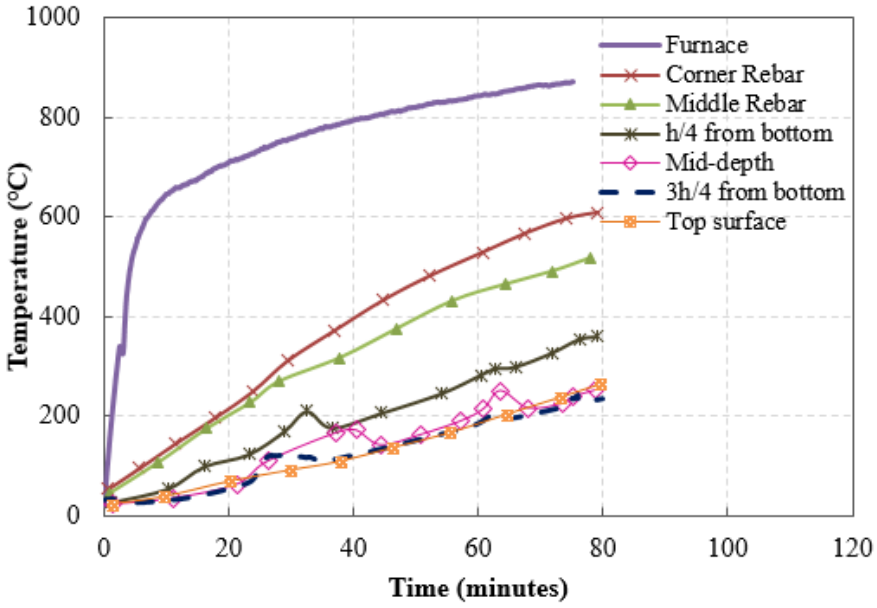

a)

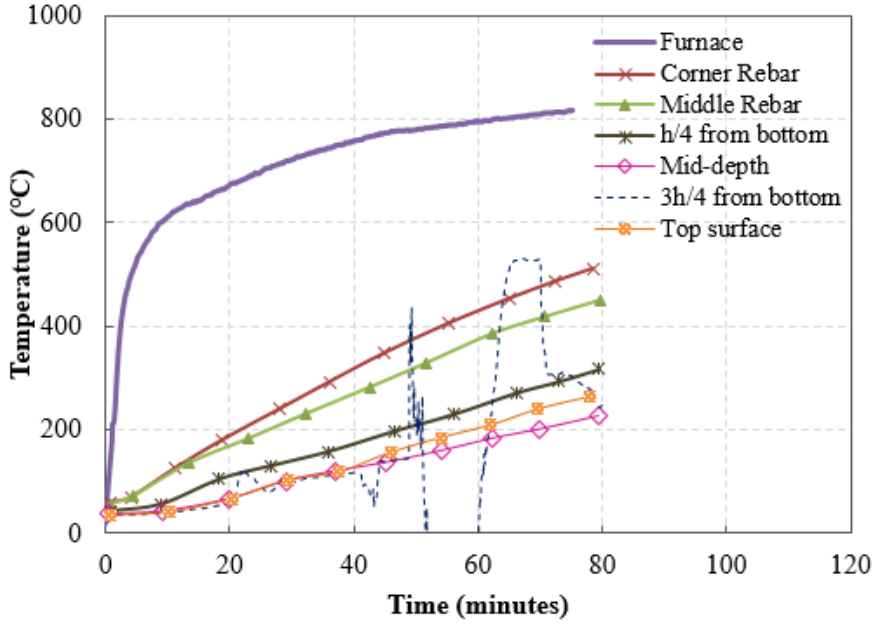

b)

Figure 3.29. Temperature progression at various depths in UHPC beams: a) U-B1, b) U-B2, c) U-B10, d) U-B11.

Figure 3.29. (cont'd)

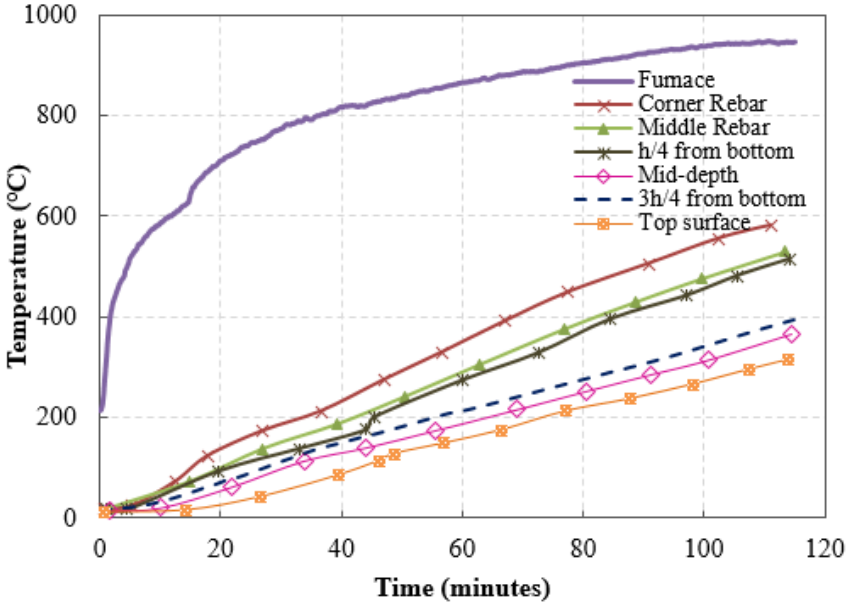

c)

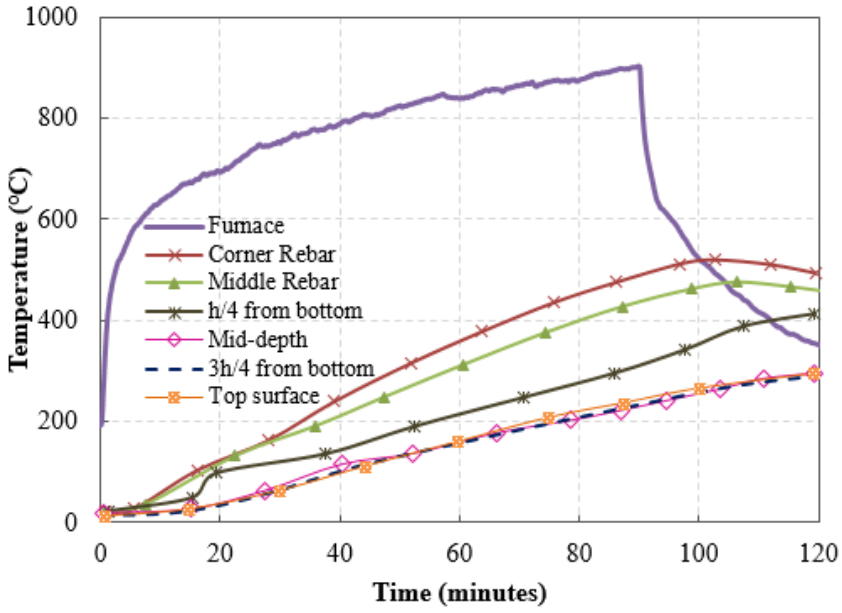

d)

In all four beams, the corner rebars experienced a higher temperature rise than middle rebar. This can be attributed to the peripheral location of corner rebar, which is subjected to heating from the side of the beam, as well as the bottom surface. The concrete temperatures in layers farther from the fire exposed bottom surface are lower than the layers closer to the fire-exposed surface. This trend is on expected lines and is attributed to the low thermal conductivity and high specific heat

of concrete, which delays temperature transmission into the inner layers of concrete. It can be seen from the plotted trends in Figure 3.29 that the measured temperature at the mid-depth of concrete is lower than that at the quarter-depth (h/4) from bottom exposed surface of concrete. However, the temperature plots of UHPC beams reveal that the pace of temperature rise beyond mid-depth (at the three-fourth quarter (3h/4) depth from fire exposed side and also on the unexposed side at the top surface) is similar to that of mid-depth, even though the mid-depth is nearer to fire exposed surface than the upper portion of the beam. Such variation in temperature rise with time in upper portion of UHPC beam is not alike temperature raise in NSC and HSC beams, as reported in many previous fire tests [1, 2]. This difference in sectional temperature progression in UHPC beams can be attributed to fire-induced spalling that occurs in the compression zone (top layers) of the beam; which in turn exposes deeper layers (behind the spalled layer on sides) of concrete directly to fire. The spalling that occurred is schematically shown in Figure 3.30and further discussion is laid out in the following sections.

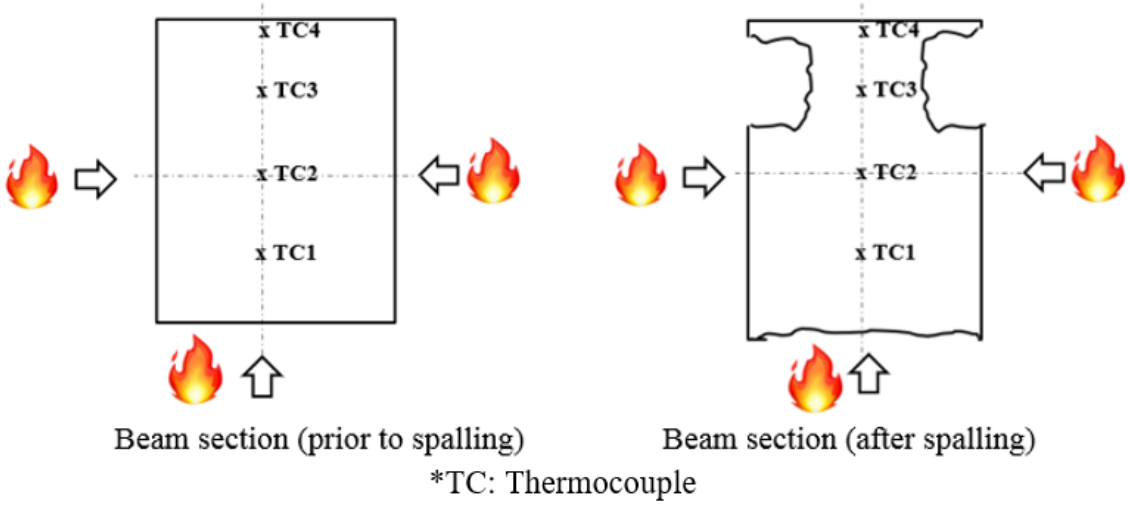

Figure 3.30. Schematic illustration of spalling pattern in tested UHPC beams.

Analysis of measured temperature data from tests show that load level, fire exposure scenario, and presence of PP fibers in concrete have a major influence on the temperature progression in UHPC

beams. The effect of these factors on the thermal response is through their influence with the progression of cracking and spalling of concrete. To further illustrate the variation of temperature trends in different UHPC beams, temperature rise at rebars and two concrete locations (mid-depth and top surface) in the four tested beams are compared in Figure 3.31. The temperature rise in beams with PP fibers (U-B10 and U-B11) occurs at a slower rate than the beams without PP fibers (U-B1 and U-B2). This is on expected lines since the presence of polypropylene fibers in beams U-B10 and U-B11 helped to mitigate spalling thus minimizing loss of cross section during fire exposure, thereby slowing down temperature rise in the interior of the section. In beams with PP fibers, the measured temperature at rebars and top surface follow closely with each other. It can be observed that the temperature at mid-depth in beam U-B11 is somewhat lower than that in beam U-B10. Due to the slightly higher load level (5%) in beam U-B11, more cracks might have opened up in beam U-B11 as compared to beam U-B10. The tensile cracks have possibly contributed in releasing pore pressure, leading to lesser spalling and thus, slightly slower temperature rise in beam U-B11.

The differences in temperature rise in the beams without PP fibers, U-B1 and U-B2, can be attributed to the extent of spalling, mainly resulting from different loading levels. Temperatures rise at a higher pace in beam U-B1 (subjected to lower load level) as compared to other beams due to pore pressure buildup leading to a higher level of spalling in this beam. Some undulations in the form of peaks can be seen in the sectional time-temperature trends of beam U-B1. Specifically, the temperature peaks were recorded by thermocouples in beam U-B1, located at quarter depth, mid-depth, and three-fourth quarter depth from the bottom surface and at time intervals of 25 to 40 minutes and 60 to 65 minutes into fire exposure. The potential cause of the undulations or peaks in the thermal response of beam U-B1 can be from sudden temperature rise resulting from loss of

cross-section due to localized spalling taking place in beam U-B1 at the sides of the beam. These peaks, however, were not observed in measured temperature trends in other tested UHPC beams due to lower levels of spalling experienced by them as compared to beam U-B1.

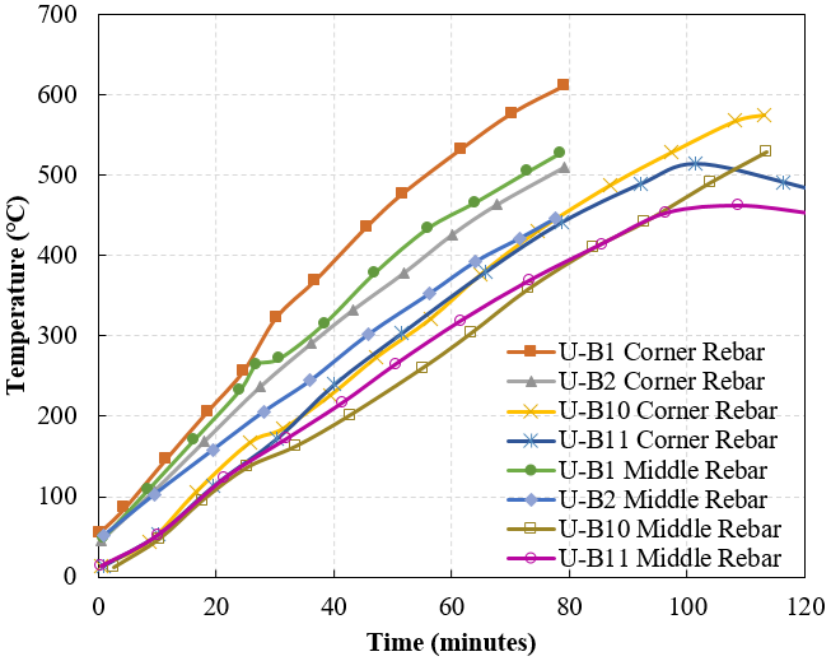

a)

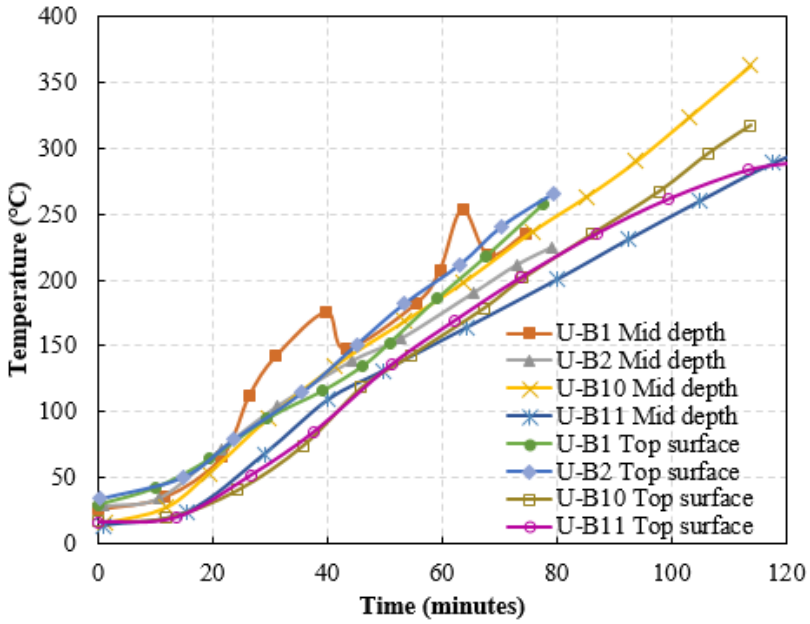

b)

Figure 3.31. Comparison of (a) rebar, (b) concrete temperatures as a function of fire exposure time.

Structural Response

The structural response of the four tested UHPC beams can be gauged through variation of mid span deflection with fire exposure time, as plotted in Figure 3.32. Only deflections measured through displacement transducers are presented here because the data obtained through high-temperature strain gauges were quite inconsistent beyond 200°C and thus, was deemed unreliable. Because of its erratic nature, the strain gauge data cannot be used to draw definitive conclusions. This type of erratic measurements in strain gauges (due to instability of strain gauges beyond 300°C) has been reported in numerous previous fire tests [125,136].

The progression of deflection in each beam can broadly be grouped under three stages. In stage 1; i.e. the first 40 min of fire exposure, deflections in all four beams increase at a slow and steady pace, and this is mainly influenced by level of structural loading present in the beam and extent of thermal strains resulting from the development of thermal gradients along the beam depth. Beam U-B2, which was subjected to a higher load level (60% of its room temperature capacity), undergoes slightly higher deflection as compared to the other three beams with lower level of loading. Spalling started in all four beams at about 10 min into fire exposure but was the highest in beam U-B1. Since temperatures in concrete and steel reinforcement during stage 1 remained low (below 400°C), these materials do not experience much degradation in strength or modulus in this stage, keeping the rise in deflection to low levels.

In stage 2 of fire exposure, deflection increases at a relatively higher pace in all four beams, and this is mainly due to higher mechanical strains developing due to faster degradation of strength and modulus properties in concrete and steel reinforcement, as a result of higher sectional temperatures (in excess of 400°C) in the beams. Stage 2 period in beams U-B1 and U-B2 (made without polypropylene fibers), is between 40 and 60 min of fire exposure, whereas, for beams U-

B10 and U-B11 (made with polypropylene fibers), stage 2 represents a period from 40 to 90 min of fire exposure. The longer duration of stage 2 response in beams with PP fibers can be attributed to gradual degradation of strength and reduced loss of concrete cross-section (due to minimal fire-induced spalling) in these beams. Upon comparison of structural response of beams without PP fibers, it can be seen that the deflection rise in beam U-B1 is at a higher pace than that in U-B2 and this can be attributed to higher level of spalling occurring in beam U-B1.

In stage 3; i.e. beyond 60 min of fire exposure for beams U-B1 and U-B2, and beyond 90 min for beams U-B10 and U-B11; deflections increase at a very rapid pace. This can be mainly attributed to the rapid degradation in strength and modulus properties of concrete and rebars. In addition, the drastic increase in the beam deflections prior to failure is mainly due to yielding of steel and creep strains that become predominant at high temperature levels (beyond 500°C), just before the failure is attained. However, due to the presence of a cooling phase, beam U-B11 did not attain such high temperatures and thus, significant creep deformation did not occur in this beam. Beyond 130 min, mid-span deflection in beam U-B11 begins to recover as temperatures in beam U-B11 begin to cool down during the cooling phase of fire exposure (design fire DF2). However, upon cooling down completely to ambient temperature, only 14% of the final deflection in U-B11 reverted back and a large portion of the deflection remained unrecovered. The large permanent deflection can be attributed to the unrecoverable residual plastic strains in concrete and rebars, and transient creep strains in concrete. In addition, loss of cross-section due to spalling in the compressive zone on the sides of the beam U-B11 during fire exposure contributed to irrecoverable deflections in the beam.

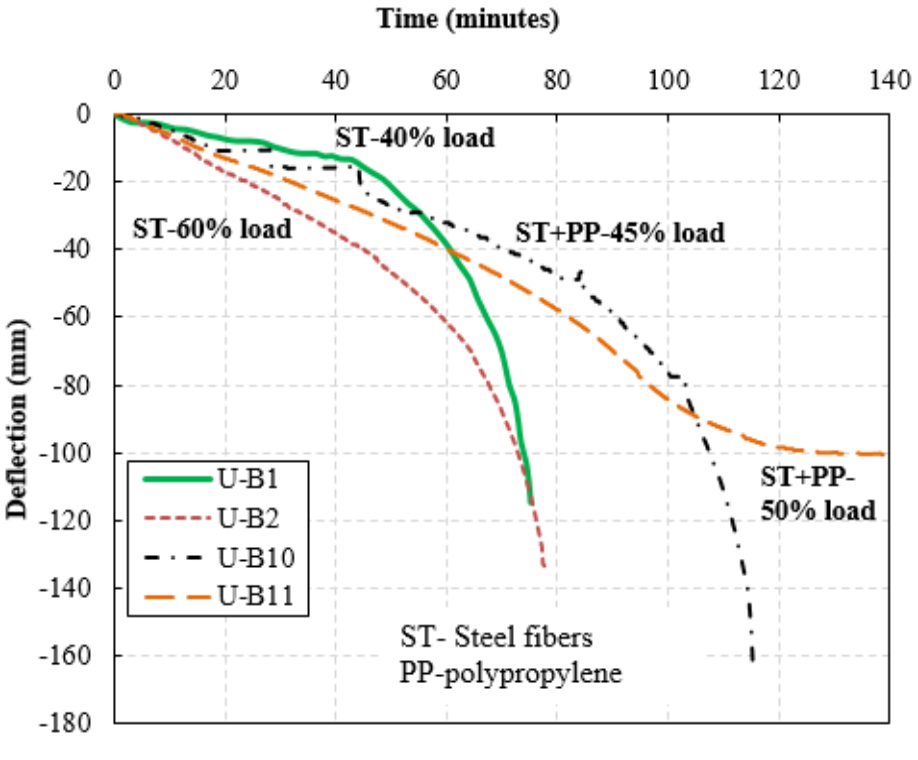

(a)

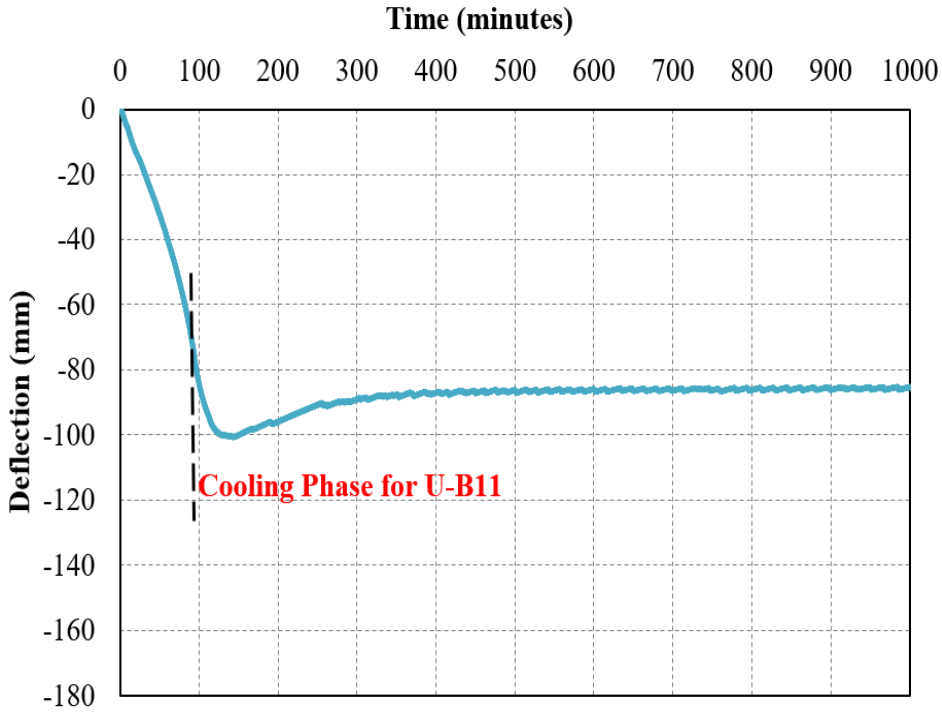

(b)

Figure 3.32. Midspan deflection as a function of time in (a) all UHPC beams, (b) beam U-B11.

Spalling Response

The progression and extent of spalling during each fire test were gauged and these measurements are summarized in Table 3-9. The spalled volume across the length of beam was non-uniform owing to the non-homogenous nature of concrete. Hence, the maximum spalling depth was measured by dividing each beam into segments of 300 mm along its entire length, and the average of the maximum spalling depth is calculated. As can be seen in Table 3-9, the maximum spalling depth is similar in the tested UHPC beams. However, the average maximum spalling depth is variant in each beam and aligns with the measured spalled weight ratio, providing a more representative measurement of spalling depth.

Spalling in all four beams (including the beams with PP fibers), started after about 10 min into fire exposure and this was accompanied by loud bangs. The spalling was violent as concrete pieces were hitting the walls of the furnace with high velocity. Around 40 min into fire exposure, this explosive spalling stopped. In beams U-B1 and U-B2, fabricated without polypropylene fibers, spalling recommenced after 60 min of fire exposure (second round of spalling). This can be attributed to the heating of inner concrete layers, which were subjected to direct fire exposure after early spalling. Concrete in UHPC beams without PP fibers have low permeability and when subjected to heating, high levels of pore pressure build-up again due to temperature-induced moisture migration to interior impermeable parts of the beam cross-section. However, concrete in beams fabricated with PP fibers, U-B10 and U-B11, did not encounter the second round of spalling and this can be attributed to the subsiding of pore pressure through micro channels enabled by melting of PP fibers that occur around 160°C. The overall intensity of spalling and the violent sounds of concrete chunks hitting the walls of furnace were significantly less intensive during the fire tests of beams with PP fibers.

Table 3-9. Summary of fire test results.

Beam designation	Fiber	Fire exposure	Applied loading kN, (% of capacity)	Maximum spalling depth (mm)	Average maximum spalling depth (mm)	Spalled weight ratio (%)	Extent of spalling	Fire resistance (min)
U-B1	Steel	DF*1	38 (40%)	44	38	13.20%	Severe	75
U-B2	Steel	DF1	60 (60%)	32	19	7.50%	Severe	78
U-B10	PP* + Steel	DF1	43 (45%)	32	16	7.30%	Severe	114
U-B11	PP + Steel	DF2	50 (50%)	32	13	5.40%	Moderate	No Failure

*PP: Polypropylene, *DF: Design Fire

The state of UHPC beams after the fire tests, together with a schematic representation of the section (with the spalling pattern) is shown in Figure 3.33. Although all four beams were exposed to fire from three sides, much of the spalling was mainly in upper compression zone on either side of the beams with only minor levels of spalling or scaling at the bottom surface, as can be seen in Figure 3.33. The extent of spalling in the tested UHPC beams is mainly dependent on the permeability in the concrete, as all beams had similar tensile strength to withstand generated stresses, through the addition of steel fibers in the same quantity in each batch mix.

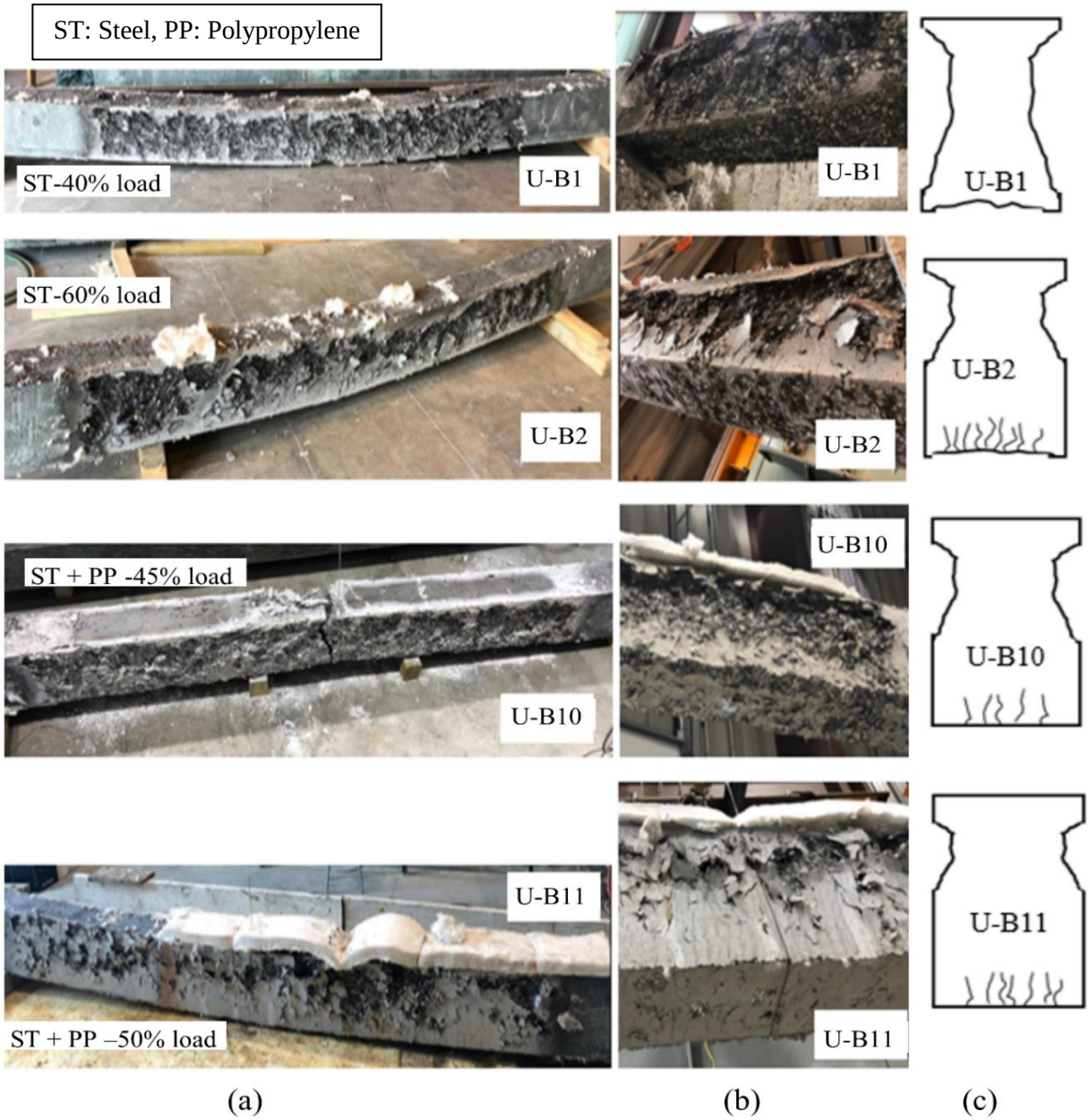

Figure 3.33. Fire test results: (a) state of UHPC beams after fire tests, (b) bottom surface in tested beams, (c) schematic illustration of spalling and cracking pattern in tested beams.

Permeability under elevated temperature exposure is influenced by the presence of PP fibers and cracking pattern that develops, which in turn depends on the level of applied loading during fire exposure. As presented in Figure 3.33, beam U-B1 experienced maximum spalling (13.2% by weight) due to the absence of PP fibers and lower cracking developed as this beam was subjected to a lower load level (40%). The extent of spalling in beam U-B2 (7.5% by weight) is much lower

due to the higher level of applied loading (60%), which aided in tensile crack development, and this way the pore pressure could be released. The percentage of spalled concrete in beam U-B10 was also lower (7.3%) than the beams without PP fibers due to dissipation of pore pressure through melting of polypropylene fibers at about 160°C. The extent of spalling in beam U-B11 (with PP fibers) is further lower (5.4%) and this is due to micro cracking induced by a relatively higher load ratio (50%).

The stress build-up in concrete due to temperature-induced vapor pressure, generated during exposure to fire, cannot escape due to extremely low permeability of UHPC. The concrete permeability varies within the cross section of the beam due to crack patterns resulting from variation in the level of bending moment resulting from applied loading. The higher level of cracking in concrete in the tension zone (closer to the bottom most layers of the beam), lead to an increased permeability at those layers and thus lower pore pressure. However, due to absence of tensile cracking in the upper portion of concrete (especially on the sides), pore pressure is higher in these portions and contributes to higher resultant tensile stress, which in turn results in higher spalling in the upper portion of the UHPC beam.

This trend of predominant spalling in the compressive zone of the UHPC beam is quite different from that observed in NSC and HSC beams [77,91,137], where major portion of spalling was in tension face (bottom surface) of the beam. Based on previously reported test data, in NSC beams, the extent of spalling is minimal or almost negligible throughout the fire exposure. In a few of the previous fire tests on NSC beams, minor spalling was observed but only just a few minutes prior to failure, which has a minor influence on the fire performance of the beam. Unlike NSC beams, some level of spalling occurs in HSC beams under certain fire conditions, and the spalling pattern was found to be dependent on fire scenario, load level, and support conditions [11]. Observations

in previous fire tests indicate that spalling in HSC beams is usually confined to the bottom surface and edges of the beam, and occurred after 40 minutes of fire exposure [11,137]. This type of late-stage spalling, also known as corner spalling or sloughing off, can be attributed to the thermomechanical stresses in the surface giving rise to a crack pattern at corners and edges. Due to the late onset of this spalling, the concrete tensile strength had already reduced from fire exposure and thus, the corners (edges) tend to fall-off owing to thermal cracking [138]. In contrast, spalling in compression zone similar to UHPC beams has been observed only in very few tests in HSC beams [77,91,137], during the early stages of fire exposure (after 10 minutes). However, the spalling in such HSC beams was much less severe than UHPC beams in terms of spalled volume and its effect on thermal and structural response of the beam.

In addition, it can be concluded from the previous tests that the nature and location of spalling depend on the time of occurrence; early stage spalling is explosive and mainly in the compression zone, whereas intermediate and later stage spalling are non-explosive and in the tension zone of the beam. According to the fire test observations, UHPC is more susceptible to early stage explosive spalling in the compression zone with a second round of spalling in beams without PP fibers. This spalling pattern is distinctive to UHPC and can be attributed to its very densely packed microstructure, with much lower permeability, as compared to conventional NSC and HSC.

Of the four beams tested under fire exposure, three beams, namely U-B1, U-B2, and U-B10, failed in flexural mode exhibiting a distinct flexural cracking pattern in the tension zone through the formation of multiple microcracks, accompanied with the spread of a single macrocrack in the mid-span region. The number of cracks developed in beams under fire was significantly higher and also cracks propagated deeper into compression zone as compared to control beam. The development of such large number of microcracks in the tension face of the beam can be attributed

to the bridging effect facilitated by the presence of steel fibers in UHPC [108,139]. The macrocrack at mid-span in beams U-B2 and U-B10 propagated gradually to the top layer of concrete and led to breaking up of these beams into two parts. Beam U-B1 failed abruptly in a brittle manner as compared to a gradual failure experienced in beams U-B2 and U-B10. The fourth beam, U-B11, did not fail since the fire exposure had a well-defined decay phase and this resulted in a partial recovery of strength and stiffness in the beam when the cooling phase started.

The level of spalling influenced the failure modes in the UHPC beams. Due to the excessive spalling in the upper portions of the beam, the concrete in compression zone attained ultimate strain at certain locations in the beam before yielding of tensile steel reinforcement, resulting in localized crushing in top concrete. The localized top crushing phenomenon was observed in beams U-B1 and U-B11, and is shown in Figure 3.34. Beams U-B2 and U-B10 did not experience localized top crushing (compressive cracking) as the yielding of tensile reinforcement followed by rebar rupture occurred in these beams. This phenomenon of localized crushing in top concrete layers is unique to UHPC beams and not observed in NSC or HSC beams, where fire-induced spalling in beams mostly resulted in loss of concrete in tensile zone (at bottom surface) and thus exposure of tensile reinforcement directly to fire [91].

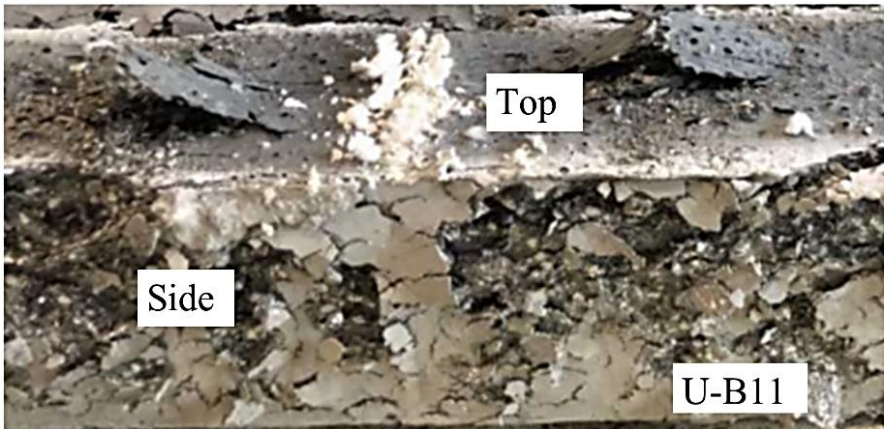

Figure 3.34. Localized compression zone failure in UHPC beam.

Fire Resistance

The measured fire resistance (failure time) in the four tested UHPC beams is given in Table 3-9. The time to failure is defined as the fire resistance for the beam and failure is said to occur when the strength of the beam decreases to a level at which the beam cannot sustain the effects of applied loading. Three out of the four tested UHPC beams that were subjected to design fire DF1, without cooling phase, attained failure. The fourth beam, U-B11 which was subjected to design fire DF2, with a well-defined cooling phase, did not fail. The variations of failure times in different beams can be attributed to variations in test conditions (fire scenario) and beam characteristics (loading, presence of polypropylene fibers).

The fire resistance of the beams U-B1 and U-B2, made without polypropylene fibers, is 75 and 78 min respectively, and is much lower than that of the beam U-B10, with PP fibers, at 114 min. This increased fire resistance in beam U-B10 can be clearly attributed to the contribution of PP fibers in mitigating spalling, which in turn helps to achieve the higher fire resistance in U-B10. Beam U-B1 was subjected to a lower load level (40%) as compared to U-B2 (60%); however, beam U-B2 had higher fire resistance (78 min) as compared to beam U-B1 (75 min). This is because, under higher loads, the extent of spalling in UHPC beams is lower due to the release of pore pressure through load-induced cracks, which in turn resulted in higher fire resistance in beam U-B2.

3.7. Summary

Both material level and structural level tests were conducted to evaluate the behavior of UHPC under fire conditions. Results from these experiments can be utilized to draw the following conclusions:

- Ultra-high performance fiber reinforced concrete beams are highly susceptible to fire-induced spalling due to their dense microstructure, and lower permeability, and this can

lead to lower fire resistance in UHPC members, as compared to conventional concrete members.

- In UHPC beams, fire-induced spalling mainly occurs in the upper portion (compression zone), which is in contrast to NSC and HSC beams where majority of spalling is confined to fire exposed bottom surface and bottom corners. This pattern of spalling in compression zone results in a faster temperature rise in the inner compressive layers of concrete (including compression rebars).
- Load level and fire scenario have an influence on the extent of spalling and fire performance of UHPC beams. The extent of spalling is less severe in UHPC beams under higher load levels due to the alleviation of pore pressure resulting from increased cracking in the tension zone of the beam. Also, UHPC beams exhibit better performance under design fire exposure with distinct cooling phase, as compared to standard fire exposure.
- The addition of polypropylene fibers to UHPC significantly reduces the extent of fire-induced spalling in UHPC beams and this in turn enhances fire resistance of the beam.
- UHPC exhibits slightly higher thermal conductivity and thermal expansion, whereas specific heat and mass loss are lower at elevated temperatures as compared to those in NSC and HSC.
- The relative retention of compressive strength and elastic modulus in UHPC is lower as compared to NSC, but in the same range as that in HSC. The presence of steel fibers in UHPC leads to a ductile failure in tension with the bridging of cracks and a slower loss in tensile strength at 300-750°C as compared to NSC and HSC.

- The addition of polypropylene to UHPC lowers the risk of spalling without significantly altering the mechanical and thermal properties throughout the 20–750°C temperature range.
- There is no significant influence of heating rate on mechanical property degradation in UHPC according to the two heating rates adopted in this study i.e. 0.5°C/min and 2°C/min. This implies that a lower heating rate of 0.5°C/min can be utilized for the measurement of mechanical properties of UHPC omitting the step of pre-drying in the oven, and also minimizing the probability of spalling.
- The proposed empirical relations of temperature-dependent thermal and mechanical properties can be utilized as input data in computer models for evaluating the realistic fire response of UHPC structures.

CHAPTER 4

4. Numerical Model

4.1. General

The literature review in Chapter 2 highlighted the lack of numerical models for evaluating thermo-mechanical response of UHPC beams under fire conditions. Additionally, most of the available numerical models to evaluate fire response of RC beams do not account for fire-induced spalling, which is critical in determining the fire performance of UHPC members. Only limited studies have focused on developing approaches to assess and predict the spalling of concrete under fire conditions [80,140–142]. Even in these limited studies, spalling was evaluated with consideration to stress generated from thermal and pore pressure effects, but without explicitly accounting for load-induced mechanical stress. Additionally, there is a lack of reliable high-temperature material properties for modeling spalling progression in concrete.

Therefore, to overcome some current drawbacks, a numerical model is developed in this study to evaluate the response of UHPC beams under the effect of fire exposure and structural loading. As part of the numerical model, a main program was developed for the fire resistance analysis of RC beams, and a sub-model was incorporated for spalling analysis. The developed model is an extension and advancement to the hydrothermal spalling model developed by Dwaikat and Kodur [84,91] for NSC and HSC beams. The updated model specifically accounts for stresses due to structural loading and thermal gradients in addition to pore pressure stresses, for predicting spalling and also spalling is evaluated at member level as opposed to analysis of a single critical section. Further, permeability based on the effects of cracking induced by structural loading, pore pressure, and temperature distribution is applied to evaluate spalling. The numerical model is

validated against measured response parameters from full scale fire tests. Details of the main model for fire resistance analysis and numerical procedure for spalling calculations are presented here.

4.2. Analysis Procedure

The fire resistance analysis is carried out by applying a macroscopic finite-element based approach, wherein temperature-dependent sectional moment-curvature relations are utilized to trace the response of a concrete beam in the entire range from loading till collapse under fire [36]. The response of a fire exposed RC beam is traced by undertaking a coupled thermo-structural analysis at various fire exposure times, till the failure of the beam or end of fire exposure. All critical factors, including the occurrence of spalling, can be accounted for in the fire resistance analysis. A flowchart illustrating the numerical procedure for fire resistance calculations, including spalling calculations, is shown in Figure 4.1. The numerical model is developed in FORTRAN and the post-processing of results is carried out utilizing MATLAB.

For the fire resistance analysis, the RC beam is divided into a number of segments along its length and the mid-section of each beam segment is further discretized into a mesh of two-dimensional bilinear iso-parametric 4-noded rectangular elements (utilizing bilinear interpolation functions) connected by nodes (see Figure 4.2). The mid-section in each segment is assumed to represent the overall behavior of that segment. The fire resistance analysis is performed in small increments over time. At each time interval, the analysis is performed through the following main steps discussed herein:

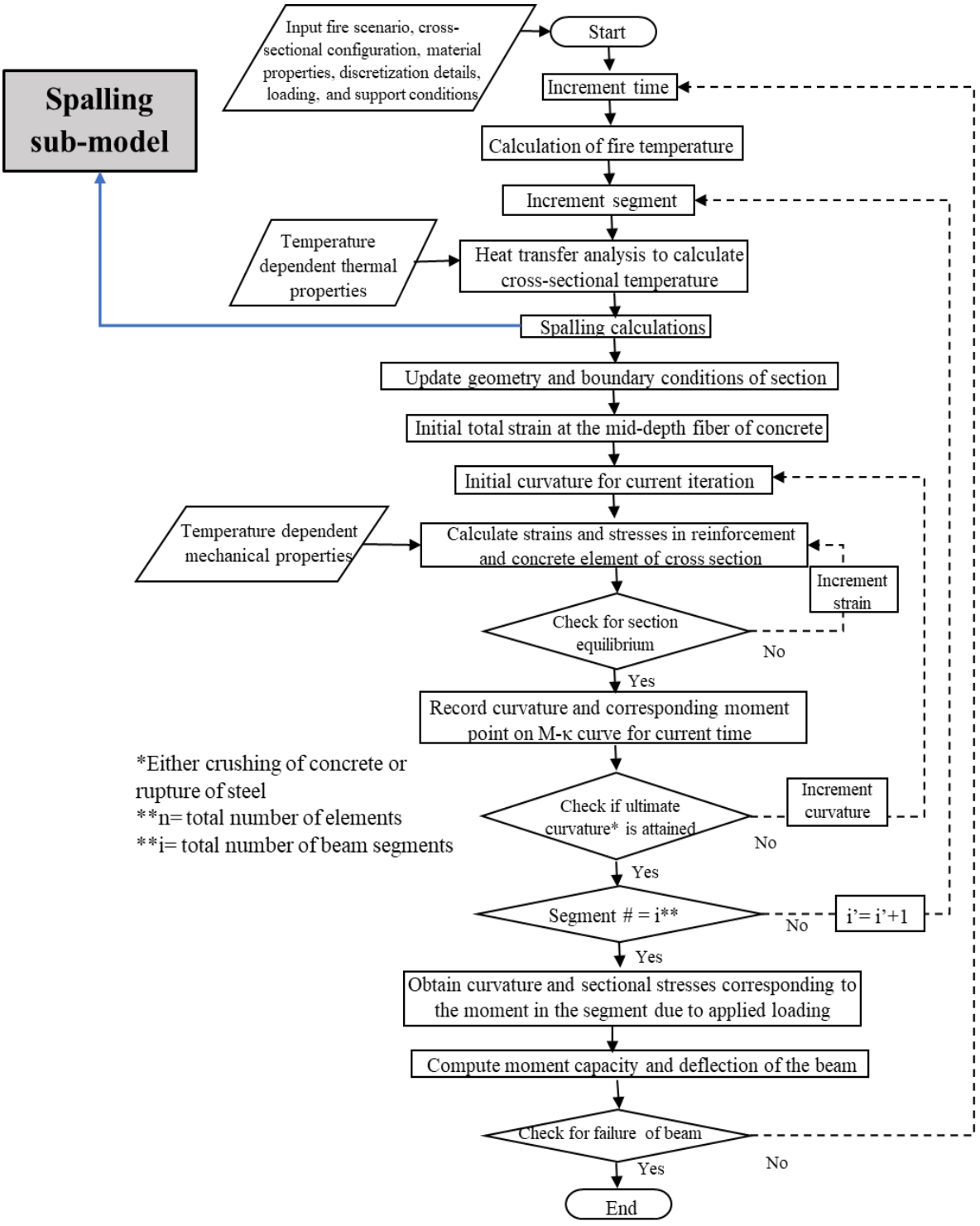

Figure 4.1. Flow chart illustrating steps for spalling calculation and fire resistance analysis of a typical RC beam.

Figure 4.1. (cont'd)

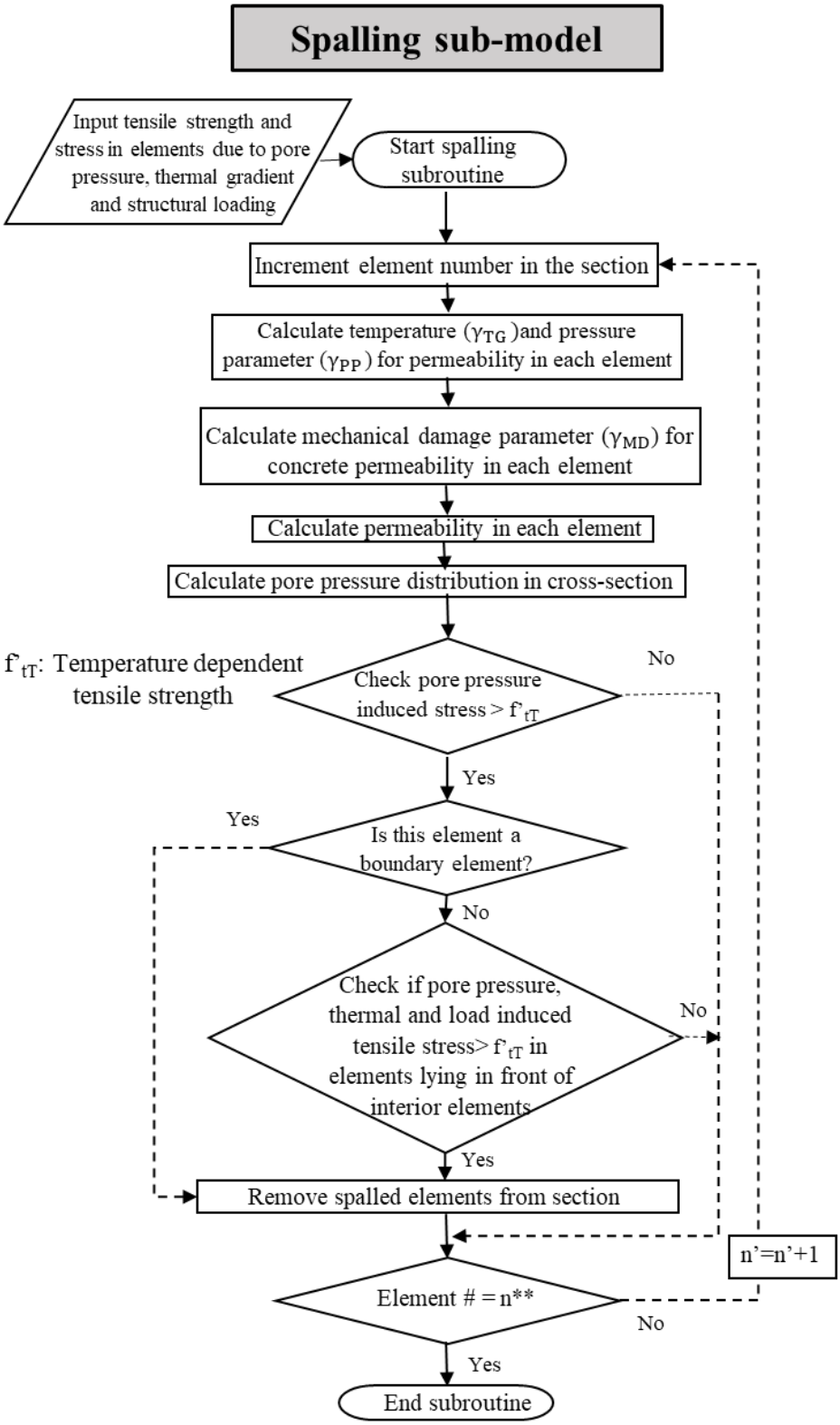

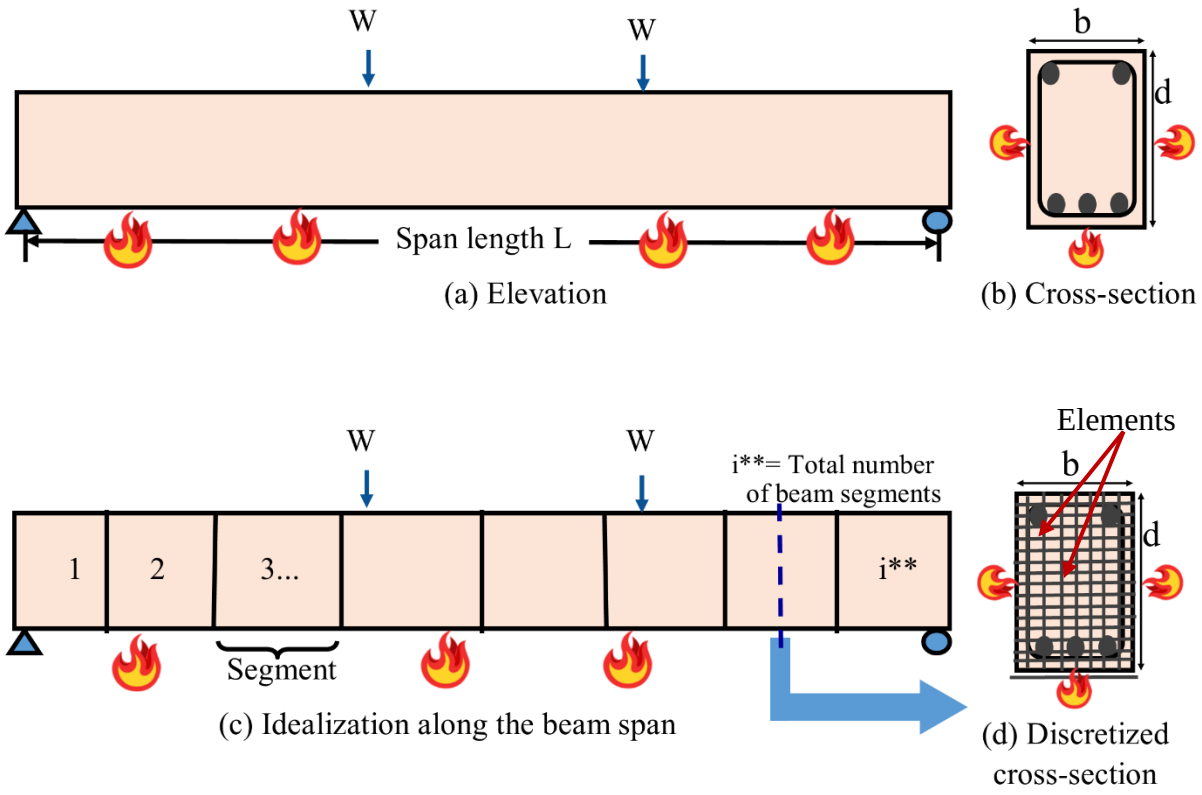

Figure 4.2. Typical beam layout and discretization of beam into segments and elements.

4.2.1. Evaluation of fire temperatures:

The three sides of the beam (bottom surface and two sides) are assumed to be exposed to fire, while ambient conditions prevail on the top surface to simulate the presence of slab. The fire temperature is calculated based on standard fire exposure such as ASTM E119 [99] or ISO 834 [100], or any design fire scenario [96] can be specified through time-temperature relations. For instance, the time-temperature relation for ASTM E119 standard fire can be approximated by the following equation:

$$T_f = T_0 + 750[1 - \exp(-3.79553\sqrt{t_h})] + 170.41\sqrt{t_h} \quad (4\text{-}1)$$

where t_h = time(h); T_0 = initial temperature (°C); and T_f = fire temperature (°C). The design fires consist of a growth phase and decay phase, and are represented by parametric fires specified in

Eurocode 1 [143]. The time-temperature relationships of design fire are influenced by the compartment characteristics including fuel load, ventilation openings, and wall lining materials in different types of occupancies (buildings). Figure 4.3 shows the time-temperature curves for ASTM E119 standard fire and a design fire. The design fire in Figure 4.3 is assumed to occur in a room with dimensions of 6x4x3 m^3 having a fuel load of 250 MJ/m^2 and a ventilation factor of 0.04 with an opening dimension of 2.25x1.5 m^2.

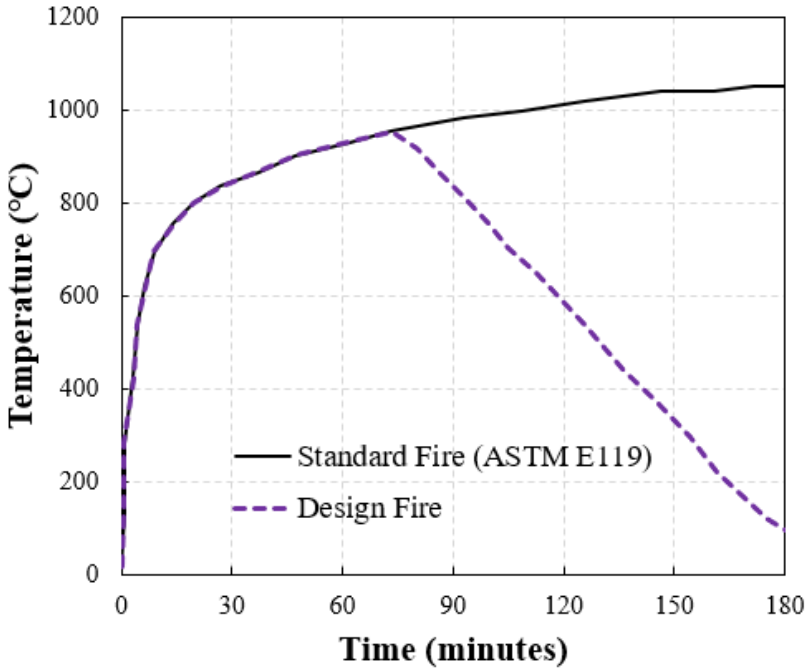

Figure 4.3. Time-temperature curves for standard and design fire scenarios.

4.2.2. Evaluation of sectional temperatures:

At each time step, the temperature distribution in the mid-section of each segment is determined by undertaking thermal analysis. For this thermal analysis, the mid-section of each beam segment along the beam length is discretized into a two-dimensional mesh of quadrilateral elements. Within the solid cross-section, conduction is the dominant heat transfer mechanism. The heat transfer from the surrounding environment (exposed to fire or unexposed) to the boundary elements is through convection and radiation. Steel reinforcement is not explicitly considered in the thermal analysis

due to its insignificant contribution to temperature distribution across the member cross-section [144]. Nonetheless, the temperatures at the location of steel reinforcement are utilized for calculating the temperature-dependent mechanical properties of rebars to analyze spalling and structural response.

Based on the conservation of energy, the governing equation for one-dimensional heat transfer is given as:

$$\rho c \frac{dT}{dt} = -\frac{dq}{dx} + Q \tag{4-2}$$

where ρ = density; c = specific heat; T = temperature; t = time; x = distance; q = heat flux; Q = internal heat source. Applying Fourier's law, which relates the heat flux to the temperature gradients as $q = -k\frac{dT}{dx}$, the above equation can be written as:

$$\rho c \frac{dT}{dt} = \frac{d(k\frac{dT}{dx})}{dx} + Q \tag{4-3}$$

where k = thermal conductivity. Thus, the governing transient heat conduction equation within a rectangular a two-dimensional beam cross-section is written as:

$$k\nabla^2 T + Q = \rho c \frac{\partial T}{\partial t} \tag{4-4}$$

where k = thermal conductivity; ρ = density; c = specific heat; ∇ = Laplacian differential operator; T = temperature; t = time, and Q = internal heat source. The convective and radiative boundary heat flux on the boundary is expressed as:

$$q_{rad} = h_{rad}(T - T_E) \tag{4-5}$$

$$q_{con} = h_{con}(T - T_E) \tag{4-6}$$

where q = heat flux; h = heat transfer coefficient; T_E = temperature of the environment surrounding the boundary depending on exposure conditions (fire or room temperature). The subscripts 'rad'

and ‘con’ represent radiation and convection, respectively. The total heat flux on the boundary of the beam, using Fourier’s law can be defined as:

$$k\left(\frac{\partial T}{\partial y}n_y + \frac{\partial T}{\partial z}n_z\right) = -(h_{rad} + h_{con})(T - T_E) \quad (4\text{-}7)$$

where n_y and n_z = components of the vector outward normal to the surface in the plane of the cross section. The radiation heat transfer coefficient is given by:

$$h_{rad} = 4\sigma\varepsilon(T^2 + T_E^2)(T + T_E) \quad (4\text{-}8)$$

where T_E = temperature of the environment surrounding the boundary depending on exposure conditions (fire or room temperature); σ = Stefan-Boltzman constant = $5.67\text{x}10^{-8}$ ($W/m^2.K^4$), and ε = emissivity factor. In the current analysis, the value of h_{con} is considered as 25 $W/m^2.K$ for fire-exposed surface and 9 $W/m^2.K^4$for unexposed surface.

Galerkin finite element formulation is applied to solve the heat transfer partial differential equation. In this formulation, the material property matrices (stiffness matrix K_e, mass matrix M_e) and the equivalent nodal heat flux (F_e) are generated for each element. These matrices are given by the following equations:

$$K_e = \int_A k\left[\frac{\partial N}{\partial x}\frac{\partial N^T}{\partial x} + \frac{\partial N}{\partial y}\frac{\partial N^T}{\partial y}\right]dA + \int_\Gamma N\alpha N^T ds \quad (4\text{-}9)$$

$$M_e = \int_A \rho c N N^T \, dA \quad (4\text{-}10)$$

$$F_e = \int_A NQ \, dA + \int_\Gamma N\alpha T_E ds \quad (4\text{-}11)$$

where N = vector of the shape functions, k = thermal conductivity, α = heat transfer coefficient depending on the boundary condition Γ, Q = internal heat source; s = distance along the boundary, A = area of the element (in discretized mesh), and T_E = fire or ambient temperature depending on boundary condition Γ. Once the element matrices are computed, they are assembled into a global system of differential equations and is expressed as:

$$M\dot{T} + KT = F(t) \quad (4\text{-}12)$$

where K = global stiffness matrix, M = global mass matrix, and F = equivalent nodal heat flux, and $\dot{T}$ = temperature derivative with respect to time, t. A finite difference procedure (θ algorithm) in the time domain is applied to solve the above equation and the following equation is obtained:

$$(M + h\theta K)T_{n+1} = (M - h(1-\theta)K)T_n + h(\theta F_{n+1} + (1-\theta)F_n) \quad (4\text{-}13)$$

where h is the time step; T_n and T_{n+1} are the temperatures at the beginning and end of time step and θ is a constant parameter (value between 0 and 1) that determines the stability and accuracy of the numerical procedure applied to solve the nonlinear heat transfer equation. To achieve unconditional stability the value of θ should be ≥0.5 [136]. Therefore, the value of θ is taken as 0.9 in the present study. In each time step, an iterative process is required to solve the above equation due to the nonlinearity of both material properties and boundary conditions. By knowing the fire and ambient temperatures at different time-steps, and utilizing the high-temperature thermal properties of concrete, the temperature rise in each element of the discretized section can be calculated through the described heat transfer analysis procedure. The concrete elemental temperatures are computed by averaging the four nodal temperatures of the rectangular elements. The temperature at the center of the rebar is taken as the temperature of the steel reinforcement for subsequent analysis.

4.2.3. Evaluation of spalling:

The extent of fire-induced spalling is calculated by incorporating a hydro-thermo-mechanical spalling sub-model. Spalling in fire exposed concrete member at any given time step is evaluated by taking into consideration the stresses generated due to pore pressure, thermal strains, and also structural loading. Knowing the elemental (sectional) temperatures from thermal analysis, pore pressure in an element, and associated tensile stress, is calculated through a finite element based

mass transfer analysis which takes into account vaporization of water present in heated concrete [84]. Based on the sectional temperatures, thermal stress in each element is evaluated. Also, load-induced (mechanical) stress arising from the applied load present on the beam is evaluated at each time step.

Spalling in concrete elements is evaluated based on two mechanisms. For the purpose of this paper, the elements located in the first layer of a discretized concrete section close to the fire-exposed surface are termed as boundary elements, whereas the elements located in layers beneath the first fire-exposed layer i.e. in second, third, fourth layer, and so on are termed as interior elements. As per the first mechanism, the spalling of concrete boundary elements will occur if the resulting tensile stress due to pore pressure build-up exceeds the decreasing tensile strength due to the rise in sectional temperature. However, in the boundary elements lying close to the fire-exposed surface, water vapor escapes due to high temperatures and therefore, pore pressure may not always be high in boundary elements.

Besides the portion of escaped water vapor, another part of the water vapor moves inwards towards cooler regions, condenses, and acts as an impermeable wall known as moisture clog. The moisture clog hinders further inward migration of water vapor and leads to the build-up of pore pressure in interior elements. The lower the permeability of the concrete, the closer to the heated surface will be the formation of moisture clog [145]. Therefore, it can be foreseen that interior elements will be more vulnerable to spalling, rather than boundary elements. Further, pore pressure peaks can be expected to develop in elements lying in the third or fourth layer (beneath the exterior surface layer), as temperatures are low in the layers beneath them. When the stress due to pore pressure exceeds the tensile strength in the interior elements, spalling cannot directly occur, as additional stress is needed for pushing and breaking-out the front layers, where pore pressure may be much

lower. This additional stress is imparted by transverse tensile stresses induced by thermal gradient and structural loading, i.e. thermal stress and mechanical stress respectively. In this manner, the cracks or damage initiated in the interior element due to pore pressure, will extend and facture in mode II or compressive mode [146].

Henceforth, as per the second mechanism, when tensile strength is exceeded by pore pressure in any interior element, and the resultant tensile stress due to thermal gradient, load and pore pressure in the elements in front of the interior element is higher than the thermally degraded tensile strength, spalling occurs in those interior and boundary elements. When spalling occurs in an element, that element is removed from the cross-section and the reduced cross-section with updated boundary conditions is considered for subsequent analysis. The detailed procedure for evaluating spalling, including computation of stresses, is provided in section 4.3.

4.2.4. Structural response calculations:

The procedure for structural response calculations is adopted from Dwaikat and Kodur [147]. The strength calculations are carried out using the same rectangular meshing as thermal analysis at an elemental level. The cross-sectional temperatures computed in the thermal analysis, together with the updated geometry of the beam based on the spalling analysis, form the input to structural analysis. Utilizing these input parameters, time (temperature) dependent segmental moment-curvature (M-κ) relations are generated at the midsection of each segment at various time steps. For the moment-curvature analysis, the following assumptions are made:

- Plane sections before bending remain plane after bending.
- There is no slip between steel reinforcement and concrete at various temperatures.
- The failure of the member is through flexural strength limit and not by shear strength limit, since the mid-span of the concrete beam is under pure flexure loading.

- The tensile strain hardening response of UHPC after initiation of cracking due to fiber bridging is accounted for by the tensile stress-strain curve.

The total strain in any element of concrete or rebar can be related to the curvature of the beam by:

$$\varepsilon_t = \varepsilon_0 + \kappa y \quad (4\text{-}14)$$

where ε_t= total strain, ε_0= strain at the geometrical centroid of beam cross-section, κ=curvature, and y= distance from the geometrical centroid of beam cross-section to the center of the element. At any time step, and for an assumed value of ε_0 and κ (curvature), the total strain in each element (concrete or steel rebar) can be computed using the above equation. The total strain in concrete at any time step comprises four components namely thermal, mechanical, creep, and transient strain. Thus, the total strain can be written as:

$$\varepsilon_t = \varepsilon_{th} + \varepsilon_{me} + \varepsilon_{cr} + \varepsilon_{tr} \quad (4\text{-}15)$$

where ε_t= total strain, ε_{th}= thermal strain, ε_{me}= mechanical strain, ε_{cr}= creep strain, and ε_{tr}= transient strain in concrete element at a given temperature, T. Thermal strain can be calculated utilizing the elemental temperature and thermal expansion of the concrete. Creep strain in concrete is assumed to be a function of time, temperature, and stress level, and is computed based on the approach by Harmathy [4] using the following expression:

$$\varepsilon_{cr} = \beta_1 \frac{\sigma}{f_{c,T}} \sqrt{t}\ e^{d(T-293)} \quad (4\text{-}16)$$

where $\beta_1 = 6.28\text{x}10^{-6}\ s^{-0.5}$ (constant) , $d = 2.658\text{x}10^{-3}\ K^{-1}$(empirical constant) , T = current concrete temperature (K), t = time (s), $f_{c,T}$ = concrete strength at temperature T, and σ= current stress in the concrete. The transient strain, which is specific to concrete under fire conditions, is computed based on the relationship proposed by Anderberg and Thelandersson [148]. The transient strain is related to thermal strain as follows:

$$\Delta\varepsilon_{tr} = k_2 \frac{\sigma}{f_{c,20}} \sqrt{t}\ \Delta\varepsilon_{th} \quad (4\text{-}17)$$

where k_2 = a constant that ranges between 1.8 and 2.35 (a value of 2 is used in the analysis); $\Delta\varepsilon_{th}$ = change in thermal strain; $\Delta\varepsilon_{tr}$ = change in transient strain and $f_{c,20}$ = concrete strength at room temperature.

Similar to concrete, the total strain in steel reinforcement at any time step comprises of three components namely thermal, mechanical (or stress related strain), and creep strain. Thus the total strain in steel reinforcement can be written as follows:

$$\varepsilon_{ts} = \varepsilon_{ths} + \varepsilon_{mes} + \varepsilon_{crs} \quad (4\text{-}18)$$

where ε_{ts}= total strain, ε_{ths}= thermal strain, ε_{mes}= mechanical strain, and ε_{crs}= creep strain in steel reinforcement at a given temperature, T. The thermal strain can be computed by knowing the values of coefficient of thermal expansion and temperature of the reinforcing steel. The creep strain in steel is computed based on Dorn's theory and the model proposed by Harmathy [149] with some modifications to account for different values of yield strength of steel. Accordingly, the creep strain in steel can be written as:

$$\varepsilon_{crs} = (3Z\varepsilon_{t0}^2)^{1/3}\,\theta^{1/3} + Z\theta \quad (4\text{-}19)$$

where,

$$Z = \begin{cases} 6.755 * 10^{19}\left(\frac{\sigma}{f_y}\right)^{4.7} & \frac{\sigma}{f_y} \le \frac{5}{12} \\ 1.23 * 10^{16}\,(e^{10.8\left(\frac{\sigma}{f_y}\right)}) & \frac{\sigma}{f_y} > \frac{5}{12} \end{cases}$$

$\theta = \int e^{-\Delta H/RT} dt$; $\frac{\Delta H}{R}$ = 38900ºK; $\varepsilon_{t0} = 0.016\left(\frac{\sigma}{f_y}\right)^{1.75}$; t = time (hours), σ = stress in steel as function of temperature; and f_y= yield strength of steel. Following the calculation of the strain components, the mechanical strain in concrete or steel element can be evaluated by:

$$\varepsilon_{me} = \varepsilon_t - \varepsilon_{th} - \varepsilon_{tr} - \varepsilon_{cr} \quad \text{for concrete} \quad (4\text{-}20)$$

$$\varepsilon_{mes} = \varepsilon_{ts} - \varepsilon_{ths} - \varepsilon_{crs} \quad \text{for steel} \quad (4\text{-}21)$$

For the estimated mechanical strain, the stresses and subsequently the corresponding forces in each element can be computed using temperature dependent stress-strain relationships. An iterative procedure, as shown in Figure 4.1, is applied to evaluate the concrete strain and stress for a given (assumed) curvature, till force equilibrium and strain compatibility are satisfied, within a pre-defined numerical (convergence) tolerance. When the compatibility, equilibrium, and convergence criteria are satisfied, the corresponding moment and curvature are computed. The moment corresponding to the assumed curvature represents one point on the M-κ curve at that time step; and a series of such points form one M-κ curve. At any given time (temperature), points on M-κ curve are computed until the ultimate curvature is attained. A series of such curves are generated at various time steps for each segment of the beam. The M-κ relations capture material non-linearity as they are generated taking into account temperature-dependent degradation in mechanical properties of constituent materials, namely concrete and reinforcement.

The maximum value of the moment in the M-κ relations determines the moment capacity of each segment of the beam. The deflection of the beam is calculated using the moment-area method [150]. According to the moment-area method, bending moment due to applied structural loading at each segment along the length of the member is determined. Utilizing the segmental M-κ relationships, the curvature distribution along the beam length is evaluated corresponding to the calculated bending moment at that segment. Then, rotations are calculating by integrating the area under the curvature distribution diagram along the length of the beam. Finally, deflections are calculated by computing the first moment of area of the integrated area under the curvature distribution.

The above computed moment capacity and deflection in the beam are utilized to check the failure of the beam. At each time increment, each segment of the beam is checked to detect if the moment

capacity or deflection has exceeded the limiting criterion. According to the strength criteria, failure is said to occur when the moment capacity in a segment exceeds the applied moment due to the external (structural) load. According to the deflection criteria, failure of the beam is said to occur when deflection exceeds $L^2/400d$ or the rate of deflection exceeds $L^2/9000d$ (mm/min) where, L is the span length of the beam (mm) and, d is the effective depth of the beam (mm).

4.3. Procedure for Modeling Fire-Induced Spalling

When exposed to fire, concrete beams can undergo spalling, and consequently, early failure can occur in an RC beam. Therefore, due consideration should be given for accounting spalling in tracing the response of a fire-exposed concrete member, especially when concretes of higher strength are involved. A spalling sub-model, originally developed by Dwaikat and Kodur [84], is updated to incorporate a number of new features. The new features of spalling sub-model include accounting for stresses due to structural loading and thermal gradients in determining spalling, realistic permeability variation with temperature, and consideration to varying spalling levels occurring along the beam length (rather than assuming the same spalling level as in the mid-span section). The step-by-step procedure spalling calculations are illustrated in the spalling sub-model flowchart in Figure 4.1.

Following thermal analysis (as laid out in section 4.2.2), the main steps involved in spalling calculations in each segment in a typical fire exposed RC beam (see Figure 4.4 (a)) are discussed here. Prior to fire exposure, the top fibers of concrete are subject to compression and the bottom fibers are subject to tension; due to mechanical stresses σ_{me} (Figure 4.4 (b)) in the longitudinal (flexural) direction, resulting from applied loading on the beam. The mechanical stress distribution in RC beam, presented in Figure 4.4 (b), is illustrated for the cracked section under service load and fire exposure. Upon initiation and propagation of cracking in concrete during the cracked

stage, the tensile stress in the bottom layers of beam cross-section decreases while the compressive stress in the upper portion (top layers) of the beam increases, and the neutral axis shifts upwards as compared to the uncracked stage. When a beam is exposed to fire from three sides, thermal gradient develops along the depth (Figure 4.4 (c)), as the temperature in layers close to fire-exposed surface of concrete is much higher than inner concrete layers.

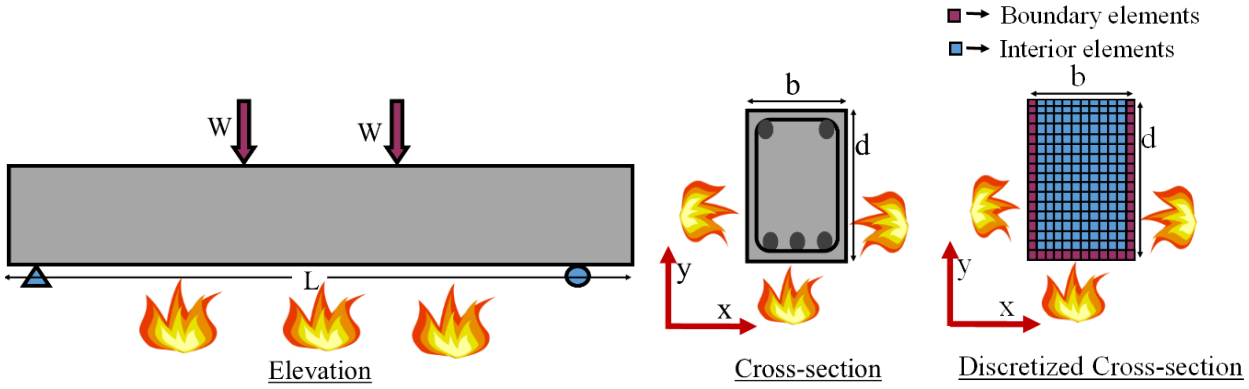

(a) Typical RC beam under fire conditions

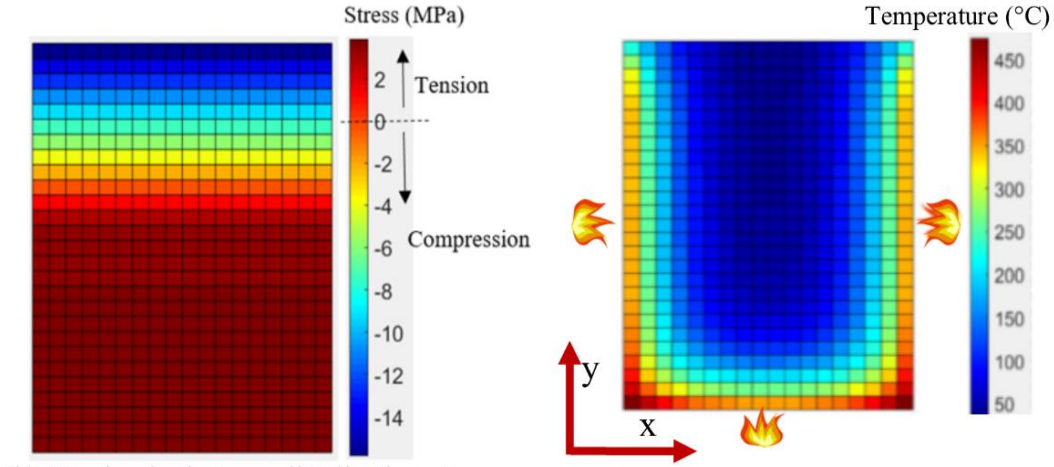

(b) Mechanical stress distribution at ambient conditions

(c) Temperature distribution at fire exposure time, t

Figure 4.4. Illustration of evolution of stresses and spalling in RC beam at each time step of analysis.

Figure 4.4. (cont'd)

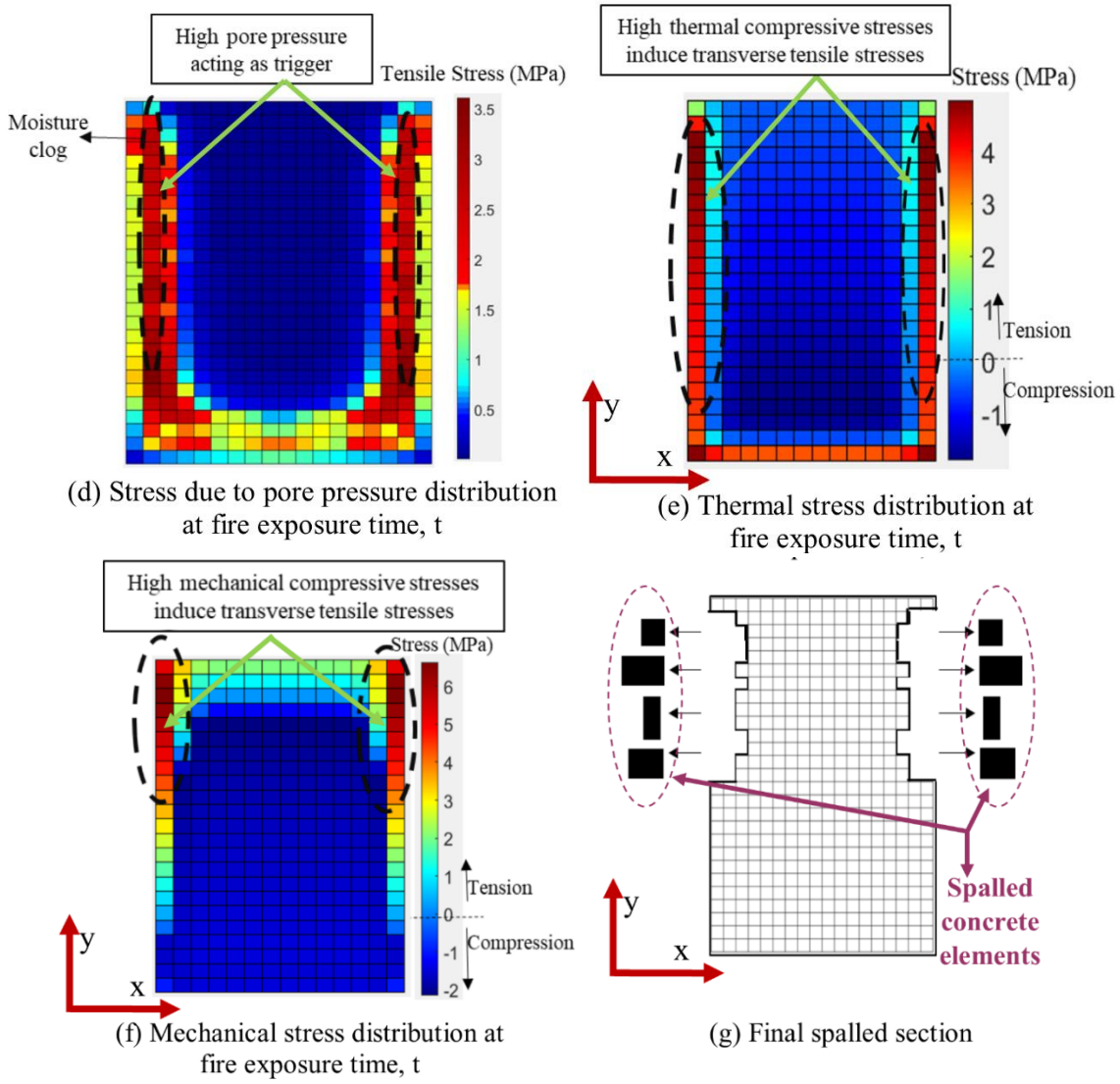

With the increased sectional temperatures, additional stresses are generated due to pore pressure (σ_p) and thermal gradients (σ_{th}) in concrete elements as illustrated in Figure 4.4 (d) and Figure 4.4 (e) respectively. At the same time, the strength and stiffness properties of concrete and steel decrease due to increasing temperature, which in turn affects the mechanical stress (σ_{me}) distribution with time as shown in Figure 4.4 (f). The thermal stress (σ_{th}) and mechanical stress (σ_{me}) are in the direction of spalling i.e. transverse or 'x' direction, shown in Figure 4.4 (e) and (f). The increasing stress and decreasing tensile strength determine the occurrence of spalling

according to the two sets of mechanisms applied for boundary and interior elements. The set of criteria for evaluating spalling is further elaborated below. At each time increment, based on the spalling mechanism, the spalled elements (area) are removed from the cross-section, and the remaining cross-section (refer to Figure 4.4 (g)) forms the input for subsequent analysis in the next time steps.

4.3.1. Criteria for determining spalling:

With increasing sectional temperatures, water present in concrete (elements) evaporates. However, much of the vapor in elements in the first layer close to the fire exposed surface (i.e. boundary elements) escape outside, and therefore; high pressure may not build up immediately near the heated boundary. Instead, peak values of pressure develop in the saturation layer (termed as moisture clog) located at a certain distance inwards (interior elements) from the fire-exposed surface as illustrated in Figure 4.4 (d). Due to this pore pressure build-up, tensile stresses get developed in the elements. In the boundary elements, lying close to the heated surface, the value of pore pressure and associated tensile stress (σ_p) is low, since much of the vapor escapes. For the spalling or breaking-out of interior elements with high pore pressure, the boundary elements (in front of the interior elements), with low pore pressure also have to spall. However, since the σ_p is low in boundary elements, σ_p might not be sufficient to cause spalling independently.

In addition to tensile stress due to pore pressure developed in an element, stresses also result from the onset of thermal gradients (σ_{th}) and due to structural loading (σ_{me}). The thermal stress (σ_{th}) in the flexural direction is compressive at boundary elements close to the three heated surfaces (two sides and bottom surface) due to restrained thermal expansion and is tensile in the cooler interior regions. The mechanical stress (σ_{me}) in the longitudinal direction can be either compressive or tensile in an element, depending on the loading conditions, degraded strength, and the location of

that element within a section. When thermal and mechanical stresses in an element are compressive in the flexural direction, they induce tensile stresses in the transverse direction [146].

As shown in Figure 4.4 (e-f), transverse tensile stress (in 'x' direction) gets induced in several elements close to the heated surfaces (boundary elements) in the beam, where lower values of pressure are built up. Spalling of concrete is predicted to occur through a two-step process resulting in fracture of concrete parallel to the heating surface as illustrated in Figure 4.5. According to continuum damage mechanics approach, microcracks follow a tortuous path and can open in two possible modes: mode I, i.e. when microcrack is acted upon by normal tensile stress, and mode II, i.e. shear-sliding of micro-crack takes place when acted upon by compressive stress parallel to the plane of crack as shown in Figure 4.5 [90,146,151,152]. In the first step, spalling gets initiated by cracking and crack propagation resulting from exceeding tensile strength by tensile stresses developed due to pore pressure. Typically, pore pressure is built-up in the interior elements at some distance from the heated surface. In the second step, further opening of cracks is facilitated by the induced transverse tensile thermal and mechanical stress in addition to pore pressure in the boundary elements [153]. These two steps together lead to spalling in interior and boundary elements.

Step 1: Fracture of concrete in an element gets initiated when interatomic bonds stretch and get broken. This results from the increase in pore pressure, which exerts (tensile) stress in mode I, breaking the interatomic bonds for the onset of fracture. This is evaluated at each time step by checking the value of tensile stress, due to pore pressure (σ_p) in each concrete element, against the tensile strength (f'_{tT}) which is decreasing with increasing temperature (Figure 4.5), given as:

$$\sigma_p > f'_{tT} \tag{4-22}$$

When the above criterion is satisfied in boundary elements i.e. elements in the first fire-exposed layer, spalling occurs. However, if this condition is true for interior elements, which are lying beneath the boundary elements, additional stress is required for the boundary elements with lower pore pressure to spall-off. The cracks that originate from the build-up of pore pressure in the interior elements can only nucleate and propagate if additional tensile stresses are present in the elements, lying in front of the interior elements.

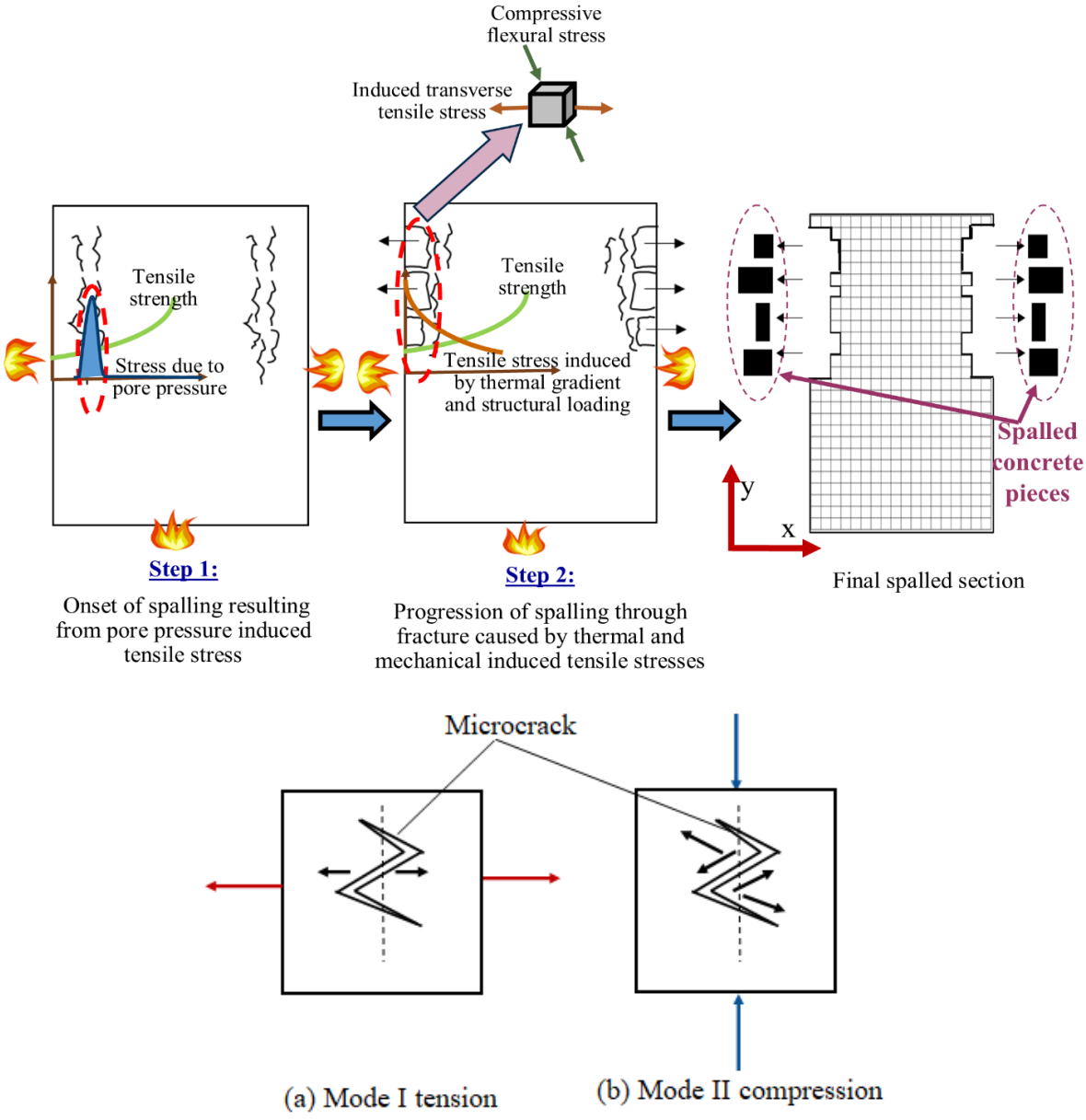

Figure 4.5. Illustration of two-step spalling phenomenon.

Step 2: In addition to the above tensile stresses due to pore pressure, compressive stresses develop in the flexural direction (parallel to the direction of heating) in the elements, due to thermal gradients and structural loading on the beam. This in turn leads to tensile stresses being induced in the direction perpendicular to heating (transverse direction). The resulting tensile stress (from thermal (σ_{th}) and mechanical stress (σ_{me})) in the transverse direction can be evaluated by considering Poisson's ratio of concrete. Poisson's ratio decreases with temperature rise due to the weakening of microstructure and this temperature dependency is incorporated in this analysis by a bilinear relationship proposed by Gernay et al. [154] as follows:

$$\nu(T) = \begin{cases} \nu_0 \left(0.2 + 0.8 * \frac{T_\nu - T}{T_\nu - 20}\right) & T \leq T_\nu \\ \nu_0 * 0.2 & T > T_\nu \end{cases} \quad (4\text{-}23)$$

where ν_0 is Poisson's ratio at room temperature and T_ν is the transition temperature which is equal to 500°C.

In step 2, the sum of transverse tensile thermal and mechanical stresses and tensile stress due to pore pressure is compared with the temperature-dependent tensile strength of concrete (f'_{tT}) in the elements lying in front of the interior elements identified in step 1, and spalling is said to occur when below condition is met in those boundary elements:

$$[\sigma_p + \sigma_{th} + \sigma_{me}] > f'_{tT} \quad (4\text{-}24)$$

The mode II fracture mechanism adopted in step 2 (resulting from thermal and mechanical stresses) assists the growth of microcracks and damage produced in step 1 (due to pore pressure), eventually resulting in the separation of the spalled elements.

4.3.2. Stress due to pore pressure:

Following sectional temperature calculations, temperature-induced pore pressure in each element as proposed by Dwaikat and Kodur [5,84]. These assumptions were followed for the pore pressure calculations:

- The solid skeleton of the concrete structure is undeformable because the thermal and mechanical deformations of the solid phase are smaller in comparison to the volume changes resulting from other processes such as evaporation.
- Water vapor is assumed to behave as an ideal gas.
- Water is an incompressible liquid. This assumption is valid because the volumetric deformation of liquid water due to pressure is much smaller than the volumetric changes due to other processes such as evaporation.
- Mobility of liquid water is ignored. This assumption is valid because Darcy's coefficient (permeability) for liquid water in concrete is much smaller than that for water vapor.
- The effect of air is ignored in the analysis. This assumption is considered to be valid because the mass of air in concrete is much smaller than the mass of water.
- The effect of latent heat and heat of dehydration is not accounted for in the analysis. Accounting for latent heat and heat of dehydration will slightly reduce the predicted temperatures. Thus, latent heat and heat of dehydration can be conservatively ignored in the analysis.

The governing equations for the calculation of vapor pressure in concrete are derived using four main principles; namely: (i) Conservation of mass for liquid water, (ii) Ideal gas law, (iii) Total volume of all different components in a unit volume of concrete equals unity, and (iv) Conservation of mass for water vapor.

The basic equations that govern the conservation of mass for liquid water is given by:

$$E = m_{LW0} - m_L + m_D \tag{4-25}$$

Differentiating the above equation with respect to time,

$$\frac{dE}{dt} = \frac{dm_L}{dt} + \frac{dm_D}{dt} \tag{4-26}$$

Using the chain rule,

$$\frac{dE}{dt} = -\frac{dm_L}{dP_V}\frac{dP_V}{dt} - \frac{dm_L}{dT}\frac{dT}{dt} + \frac{dm_D}{dT}\frac{dT}{dt} \quad (4\text{-}27)$$

where E = mass of evaporated water, m_{LW0} = mass of liquid water at t=0 (initial mass of liquid water), m_L = mass of liquid water at any time t, m_D = mass of liquid water formed due to dehydration, T = temperature, P_V = vapor pressure, and t = time.

Rearranging the ideal gas law which related pressure, volume, mass, and temperature for water vapor as in the following set of equations:

$$P_v V_v = n_v RT = \frac{m_v}{M} RT \quad (4\text{-}28)$$

Differentiating P_v with respect to time and rearranging,

$$\frac{dm_v}{dt} = \frac{V_V M}{RT}\frac{dP_v}{dt} - \frac{dm_v}{T}\frac{dT}{dt} + \frac{m_V}{V_V}\frac{dV_V}{dt} \quad (4\text{-}29)$$

where m_V = mass of water vapor, R = gas constant, n_V = number of moles of water vapor, M = molar mass of water, V_V = volume fraction of water vapor, and T = temperature (^oK).

For a unit volume of concrete, the sum of the volume fractions of all phases equals unity, which leads to:

$$V_v + V_L + (V_{S0} - V_D) = 1 \quad (4\text{-}30)$$

Rearranging the above equation and using the volume-mass-density relationship,

$$V_v = 1 - \frac{m_L}{\rho_L} - (V_{S0} - \frac{m_D}{\rho_L}) \quad (4\text{-}31)$$

Differentiating the above equation with respect to time,

$$\frac{dV_v}{dt} = \frac{1}{\rho_L}\left(\frac{dm_D}{dt} - \frac{dm_L}{dt}\right) - \frac{1}{\rho_L^2}\frac{d\rho_L}{dT}\frac{dT}{dt}(m_D - m_L) \quad (4\text{-}32)$$

$$\frac{dV_v}{dt} = \frac{1}{\rho_L}\frac{dE}{dt} - \frac{1}{\rho_L^2}\frac{d\rho_L}{dT}\frac{dT}{dt}(m_D - m_L) \quad (4\text{-}33)$$

$$\frac{dm_v}{dt} = \frac{V_V M}{RT}\frac{dP_v}{dt} - \frac{m_v}{T}\frac{dT}{dt} + \frac{m_v}{V_v \rho_L}\left(\frac{dE}{dt} - \frac{1}{\rho_L}\frac{d\rho_L}{dT}\frac{dT}{dt}(m_D - m_L)\right) \quad (4\text{-}34)$$

where V_L = volume fraction of liquid water, V_{S0} = initial volume fraction of solid, V_D = volume fraction of dehydrated liquid water, and ρ_L = density of liquid water.

Based on the conservation of mass of water vapor, the following equation can be obtained for one-dimensional problems:

$$\frac{dm_v}{dt} = -\frac{dJ}{dx} + \frac{dE}{dt} \tag{4-35}$$

Using Darcy's Law in the above equation, which relates the mass flux to the pressure gradients as $J=-\lambda\frac{dP_v}{dx}$, wherein $\lambda=m_v\frac{k_T}{\mu_V}$:

$$\frac{dm_v}{dt} = \frac{d(\left(m_v\frac{k_T}{\mu_V}\right)\frac{dP_v}{dx})}{dx} + \frac{dE}{dt} \tag{4-36}$$

For two-dimensional cases, the above equation can be expressed as:

$$\frac{dm_v}{dt} = \nabla(m_v\frac{k_T}{\mu_V})\nabla P_v + \frac{dE}{dt} \tag{4-37}$$

Substituting $\frac{dm_v}{dt}$ in the above equation:

$$\frac{V_V M}{RT}\frac{dP_v}{dt} - \frac{m_v}{T}\frac{dT}{dt} + \frac{m_v}{V_v\rho_L}(\frac{dE}{dt} - \frac{1}{\rho_L}\frac{d\rho_L}{dT}\frac{dT}{dt}(m_D - m_L)) = \nabla(m_v\frac{k_T}{\mu_V})\nabla P_v + \frac{dE}{dt} \tag{4-38}$$

Substituting $\frac{dE}{dt}$ and rearranging the above equation, the governing equation for pore pressure is obtained as follows:

$$m_v\frac{k_T}{\mu_v}\nabla^2 P_v + \left[\left(1-\frac{m_v}{V_V\rho_L}\right)\left(-\frac{dm_L}{dT}+\frac{dm_D}{dT}\right) + \frac{m_v}{T} + \frac{m_v}{V_V\rho_L^2}\frac{d\rho_L}{dT}(m_D - m_L)\right]\frac{dT}{dt} = [\left(1-\frac{m_v}{V_V\rho_L}\right)\frac{dm_L}{dP_v} + \frac{V_V M}{RT}]\frac{\partial P_v}{\partial t} \tag{4-39}$$

where J = mass flux of water vapor, λ = Darcy's coefficient of permeability, k_T = intrinsic permeability of concrete at temperature, T, and μ_V = dynamic viscosity of water vapor. The governing equation for pore pressure has the same form as heat transfer equation.

The initial boundary conditions for pore pressure calculations are considered as:

$$P_{V0} = RH.\, P_{S0} \tag{4-40}$$

where RH = initial relative humidity in the concrete, and P_{S0} = initial saturation pressure, which can be computed using the steam tables according to the initial temperature of concrete. For predicting the liquid water inside concrete, isotherms proposed by Bazant [7] are utilized. The pore pressure for the boundary conditions is assumed to be fixed and equal to initial pore pressure P_{V0}. On the surface boundaries of the beam, transfer of water vapor is assumed to take place through diffusion and the governing mass transfer equation can be written as:

$$\lambda \left(\frac{\partial P_V}{\partial y} n_y + \frac{\partial P_V}{\partial z} n_z\right) = -D_0(\rho_V - \rho_{V\infty}) \tag{4-41}$$

where D_0 = diffusion coefficient of water vapor at the boundaries of the beam, ρ_V = density of water vapor in the concrete boundaries, and $\rho_{V\infty}$ = density of water vapor in the surrounding environment. Using ideal gas law in the above equation:

$$\lambda\left(\frac{\partial P_V}{\partial y} n_y + \frac{\partial P_V}{\partial z} n_z\right) = -\frac{D_0 M}{RT}\left(P_V - \frac{RT\rho_{V\infty}}{M}\right) \tag{4-42}$$

Galerkin finite element formulation is applied to solve the pore pressure development partial differential equation. In this formulation, the material property matrices (stiffness matrix K_e, mass matrix M_e) and the equivalent nodal flux (F_e) are generated for each element. These matrices are given by the following equations:

$$K_e = \int_A m_v \frac{k_T}{\mu_v}\left[\frac{\partial N}{\partial x}\frac{\partial N^T}{\partial x} + \frac{\partial N}{\partial y}\frac{\partial N^T}{\partial y}\right] dA + \int_\Gamma N \frac{D_0 M}{RT} N^T ds \tag{4-43}$$

$$M_e = \int_A \left[\left(1 - \frac{m_v}{V_V \rho_L}\right)\frac{dm_L}{dP_v} + \frac{V_V M}{RT}\right] NN^T\, dA \tag{4-44}$$

$$F_e = \int_A N\left[\left(1 - \frac{m_v}{V_V\rho_L}\right)\left(-\frac{dm_L}{dT} + \frac{dm_D}{dT}\right) + \frac{m_v}{T} + \frac{m_v}{V_V \rho_L^2}\frac{d\rho_L}{dT}(m_D - m_L)\right]\frac{dT}{dt}\, dA + \int_\Gamma N \frac{D_0 M}{RT}\frac{RT\rho_{V\infty}}{M} ds \tag{4-45}$$

The element matrices are assembled into global stiffness, mass, and flux matrices, which are solved by the finite difference procedure (θ algorithm) in the time domain. The stress due to developed

pore pressure (σ_p) is determined by multiplying pressure (Pv) with Biot's coefficient, which is conservatively considered as unity from published literature [155]. The permeability of concrete during fire exposure varies within the cross-section of the beam due to continuously changing cracking patterns resulting from changing thermal and pressure gradients, along with variation in the level of mechanical stresses (bending moment) resulting from applied loading. The higher level of micro cracking developed in concrete layers in the tension zone (closer to the bottom-most layers of the beam), lead to an increased permeability at those layers. This will facilitate escape of gasses (vapor) thus alleviating pore pressure build-up, which in turn mitigates spalling. Thus, varying permeability is to be considered in spalling analysis, and expressions for varying permeability is proposed in section 4.3.5.

4.3.3. Stress due to thermal gradients:

During fire exposure, the thermal stress (σ_{th}) depends on the thermal gradients developed within the cross-section, in which the temperature at the exposed surface of concrete is much hotter than that at the non-exposed surface or concrete core. Thermal expansion in concrete elements can be calculated from the knowledge of elemental temperature and coefficient of thermal expansion of concrete. However, each heated element is attached to nearby cooler elements and is not free to attain the full thermal expansion, as it would violate the geometrical constraints (principle of plane cross-sections remain plane after deformation). This restriction to the free expansion of elements (layers) results in the generation of thermal stress (σ_{th}). Thermal stress in one-dimension can be calculated by dividing the cross-section into a number of equal area elements along with the depth. The hypothetical strain (ε_i) at any layer (i) of concrete, if it were free to expand is:

$$\varepsilon_i = \alpha_i T_i \tag{4-46}$$

where α_i is the coefficient of thermal expansion, and T_i is the temperature in the fiber 'i'. To restrain this thermal strain and to restore the configuration as plane, restraining stress (σ_i) of compressive nature (negative sign implies compression) gets developed at elements or layers:

$$\sigma_i = -E\varepsilon_i \tag{4-47}$$

where E is the modulus of elasticity, which is considered to be constant (hypothetically for illustration) over the whole depth of the section. Realistically, the elastic modulus and thermal expansion (coefficient) of concrete vary with temperature. The resultant of this stress (σ_i) introduces internal restraining axial force ΔN at a distance '$\bar{y}$' from the centroid and a bending moment ΔM_y defined as:

$$\Delta N = \int \sigma_i \, dA = -\int E\varepsilon_i \, dA \tag{4-48}$$

$$\Delta M_y = \int \sigma_i \, \bar{y} \, dA = -\int E\varepsilon_i \, \bar{y} \, dA \tag{4-49}$$

where dA is the segmental area of each layer. This artificial restraint force gets balanced through developing a set of equal and opposite external forces at the ends of the member, i.e., axial force ($-\Delta N$) and bending moment ($-\Delta M_y$). The corresponding thermal stress developed from thermal restraint force is:

$$\Delta\sigma = \frac{-\Delta N}{A} + \frac{-\Delta M_y \, \bar{y}}{I} \tag{4-50}$$

where A is the total member cross-sectional area and I is the moment of inertia about horizontal axis 'x'. The actual stress due to temperature (σ) is the sum of σ_i and $\Delta\sigma$:

$$\sigma = \sigma_i + \Delta\sigma = -E\varepsilon_i + \frac{-\Delta N}{A} + \frac{-\Delta M_y \, \bar{y}}{I} \tag{4-51}$$

When analyzed in flexural direction, thermal stress in a simply supported fire exposed beam is compressive near the heated surfaces and turns into tensile stress in the cooler parts of the beam. As a result, the induced transverse thermal stress (σ_{th}) is tensile near heated boundaries and compressive in the interior portion as shown in Figure 4.4 (e).

4.3.4. Stress due to structural loading:

Under fire conditions, the mechanical stress resulting from structural loading keeps changing with time due to the degradation of mechanical properties with rise in temperature. The mechanical stresses in each element are obtained by utilizing the temperature-dependent stress-strain relations of concrete corresponding to the mechanical strain computed from the strength analysis explained in Section 4.2.4. This load-induced (mechanical) stress (σ_{me}) can be either compressive or tensile, depending upon the location of the concrete layers with respect to the location of the neutral axis, which shifts with fire exposure time. The mechanical stress in the flexural direction will induce transverse stresses (as shown in Figure 4.4 (f)). It is noteworthy that due to the degradation of strength and modulus with temperature in concrete and steel, the load-induced stress increases with increasing temperature in the section. Further, in case of any loss of cross-section due to the occurrence of fire-induced spalling, the mechanical stresses will further increase.

4.3.5. Permeability simulation:

With fire exposure time, the above-discussed stresses increase but part of the stresses can be relieved if the permeability of concrete is high. Thus, the permeability in concrete dictates the spalling in a fire-exposed concrete member. The permeability varies along the beam length and over the beam cross-section, and also changes with fire exposure time due to microstructural changes. This is due to increased cracking induced by higher stress resulting from temperature, vapor pressure, and structural loading [87,141]. There is a lack of experimental data and also a lack of relations for expressing the variation of permeability with temperature, accounting for the combined action of these mechanisms. In most of the previous spalling models, the same value of permeability throughout the section was assumed to determine spalling. To capture permeability variation of concrete in the beam cross-section, an expression for the variation of permeability as

a function of temperature, pore pressure, and extent of mechanical damage (cracking) is proposed in this study:

$$k_D = k_0 * \gamma_{TG} * \gamma_{PP} * \gamma_{MD} \quad (4\text{-}52)$$

where k_D = intrinsic permeability accounting for damage; k_0 = initial undamaged permeability; γ_{TG} = temperature gradient parameter; γ_{PP} = pore pressure variation parameter; γ_{MD} = mechanical damage parameter. The intrinsic gas permeability of undamaged concrete, k_0 is assigned a value of $6.5x10^{-16}$ m^2, $2x10^{-17}$ $m^{2,}$ and $2.3x10^{-18}$ m^2 for NSC, HSC, and UHPC respectively based on the reported values from previous experimental studies [67,125,156,157]. In these reported tests, the gas permeability of concrete was measured utilizing the experimental setup according to the RILEM-CEMBUREAU method [63,158] and the intrinsic gas permeability was calculated by the Klinkenberg method [64]. For the permeability relation, intrinsic permeability is considered, as it is not influenced by the testing medium and the properties of the fluid in the pores, and solely depends on the concrete pore structure; therefore, it represents a true permeability variation. Also, the directionality of damage and resulting variation in permeability are disregarded for the sake of simplicity. The different damage parameters induced by pore pressure, temperature, and mechanical mechanisms in the proposed permeability expression are defined as:

$$\gamma_{TG} = 10^{C_T(T-T_o)} \quad (4\text{-}53)$$

$$\gamma_{PP} = \left(\frac{p_g}{p_o}\right)^{C_p} \quad (4\text{-}54)$$

$$\gamma_{MD} = \left[1 + (\alpha D)^{\beta} + \frac{(\alpha D)^{2\beta}}{2} + \frac{(\alpha D)^{3\beta}}{6}\right] \quad (4\text{-}55)$$

Eqns. 4-53 and 4-54 take into account the variation of permeability with temperature and pressure, and these expressions are based on the work of Gawin et al. [93]. Further based on the hygro-thermal model by Dwaikat and Kodur [84], the coefficients of temperature, C_T and pressure, C_P are taken as 0.0025 and 0.368 respectively. The evolution of permeability due to tensile

microcracking induced by mechanical damage is captured through the relation proposed by Pijaudier-Cabot et al. [159] in Eqn. 4-55, where α and β are fitted parameters based on their study, and are equal to 11.3 and 1.64, respectively. Figure 4.6 shows the variation of concrete permeability as a function of temperature for different values of mechanical damage and an initial concrete permeability of 10^{-18} m^2. The increase in permeability with temperature is non-linear Figure 4.6, however, due to the logarithmic scale, the permeability trends appear to be linear.

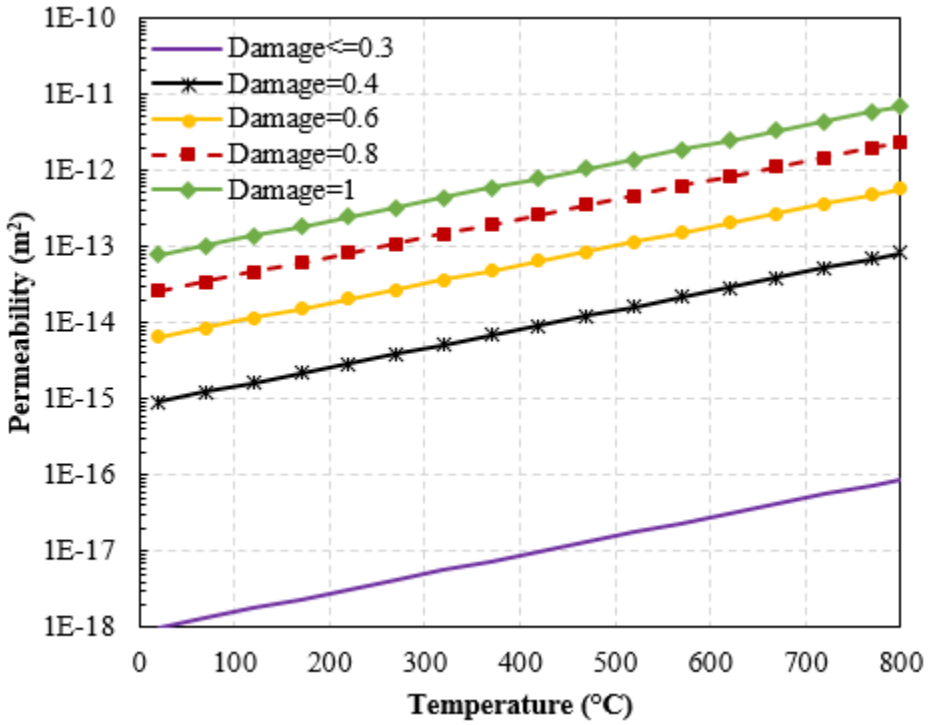

Figure 4.6. Variation of permeability as a function of temperature and mechanical damage.

Values for damage variable, D in Eqn. 4-55 range from 0 to 1 depending on the level of tensile strain developed at that time instant of fire exposure. Further, this tensile strain also depends on the tensile stress-strain response of concrete, which not only varies with temperature, but also with concrete type. Typical stress-strain behavior of UHPC in tension can be idealized into three stages [160] as shown in Figure 4.7 (a). The initial part is linear elastic up to cracking (stress) which is followed by the second stage of strain hardening accompanied by the initiation of multiple

cracking facilitated by bridging of steel fibers. This is further followed by the third part, which is the softening branch that represents crack openings.

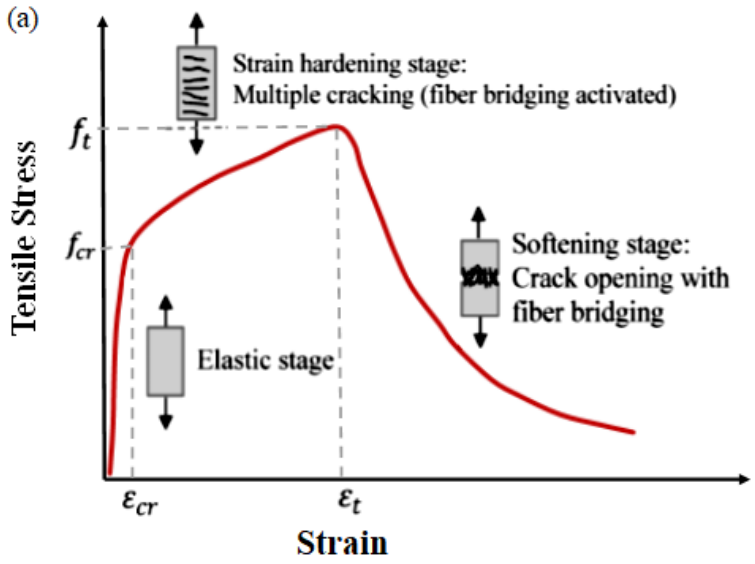

$$D = \begin{cases} 0 & \varepsilon \le \varepsilon_{cr} \\ \varepsilon / (\varepsilon_t - \varepsilon_{cr}) & \varepsilon_{cr} < \varepsilon < \varepsilon_t \\ 1 & \varepsilon \ge \varepsilon_t \end{cases}$$

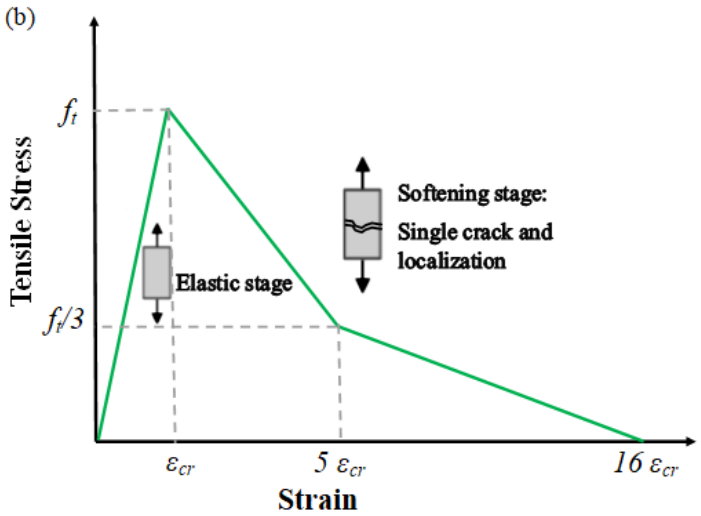

$$D = \begin{cases} 0 & \varepsilon \le \varepsilon_{cr} \\ \varepsilon / (5\varepsilon_{cr} - \varepsilon_{cr}) & \varepsilon_{cr} < \varepsilon < 5\varepsilon_{cr} \\ 1 & \varepsilon \ge 5\varepsilon_{cr} \end{cases}$$

Figure 4.7. Tensile stress-strain curves with damage values for permeability: (a) UHPC (with steel fibers); (b) plain NSC/HSC.

Unlike UHPC, plain NSC and HSC, without any fibers, exhibit elastic behavior under tension till the first crack. After cracking, the plain concretes (without fibers) do not exhibit strain hardening and a bilinear descending branch is adopted [161] for representing the localization of cracks around a single macro crack as shown in Figure 4.7 (b).

In permeability calculations, the damage value is 0 in the pre-cracking stage; this implies that permeability is unchanged due to applied loading (service level loading) in this stage. In the post-cracking region, damage is defined as ratio of strain level and ranges from 0 to 1 as illustrated in Figure 4.7, upto the strain level before widening of cracks. Beyond critical stage of cracking (which is ε_t for UHPC and $5\varepsilon_{cr}$ for NSC/HSC in Figure 4.7), macro crack localization takes place with wider crack openings, which in turn leads to significant increase in permeability; and hence, damage variable (D) is taken as 1 in this stage.

The above set of calculations is incorporated as a 'spalling sub-model' and built into the macroscopic finite element (FE) based model for evaluating fire resistance of RC beams. At each time step, calculations are carried out to evaluate various stresses as discussed above. The occurrence of spalling in an element is evaluated by applying the spalling criterion. If spalling occurs, the spalled concrete element is removed from the cross-section at each segment. The updated reduced concrete section and the new boundary conditions are considered in the following time steps of analysis.

4.4. Model Validation

The validity of the above-developed fire resistance model and spalling sub-model is established by comparing predictions from the analysis with measured data from tests on UHPC beams, under ambient and fire conditions. For validation at ambient conditions, beam U-B3 tested by Kodur et al. [108] is selected. For validation under fire conditions, the four UHPC beams tested by Banerji

et al. [96] as described in Chapter 0 are selected. UHPC beams U-B1, U-B2, and U-B3 consisted of steel fibers, and beams U-B10 and U-B11 consisted of both steel and polypropylene fibers. In addition, the model was also validated against NSC and HSC beams (B5, B3, and B1), tested by Dwaikat and Kodur [11] to illustrate the capability of the model for different concrete types. The NSC and HSC beams were made of plain concrete mix (no fibers). Details on the specific geometry and material properties of selected RC beams are given in Table 4-1. The elevation and cross-sectional details of the RC beams are shown in Figure 4.8, and the fire scenarios followed in the tests are depicted in Figure 4.9.

Table 4-1. Summary of test parameters and results from fire resistance analysis.

Property	**Beam details**							
Beam designation	U-B3	U-B1	U-B2	U-B10	U-B11	B5	B3	B1
Concrete type	UHPC-St	UHPC-St	UHPC-St	UHPC-StPP	UHPC-StPP	HSC	HSC	NSC
Type of fibers	Steel	Steel	Steel	Steel PP	Steel PP	No fiber	No fiber	No fiber
Fire scenario	Room Temp.	Design Fire 1	Design Fire 1	Design Fire 1	Design Fire 2	Design Fire 3	ASTM E119	ASTM E119
Initial permeability (m^2)	$2.3x10^{-18}$	$2.3x10^{-18}$	$2.3x10^{-18}$	$2.3x10^{-18}$	$2.3x10^{-18}$	$2x10^{-17}$	$2x10^{-17}$	$6.5x10^{-16}$
Concrete comp. strength (MPa)	173	173	173	176	176	106	106	58
Concrete tensile strength (MPa)	6	6	6	6	6	3.6	3.6	2.7
Relative humidity (%)	NA	68.5	61.5	32.18	32.65	91.8	87.5	81.5
Load ratio (%)	NA	0.40	0.60	0.45	0.50	0.63	0.53	0.55
App. load (kN)	Monotonic	38	60	43	50	60	50	50
Fire resistance-measured (min)	NA	75	78	114	No Failure	146	160	180
Fire resistance-predicted (min)	NA	82	73	112	No Failure	142	162	175
Extent of spalling-measured (%)	NA	11.5	7	6.35	3.7	7	3.3	1.7
Extent of spalling-predicted (%)	NA	11.7	7.3	5.4	3.6	7.8	3	0

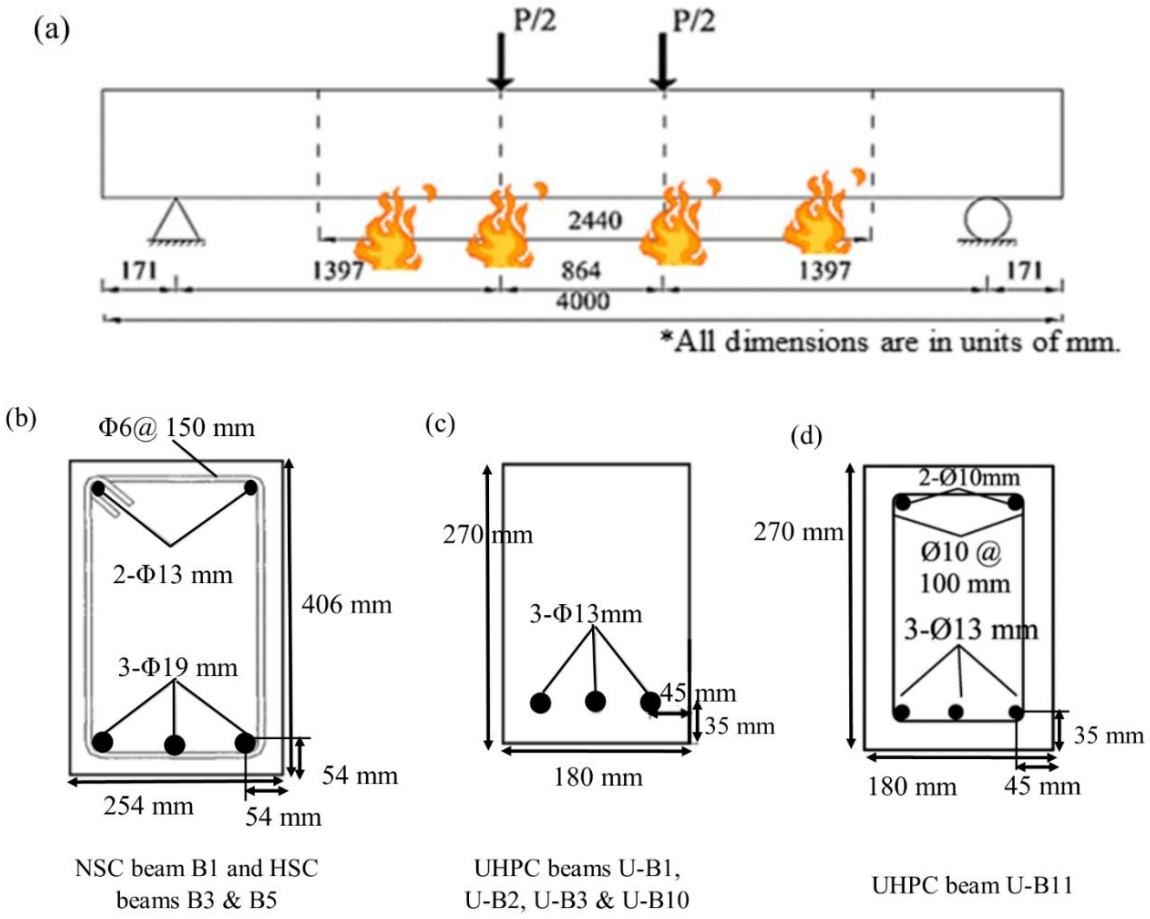

Figure 4.8. Elevation and cross-section of the analyzed RC beams.

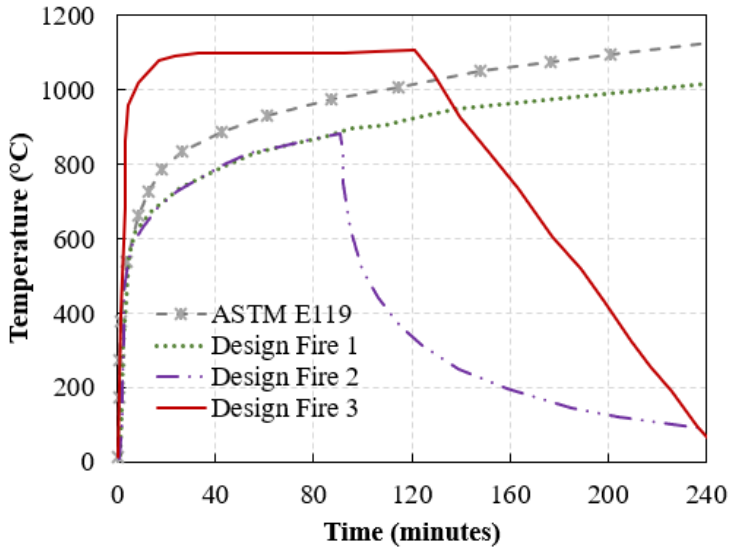

Figure 4.9. Time-temperature curves adopted for fire exposure in the tests of analyzed RC beams.

4.4.1. Analysis Details

For the analysis, the beam was discretized into 40 segments, of 91.5 mm each along the length. The cross-section in the middle of each segment is assumed to represent the overall behavior of the segment. The cross-section of all segments along the length of the beams was further discretized into 10 mm x 10 mm quadrilateral elements for UHPC and HSC, whereas the cross-section for NSC was discretized into 18 x 18 mm elements based on mesh sensitivity analyses. The model calculations are carried out in time steps with an incremental time of 1 minute. The mesh size and time-step for the analyses are carefully selected to minimize convergence problems. In addition, the element size influences the calculations for extent of spalling, and this is mainly due to two reasons. Firstly, the pore pressure values peak near the moisture clog, and these peaks are very sharp, causing them to be hard to capture and resulting in inaccurate spalling calculations with coarser mesh. Secondly, the analysis incorporates spalling by removal of elements. If the element size is larger than appropriate, the spalling prediction will be less accurate and less continuous with sudden jumps in the computed extent of spalling. Finer mesh size (by reducing the size of element) and smaller time increments (time-step) may improve the accuracy of the predictions from the numerical analysis but might also increase computational time, as the analysis requires increased iterations to converge. Thus, a balance between accuracy and computational time is realized by selecting the above level of discretization. The fire resistance analysis was carried out until the beam could not sustain the applied loading.

4.4.2. Material Properties

For steel reinforcement, the temperature dependent stress-strain relations are adapted from high temperature tensile tests reported in the literature [14,162,163]. The stress-strain response of steel reinforcement under tension and compression at various temperatures comprise a linear elastic

range, yield plateau, a strain hardening range, and a softening range. Incorporating temperature dependent strain hardening properties of steel reinforcement leads to realistic predictions of the moment capacity of beams. For the validation study, the yield strength of steel rebars was specified as 420 MPa. The high-temperature stress-strain response of reinforcing steel incorporated in the model is shown in Figure 4.10. Reinforcing steel does not experience a substantial loss of strength in the 20-400°C temperature range. However, at temperatures of 500°C or above, the reduction in yield and ultimate strengths is considerable.

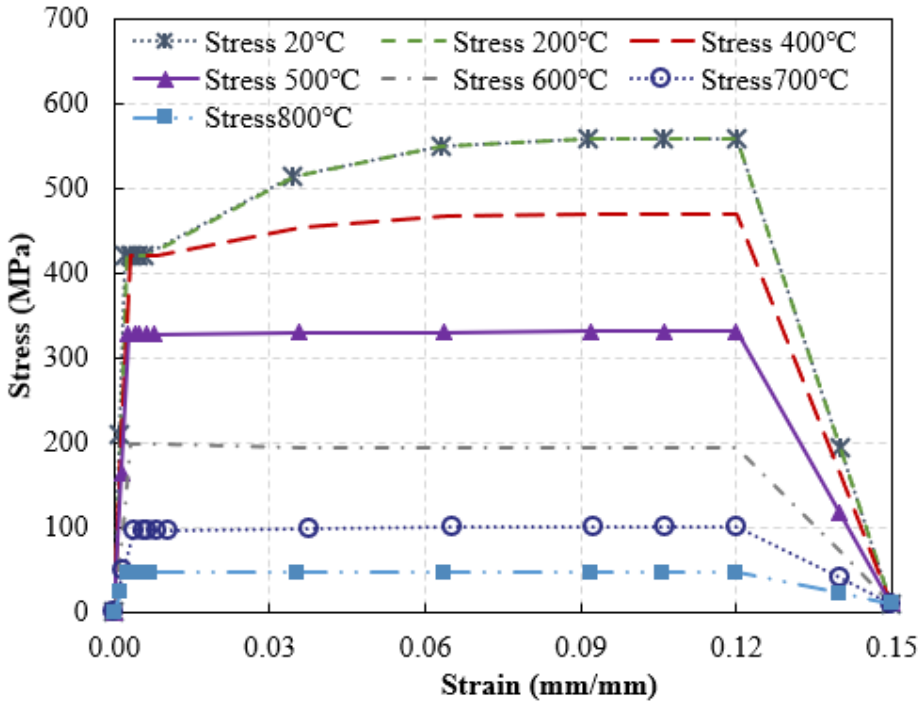

Figure 4.10. Stress-strain response of reinforcing steel at different temperatures (°C).

The temperature dependent thermal and mechanical properties are incorporated in the model from relations provided in ASCE manual [164] for NSC, and from the work of Kodur et al. for HSC [13]. For high temperature material properties of UHPC, design codes do not specify any relations, and very limited test data and associated property relations are currently available. Therefore, property relations are developed as a part of this thesis for undertaking detailed numerical analysis

of UHPC structures. Since the test data at material level revealed that the influence of polypropylene fibers on the thermal and mechanical properties of UHPC (with steel fibers) is insignificant, a single set of developed property relations is applicable for both types of UHPC (with only steel fibers and with steel and polypropylene fibers). The temperature dependent thermal property relations for UHPC proposed by Kodur et al. [118] based on the experiments (as discussed in chapter 0) were used in the model. For defining the compressive behavior of UHPC, the empirical relations proposed for mechanical properties at various temperatures by utilizing the test data in Chapter 0 were incorporated, published in the works of Banerji and Kodur [165]. The compressive stress-strain curves for UHPC (with only steel fibers and with steel and polypropylene fibers) at various temperatures are shown in Figure 4.11. The compressive stress at elevated temperatures is normalized by the compressive (peak) strength at ambient temperature.

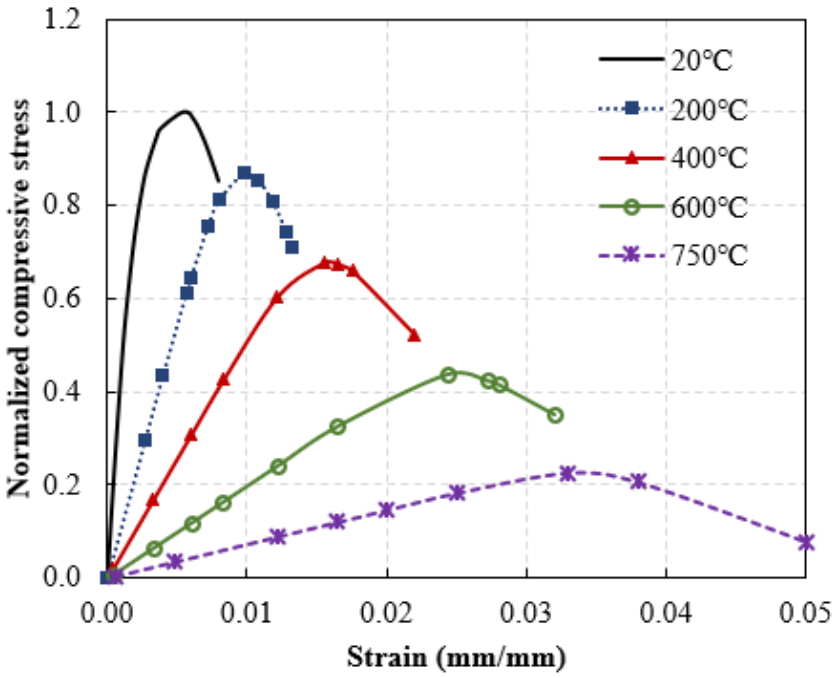

Figure 4.11. Stress-strain response at different temperatures (°C) of UHPC (with and without polypropylene fibers) under compression.

While there is limited information on the temperature dependent stress-strain relations under compression, there is no information on the high temperature tensile stress-strain behavior of

UHPC [165]. Therefore, data obtained from direct tensile tests on UHPC at room temperature was extended by adapting existing high temperature relations for other types of concrete available in the literature [38,166,167]. The rate of degradation of tensile strength is taken from the undertaken splitting tensile tests discussed in Chapter 0. The tensile stress-strain relations adapted for UHPC (with only steel fibers and with steel and polypropylene fibers) are shown in Figure 4.12, wherein, the strength at elevated temperatures are normalized using the peak strength at ambient temperature. The tensile stress-strain model captures linear elastic range upto initial cracking, followed by strain hardening facilitated by fiber bridging till peak stress, which is further followed by softening branch due to crack opening.

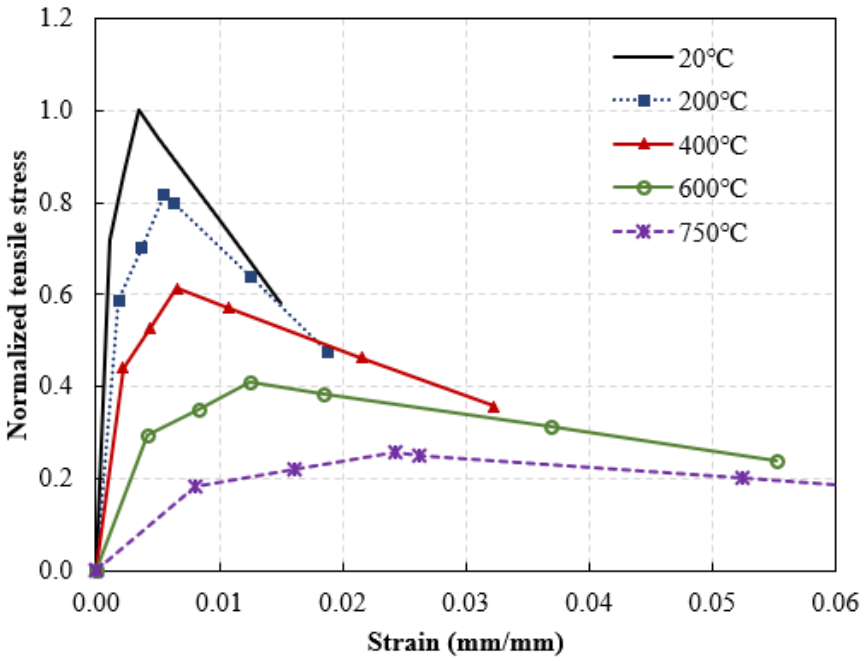

Figure 4.12. Stress-strain response at different temperatures (°C) of UHPC (with and without polypropylene fibers) under tension.

Previous studies in the literature have revealed that with the increase in the content of steel fibers, both compressive and tensile strength of UHPC increase, with inconsiderable alterations in elastic

modulus. To capture the effect of steel fiber content on strength properties of UHPC, relations proposed by Wu et al. [168] have been incorporated in this analysis:

$$f'_C = 121.25 + 61.73 * (SF) - 20.73 * (SF)^2 + 2.49 * (SF)^3 \quad (4\text{-}56)$$

$$f'_T = 4.7 + 0.15 * (SF) + 0.48 * (SF)^2 \quad (4\text{-}57)$$

where f'_C and f'_T are the compressive and tensile strength respectively of steel-reinforced UHPC (i.e. with non-zero steel fiber content) and SF is the steel fiber content by % of volume. As per the strength tests presented in Chapter 0, it was observed that the addition of 0.11% polypropylene (PP) fibers by volume led to slight reduction in the initial compressive strength of UHPC due to lower density and formation of weaker zones in the specimen. Previous studies have reported that with increase in PP fiber dosage, the risk of fire-induced spalling reduces but the compressive strength of concrete further reduces. For reliable fire resistance evaluation of members made with UHPC mix incorporating PP fibers, information on the corresponding compressive strength is required. Rasul et al. [169] proposed the following relation for the effect of PP fiber content on the compressive and tensile strength of UHPC based on results from their experimental study:

$$f'_{C-PP} = f'_C - 136.8 * (PPF) + 96.8 * (PPF)^2 \quad (4\text{-}58)$$

$$f'_{T-PP} = f'_T - 1.73 * (PPF) - 3.3 * (PPF)^2 \quad (4\text{-}59)$$

where $f'_{C\text{-}PP}$ is the compressive strength of UHPC with PP fibers, f'_C is the compressive strength of UHPC without PP fibers (with only steel fibers), $f'_{T\text{-}PP}$ is the tensile strength of UHPC with PP fibers (and steel fibers), f'_T is the tensile strength of UHPC without PP fibers, and PPF is the polypropylene fiber content by % of volume.

Along with data on tensile strength, information on permeability of concrete is critical for predicting fire-induced spalling in concrete. The initial gas permeability of undamaged concrete at room temperature is taken as 6.5×10^{-16} m^2, 2×10^{-17} m^2, and 2.3×10^{-18} m^2 for NSC, HSC, and

UHPC respectively based on the reported values from previous experimental studies [67,125,156,157]. In addition, when polypropylene (PP) fibers are added, permeability of concrete increases at temperatures above 160℃, i.e. after melting of polypropylene fibers. The increase in permeability after melting of PP fibers is related to the increase in fiber connectivity, depending on the dosage (or volume fraction) and the aspect ratio (length/diameter) of PP fiber [57,170]. Fiber connectivity results from the arrangement and percolation of fiber clusters which generate randomly according to their gradation [130,171–175].

Based on PP fiber percolation model developed by Tran et al. [176], concrete is treated as a composite of fibers and concrete matrix arranged in series or parallel with the fluid flow, and its permeability can be equated as:

$$k = pk_{fm}^{P} + (1 - p)k_{fm}^{NP} \quad (4\text{-}60)$$

where p= is the probability of percolation of fiber tunnels, k_{fm}^{P} corresponds to the combined permeability of fibers and concrete matrix when fiber tunnels and UHPC matrix are in parallel with fluid flow, and k_{fm}^{NP} corresponds to the combined permeability of fibers and concrete matrix when fiber tunnels and UHPC matrix are in series with fluid flow. The fiber percolation probability 'p' is dependent on PP fiber dosage (ϕ), length of fiber (l_f) and diameter of fiber (d_f), and can be modeled as:

$$p = \alpha\phi^{a} l_f^{b} d_f^{c} \quad (4\text{-}61)$$

where $\alpha=10^{-20}$, a=0.91, b=2.78, c=-5.37. These values are fitted by Li et al. [130] based on their experimental results. For the cases in which fiber tunnels are fully percolated (i.e. p=1) and not percolated at all (i.e. p=0) representing that fiber tunnels and UHPC matrix are in parallel and series respectively, k_{fm}^{P} and k_{fm}^{NP} are derived as [177,178]:

$$k_{fm}^{P} = \phi * k_f + (1 - \phi)k_m \quad (4\text{-}62)$$

$$k_{fm}^{NP} = \frac{1}{\frac{1-\phi}{k_m} + \frac{\phi}{k_f}} \quad (4\text{-}63)$$

where k_m = initial permeability of UHPC (matrix) without any PP fiber, and k_f = permeability of fiber tunnels can be expressed by the directional Poiseuille transport of fluids [179,180] along fiber tunnels as:

$$k_f(T) = h_f(T) * \frac{d_f^2}{32} \quad (4\text{-}64)$$

$$h_f(T) = (3.1 * 10^{-5} T^2) - 0.0087 * T + 0.69 \quad (4\text{-}65)$$

h_f (T) defines the incremental rise in permeability from the point of initial melting at 160℃ to complete burning of PP fibers at about 300℃. It should be noted that there is a lack of data on high-temperature mechanical properties with varying PP and steel fiber dosage. Hence, the room temperature test data and associated empirical relations were extended to high temperature for the analysis, based on the property tests undertaken as a part of this study (in Chapter 0).

Lastly, the material properties of concrete and steel during cooling phase are needed for modeling the response of RC beams under realistic fire exposure. These properties are calculated through modification of the temperature dependent material properties described above. The residual yield strength of the rebar primarily depends on the maximum temperature attained in the steel reinforcement. If the maximum temperature in reinforcing steel does not exceed 600°C, steel rebars exhibit a reversible behavior [181]. When temperature in steel rebar exceeds 600°C, the residual yield strength for reinforcing steel is calculated using the temperature-induced degradation trends reported by Neves et al. [182]. For concrete, a 10% loss in compressive and tensile strength is considered during cool down to room temperature, according to Eurocode 4 provisions [183]. Partial recovery in thermal strain of concrete is assumed based on test data reported in literature [184], whereas transient creep strain of concrete are irreversible and do not recover during cooling down [181]. Specific heat and thermal conductivity of concrete are taken as irreversible as these

thermal properties mainly depend on moisture of concrete and water is not re-condensed in concrete during cooling phase [185]. The residual properties of concrete are adopted from studies on conventional concrete types as currently, there is a lack of residual test data and residual property relations for UHPC subjected to cooling phase.

4.4.3. Validation under Ambient Conditions

To establish validation of the developed model at room temperature, predicted load-deflection response at mid-span of beam U-B3 is compared to the measured response in Figure 4.13 (a). Beam U-B3 exhibited a linear elastic load-deflection response until initial cracking occurred in concrete at an applied loading of 26 kN. In the post-cracking stage, deflection increased at a higher rate due to a reduction in stiffness of the beam resulting from an increased number of cracks and their progression. As a result of higher cracking in concrete, stresses in steel reinforcement bars increased at a faster rate and the rebars yielded at an applied loading of 81 kN. After the yielding of steel rebar, beam U-B3 endured strain hardening with an increase of load-carrying capacity till reaching the peak load. From Figure 4.13 (a), it can be observed that the peak load is predicted by the model as 100 kN, which is very close to the measured peak load of 97 kN. The attainment of peak load is followed by a rapid rise in deflection owing to the softening of concrete till failure of the beam. Compared with the measured response, the predicted post-peak load-deflection response of beam U-B3 is slightly stiffer which can be attributed to variations involved in the adaptation of the geometry of the beam and the softening response of UHPC and steel rebars in the numerical model.

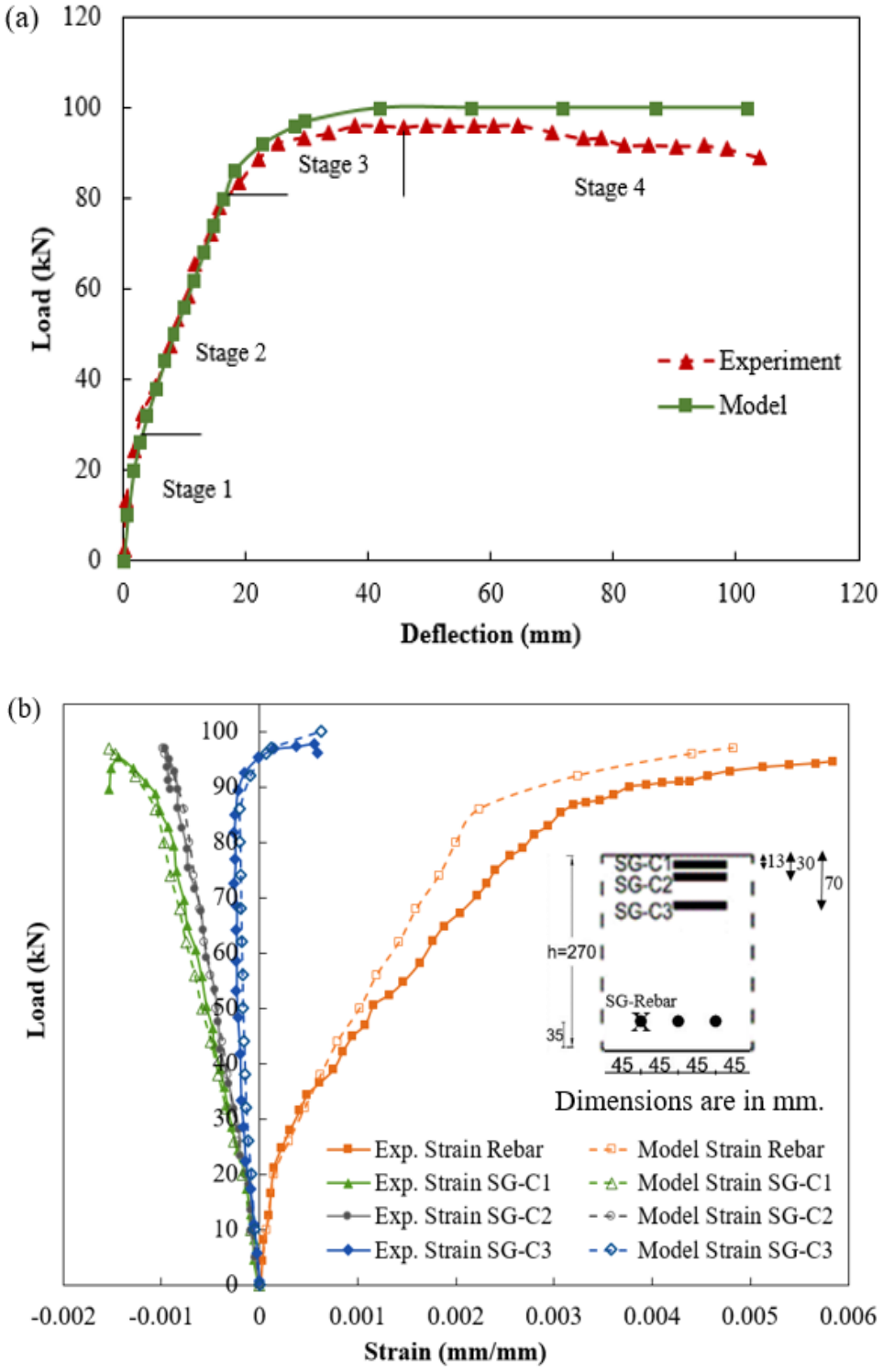

Figure 4.13. Comparison of predicted and measured (a) load-deflection, (b) load-strain response of UHPC beam U-B3 under ambient conditions.

Further, the predicted load-strain response of beam U-B3 is compared in Figure 4.13 (b) with the measured strain values from strain gauges installed at various concrete depths and on steel rebar. The positive values of strain imply compression and the negative values of strain denote tension respectively. The strain gauges SG-C1 and SG-C2, placed in proximity to the top compression layers of the beam, measured consistently increasing compressive strains during the entire loading. The strains recorded by strain gauge SG-rebar, mounted on corner rebar, were increasing tensile strains throughout the loading. Strain gauge SG-C3, placed at 70 mm from the top surface of beam U-B3, recorded transition of strains from compressive to tensile. The transition of strains implies neutral axis shifting which is due to the combined effects of cracking of concrete and increase in internal forces within the beam with an increase in applied loading (moment). Figure 4.13 (b) shows that the load-strain response predicted by the model follows closely with the test data throughout the depth of the beam during the entire loading range. Only the predicted load-strain response of rebar shows deviation with measured response at higher strain values which can be attributed to the slight variation in the exact locations of strain gauges in the model as compared to the experiment due to restrictions associated with model discretization. The comparison of predicted response parameters shows that the developed numerical model can be utilized to predict the response of UHPC beams at ambient conditions.

4.4.4. Validation under Fire Conditions

The validity of the developed model under fire conditions is established by comparing thermal, structural, and spalling response predictions from the numerical model for each beam with the measured data from fire tests.

4.4.4.1. Thermal Response

As part of thermal response validation, the measured and predicted temperatures at various cross-sectional locations in the UHPC beams U-B1, U-B2, U-B10, and U-B11 are compared in Figure 4.14. While beams U-B1, U-B2, and U-B10 were subjected to “design fire 1” without a cooling or decay phase, beam U-B11 was subjected to “design fire 2” with a cooling phase. Thus, the rebar and concrete temperatures in UHPC beams U-B1, U-B2, and U-B10 increase consistently throughout the fire exposure time, whilst cross-sectional temperatures in U-B11 increase to a maximum temperature and then decrease. In all four beams, the predicted and measured temperatures at locations closer to the fire-exposed sides, are higher than the interior concrete layers farther from the exposed surface. This can be attributed to low thermal conductivity and high specific heat of concrete that delays heat penetration to the inner concrete layers [186]. The predicted and measured temperatures for the UHPC beams plotted in Figure 4.14 follow closely except for some discrepancies which are discussed below.

For all the analyzed beams, slightly higher temperatures are predicted by the model, making temperature predictions slightly conservative. The marginal variation between predicted and measured temperatures can be attributed to variation in the actual extent of spalling during the fire test and the predicted spalling in the analysis. Some undulations in the form of peaks can be seen in the sectional temperature trends of beam U-B1 at quarter depth and mid-depth from the bottom exposed surface, potentially due to sudden temperature rise resulting from loss of cross-section due to localized spalling taking place in U-B1 at the sides of the beam. The current numerical model was not able to capture these abrupt temperature undulations, however, the temperature predictions for beam U-B1 were in range with the reported data. These temperature protuberances

were not present in the measured temperature trends of the other UHPC beams due to lower levels of spalling experienced by them as compared to beam U-B1.

For beam U-B11, the model predicts a faster descend in temperatures than the measured ones during the cooling phase of the fire exposure. This can be attributed to the differences in the residual thermal properties of UHPC used for the analysis with the actual property variation, due to the lack of data on the thermal properties of UHPC in the cooling phase. Overall, predicted and measured temperature trends match reasonably well and temperatures are close to each other for the beams and thus, the model is deemed to be capable of capturing the thermal response. The thermal gradients developed in the cross-section due to the temperature variation within the beam section under fire exposure play a key role in characterizing thermo-mechanical and the spalling response of the beam.

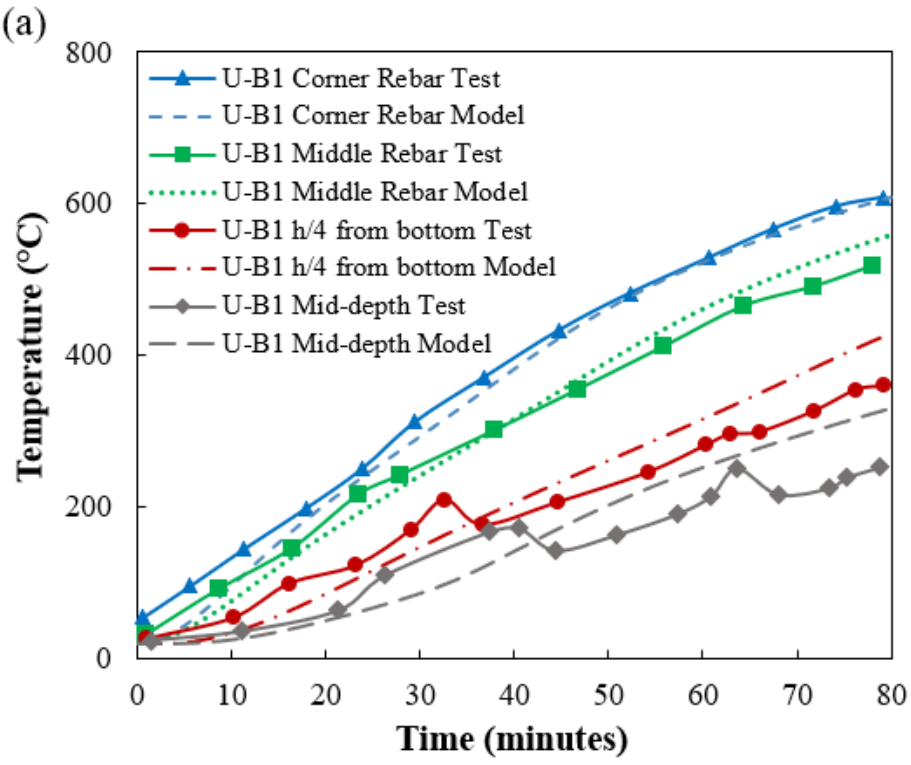

Figure 4.14. Comparison of predicted and measured temperatures for UHPC beams: (a) U-B1; (b) U-B2; (c) U-B10; (d) U-B11.

Figure 4.14. (cont'd)

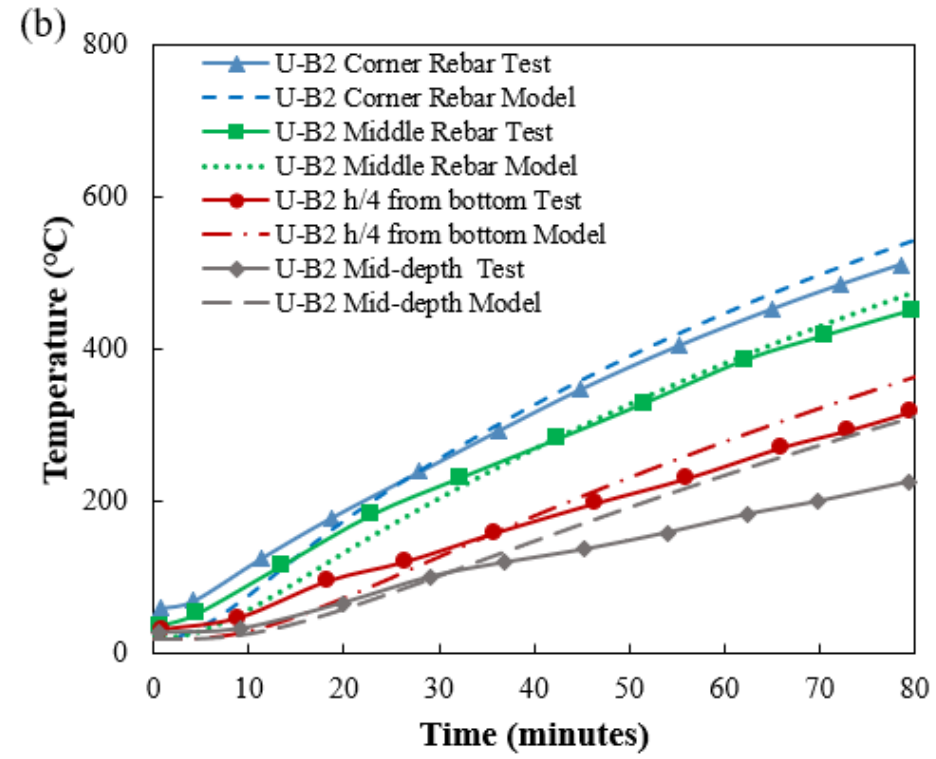

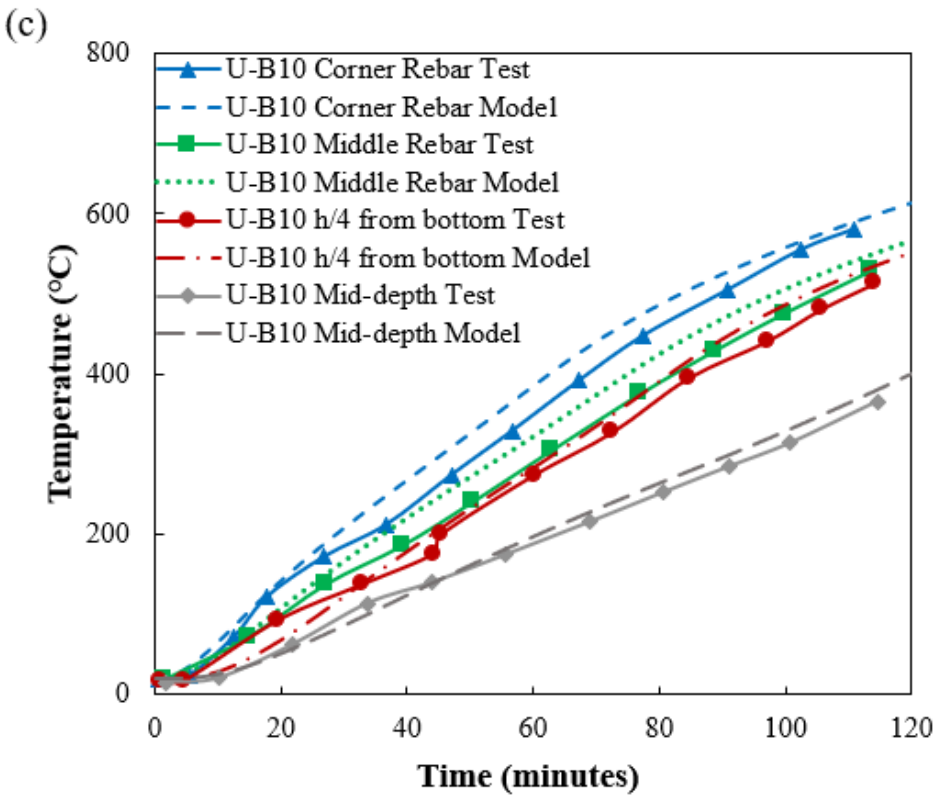

Figure 4.14. (cont'd)

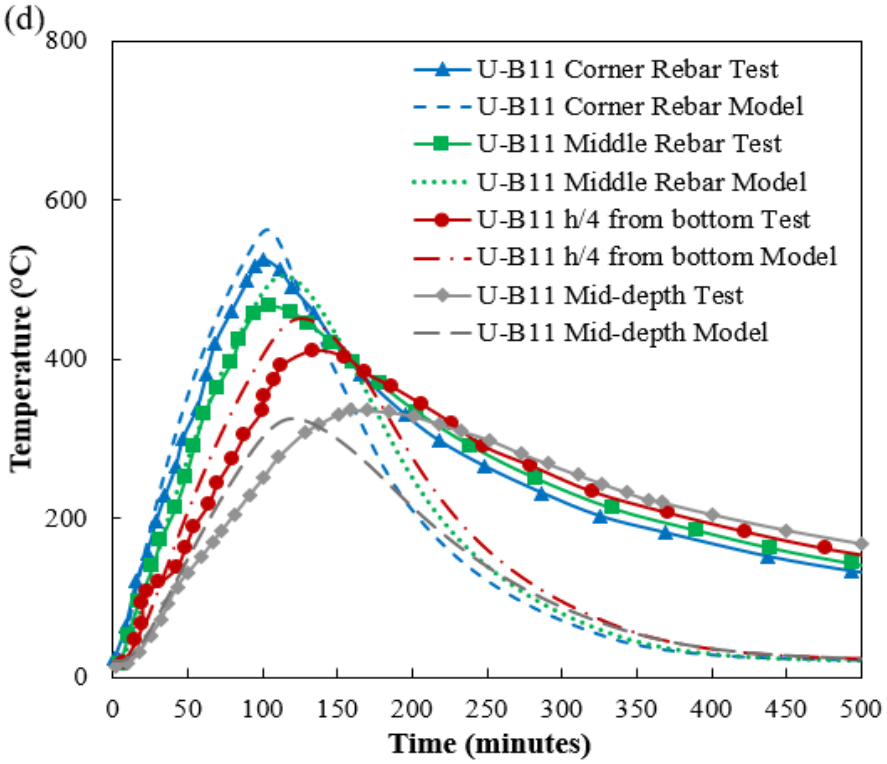

Figure 4.15 shows a comparison of predicted and measured temperatures as a function of fire exposure time at corner rebar for the analyzed UHPC beams U-B1, U-B2, U-B10, and U-B11. The temperature rise in the beams with polypropylene (PP) fibers (U-B10 and U-B11) occurs at a slower rate than the beams without PP fibers (U-B1 and U-B2). Polypropylene fibers in beams U-B10 and U-B11 helped to mitigate spalling and minimized loss of cross-section during fire exposure, thereby slowing down temperature rise in the interior of the section. The rapid rise in sectional temperatures in UHPC beams without PP fibers (U-B1 and U-B2) after the first 10 minutes of a fire is due to the occurrence and progression of spalling, which led to the loss of cross-section and in turn exposed interior layers to increasing heating. Among the beams without PP fibers, the temperature rise is at a higher pace in beam U-B1 (subjected to lower load level) as

compared to beam U-B2 due to a higher level of spalling in U-B1; further discussion on spalling results is laid out in the following sections.

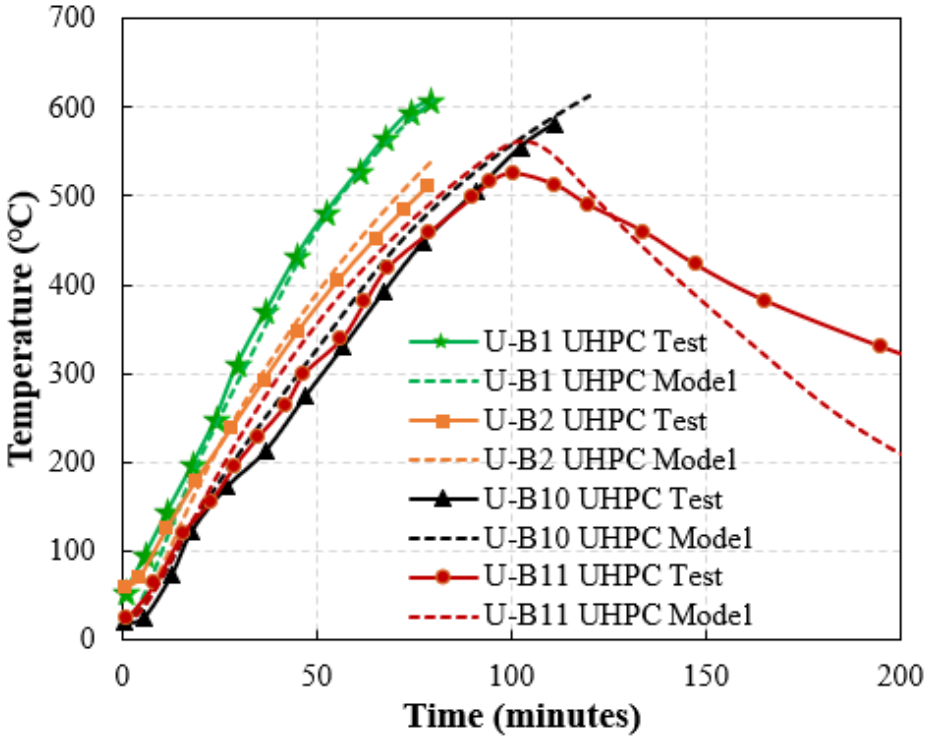

Figure 4.15. Measured and predicted corner rebar temperatures as a function of time for UHPC beams.

The model is also validated for beams made using other concrete types, namely, normal strength concrete (NSC) beam B1 and high strength concrete (HSC) beams B3 and B5 tested by Dwaikat and Kodur [11]. A comparison of predicted and measured temperatures at corner rebar locations in beams B1, B3, and B5 is shown in Figure 4.16. The plotted trends in the figure show that there is a good agreement between the measured and the predicted temperatures for all beams. A closer look at test data for the two HSC beams shows that slightly higher rebar temperatures were predicted for HSC beam B5 as compared to HSC beam B3. This is because beam B5 was subjected to "Design Fire 3" with high severity and also this beam experienced higher levels of spalling than the other HSC beam, B3 (subjected to ASTM E119). Further, the predicted rebar temperatures in HSC beams are marginally higher than that in NSC beam B1, due to the higher thermal

conductivity of HSC. Due to high compressive strength of UHPC, the beams made of UHPC have smaller cross-sections (lower thermal mass) as compared to beams made of NSC and HSC. Additionally, UHPC has higher thermal conductivity than NSC and HSC. Therefore, although the UHPC beams were subjected to fire exposure scenarios with lower fire severity, a comparison of Figure 4.15 and Figure 4.16 shows that the sectional temperatures in all the UHPC beams were higher as compared to NSC and HSC beams.

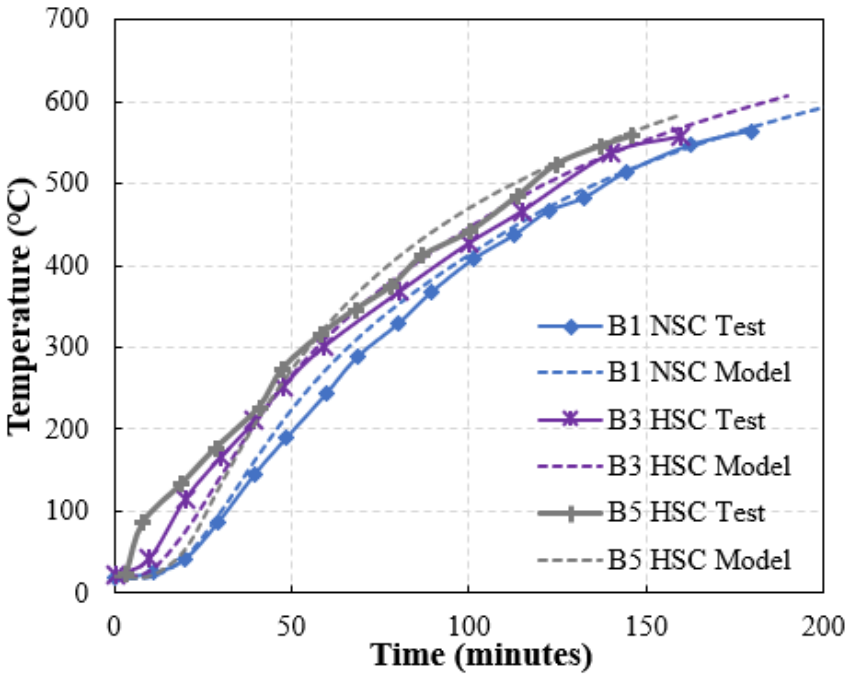

Figure 4.16. Measured and predicted corner rebar temperatures as a function of time for NSC and HSC beams.

4.4.4.2. Spalling Response

The validity of the spalling predictions is established by comparing spalling progression (time at which spalling started and stopped) and its extent, with the measured values from fire tests. The progression of spalling was recorded during the fire test, by making visual observations through the windows of the furnace. Also, the extent of spalling in beams was measured by taking measurements of remaining concrete in beams after the completion of fire test [96]. The measured and predicted extent of spalling at the end of fire tests are presented in Table 4-1. In the case of

NSC beam B1 and HSC beam B3, the extent of spalling is minimal (1.5 and 3.3% respectively) and most of this occurred as “late spalling”, just prior to failure (as observed through furnace windows). As discussed earlier, late spalling has a minor influence on the overall fire response of concrete members [91]. Thus, the spalling response for the beams, which experienced spalling at early and intermediate stages of fire exposure are compared. It should be noted that among all the beams, NSC beam did not experience much spalling.

The extent of spalling in HSC (B5) and UHPC (U-B1, U-B2, U-B10, and U-B11) beams is plotted as a function of fire exposure time in Figure 4.17. In the reported test data, the extent of spalling was assumed to vary linearly between start and stop time of spalling, as it is not possible to measure exact spalled volumes real-time during the fire test. Additionally, the spalling pattern was not uniform throughout the length of the beam; thus, even the volumetric measurements of spalling at the end of the tests were difficult to obtain with high accuracy. Similar to the test, the volumetric amount of spalling from the model was non-uniform along the length of the beam; hence, the average value of the extent of spalling is calculated. Therefore, the plotted comparison in Figure 4.17 is more of a qualitative assessment.

From Figure 4.17, it can be seen that for HSC beam B5, the model predicts spalling to start at about 16 min and to stop at 32 min after fire exposure. The measured start and end times of spalling were 10 and 35 min after fire exposure, respectively. For the UHPC beams without polypropylene fibers (U-B1 and U-B2), the visual observations recorded in the test indicated that early spalling occurred from 10 to 40 min, and intermediate spalling followed between 60 to 70 min of fire exposure. The predicted times for start and end of spalling were 16 and 33 min for beam U-B1, and were 12 and 31 min for beam U-B2. For the UHPC beams with polypropylene fibers (U-B10 and U-B11), the measured start and end times of spalling were 10 and 40 min, with higher intensity

of spalling in 20 to 40 min after fire exposure. The predicted times for start and end of spalling were 18 and 30 min for beam U-B10, and were 24 and 36 min for beam U-B11. The program estimates the start time of spalling with adequate accuracy for all the beams but there is a variation between the predicted and the measured end time of spalling for the UHPC beams U-B1 and U-B2. Nonetheless, this variation might be admissible as the predictions for the associated response parameters: amount of spalling, failure time, and thermomechanical response are within close range of the measured data. However, the spalled volume compared in Table 4-1 is fitting from a qualitative point. The model predicts slightly higher extent of spalling for B5, U-B1, and U-B2, which is reasonably a conservative estimate. As compared to UHPC beams without polypropylene fibers, lower spalling is predicted in UHPC beams with polypropylene fibers due to the release of pore pressure and increase in permeability through melting of polypropylene fibers.

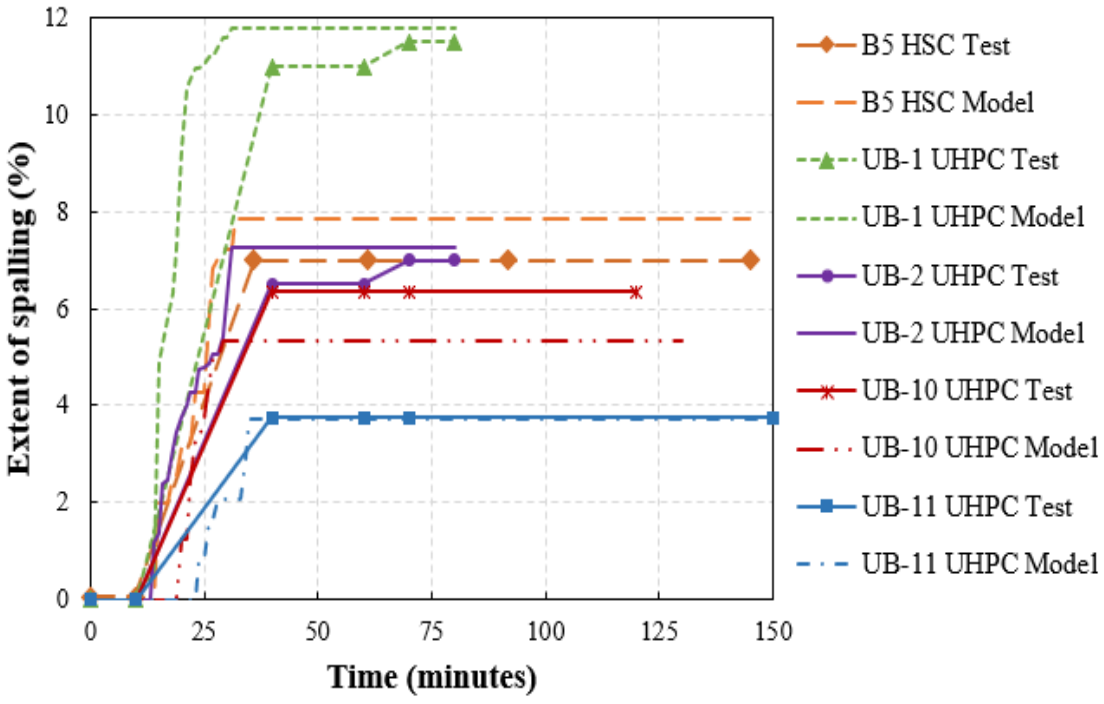

Figure 4.17. Measured and predicted extent of spalling for the analyzed beams.

In order to further investigate the spalling response, the variation of computed pore pressure at mid-span section of different concrete beams is plotted in Figure 4.18 at 40 mm from the exposed right surface and 0.15 times of section depth from top surface i.e. 60 mm depth for NSC/HSC beam and 40 mm depth for UHPC beam. From Figure 4.18, it can be observed that pore pressure increases with fire exposure time, reaches a peak value, and then drops with further increase in time. When concrete member is heated, the moisture in concrete evaporates and a portion of this moisture migrates into the inner layers of concrete. This migrated water vapor undergoes condensation and results in saturation of concrete microstructure, which in turn prevents further moisture migration and leads to an increase in pore pressure. As the temperature in inner concrete layers increases with fire exposure time, the drying zone near the exposed surface increases resulting in a decrease in pore pressure after reaching a peak. In addition to concrete drying, a drop in pore pressure can be attributed to release in pressure because of cracking and spalling of concrete.

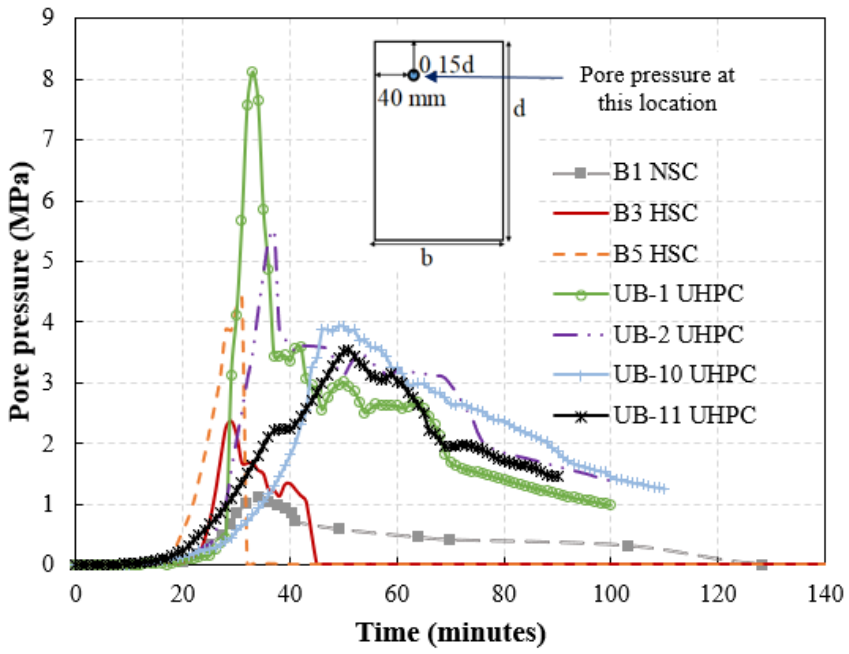

Figure 4.18. Comparison of predicted pore pressure as a function of time in NSC, HSC, and UHPC beams.

Because of high permeability in NSC, much of the vapor oozes out and only low levels of (pore) pressure build up in the NSC beam, with a peak pressure of around 1 MPa at 34 min into fire exposure. However, higher pore pressure develops in the HSC and UHPC beams, and this is attributed to their dense microstructure and lower permeability that hinder the vapor pressure to escape. As a result, a peak pore pressure of about 4.5 MPa develops in HSC beam at 30 min into fire exposure and a much higher peak pore pressure of 8 MPa develops in UHPC beam without polypropylene fibers at 35 min into fire exposure. A peak pore pressure of 4 MPa develops in UHPC beam with polypropylene fibers, which is lower than that developed in UHPC beams without polypropylene fibers, and can be attributed to the benefit accumulated by enhanced permeability through melting of polypropylene fibers at 160°C and the formation of microchannels in concrete that help disperse pore pressure buildup. It should be noted that it is not feasible to measure pore pressure during fire tests due to lack of measuring techniques and sensors that can withstand high temperatures and precisely measure pore pressure without leakage. However relative pore pressure predictions plotted in Figure 4.18 are in line with the expected trends and can be used to draw inferences on the effect of concrete type on spalling specifically. The analysis results further indicate that the accumulated fire-induced pore pressure is highly dependent on the permeability and microstructure of the specific concrete type.

The evolution of different stresses resulting from pore pressure, temperature, and loading during fire exposure and its effect on the occurrence of spalling is studied. RC beams made of HSC (B5) and UHPC (U-B1), are selected for a relative comparison. The predicted spalling at the end of fire exposure along the length together with the observed view of the beams after fire tests, is plotted in Figure 4.19 (a) and Figure 4.19 (b) for UHPC and HSC respectively.

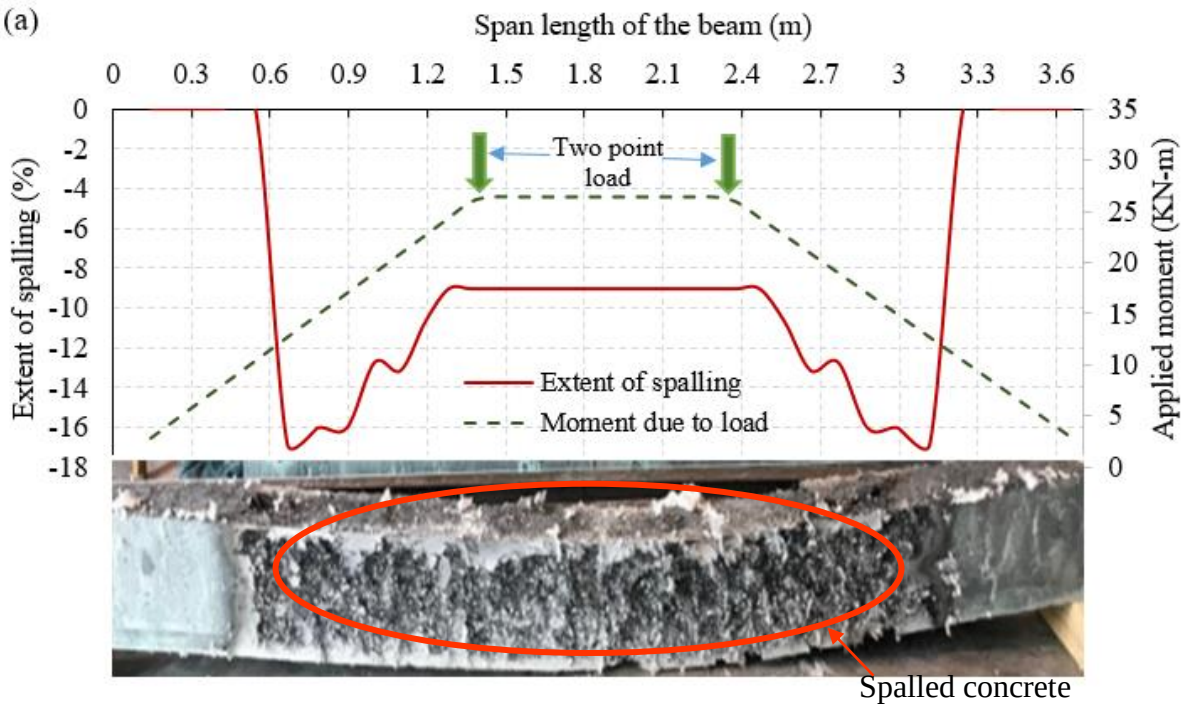

UHPC beam U-B1 after fire test

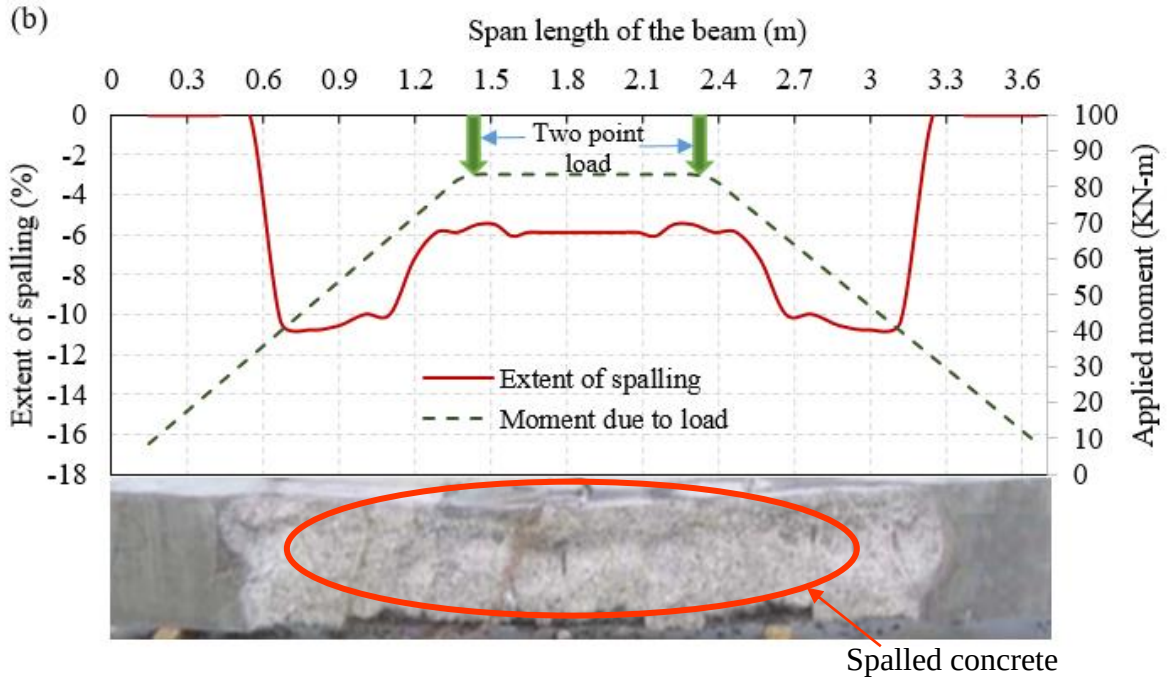

HSC beam B5 after fire test

Figure 4.19. Spalling predictions along the length of the beam: (a) UHPC U-B1; (b) HSC B5.

As can be seen, there is no spalling in the unexposed length at the end portions of the beam, which is on expected lines. It can be observed that the spalled cross-section of the beams after fire tests is non-uniform along the length. The predicted extent of spalling at various segments along the length of the beam is in the range of about 9 to 16% in the UHPC beam and around 6 to 10% in the HSC beam. Upon comparison of the beams after the fire test in Figure 4.19, it can be seen that while the corners in the tested UHPC beam are roughly intact, the corners of the HSC beam after fire test have fallen-off. Falling-off of corners, termed as corner spalling, takes place in the later stages of fire exposure and does not give rise to unforeseen loss of sectional (moment) capacity [138,187].

When there is no loss in cross-section of the beam due to spalling, the boundary exposed to fire does not change along the entire length of the beam. However, the bending moment for a given applied loading is different along the beam length even if the entire section is intact. Therefore, the distribution of thermal and pore pressure stresses remains same along the beam length but the varying bending moment results in a non-uniform distribution of mechanical stresses; which also lead to an irregular load-induced cracking pattern. The segments close to mid-span of the beam are subjected to higher mechanical stresses due to higher bending moment, which in turn enhances cracking and then increase permeability. The increased permeability results in lower pore pressure and relatively lower extent of spalling. The applied moment decreases in the segments away from the mid-span, which in turn results in lower cracking and lower permeability leading to higher extent of spalling in these segments. At each time step, if spalling occurs, the spalled elements are removed and as a result in the subsequent time steps, distribution of temperatures, pore pressure and stresses will be much different, leading to an irregular pattern of spalling in the beams. To

further illustrate this phenomenon, the distribution of temperature, pore pressure and stresses at mid-span in the selected HSC and UHPC beam at a given fire exposure time is analyzed.

Mechanical stress distribution due to structural loading in the longitudinal direction (at room temperature) is plotted for UHPC beam U-B1 in Figure 4.20 (a) and for HSC beam B5 in Figure 4.21 (a). Due to applied loading, compressive stresses develop at the upper section of the beam while tensile stresses develop at the bottom section. The predicted sectional temperatures after 15 minutes into fire exposure are shown in Figure 4.20 (b) and Figure 4.21 (b) for UHPC and HSC beams respectively. The temperatures and associated thermal gradients are higher in HSC beam B5 as compared to UHPC beam U-B1 due to a higher rate of heating under severe fire scenario in beam B5. In Figure 4.20 (c) and Figure 4.21 (c), the respective pore pressure distributions at 15 minutes are compared in beams U-B1 and B5. Tensile stress resulting from pore pressure (σ_p), as shown in Figure 4.20 (c) and Figure 4.21 (c), is higher in UHPC beam U-B1 (5.3 MPa) as compared to HSC beam B5 (2.5 MPa) at 15 min. This higher σ_p in beam U-B1 can be attributed to lower permeability and dense microstructure in UHPC. Further, the permeability in lower portions of the HSC beam B5 tends to be higher as it experienced higher tensile cracking induced by higher levels of applied load (63%), as compared to UHPC beam U-B1 subjected to a lower load level (40%). In both the beams, pore pressure accumulation is in the interior elements lying in inner concrete layers at some depth from the heated surface, whereas the boundary layers have low pore pressure. This clearly indicates that pore pressure alone does not cause spalling, but additional tensile stress in the transverse direction (resulting from thermal gradients and structural loading) is required for spalling to occur.

(a) Mechanical stress contours at room temperature

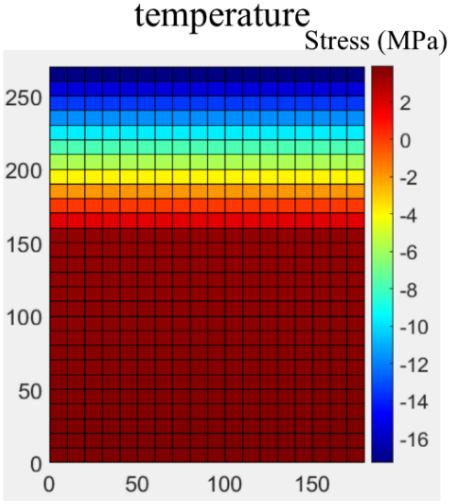

(b) Temperature contours at t=15 minutes

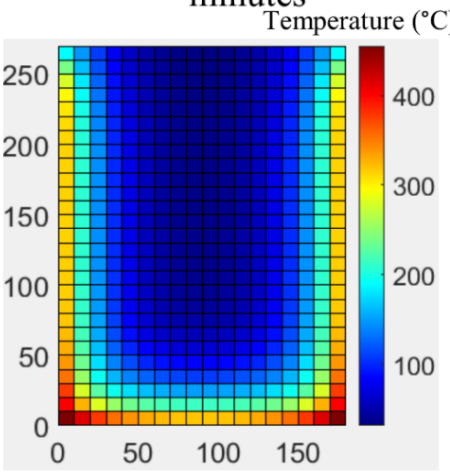

(c) Pore pressure stress at t=15 minutes

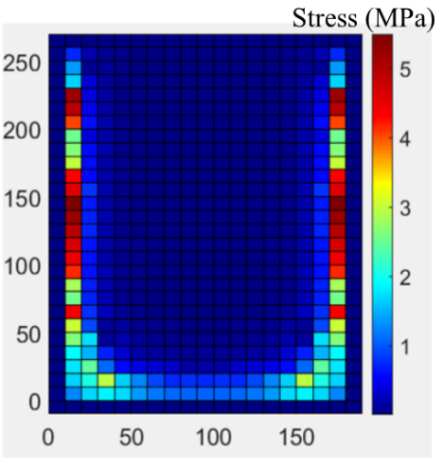

(d) Mechanical load induced transverse stress at t=15 minutes

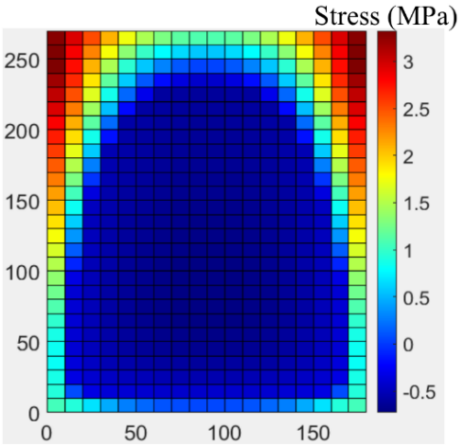

(e) Temperature induced transverse stress at t=15 minutes

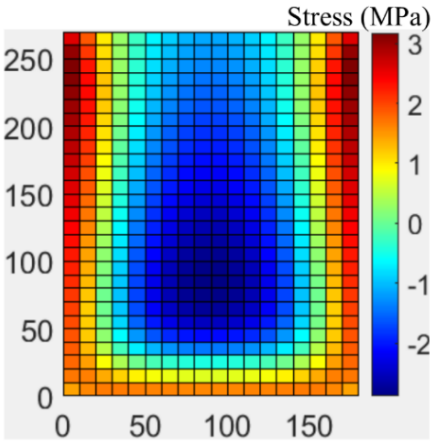

(f) Final spalled UHPC beam section

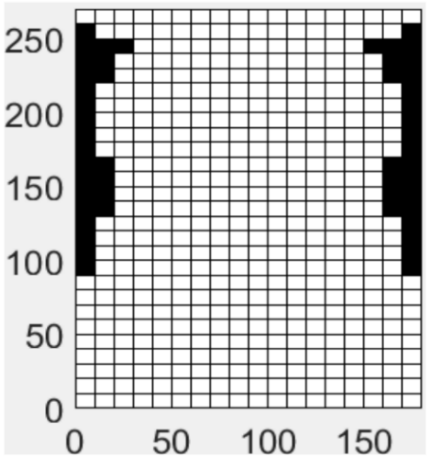

Figure 4.20. Cross-sectional analysis results at mid-span for UHPC beam U-B1.

(a) Mechanical stress contours at room temperature

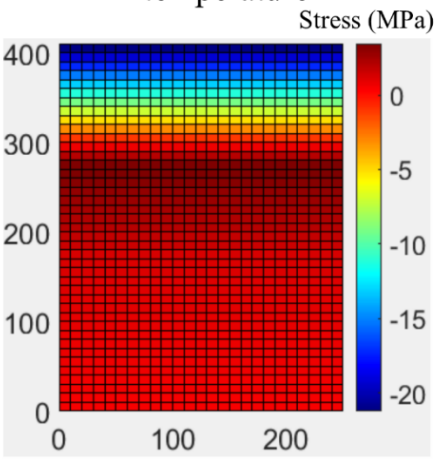

(b) Temperature contours at t=15 minutes

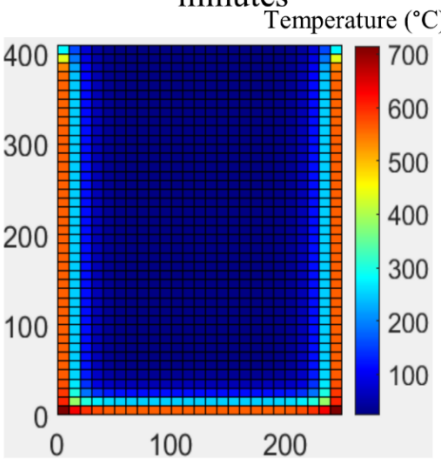

(c) Pore pressure stress at t=15 minutes

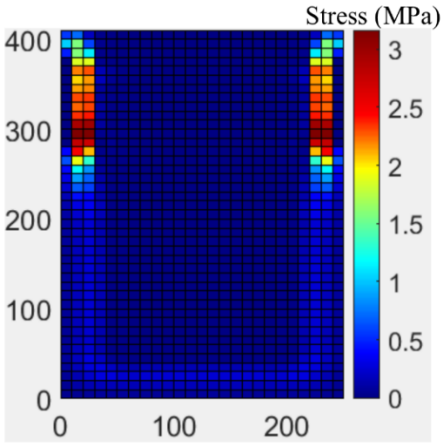

(d) Mechanical load induced transverse stress at t=15 minutes

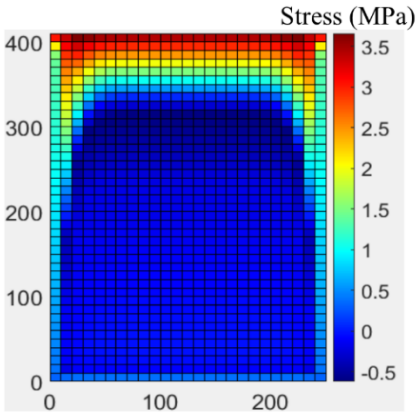

(e) Temperature induced transverse stress at t=15 minutes

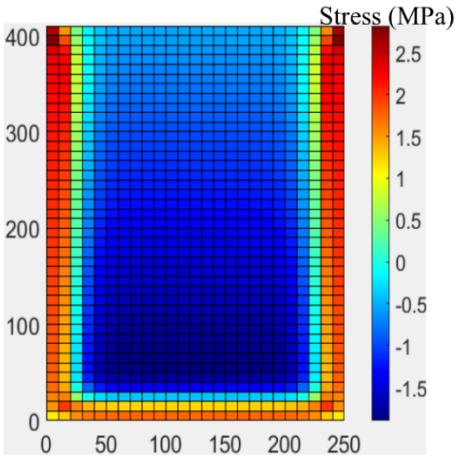

(f) Final spalled HSC beam section

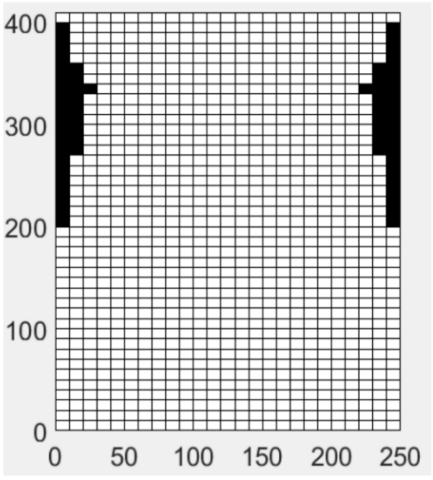

Figure 4.21.Cross-sectional analysis results at mid-span for HSC beam B5.

With an increase in fire exposure time, mechanical stress (σ_{me}) increases as a result of the applied structural loading and temperature-induced strength degradation in concrete and rebars. For beams U-B1 and B5, the load-induced mechanical stress (σ_{me}) distribution in the transverse direction is plotted in Figure 4.20 (d) and Figure 4.21 (d) respectively. It can be seen from the figure that σ_{me} is tensile in the upper portions on the sides of both the beams, including outer layers (boundary elements) where stress due to pore pressure is minimal. Thus, the effect of σ_{me}, together with stress due to pore pressure induces fracture in the heated concrete layers. Further, mechanical stress has a two-fold impact on the spalling and overall fire response of concrete beams. On one hand, higher σ_{me} induces a higher level of cracking and relieves some of the pore pressure, while on the other hand; higher σ_{me} generates higher transverse tensile stresses that aid in spalling.

In Figure 4.20 (e) and Figure 4.21 (e), the variation of temperature-induced tensile stress (σ_{th}) in the transverse direction is plotted for UHPC beam U-B1 and HSC beam B5. In both the beams, the induced σ_{th} is tensile in the heated boundary layers on the three exposed sides. If spalling were assumed to occur with consideration to only σ_{th}, the outer concrete layers would spall from both sides and the bottom surface of the beam cross-section, thus estimating a high spalled cross-sectional area, which is not realistic as per observations in fire tests or real fire incidents. Thus, high levels of thermal and mechanical stresses contribute to the progression of spalling, initiated by stresses due to pore pressure. For the evaluation of realistic spalling of a beam, all three stresses have to be considered. For UHPC beam U-B1 and HSC beam B5, the final (at the end of the analysis) spalled cross-section at mid-span is plotted in Figure 4.20 (f) and Figure 4.21 (f), respectively. Spalling was predicted to occur mainly in the upper portions of the beams and the calculated extent of spalling at mid-span in UHPC beam was 9%, whereas in HSC beam was 6%, which is close to the reported test data shown in Table 4-1. Higher spalling occurred in UHPC

beam as compared to HSC beam and this can be attributed to higher permeability in HSC due to higher load-induced cracking and less compact microstructure than UHPC.

4.4.4.3. Structural Response

The structural response of the beams is validated by comparing mid-span deflection generated from the analysis with measured deflection for UHPC beams in Figure 4.22, and for NSC and HSC beams in Figure 4.23. Under fire conditions, the deflections in a beam result from the effects of thermal expansion, degradation of material properties, and high temperature creep. Further, any loss of cross-section due to spalling can reduce the overall stiffness and increase levels of deflection. Overall, the model predictions are in good agreement with deflections measured in fire tests.

Among the UHPC beams that experienced failure (U-B1, U-B2, and U-B10) in Figure 4.22 (a), the rate of increase in deflection was slower in beam U-B10 as compared to beams U-B1 and U-B2. This can be attributed to the slower degradation of stiffness due to reduced loss of concrete section through spalling mitigation facilitated by the melting of polypropylene fibers present in beam U-B10. Among the beams without PP fibers, in the final stage of fire exposure (prior to failure), the rate of increase in deflection is significantly higher in U-B1 than U-B2, despite being subjected to lower load level (40%) than beam U-B2 (60%), and this is because beam U-B1 experienced higher spalling as compared to beam U-B2. The other UHPC beam with PP fiber, U-B11 sustained during fire exposure and subsequent cooling of fire exposure without failure as shown in Figure 4.22 (b). The level of recovery in U-B11 during cooling phase is governed by rate of decay in fire temperature, load level, and extent of spalling. The trend of predicted recovery in mid-span deflection agrees well with the measured response during fire tests, however, some

discrepancies in the final deflection can be observed due to the lack of reliable mechanical properties data for UHPC during cooling down.

Upon comparison with the progression of deflections in NSC and HSC beams in Figure 4.23, it can be seen that the mid span deflections in UHPC beams increase at a higher rate with time. The higher deflection in the UHPC beams resulted from lower capacity due to smaller cross-section along with faster degradation of strength and modulus properties of UHPC with temperature, as well as loss of concrete cross-section resulting from severe spalling. A comparison of deflections of the two HSC beams (B3 and B5) shows that beam B5 experienced higher mid-span deflection than beam B3. Deflection increased at a faster rate in beam B5 due to higher spalling resulting from higher load level, and severe fire exposure ("Design Fire 3"). Beam B1 (NSC) exhibited a gradual rise in deflection throughout the entire duration of fire exposure, and its deflection is lower than that of the other HSC and UHPC beams. The lower deflection in NSC beam B1 can be attributed to slower degradation in strength and modulus properties of concrete, as well as an almost negligible amount of spalling.

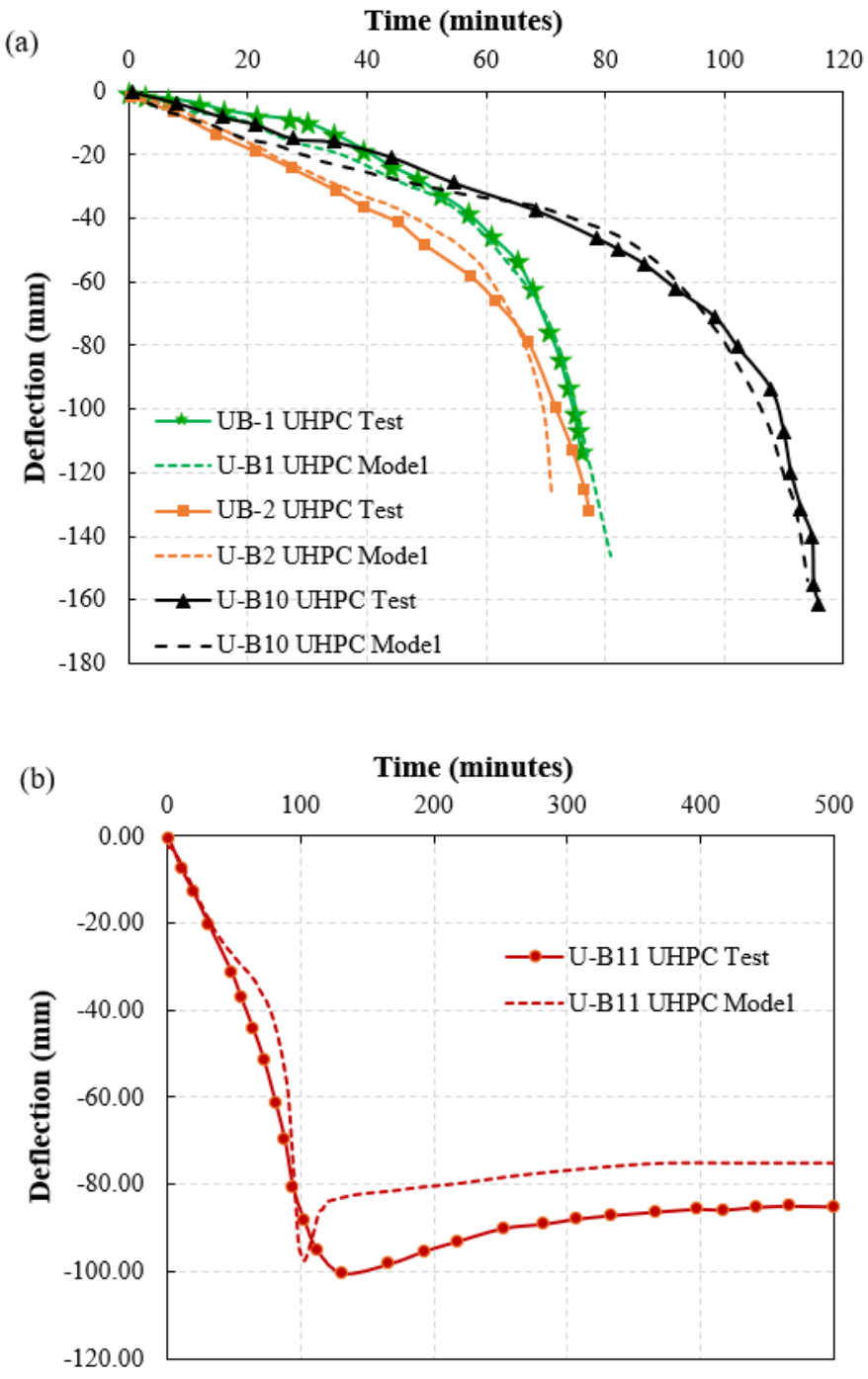

Figure 4.22. Measured and predicted mid-span deflections of UHPC beams.

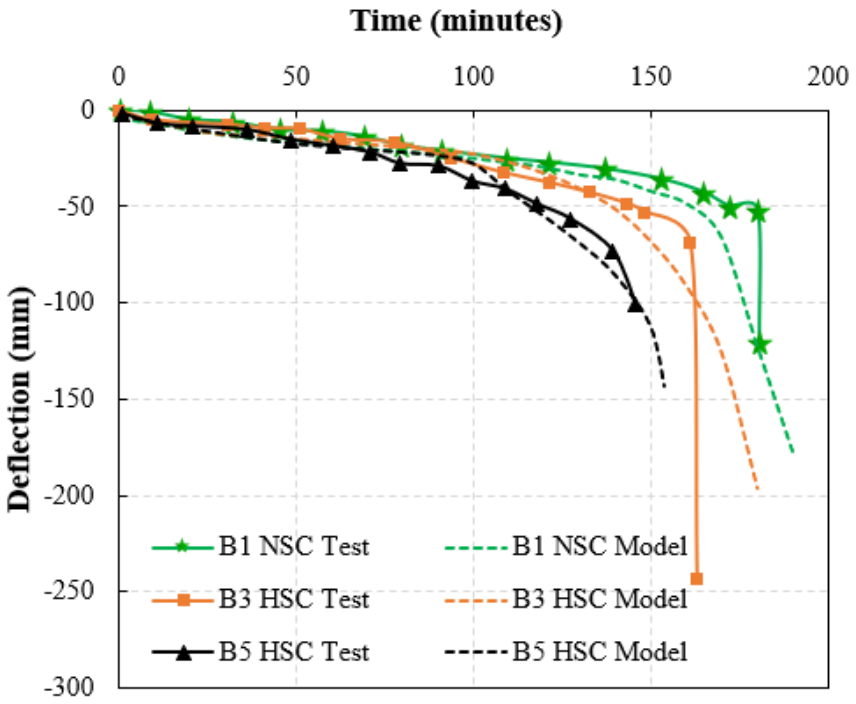

Figure 4.23. Measured and predicted mid-span deflections of NSC and HSC beams.

4.4.4.4. Fire Resistance

The fire resistance or failure time of the beams from the model is compared with the measured fire resistance values in Table 4-1. The failure time is evaluated by applying the strength and deflection failure criteria [11,188]. The deflection criteria governed the failure for all the analyzed beams. For NSC beam B1, the measured failure time (fire resistance) was 180 minutes and the predicted value was 175 minutes. For HSC beams B3 and B5, the measured fire resistances were 160 and 146 minutes, while the predicted fire resistances were 162 and 142 minutes, respectively. For UHPC beams without PP fibers, U-B1 and U-B2, the measured fire resistances were 75 and 78 minutes, while the predicted fire resistances were 82 and 73 minutes, respectively. For UHPC beam with PP fiber, U-B10, the measured fire resistance was 114 minutes and the predicted value was 112 minutes. Beam U-B11, which was subjected to a fire scenario with a well-defined cooling phase (Design Fire 2), did not endure failure in the model predictions and the fire test. All the

predicted fire resistances of the beams that failed are within 10% of the measured values, thus indicating that the model yields a reasonable prediction of failure times in RC beams made of different concrete types.

The extent of spalling has a significant influence on failure time as can be seen in Table 4-1. The fire resistance of beam B1 (NSC) was much higher in comparison to HSC and UHPC beams. This can be mainly attributed to the faster degradation of strength and modulus properties with temperature in HSC and UHPC, as well as the occurrence of fire-induced spalling. Spalling reduces the cross-sectional area of the concrete and thus the moment capacity and stiffness of the beam. Therefore, spalling can result in early failure and lower fire resistance in RC beams. Among the HSC beams, the slightly lower fire resistance of HSC beam B5 as compared to similar HSC beam B3 can be attributed to the higher load level and higher extent of spalling in B5, resulting from severe fire exposure. The fire resistance of the UHPC beams U-B1 and U-B2, made without polypropylene fibers was much lower than that of the beam U-B10, with polypropylene fibers. The higher fire resistance of beam U-B10 is owing to minimization of spalling by enhanced permeability through melting of polypropylene fibers. A comparison of the UHPC beams without PP fibers, subjected to same fire exposure ("Design fire 1") show that the beam U-B2 had similar fire resistance as beam U-B1, despite being subjected to higher load level (60%) than beam U-B1 (40%), and this can be attributed to lower spalling in beam U-B2 as compared to U-B1. When a concrete beam is subjected to high levels of load, permeability in concrete increases due to higher load-induced cracking, which in turn lowers the extent of spalling through some dissipation of pore pressure. Therefore, beam U-B2 had a lower loss of cross-section from reduced spalling, resulting in a similar failure time as beam U-B1.

4.5. Summary

In this Chapter, a stress-based numerical procedure for evaluating spalling is presented. This approach is incorporated as a spalling sub-model into a macroscopic finite element based model that is capable of tracing the thermo-mechanical response of RC beams from pre-cracking stage to collapse under fire conditions. The analysis predictions, namely temperature, deflection, and extent of spalling are compared against the measured values from full-scale fire resistance tests on RC beams made with different concrete types of varying strengths. Based on the results presented in this Chapter the following conclusions can be drawn:

- The proposed numerical procedure can be applied for predicting fire-induced spalling, and also fire resistance of RC beams made of different concrete types namely NSC, HSC, and UHPC made with only steel fibers, and UHPC with steel and polypropylene fibers.
- The proposed numerical procedure for evaluating spalling in RC beams takes into account stresses resulting from structural loading and thermal gradients, in addition to stresses arising from pore pressure.
- Fire-induced spalling is influenced not only by the stresses resulting from pore pressure but also by the stresses induced due to thermal gradients and structural loading. In the boundary elements, only stresses arising from pore pressure can cause spalling. However, in the interior elements, stresses due to pore pressure together with tensile stresses induced in the transverse direction by thermal and mechanical loading cause spalling.
- The level of spalling significantly influences the fire resistance of concrete beams under severe fire exposures, and neglecting fire-induced spalling can lead to un-conservative fire resistance predictions in certain scenarios, specifically in the case of high strength concrete (HSC) and ultra-high performance concrete (UHPC) beams.

- Variation of permeability within the cross-section of a concrete beam, due to progressive damage with temperature rise during fire exposure influences the occurrence of fire-induced spalling. A simplified expression for this variation in intrinsic permeability in terms of temperature, pore pressure, and load-induced cracking (damage) across the cross-section is developed.
- The pore pressure developed in a fire-exposed concrete beam is influenced by the load level, fire severity, and microstructure of concrete. The peak pore pressures, as per the numerical model predictions, are about 1 and 4.5 MPa in NSC and HSC beams respectively, while the corresponding peak pressure is about 4 MPa in UHPC beams with polypropylene fiber and 8 MPa in UHPC beam without polypropylene fiber.

CHAPTER 5

5. Parametric Studies

5.1.General

The response of fire exposed UHPC beams is influenced by a number of factors. It is critical to identify and quantify the effects of these factors to evaluate the fire resistance of UHPC members. Many of these critical factors are interdependent and this makes the prediction of fire resistance quite complex. For instance, the experimental and numerical studies show that fire resistance of UHPC beams depends on the extent of spalling, which in turn depends on many factors, including concrete permeability, tensile strength of concrete, presence of fibers, and so on. Parametric studies can generate data that can be utilized to quantify the effect of the influencing factors on the fire response of UHPC beams. The developed and validated numerical model, presented in Chapter 0, is applied to investigate the effect of various factors impacting the fire resistance of UHPC beams. This is done through a set of parametric studies, wherein the fire behavior of UHPC beam is evaluated by varying each parameter over a practical range. The results from parametric studies are utilized to develop design guidelines for evaluating the fire response of UHPC beams. The critical parameters and results from the parametric studies are presented in this Chapter.

5.2.Factors influencing Fire Resistance

Critical factors influencing fire resistance of RC beams made using normal strength concrete (NSC) and high strength concrete (HSC) have been evaluated in previous studies [137,147]. However, there are no studies in the literature to quantify the factors influencing the fire response of RC beams made using UHPC due to the lack of a validated numerical model capable of predicting fire-induced spalling in UHPC beams under fire conditions. Previous studies clearly indicate that fire severity, cross-sectional dimensions of beam, loading level, span length, concrete

cover, and permeability (or concrete strength) influence the fire response of RC beams. Further, UHPC beams are highly prone to fire-induced spalling, which is dependent on various parameters including heating rate, load level, etc. Besides test parameters, fire-induced spalling is reliant on concrete material properties including permeability, tensile strength, presence of polypropylene fibers, etc. To quantify the effect of various parameters on the fire resistance of UHPC beams, the developed and validated numerical model is applied to conduct parametric studies. The main parameters affecting the fire performance of UHPC beams are listed below and considered in this study:

- Load level
- Fire scenario
- Concrete cover thickness
- Concrete type (and permeability)
- Fiber type and volume fraction (steel/polypropylene)
- Cross-sectional dimensions
- Cross-sectional shape (rectangular beam, I beam, T beam)
- Loading type
- Beam span length
- Tensile reinforcement ratio
- Shear reinforcement (and compression bars)

5.3.Parametric studies

The results from the undertaken parametric studies to quantify the influence of each parameter on the response of UHPC beams under fire conditions are discussed in this section.

5.3.1. Selection of beam

A simply-supported UHPC beam, designated as UHPC-B0, was taken as the reference beam for the parametric studies. For the base-line case, beam UHPC-B0 is subjected to two-point loads, each of which is placed at about 1.4 m from the end supports, applying 50% of its room temperature moment capacity (refer to Figure 5.1). The reference UHPC beam had a cross-section of 180x270 mm, with a span length of 3.7 m, similar to the test beams in Chapter 0. The base-line fire resistance test was analyzed out by exposing the middle 2.4 m length of the beam to ASTM E119 [99] standard fire exposure. The UHPC beam was designed based on the available best practice recommendations as no specific design provisions for UHPC members are currently available. The UHPC beam was assumed to contain 1.5% by volume of steel fibers. The beam was provided with three 13 mm tensile reinforcing bars with a yield strength of 436 MPa. The beam had only tensile reinforcement (no shear and compression reinforcements) to effectively utilize the high compressive and tensile strength provided by UHPC. The details of properties and test parameters for the reference case are tabulated in Table 5-1.

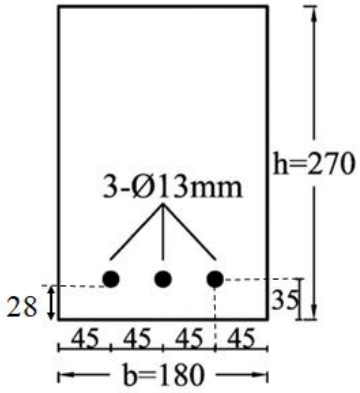

(a) Cross-section

Figure 5.1. Sectional configuration and elevation of reference UHPC beam UHPC-B0 analyzed for parametric study (Units: mm).

Figure 5.1. (cont'd)

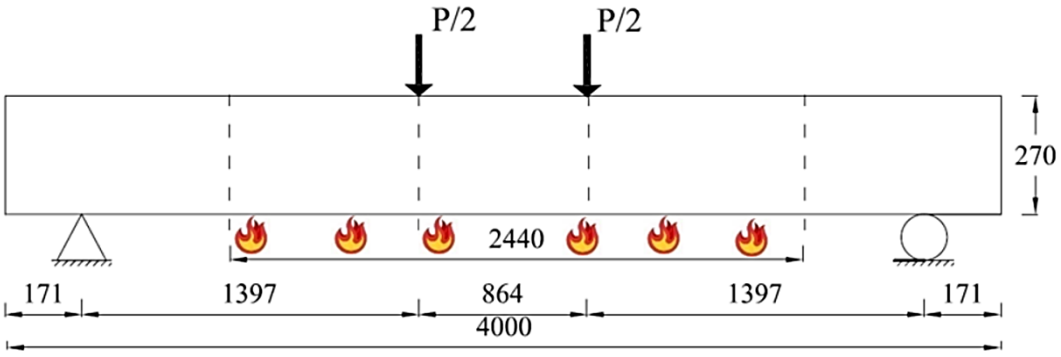

(b) Elevation

Table 5-1. Properties of reference beam UHPC-B0 used in the parametric study.

Property		**Values**
Cross section (mm)		180x270
Span-length (m)		3.66
Fire scenario		ASTM E119
Applied total load (kN)		50
Load ratio		50%
Concrete	Aggregate	Carbonate
	f'c (MPa)	175
	Clear cover thickness (mm)	Bottom-28 mm, Side- 38 mm
Steel reinforcement	Bottom rebar (mm)	3-D13
	fy (MPa)	436
Moment capacity (kN-m)		70
Steel fiber volume fraction (%)		1.5
Initial permeability (m^2)- uncracked/ room temp.		$2x10^{-18}$

5.3.2. Range of parameters

For studying the influence of critical factors on fire response of UHPC beams, eleven sets of analyses are carried out utilizing the developed numerical model. In each set of analysis, one parameter is varied within a practical range, whereas all the other properties are maintained constant. In the first set of analysis, the effect of different levels of loading that can be present on UHPC beam during a fire exposure is studied. The load level under fire exposure is varied from 30 to 70 percent of the ultimate load-carrying capacity of the beam at room temperature. The

second set of analysis investigated the influence of fire scenarios on the behavior of UHPC beams. UHPC beams were subjected to two standard fire exposures (ASTM E119 standard fire and ASTM E1529 hydrocarbon fire) and three design fire exposures. The time-temperature curves for the fire scenarios are shown in Figure 5.2.

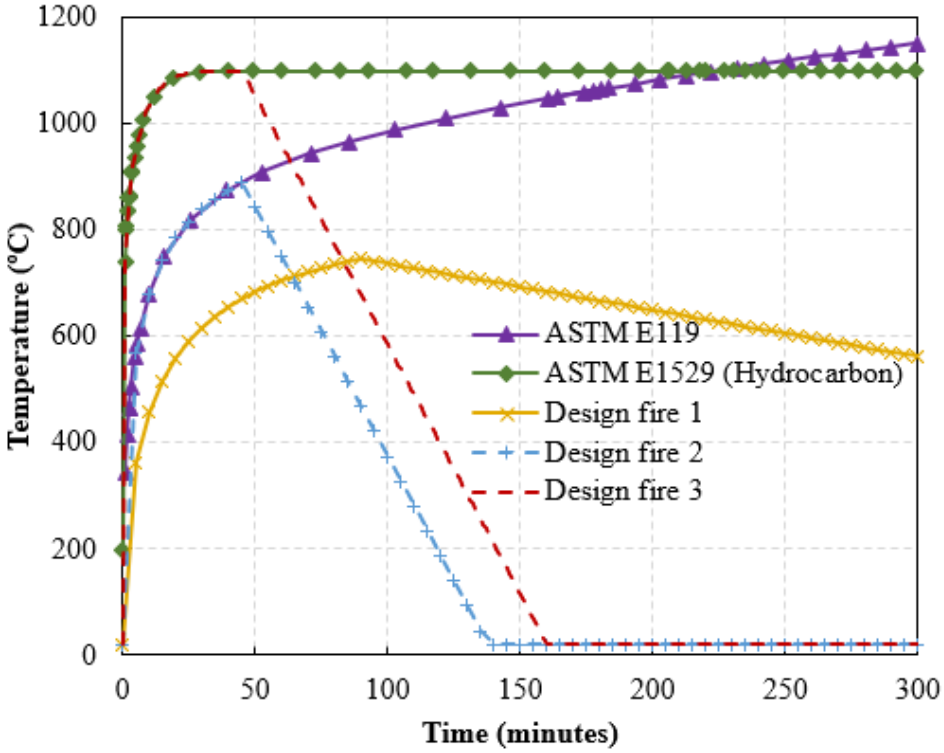

Figure 5.2. Time-temperature curves for different fire scenarios.

In the third set of analysis, the influence of tensile reinforcement ratio on fire resistance of UHPC beams is quantified by varying the number and size of tensile rebars. In the fourth set of analysis, the clear cover thickness of concrete to tensile reinforcement is varied to study the effect of cover thickness on fire resistance of UHPC beams. In the fifth set of analysis, the fire response of different concrete types with varying strength and permeability was studied. In the sixth set of analysis, the effect of specimen shape on fire response of UHPC beam is evaluated by analyzing rectangular, T-shape, and I-shape UHPC beams. In the seventh set of analysis, cross-sectional dimensions were varied for quantifying the effect of varying beam size on the fire response of

UHPC beams. In the eighth set of analysis, the influence of varying span length on the fire response of UHPC beams is evaluated. In the ninth set of analysis, the fire response of UHPC beams was compared under two different flexural loading types (point load and uniformly distributed load). Finally, in the tenth and eleventh set of analysis, the influence of varying steel and polypropylene fiber dosage on the fire behavior of UHPC beams is evaluated. Detailed range of values for each parameter is shown in Table 5-2. The primary reference beam, UHPC-B0, in each analysis set is also marked in the table.

Table 5-2. Critical parameters investigated in parametric study.

Varied Parameter	**Beam Designation**	**Parameter Value**
Load level	UHPC-B1	Load level-30% of room temperature capacity
	UHPC-B2	Load level-40% of room temperature capacity
	UHPC-B0	Load level-50% of room temperature capacity
	UHPC-B3	Load level-60% of room temperature capacity
	UHPC-B4	Load level-70% of room temperature capacity
Fire scenario	UHPC-B0	ASTM E119
	UHPC-B5	ASTM E1529 (Hydrocarbon)
	UHPC-B6	Design Fire 1
	UHPC-B7	Design Fire 2
	UHPC-B8	Design Fire 3
Tensile reinforcement ratio	UHPC-B0	3-D13, ρt=0.9%, Moment capacity-70 kNm
	UHPC-B9	3-D16, ρt=1.24%, Moment capacity-91 kNm
	UHPC-B10	4-D13, ρt=1.09%, Moment capacity-84 kNm
	UHPC-B11	4-D16, ρt=1.65%, Moment capacity-112 kNm
Clear cover thickness	UHPC-B12	Bottom-28 mm, Side- 28 mm
	UHPC-B13	Bottom-34 mm, Side- 28 mm
	UHPC-B14	Bottom-44 mm, Side- 28 mm
	UHPC-B0	Bottom-28 mm, Side- 38 mm
	UHPC-B15	Bottom-34 mm, Side- 38 mm
	UHPC-B16	Bottom-44 mm, Side- 38 mm

Table 5-2. (cont'd)

Concrete type	UHPC-St-B0	f'c=175 MPa, f't=6 MPa,
		k0=2.0x10^-18m^2,
		1.5% Steel fibers
	UHPC-StPP-B17	f'c=161 MPa, f't=5.8 MPa,
		k0=2.0x10^-18m^2,
		1.5% Steel and 0.11 %PP fibers
	NSC-B1	f'c=35 MPa, f't=2.7 MPa,
		k0=6.5x10^-16m^2,
		Plain/ no fibers
	HSC-B1	f'c=105 MPa, f't=3.6 MPa,
		k0=2.0x10^-17m^2,
		Plain/ no fibers
Specimen shape	UHPC-B18	Rectangular shape; Moment capacity-136 kNm
	UHPC-B19	T shape; Moment capacity-136 kNm
	UHPC-B20	I shape; Moment capacity-136 kNm
Sectional dimensions	UHPC-B21	150mm x 230mm, Moment capacity-41 kNm
	UHPC-B0	180mm x 270mm, Moment capacity- 70 kNm
	UHPC-B22	240mm x 360mm, Moment capacity- 129 kNm
	UHPC-B23	270mm x 410mm, Moment capacity- 165 kNm
	UHPC-B24	360mm x 540mm, Moment capacity- 379 kNm
Span length	UHPC-B25	3.66 m
	UHPC-B26	5 m
	UHPC-B0	6.5 m
	UHPC-B27	8 m
Loading type	UHPC-B28	Uniformly distributed load; Load level-50%
	UHPC-B0	Two-point load; Load level-50%
Steel vol. fraction	UHPC-B29	0.75% vol., f'c=157 MPa, f't=5 MPa
	UHPC-B0	1.5% vol., f'c=175 MPa, f't=6 MPa
	UHPC-B30	2.25% vol., f'c=178 MPa, f't=7.5 MPa
	UHPC-B31	3% vol., f'c=182 MPa, f't=9.5 MPa
Polypropylene fiber dosage	UHPC-B0	0 % vol., f'c=175 MPa, f't= 6 MPa
	UHPC-B32	0.1 % vol., f'c=162 MPa,f't=5.8 MPa
	UHPC-B33	0.2% vol., f'c=151 MPa,f't=5.5 MPa
	UHPC-B34	0.3% vol., f'c=143 MPa,f't=5.2 MPa

5.3.3. Analysis details

The fire resistance analyses of the beams were conducted by incrementing time in small steps of two minutes each. The analyzed beam was divided into 40 equal segments along its length. The mid-section of each segment was further discretized into quadrilateral elements of 10 x 10 mm size for the analysis. The fire resistance and spalling analysis procedure detailed in Chapter 0 is followed for undertaking the parametric studies. Temperature-dependent material property relations for UHPC and reinforcing steel at various stages are adopted based on the discussions in Chapter 0. The analysis generates various output parameters, such as cross-sectional temperatures, pore pressure, stresses (hydro-thermo-mechanical), strains, deflections, and moment capacity at each time increment. These results were used to evaluate the extent of spalling and also failure of the beam. The strength and deflection limit states were applied to determine failure.

5.3.4. Results of parametric studies

Results from fire resistance analyses are presented herein. The effect of various parameters on the fire response of UHPC beams is discussed below.

5.3.4.1. Effect of load level

To study the influence of load level on fire response, UHPC beams were analyzed under varying load ratios of 30%, 40%, 50%, 60%, and 70%, and exposed to ASTM E119 standard fire. The load ratio is calculated as the ratio of the bending moment due to applied loading under fire conditions to room temperature flexural capacity of the beam. The effect of load ratio on the thermal response of UHPC beams is illustrated in Figure 5.3 by plotting the temperatures at corner rebar and mid-depth as a function of fire exposure time. Results from the analysis show that the sectional temperatures are higher in UHPC beams subjected to a load ratio of below 50%. This is mainly due to the higher extent of spalling in beams under a lower load ratio, due to lower load-induced

cracking, resulting in lower permeability and in turn restricting the release of pore pressure. The extent of spalling in UHPC beams with varying load ratios is plotted in Figure 5.4 and it can be clearly observed that the extent of spalling significantly increases when UHPC beams are subjected to load ratios lower than 50%. It is worth noting that studies in the literature have demonstrated that in NSC and HSC beams, varying load ratios do not influence the thermal response of RC beams [11,189]. However, the applied loading level influences the rate of temperature rise in fire-exposed UHPC beams.

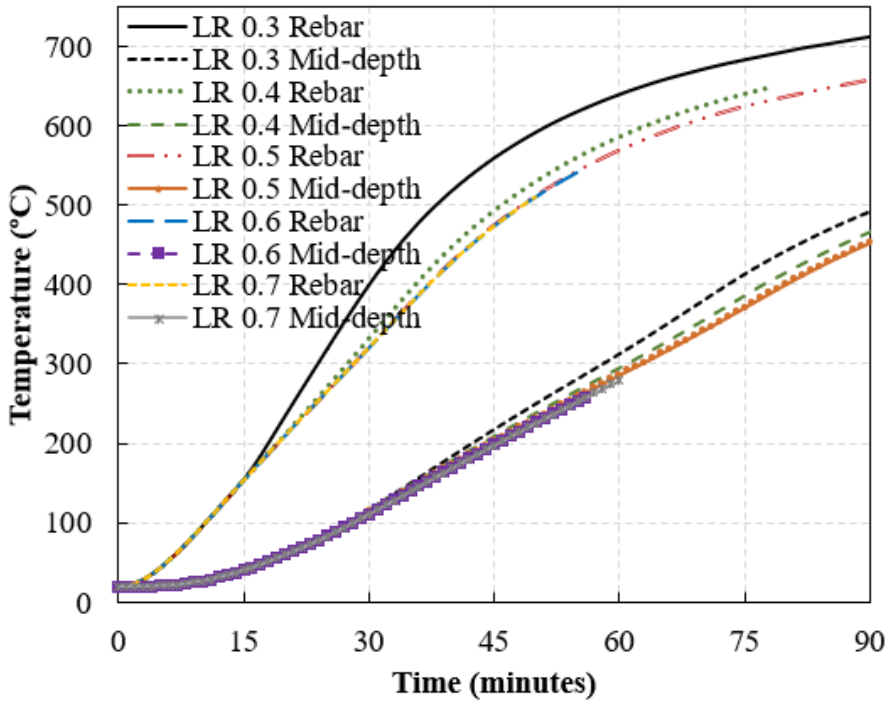

Figure 5.3. Effect of load ratio on temperature rise at corner rebar and mid-depth of UHPC beams.

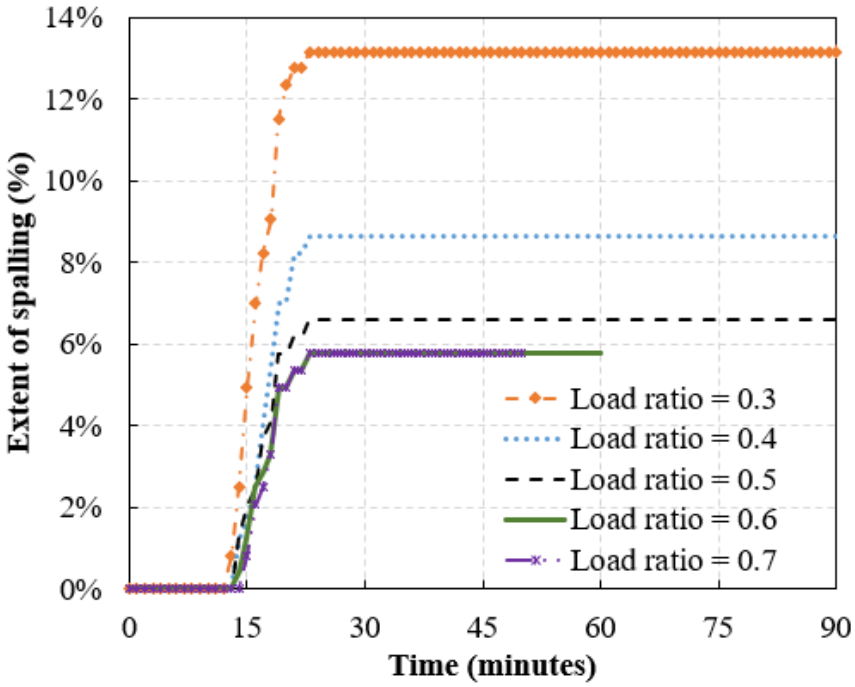

Figure 5.4. Effect of load ratio on extent of spalling in UHPC beams.

Additionally, the level of structural loading can significantly influence the structural behavior of UHPC beams under fire conditions as shown in Figure 5.5. The results in Figure 5.5 show that the deflection and rate of deflection increase with increasing load ratio. This can be attributed to the fact that a higher load ratio leads to higher internal stresses, which in turn causes early degradation in the strength and stiffness properties of concrete and steel. This degradation in properties of constituent materials leads to lower stiffness in the beam and results in increasing deflections and lower fire resistance with increasing load ratio. Therefore, it can be deduced from the current set of analysis that the effect of load ratio on fire resistance of UHPC beams is complex and counteracting in nature. On one hand, the extent of spalling and sectional temperatures tend to be lower with increasing load ratio (>40%), whereas, on the other hand, increasing load ratio causes a faster rise in deflections. Further, a higher load ratio also generates load-induced mechanical stresses which accelerate spalling.

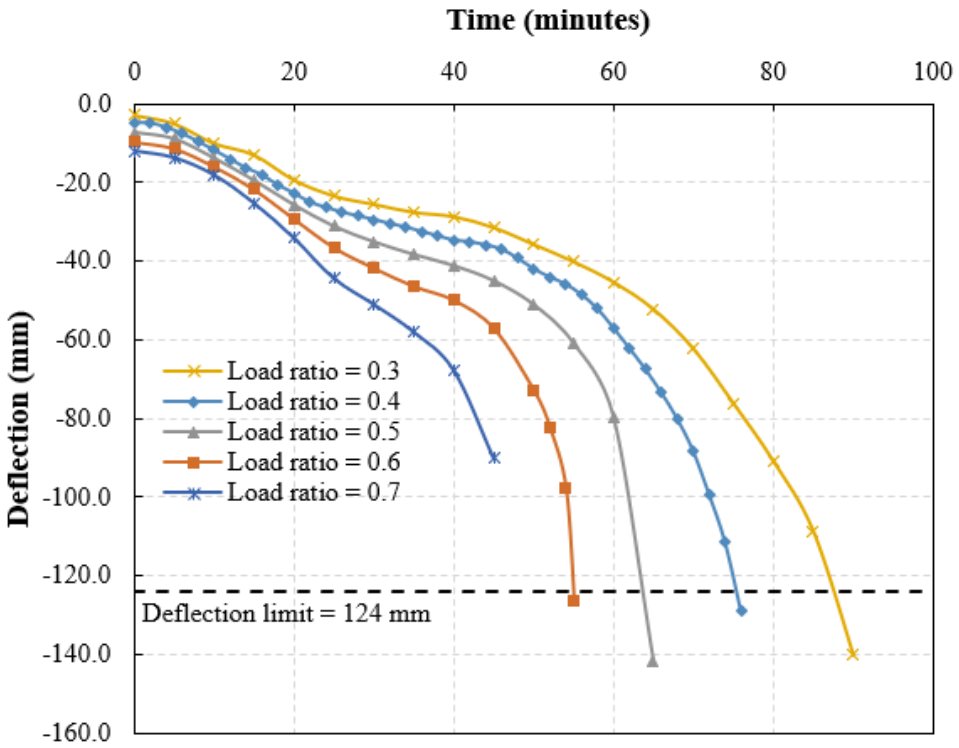

Figure 5.5. Effect of load ratio on deflection of UHPC beams.

5.3.4.2. Effect of fire scenario

UHPC beams subjected to 50% load ratio were analyzed under varying fire exposure scenarios to study the effect of fire scenario on their fire resistance. The investigated fire scenarios are shown in Figure 5.2, and include two standard fire scenarios, namely, ASTM E119 [99] and ASTM E1529 [190] hydrocarbon fire, and three design fire scenarios; namely, Design Fire 1 (DF1), Design Fire 2 (DF2), and Design Fire 3 (DF3). The design fires represent fire exposures typically encountered in buildings with varying fuel load and their respective time-temperature curves are calculated as per Eurocode 1 [143] provisions. The cooling phase of the design fires are calculated assuming ventilation-controlled conditions and the cooling rate is dependent on the duration of the heating phase [181]:

$$T_c = \begin{cases} T_{f,max} - 625(t - DHP) & DHP \leq 0.5 \\ T_{f,max} - 250(3 - DHP)(t - DHP) & 0.5 < DHP < 2 \\ T_{f,max} - 250(t - DHP) & DHP \geq 2 \end{cases} \quad (5\text{-}1)$$

where T_c=temperature (℃) of fire curve in cooling phase; $T_{f,max}$= peak fire temperature (℃) attained during heating phase; t = time in hours; and DHP = the duration of the heating phase in hours. The thermal response of the analyzed UHPC beams is illustrated by plotting the temperatures at corner rebar and mid-depth in Figure 5.6. In all the analyzed beams, the temperatures at mid-depth follow a similar trend to that at rebar locations, and temperatures at mid-depth are lower than at corner rebar due to their corresponding distance from fire exposure.

The temperature rise in the beam subjected to ASTM E119 was similar to the beam exposed to DF2, as well as the beam subjected to ASTM E1529 was similar to the beam exposed to DF 3. This is because the time-temperature curves during the heating phase of DF2 and DF3 are the same as the ASTM E119 and ASTM E1529 standard fire exposures, respectively. It can be seen from Figure 5.6 that the rate of increase in sectional temperatures of all the analyzed UHPC beams depends on the temperature rise in time-temperature curves of respective fire exposure scenarios. The beams subjected to ASTM E1529 (hydrocarbon fire) and DF3 have the fastest temperature progression, followed by ASTM E119 and DF2, and lastly followed by DF1.

Design fire DF2 has a shorter duration of heating phase than DF1 and lower fire severity than DF3. The heat propagation within the beam subjected to DF2 stops when the decay phase starts, and gradually, the rise in sectional temperatures ceases and starts to decrease. The rebar temperatures in the beam subjected to DF2 remain below the critical temperature limit of 593℃ [99]. The critical temperature is defined as the temperature at which the reinforcement loses so much of its strength that it can no longer support the applied load. However, the rebar temperatures in the beams exposed to the standard fire exposures (ASTM E119 and ASTM E1529) and the other design fires, DF1 and DF3 reach critical temperature limit of 593℃, resulting in faster degradation of stiffness and early failure of the beam prior to entering the cooling phase.

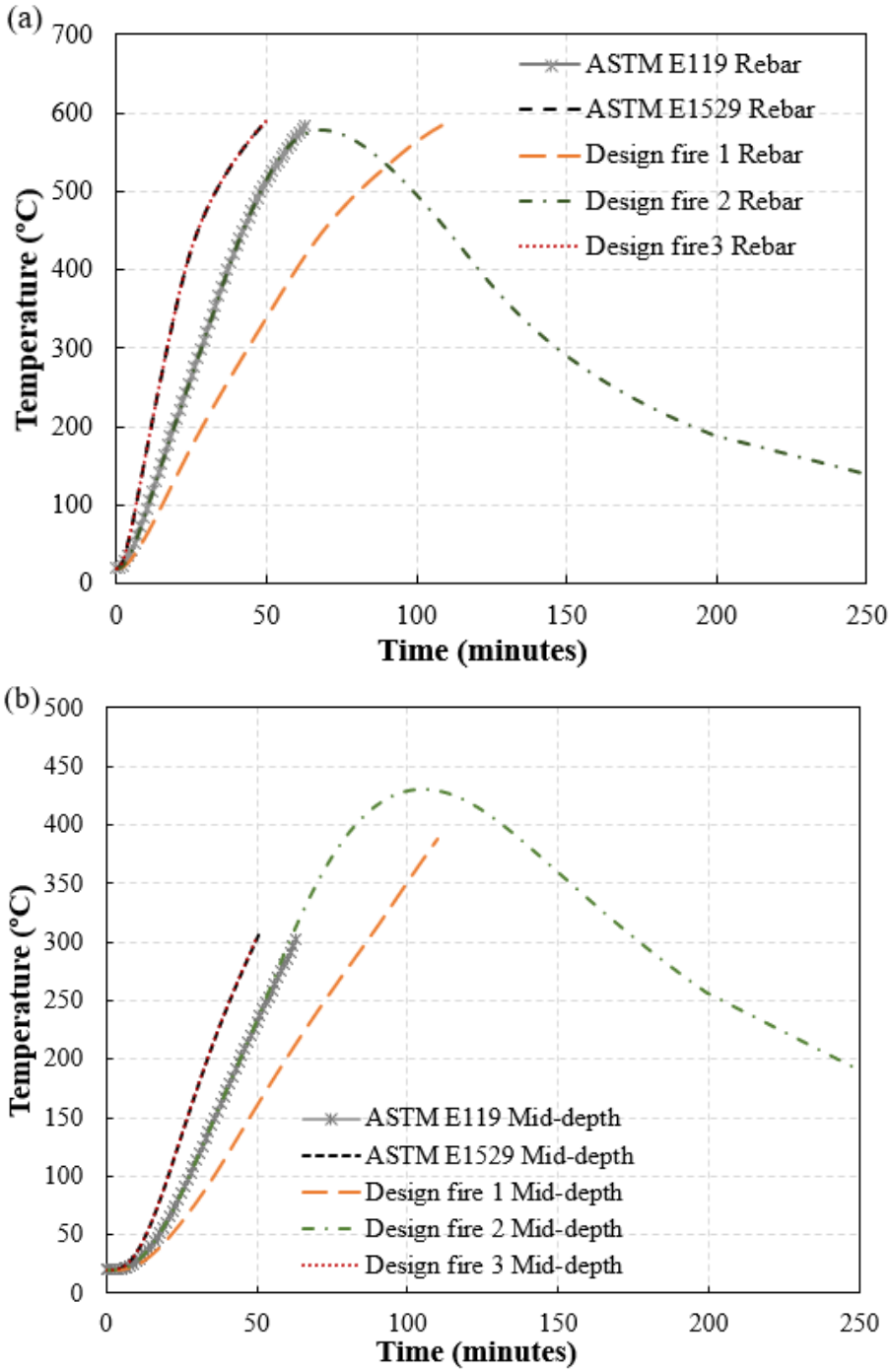

Figure 5.6. Effect of fire scenario on temperature rise at corner rebar and mid-depth of UHPC beams.

In addition, Figure 5.6 shows that despite being subjected to the fire exposure of lowest severity i.e. DF1, the corner rebar in this UHPC beam attained the critical temperature limit of 593°C. This can be attributed to the longer duration of 90 minutes in the heating phase of DF1 followed by a

slower cooling rate as compared to the other design fire exposure scenarios which although had higher fire severity, but comprised of shorter heating phase, followed by faster cooling rate. Therefore, along with the fire severity, the durations of heating phase and subsequent cooling rate are critical for inferring sectional temperatures in UHPC beams.

The extent of spalling in the analyzed UHPC beams is shown in Figure 5.7 as a function of fire exposure time. The amount of spalling is the lowest (5.35%) for the beam under DF1, due to the lower fire intensity and lower rate of heating in DF1, which in turn resulted in lower thermal gradients and slower drying of concrete conducing lower hydro-thermal stresses in the beam. ASTM E1529 and DF3 encompass high heating rates, resulting in the generation of high pore pressure and thermal stresses, leading to higher spalling (6.17%) in the UHPC beams, as compared to the beam subjected to DF1. However, the fast heating in ASTM E1529 and DF3 leads to excessive microcracking in concrete and releases pore pressure, slightly lowering the extent of spalling in the exposed beams than those exposed to intermediate fire scenarios of ASTM E119 and DF2 (6.58%). ASTM E119 and DF2 comprise a moderate heating rate which is sufficiently high to result in buildup of pore pressure and also, adequately low to hinder the escape of pore pressure by limiting cracking. Therefore, it can be deduced that fire exposure scenarios with intermediate heating rates cause a higher extent of spalling as compared to slow or fast heating.

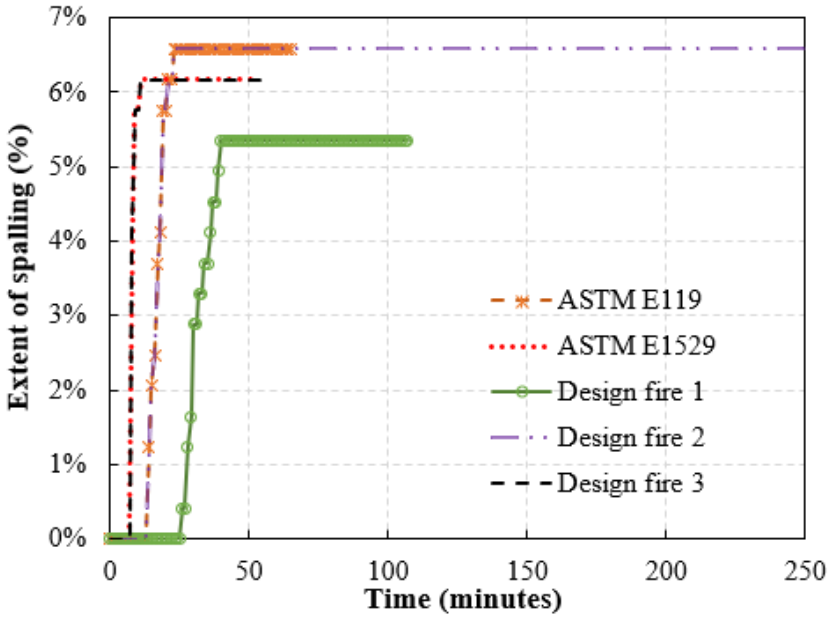

Figure 5.7. Effect of fire scenario on extent of spalling in UHPC beams.

To illustrate the comparative structural response of the analyzed UHPC beams under varying fire scenarios, their progression of mid-span deflection with fire exposure time is plotted in Figure 5.8. The beams subjected to fire scenarios with high severity, ASTM E1529 and DF3, have the lowest fire resistance (50 min) due to early rebar yielding as a result of rapid rise in rebar temperatures. The beam subjected to ASTM E119 standard fire without a cooling phase, failed at 63 min with attainment of 593°C temperatures at corner rebar. Although, the amount of spalling under ASTM E119 was slightly higher (6.58%) than that under ASTM E1529 and DF3 (6.17%), the lower fire severity of ASTM E119 in comparison to hydrocarbon fire curves led to higher fire resistance. The rebar in UHPC beam under DF2 also experienced elevated temperatures of 577°C, however, partial recovery of deflection (50%) without failure occurred in this beam. This can be attributed to the presence of cooling phase which lowered the sectional temperatures and facilitated partial recovery of strength and stiffness properties. The residual deflection in this beam can be attributed to the unrecoverable residual plastic strains in concrete and rebars, and transient creep strains in concrete. In addition, loss of cross-section due to spalling (of 6.58%) contributed to irrecoverable

deflections in the beam. Under fire scenario DF1, the beam attains high rebar temperatures above 593℃ because of the prolonged heating phase of 90 min, and fails at 107 min before temperatures start to decrease in the cooling phase. However, the beam experienced lowest spalling (5.35%) under DF1, which contributed to attainment of the highest fire resistance among the beams that failed. Therefore, these results infer that fire scenario has significant influence on the fire response of the UHPC beams, wherein the rate of increase in deflection is dependent on the severity and the rate of rise in fire temperatures.

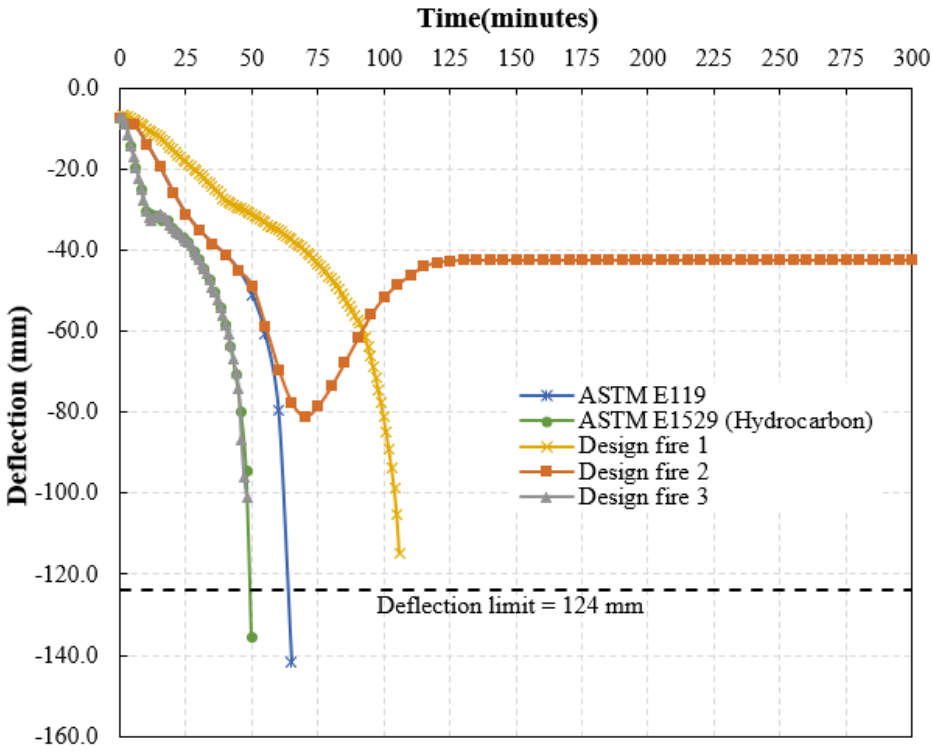

Figure 5.8. Effect of fire scenario on deflection of UHPC beams.

5.3.4.3. Effect of tensile reinforcement ratio

To study the effect of tensile reinforcement ratio, which is the ratio of the area of tension steel to the effective area of the beam cross-section, on fire resistance of UHPC beams, four different ratios were considered in the range of 0.9%-1.65%. The sectional dimensions and cover thickness were same across the analyzed beams, and only the number and diameter of tensile steel reinforcement

was varied as shown in Table 5-2. With the increase in longitudinal reinforcement, the room temperature bending moment capacity of the UHPC beams increased significantly, resulting in a 60% increase in capacity over an increase of 0.85% in reinforcement. For exclusively investigating the effect of tensile reinforcement ratio, the load ratio was maintained constant as 50% of the corresponding load carrying capacity at room temperature for each beam (shown in Table 5-2). All the analyzed UHPC beams were subjected to ASTM E119 fire exposure.

The progression of the mid-span deflection of the studied beams is plotted in Figure 5.9 as a function of fire exposure time. From the analysis results, it was found that the effect of tensile reinforcement ratio on fire resistance of UHPC beams was insignificant with negligible variations in thermal, spalling, and structural response of the beams. This unaltered response for different ratios of tensile reinforcement is because of the equivalent rate of reduction in capacity due to similar temperature rise in rebars provided with same cover in all the beams. Further, due to the equivalent thermal distribution and load ratio, the level of spalling was uniform across the analyzed beams.

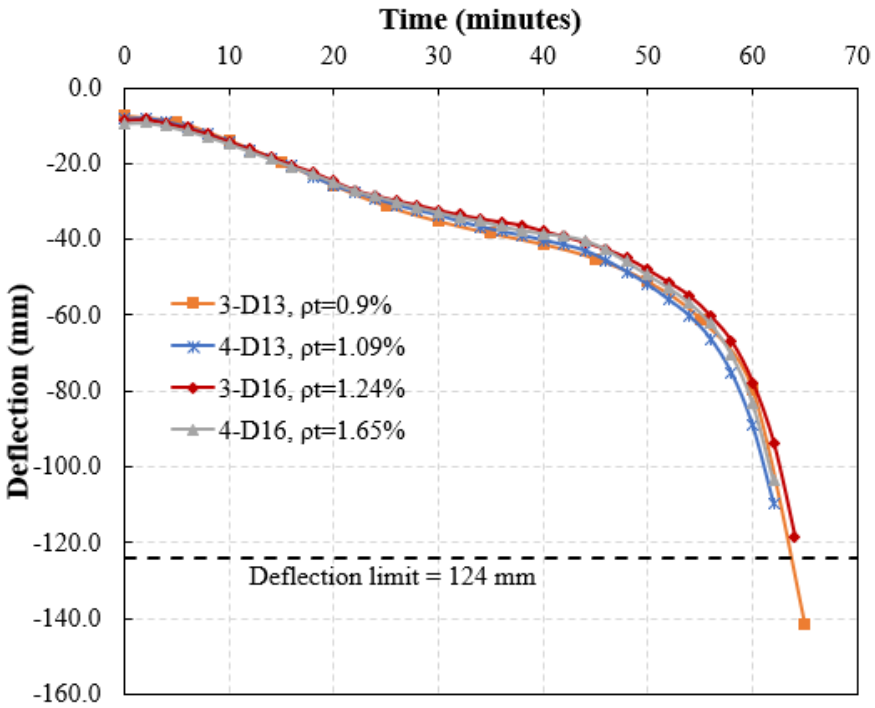

Figure 5.9. Effect of tensile reinforcement ratio on deflection of UHPC beams.

5.3.4.4. Effect of cover thickness

The effect of concrete clear cover thickness on fire resistance of UHPC beams is investigated by analyzing six beams subjected to ASTM E119 fire exposure and 50% load ratio. For the analysis, the bottom clear cover thickness to tensile rebar and side (lateral) clear cover thickness to corner rebar is varied in the range of 28 to 44 mm as shown in Table 5-2. The total depth of the beam remained unchanged at 270 mm and only the cover thickness is varied in this investigation. Varying the bottom cover thickness alters the flexural capacity of the beam due to variation in the moment lever arm. However, the variation in moment capacity for the analyzed beams with different cover thicknesses was within 4%. Thus, all the analyzed beams are subjected to 50% load ratio computed for the reference beam U-B0.

Figure 5.10 shows the effect of concrete cover thickness on temperature rise in corner rebar of UHPC beams. It can be clearly seen that with higher concrete cover thickness, either from bottom surface or lateral surface, progression of rebar temperatures is slower. The slower rise in rebar

temperatures is due to the resulting increase in distance between the fire exposed surface and tensile rebar, which lowers the ingress of heat to the steel reinforcement. This variation in temperature propagation minimized with increase in distance from the exposed layers due to low thermal conductivity of concrete. The temperatures at concrete mid-depth for the analyzed beams were similar and hence, they are not plotted here. In the analyzed beams, the extent of spalling did not vary with cover thickness as shown in Table 5-5. Fire-induced spalling of concrete is a local phenomenon and as observed in the fire tests, majority of the spalling occurs in upper compressive zone of the beam, with lower spalling in bottom portion due to cracking in the tensile zone. Therefore, the variation in cover thickness to tensile reinforcement in the bottom portion of the beam did not alter the extent of spalling.

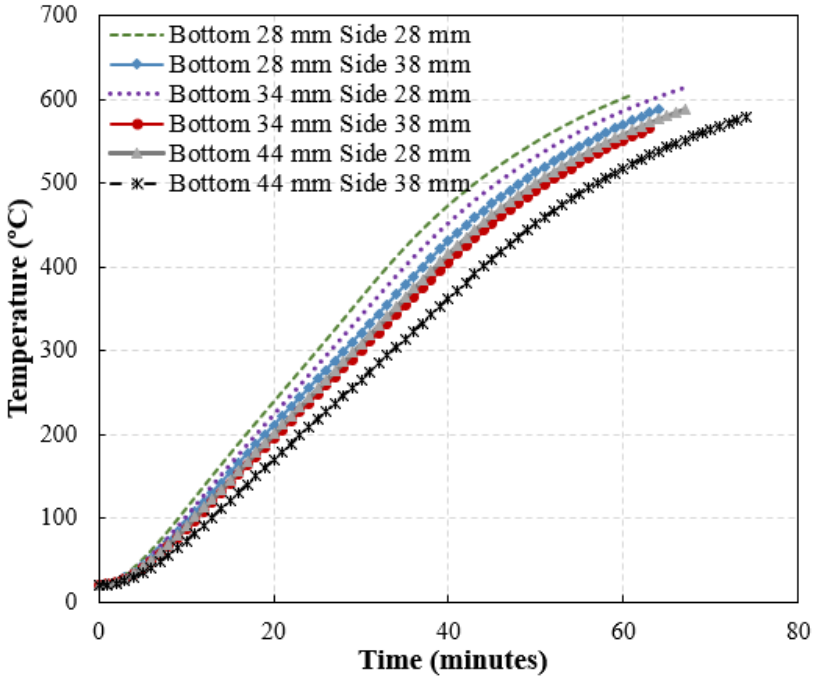

Figure 5.10. Effect of cover thickness on temperature rise at corner rebar in UHPC beams.

Figure 5.11 shows the progression in mid-span deflections of UHPC beams of varying concrete cover thickness. It can be seen from Figure 5.11 that the increase in deflection is slower and fire resistance is higher with increasing cover thickness. For instance, the fire resistance increased by

20% upon increasing bottom cover thickness from 28 mm to 44 mm and lateral cover thickness from 28 mm to 38 mm. Higher cover thickness reduces temperature propagation in steel rebars and slows down strength and modulus degradation of reinforcing bars, in turn retarding the reduction in moment capacity and further, slowing down the increase in deflection. Therefore, the analysis results indicate that fire resistance of UHPC beams can be increased by rationally increasing the concrete cover thickness. The variation in bottom cover thickness and side (or lateral) cover thickness had a similar level of impact on fire resistance of UHPC beams.

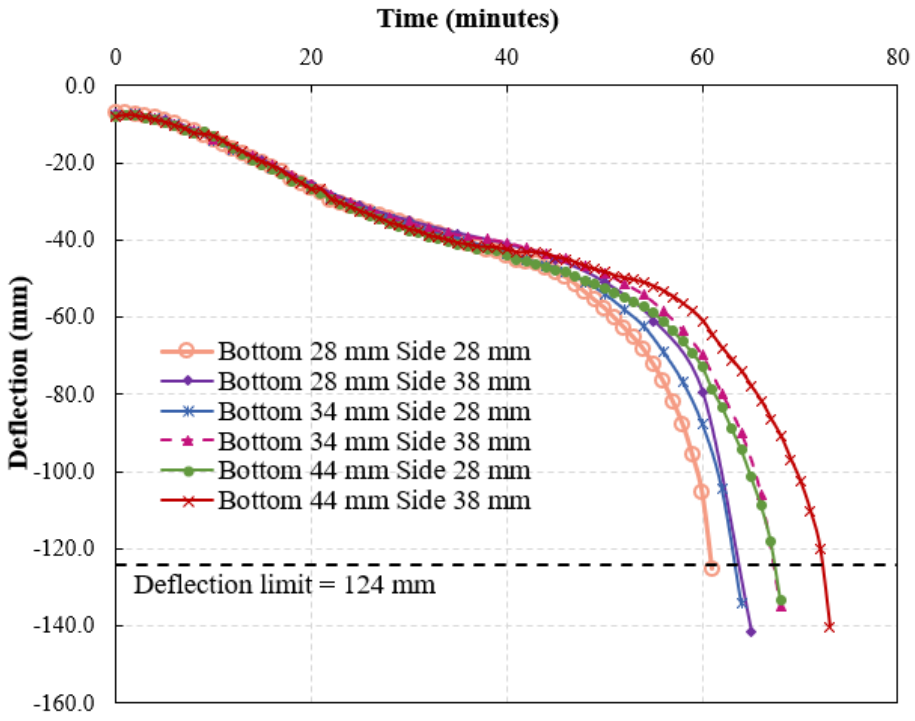

Figure 5.11. Effect of cover thickness on deflection of UHPC beams.

5.3.4.5. Effect of concrete type

To investigate the effect of concrete type, four RC beams made of NSC, HSC, conventional UHPC with only steel fibers (UHPC-St), and UHPC with both steel and polypropylene fibers (UHPC-StPP) were analyzed. UHPC-St comprised of 1.5% by volume of steel fibers and UHPC-StPP contained 1.5% by volume of steel fibers and 0.11% by volume of polypropylene fibers. All the

beams were subjected to the same fire exposure of ASTM E119 and same loading conditions under 50% load ratio. The NSC and HSC beams were designed as per ACI 318 specifications [116], whereas the UHPC beams were designed based on the available best practice recommendations since no design provisions for UHPC members are currently available in codes and standards [188]. The UHPC beams were provided only tensile reinforcement (no shear and compression reinforcements) to take advantage of its high compressive and high tensile strength. All the beams were designed to have the same bottom and lateral concrete cover thickness and same moment capacity of 70 kN-m. The cross-sectional details of the NSC, HSC, UHPC-StPP, and UHPC-St beams are shown in Figure 5.12.

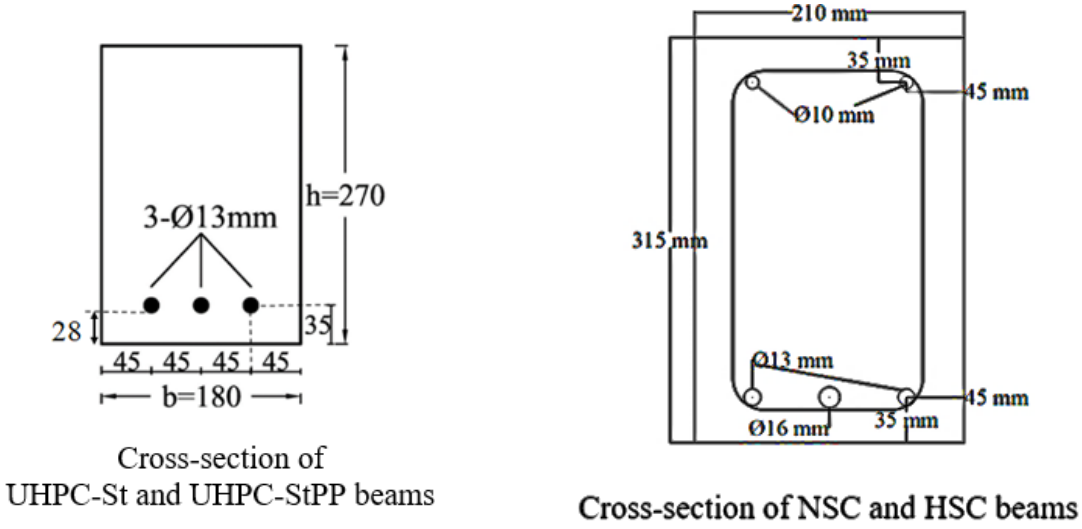

Figure 5.12. Cross-section of the analyzed beams with varying concrete type.

Thermal, mechanical, and permeability properties specific to NSC, HSC, UHPC-St, and UHPC-StPP were inputted in the program for the analysis to trace the fire response of beams. Details on material properties corresponding to concrete type can be found in section 4.4.2. The thermal response of the analyzed beams is compared by plotting the temperature progression in corner rebar and concrete (at mid-depth) with fire exposure time in Figure 5.13. In all four beams, the temperatures in concrete (at mid-depth) increased less rapidly than that in corner rebar. This can

be attributed to low thermal conductivity and high specific heat of concrete that delays heat penetration to the inner concrete layers. From the comparison of thermal response trends in Figure 5.13, it can be seen that the sectional temperatures in both UHPC-St and UHPC-StPP beams increase at a faster pace as compared to HSC and NSC beams. As shown in Figure 5.12, UHPC-St and UHPC-StPP beams were designed to have reduced cross-sectional area to utilize high compressive strength of UHPC [191]. These smaller sectional dimensions contributed to the reduction in thermal mass and utilization of more heat for temperature rise in both UHPC-St and UHPC-StPP beams as compared to beams made of NSC and HSC. Moreover, severe spalling occurred in UHPC and UHPC-StPP beams (see Table 5-5 and Figure 5.14), which led to a loss of concrete section and in turn resulted in rapid temperature rise. In addition, UHPC has slightly higher thermal conductivity as compared to NSC and HSC, which further resulted in faster progression of sectional temperatures in the UHPC-St and UHPC-StPP beams [118].

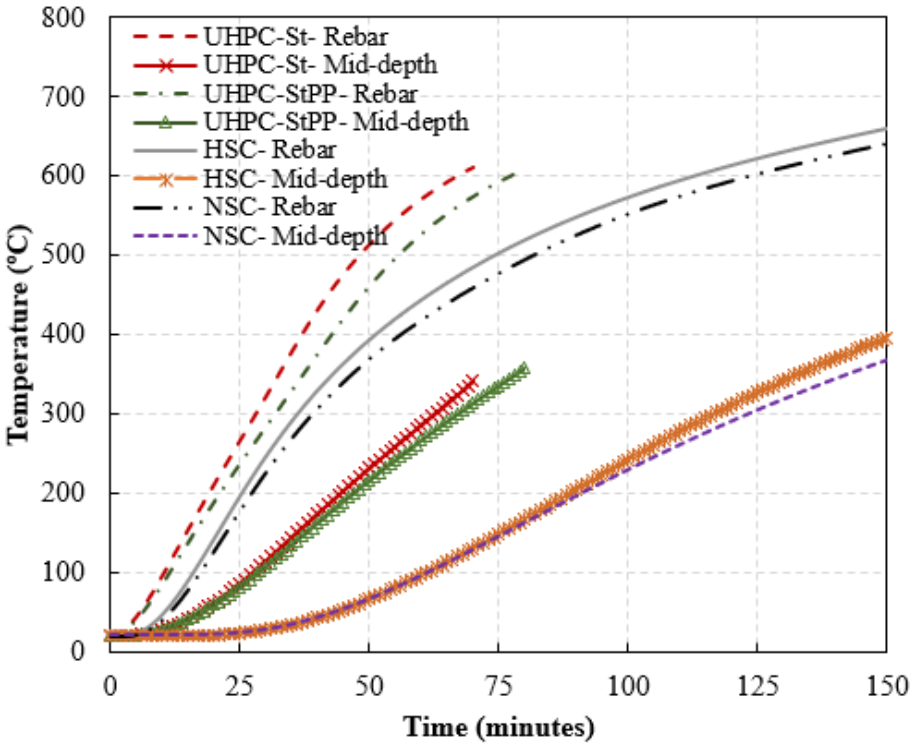

Figure 5.13. Effect of concrete type on temperature rise at corner rebar and mid-depth in beams.

Figure 5.14 shows the predicted extent of spalling in the analyzed beams and Figure 5.15 shows the pore pressure trends in the beams at 30 mm from the exposed right surface and 60 mm depth from the top surface. Because of high permeability in NSC, much of the vapor is released and only low levels of (pore) pressure build up in the NSC beam. A peak pressure of around 0.7 MPa and no spalling was predicted for NSC beam. Much higher pore pressure developed in the HSC and UHPC beams, and this is attributed to their dense microstructure and lower permeability that hinder the vapor pressure to escape. A peak pore pressure of about 2.2 MPa developed in the HSC beam and higher peak pore pressures of 4.2 MPa and 5.8 MPa developed in UHPC-StPP and UHPC-St beams respectively. The extent of spalling in UHPC-StPP beam was lower (5.29%) than that in the UHPC-St beam without polypropylene fibers (6.58%), due to the enhanced permeability and partial dissipation of pore pressure through melting of PP fibers at about 160 °C. The extent of spalling in HSC beam (4.17%) was lower than UHPC beams due to relatively lower permeability, but was much higher than the null amount of spalling in the NSC beam.

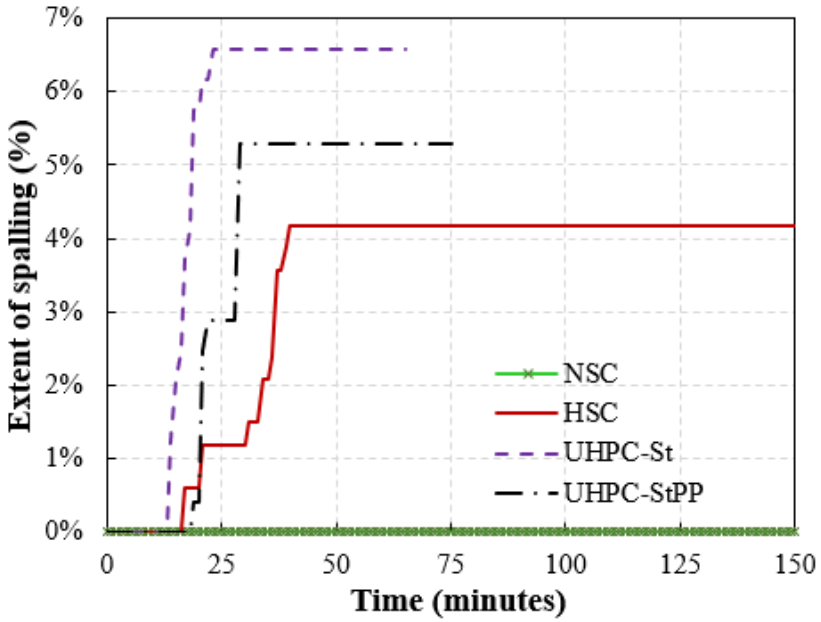

Figure 5.14. Effect of concrete type on extent of spalling in beams.

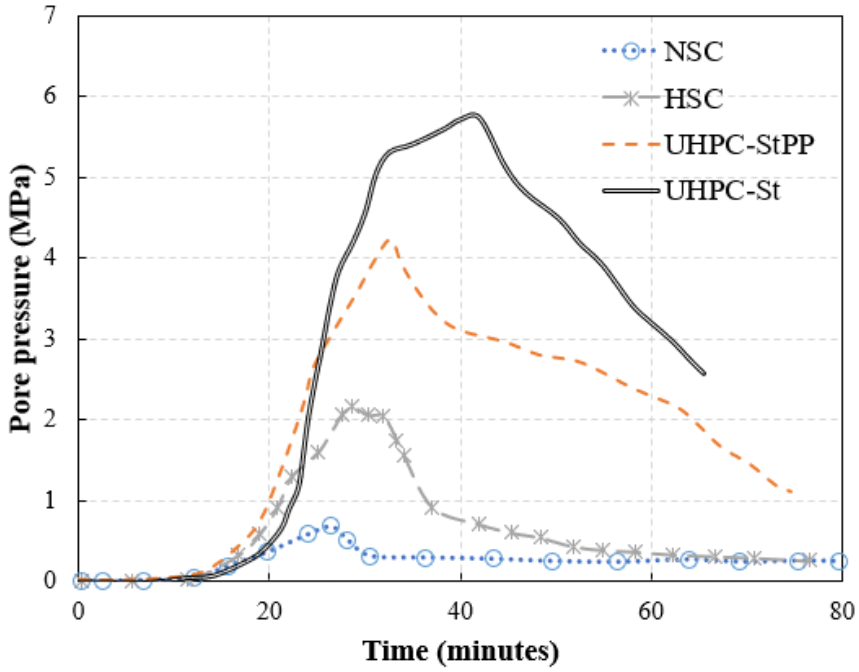

Figure 5.15. Effect of concrete type on pore pressure in beams.

The progression of mid-span deflection in the analyzed beams made of different concrete types is plotted in Figure 5.16. UHPC-St and UHPC-StPP beams experienced rapid rise in deflections as compared to a gradual increase in deflection in NSC and HSC beams. This trend can be attributed to the higher rebar (and concrete) temperatures in UHPC-St and UHPC-StPP beams and also due to faster degradation of strength and stiffness properties of UHPC at elevated temperatures, as compared to NSC and HSC. Among the two UHPC beams, the UHPC-St beam experienced a more rapid increase in deflections due to higher capacity degradation that resulted from the removal of concrete due to severe spalling. In comparison, the rate of deflection increase in UHPC-StPP beam was at a moderate pace as compared to the case of UHPC-St beam without polypropylene fibers. This can be attributed to slower deterioration of stiffness owing to reduced loss of cross-section through spalling mitigation facilitated by the melting of polypropylene fibers present in UHPC-StPP.

Furthermore, the deflection-time curves in Figure 5.16 show that the mid-span deflection of NSC beam is lower than that of HSC beam throughout the entire duration of fire exposure. The slower progression in deflections in NSC beam than other beams can be attributed to slower degradation of strength and stiffness properties of NSC and negligible extent of spalling, which in turn resulted in lower rebar temperatures. The UHPC-St beam failed in 63 min, while UHPC-StPP beam failed in 74 min. This shows that fire resistance of UHPC beams can be increased by lowering the extent of spalling through the addition of polypropylene fibers to UHPC mix. The UHPC beams (UHPC-St and UHPC-StPP) failed earlier than the NSC and HSC beams due to severe spalling, thinner cross-sections, and faster deterioration in mechanical properties. The HSC beam failed in 120 min, which is much higher than that of the UHPC beams but less than the NSC beam. The NSC beam had the highest fire resistance (125 min) among the four analyzed beams and this can be mainly attributed to minimal spalling and slower degradation of strength properties of NSC.

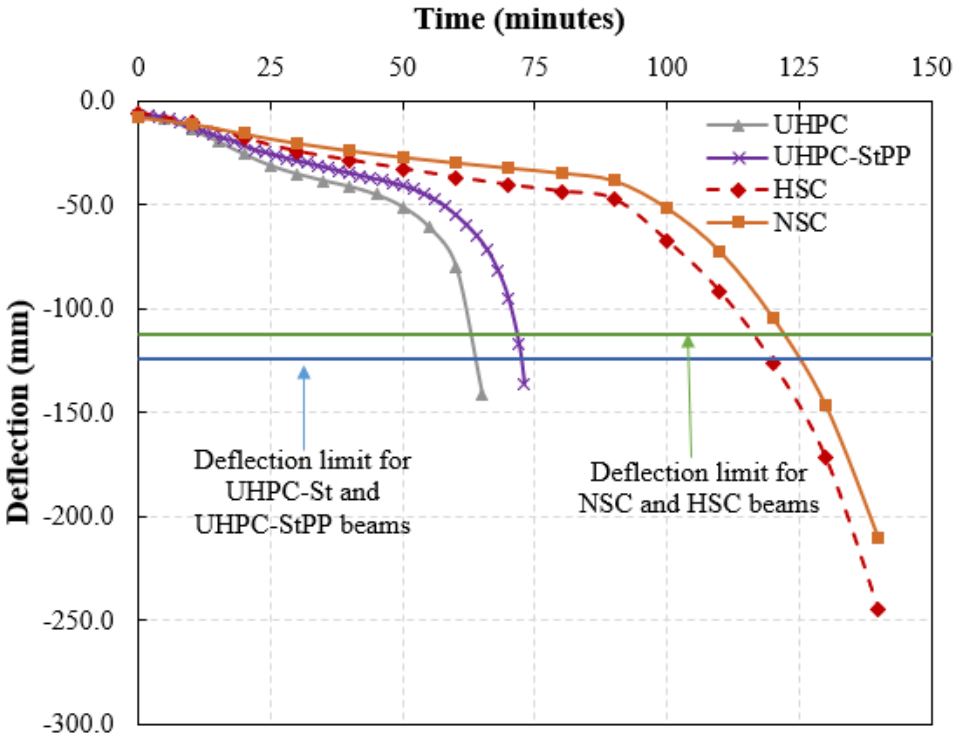

Figure 5.16. Effect of concrete type on deflection in beams.

5.3.4.6. Effect of cross-sectional shape

Using beams of thinner sectional shapes other than rectangular is becoming prevalent in structural applications, especially in high rise buildings, due to lower dead load, construction time, material and fabrication costs. At present, there is no experimental data on fire response of UHPC beams of different cross-sectional shapes such as I-section and T-section, with leaner web portion. Moreover, majority of the previous tests at room temperature conditions were carried out on rectangular sections and very few tests have been reported on beams with non-rectangular sections. The efficacy of the developed numerical model for analyzing UHPC beams of different sectional shapes was gauged by comparing model predictions for an I-section beam against test results reported by Hasgul et al. [192] at ambient conditions. The cross-sectional details and loading set-up are shown in Figure 5.17. The selected test beam was made of UHPC with 1.5% steel fibers by volume and had a compressive strength of 154 MPa and tensile strength of 8.8 MPa. The predicted and measured load-deflection responses of the I-shape beam are compared in Figure 5.18. The figure shows that the predicted load-deflection response follows closely with the measured data and captures the salient points of rebar yielding, strain hardening, peak load, and ultimate load (discussed in 4.4.3). Despite the absence of shear and compression reinforcement, the I-beam exhibited strain hardening and ductile response due to the presence of steel fibers. By means of good agreement in the predicted and measured responses, the model is deemed acceptable for evaluating the performance of UHPC beams of different sectional shapes.

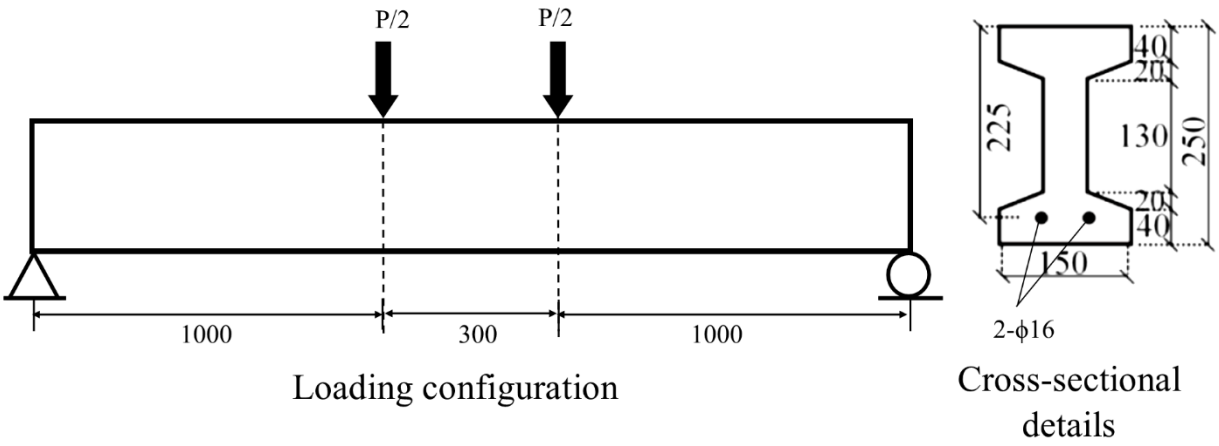

Figure 5.17.Details of I-shape UHPC beam tested by Hasgul et al. [192].

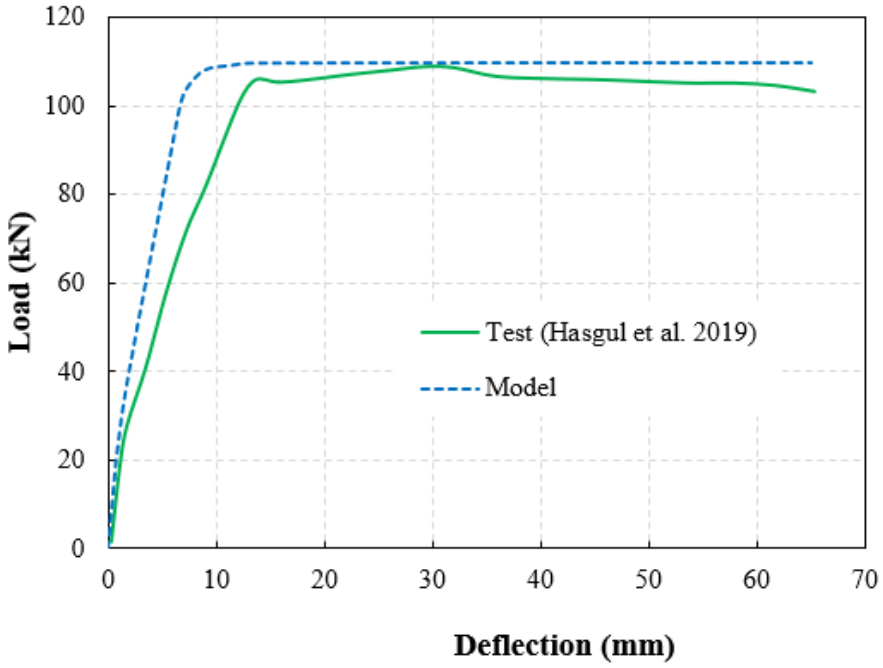

Figure 5.18. Predicted and measured load-deflection response for I beam.

To study the effect of different cross-sectional shapes on fire resistance of UHPC beams, a set of analyses was carried out on UHPC beams of rectangular, I, and T sectional shapes. The three UHPC beams of different sectional shapes were designed to have the same moment capacity of 136 kN-m. This moment capacity is higher than that of the reference beam UHPC-B0 utilized in other parametric analysis in order to conduct a reasonable comparison with the I-section and T-section beams which were designed following ACI 318 [116] provisions. Similar to the reference

beam UHPC-B0, the rectangular beam is not provided with any compression or shear reinforcement to fully utilize the strength of UHPC. While there have been a few fire tests on UHPC beams without stirrups having rectangular sections, there have been none on UHPC beams without stirrups having non-rectangular sections with thinner stems. Therefore, for evaluating the effect of sectional shape of fire performance of UHPC beams, the beams with I-section and T-section are reinforced in compression and shear, similar to traditional RC beams. The cross-sectional details of the analyzed UHPC beams of different shapes are shown in Figure 5.19. The beams were provided with same bottom and lateral cover thickness. Height to width ratio of 1.5 was maintained across all beams. All the beams were analyzed under ASTM E 119 standard fire exposure and 50% load ratio.

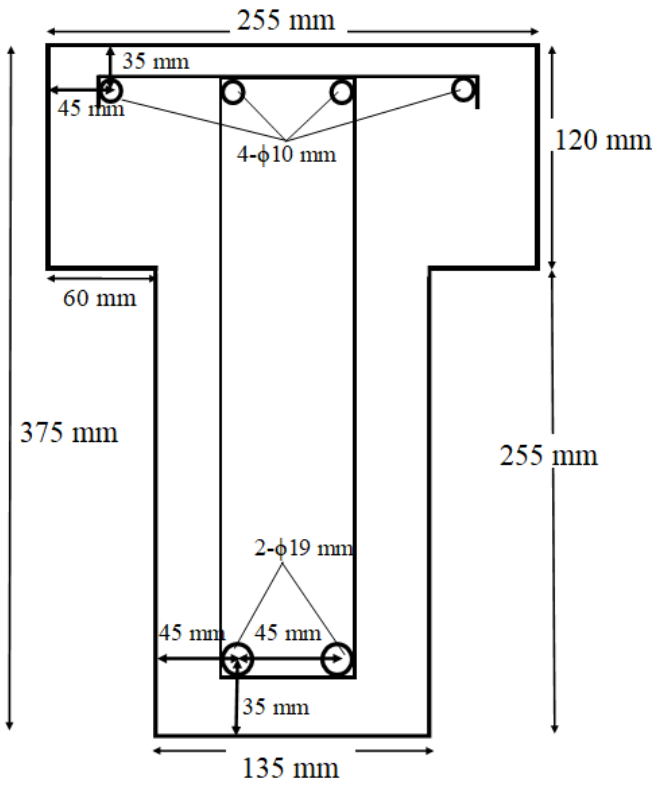

(a) T-section

Figure 5.19. Cross-sectional details of UHPC beams of different shapes.

Figure 5.19. (cont'd)

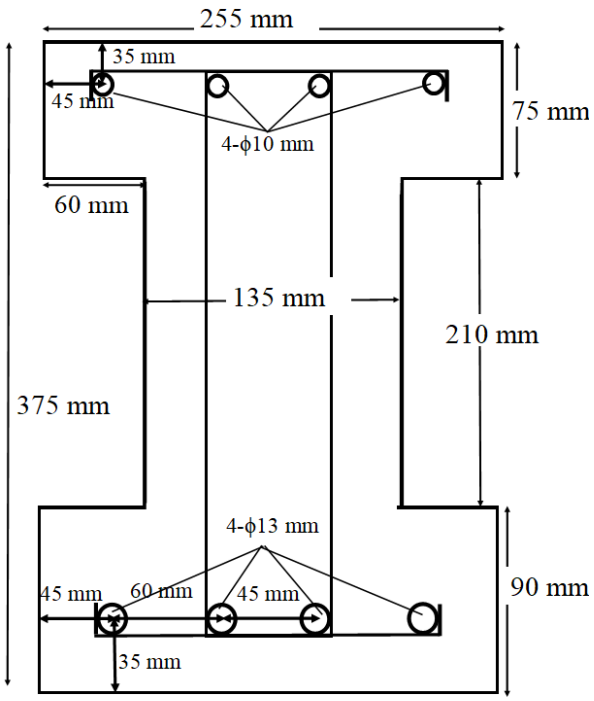

(b) I-section

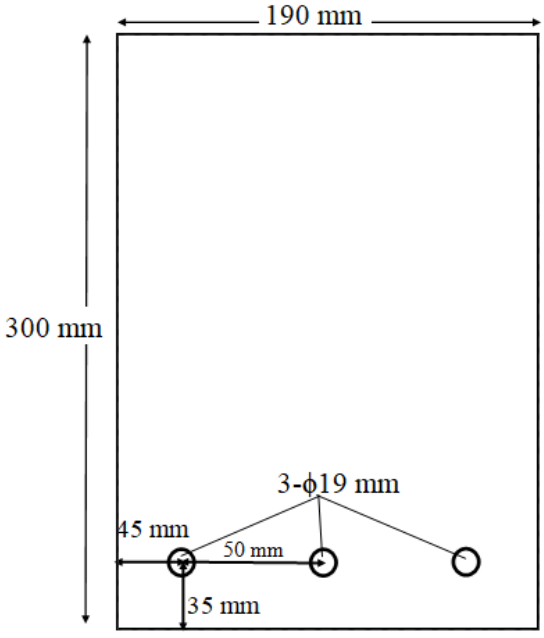

(c) Rectangular section

To assess the influence of specimen shape on the thermal response of UHPC beams of different sectional shapes, the temperatures at corner rebar and concrete mid-depth are plotted in Figure 5.20. In all the beams, the progression in temperatures at corner rebar is faster than temperatures at concrete mid-depth due to the closeness of corner reinforcement to the bottom and side fire exposed surfaces. The temperature progression in corner rebars is similar in all the beams due to the provision of same cover thickness to tensile reinforcement. However, the temperatures at concrete mid-depth are significantly higher in I-section and T-section beams as compared to rectangular beam. This can be attributed to the lower thermal mass resulting from smaller width (135 mm) in I-section and T-section beams, which causes more heat propagation as compared to the width of rectangular beam (190 mm).

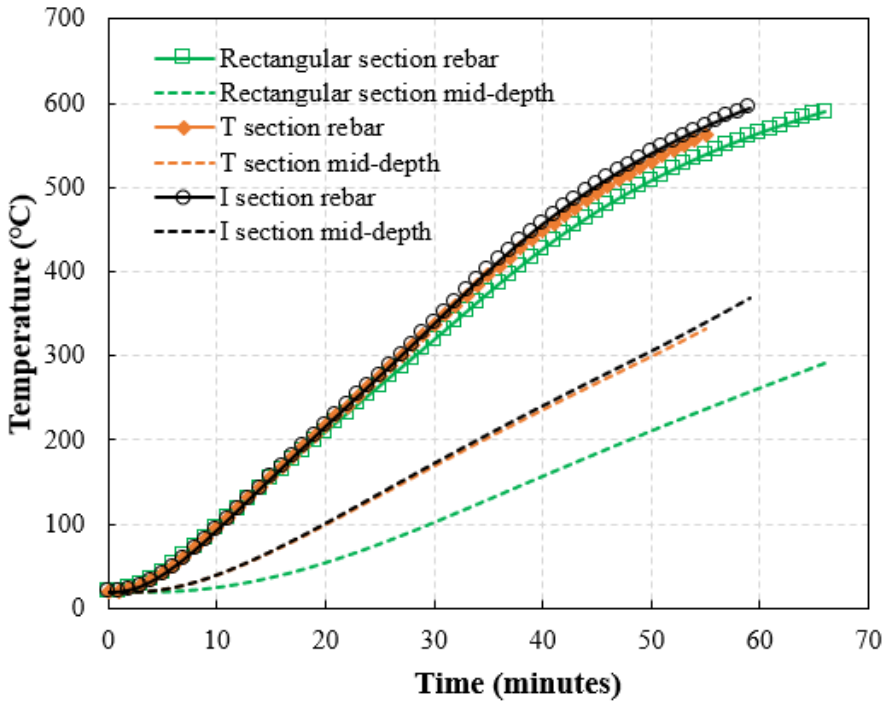

Figure 5.20. Effect of specimen shape on temperatures at rebar and mid-depth of UHPC beams.

All the UHPC beams experienced spalling and the extent of spalling in the analyzed beams is plotted in Figure 5.21 as a function of fire exposure time. The amount of spalling was lower in I-section (2%) and T-section beams (3.3%), which was lower than that in rectangular beam, 5.9%.

The lower spalling in I and T beams is due to the lower thermal gradients in the slender portion of the beams, wherein moisture migration can readily occur as compared to the wide cross-section of rectangular beam which hinders moisture movement within the beam due to the dense microstructure of UHPC. The rise in mid-span deflections in the analyzed beams of different sectional shapes is plotted in Figure 5.22. All the beams failed through strength criteria prior to reaching the deflection limit due to rapid degradation of mechanical properties owing to high rebar temperatures of above 500℃ within the first 45 min of fire exposure. Despite lower extent of spalling, its impact on fire resistance of the slender beams was detrimental. The T-section and I-section UHPC beams underwent higher deflections and had lower fire resistance of 55 min and 60 min respectively, as compared to the rectangular UHPC beam which failed later at 66 min. The thinner cross-sections in non-rectangular members specifically in stem region lead to higher heat transmission (as shown in Figure 5.20) which in turn leads to faster degradation of strength and stiffness properties of concrete and steel, resulting in early failure in contrast to conventional rectangular beam.

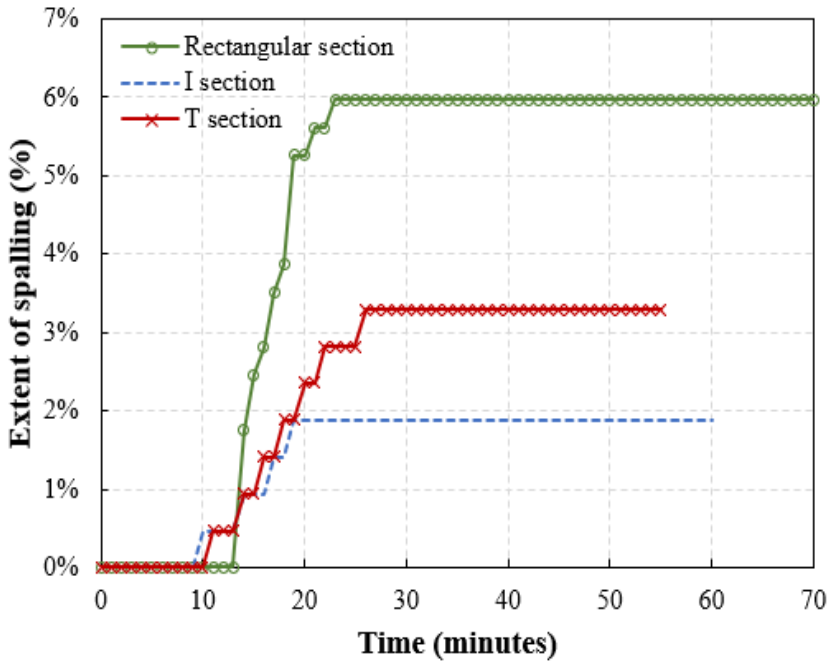

Figure 5.21. Effect of specimen shape on extent of spalling in UHPC beams.

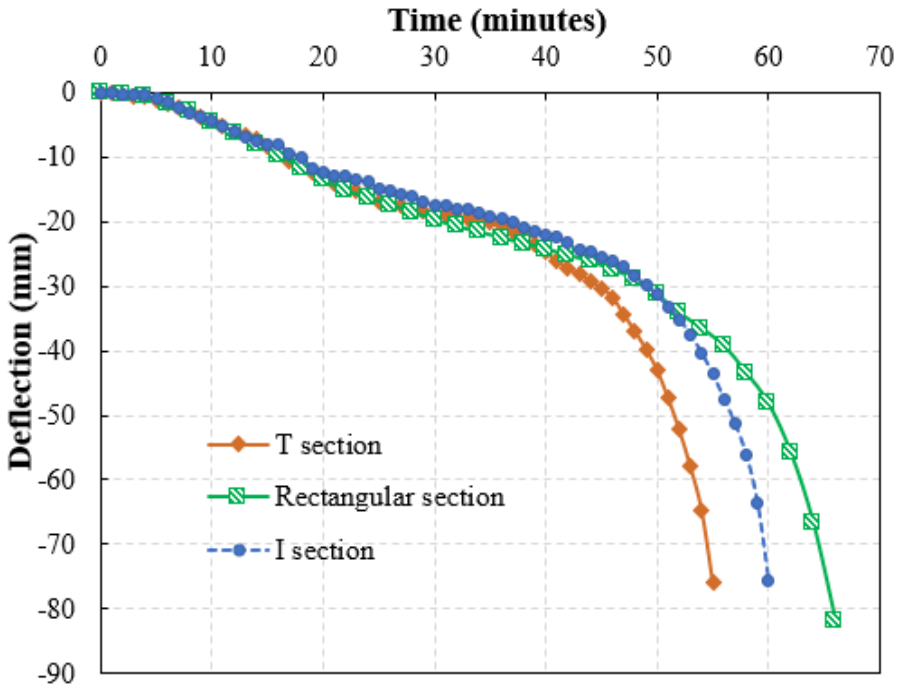

Figure 5.22. Effect of specimen shape on deflections in UHPC beams.

5.3.4.7. Effect of sectional dimensions

The influence of sectional dimensions on the fire resistance of UHPC beams is studied by analyzing five UHPC beams of different cross-sectional sizes as summarized in Table 5-2, subjected to ASTM E119 fire exposure and 50% of their respective load ratio. The clear cover thickness to tensile reinforcement and reinforcement ratio were maintained constant as 28 mm and 0.09% respectively, in all the beams in the analysis. Additionally, every beam was designed to have the same width to depth ratio of 1.5. The progression of temperatures at corner rebar and mid-depth as a function of fire exposure time is plotted in Figure 5.23. The rebar temperatures rise at a similar rate in all the beams, which is on expected lines due to the same cover thickness to tensile reinforcement in the analyzed beams. The influence of sectional dimensions can be clearly seen in the trends of temperature rise at mid-span. As the sectional size of the beam increases, heat transmission in the cross-section reduces, due to higher thermal mass provided by larger sections and thus, resulting in significantly lower temperatures at mid-depth.

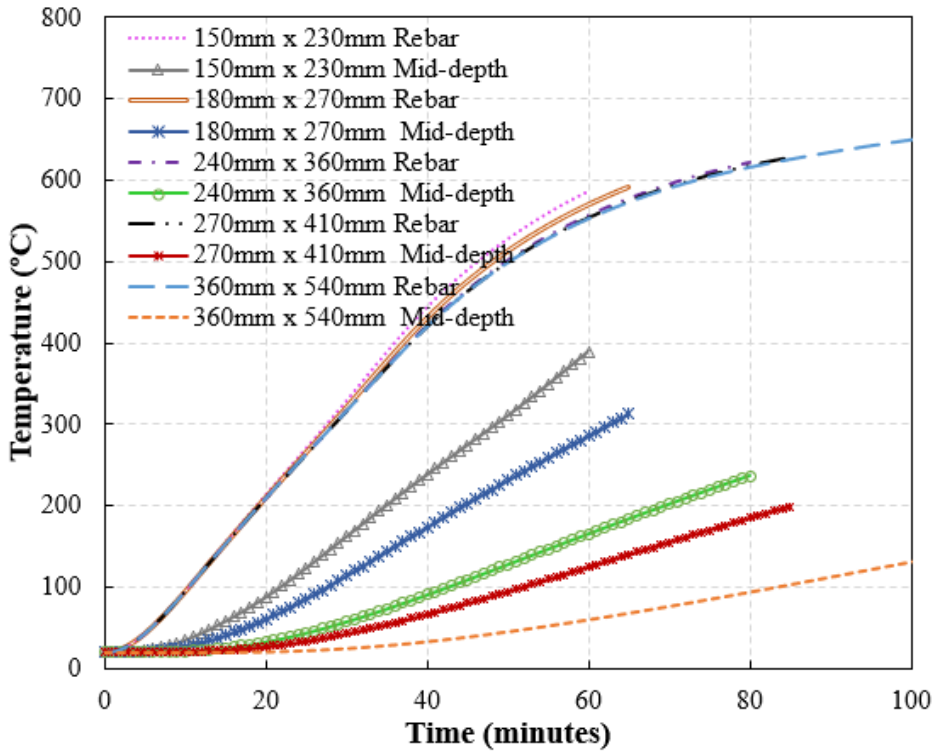

Figure 5.23. Effect of specimen dimensions on temperature rise at corner rebar and mid-depth of UHPC beams.

Figure 5.24 shows the effect of sectional size on spalling response as a function of fire exposure time. The results indicate that extent of spalling reduces with increasing cross-section of UHPC beam. This can be attributed to the considerably lower temperatures in the concrete layers of the larger sections impeding moisture evaporation, migration, and build up of pressure for inducing spalling. Also, degradation of strength properties for resisting spalling-inducing stresses is slower due to lower sectional temperatures in beams with higher sectional size.

Figure 5.25 shows the deflections of the analyzed beams and it can be seen that the deflections rise at a faster rate for beams with smaller dimensions. While the fire resistance of the beam of size 150 mm x 230 mm is 53 min, the fire resistance of the beam of size 360 mm x 540 mm is 96 min. Thus, increasing member size increases the fire resistance of the member (see Table 5-5). This is

due to slower capacity degradation of the beam owing to lower temperatures within the cross section and lower extent of spalling.

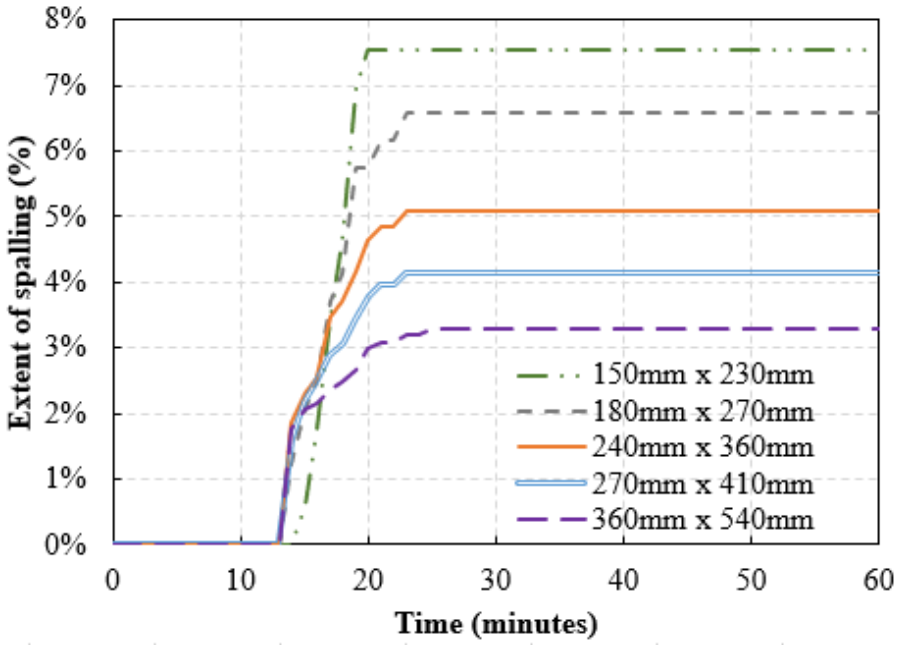

Figure 5.24. Effect of specimen dimensions on extent of spalling in UHPC beams.

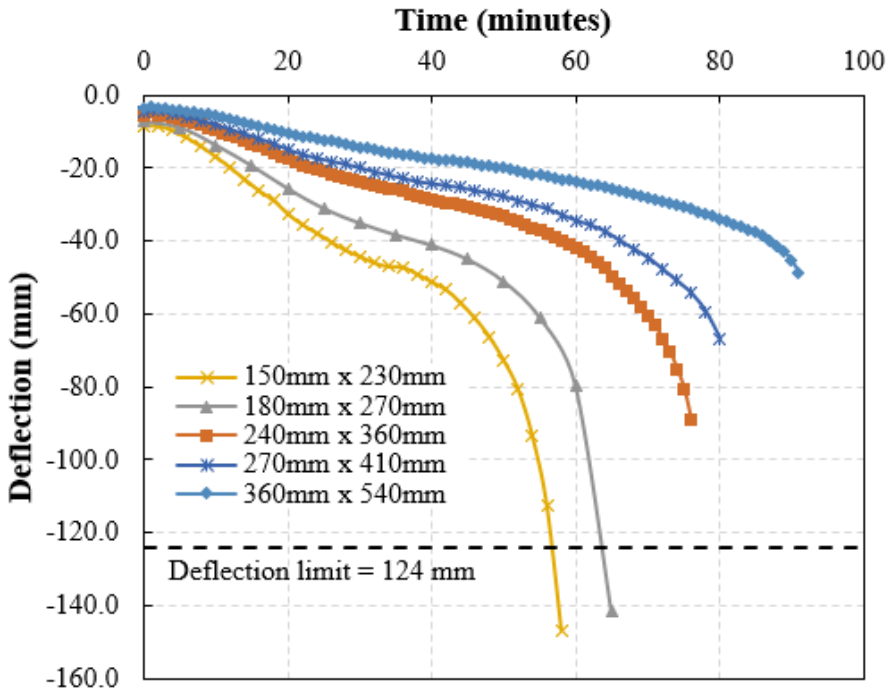

Figure 5.25. Effect of specimen dimensions on deflection of UHPC beams.

As per ACI 216, the minimum width of RC beam for 1 hour fire rating is specified as 127 mm with minimum cover thickness of 19 mm. However, the fire resistance of the analyzed UHPC beam having dimensions of 150 mm x 230 mm and cover thickness of 28 mm is lower than 1 hour. For comparison, NSC and HSC beams with same sectional dimensions of 150 mm x 230 mm, cover thickness of 28 mm, and same moment capacity of 41 kNm as the UHPC beam were analyzed, and the progression in deflections with fire exposure time is plotted in Figure 5.26. According to the analysis, the fire resistance of the NSC beam is 97 min and that of HSC beam is 87 min. Unlike the UHPC beam, both NSC and HSC beams can attain fire resistance of greater than 1 hour. Thus, utilizing ACI 216 for the prediction of fire resistance of UHPC beams is not practical and provides unrealistic and unreliable fire ratings.

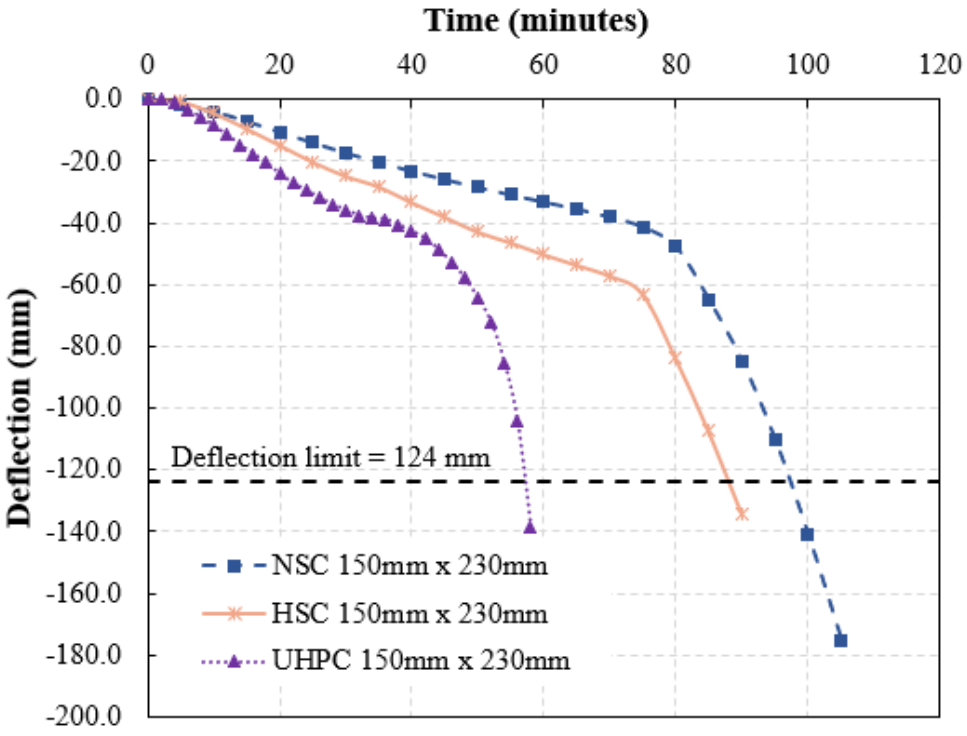

Figure 5.26. Deflections of beam with dimensions 150 mm x 230 mm made using different concrete types.

To determine the optimum minimum cover thickness for UHPC beams with different sectional sizes in order to attain fire resistance ratings of 1-3 hours, additional cases are run. Since the fire

resistance of UHPC beam with width of 150 mm was lower than 1 hour, the iterations were carried out on the other four beams in Table 5-2 having larger sectional sizes. From the analysis, the minimum width and cover thickness for 1 hour rating were found to be 180 mm and 28 mm respectively. The variation of deflection in the typical UHPC beams made using steel fibers (UHPC-St) and also UHPC beams made with both steel and polypropylene fibers (UHPC-StPP) of varying sectional sizes are plotted in Figure 5.27. The cover thickness was increased from 28 mm to 76 mm with reasonable size increments and the minimum cover thickness was determined for the different fire ratings of 1 hour, 1.5 hours, 2 hours, and 3 hours, similar to the ratings provided in ACI 216 for conventional concrete.

For minimum width of 180 mm, UHPC-St beam can attain fire rating of 1 hour with cover of 28 mm and UHPC-StPP beam can attain fire rating of 1.5 hours with cover of 44 mm. For minimum width of 240 mm, UHPC-St beam can attain fire rating of 2 hours with concrete cover of 64 mm and UHPC-StPP beam can attain fire rating of 2 hours with a lower cover thickness of 51 mm. For minimum width of 270 mm, UHPC-St beam can attain fire rating of 2 hours with concrete cover of 44 mm and UHPC-StPP beam can attain fire rating of 3 hours with a cover thickness of 76 mm. For minimum width of 360 mm, UHPC-St beam can attain fire rating of 3 hours with concrete cover of 64 mm and UHPC-StPP beam can attain fire rating of 3 hours with a lower cover thickness of 57 mm. As shown in Figure 5.27, UHPC beams with polypropylene fibers could attain higher fire resistance than the UHPC beam without polypropylene fibers, due to lower spalling and slower rise in sectional temperatures. Further, as sectional size is increased, higher fire ratings can be attained with a lower increase in cover thickness.

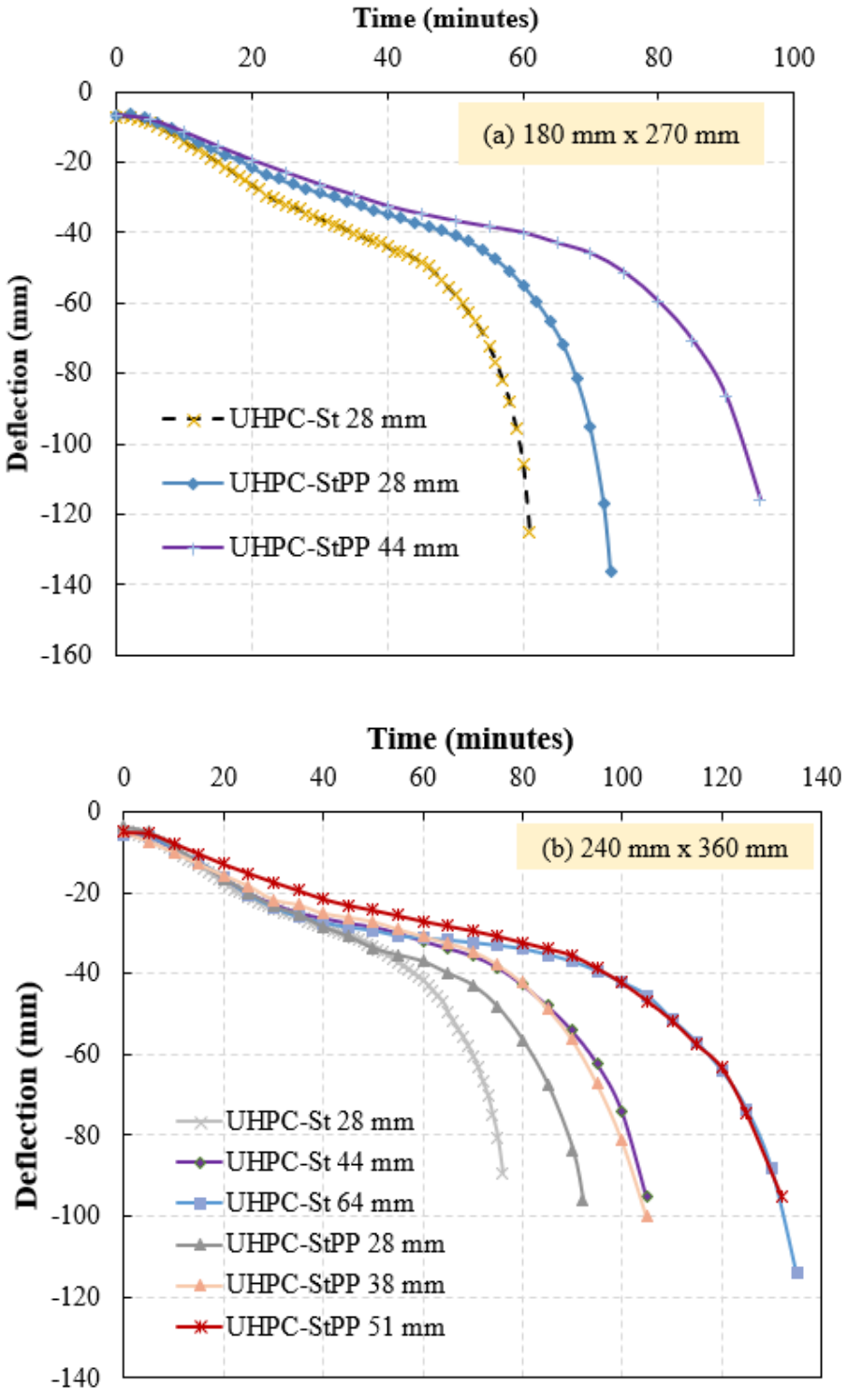

Figure 5.27. Deflections of UHPC beams with varying sectional sizes and cover thicknesses.

Figure 5.27. (cont'd)

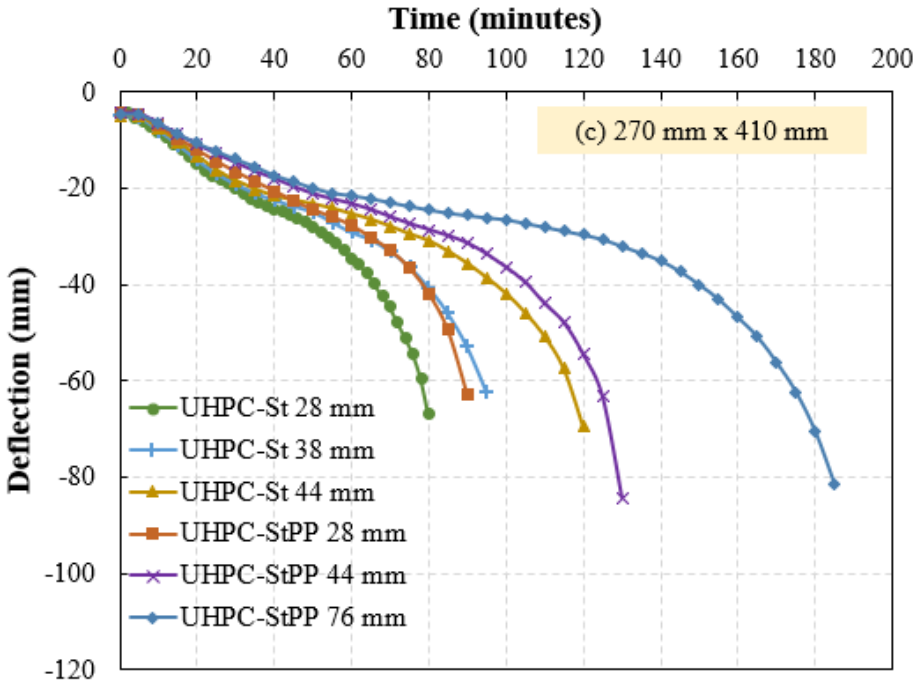

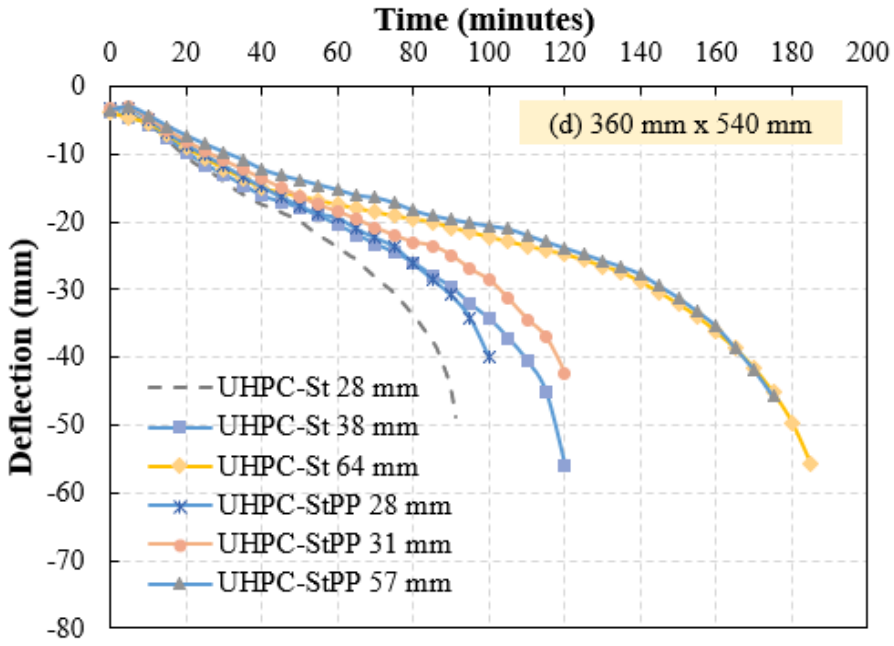

5.3.4.8. Effect of span length

To study the effect of varying span lengths on the fire response of UHPC beams, four beams with different span lengths of 3.66 m, 5 m, 6.5 m, and 8 m were analyzed under standard ASTM E119 fire exposure and 50% load level. The sectional temperatures and level of spalling at mid-span were similar in all the analyzed beams owing to the same fire exposure and same moment due to structural loading at mid-span. However, rebar temperatures in the portion of the beam between the end support and point load, for the beam with span length of 3.66 m were higher than the other beams with a greater span length, as shown in Figure 5.28. This can be attributed to the fluctuations in level of spalling along the beam length due to varying applied moment associated with varying span length.

The predicted spalling at the end of fire exposure along with the lengthwise beam segments together with the applied bending moment is plotted in Figure 5.29 for two beams with span lengths of 3.66 m and 8 m. The segments close to mid-span of the beam are subjected to higher mechanical stresses due to higher bending moment, which in turn enhances cracking and also increases permeability. The increased permeability results in lower pore pressure and a relatively lower extent of spalling. Since the applied moment is same for the analysis, the level of spalling is same for the beams in the mid-portion between the two load-points. The applied moment decreases in the segments away from the mid-span, which in turn results in lower cracking and lower permeability leading to a higher extent of spalling in these segments. The differences in spalling along the beam length result in differences in the total extent of spalling in the analyzed beams as summarized in Table 5-5. The extent of spalling in the beam with span length of 3.66 m is 6.58%, whereas spalling in the beam with span length of 8 m is 3.92%. Overall, the extent of spalling is lower in UHPC beams with higher span length.

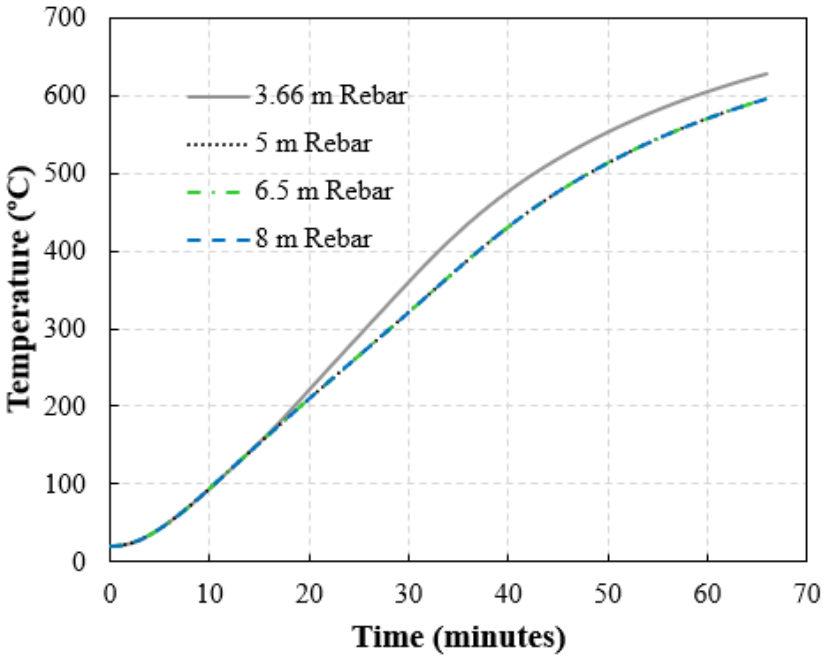

Figure 5.28. Effect of span length on corner rebar temperatures at L/5 from support in UHPC beams.

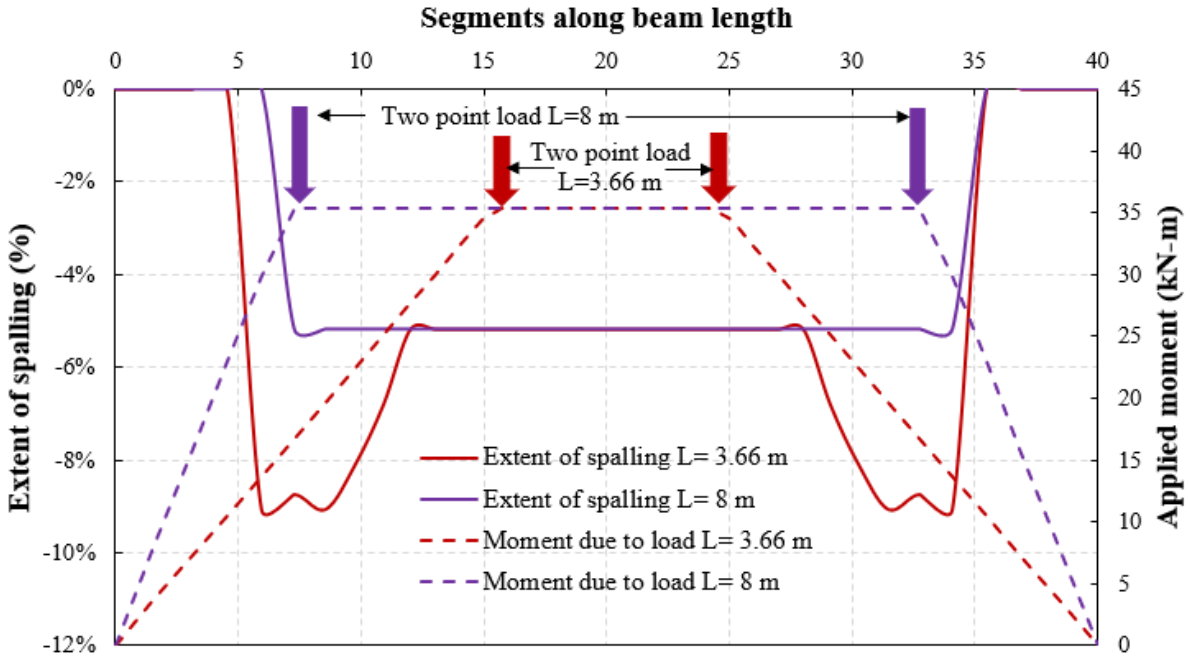

Figure 5.29. Effect of span length on extent of spalling in UHPC beams.

Figure 5.30 shows the mid-span deflections of the analyzed beams with varying span length. It can be seen from the figure that the deflection of all the UHPC beams increases with fire exposure

time. However, mid-span deflection increases with an increasing span length of the beams. Deflections are computed in the analysis by integrating curvature which accounts for changes in stiffness along the beam length. With increasing span length, the flexural stiffness reduces (due to higher span to depth ratio) resulting in higher deflections. Further, the fire resistance of UHPC beams as computed based on deflection failure criteria slightly decreases with increasing span length. For instance, fire resistance decreases from 63 to 61 minutes upon an increase in span length from 3.66 m to 8 m.

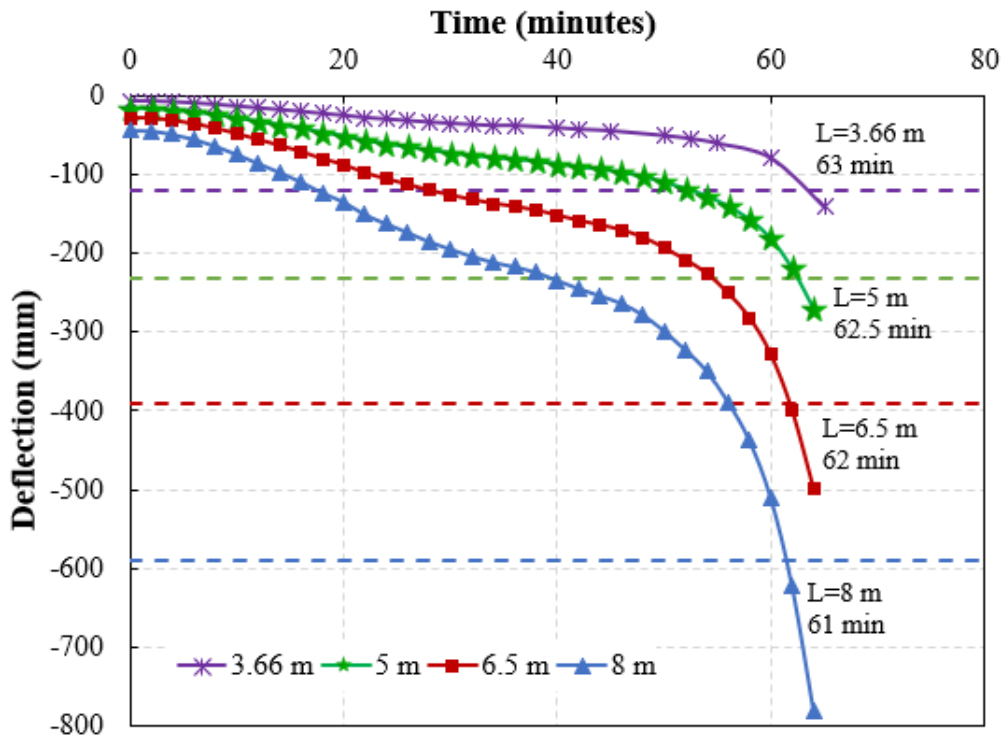

Figure 5.30. Effect of span length on deflection of UHPC beams.

5.3.4.9. Effect of loading type

To assess the influence of loading type on fire resistance of UHPC beams, the simply supported reference UHPC beam B0 is analyzed under two different loads. The first loading pattern is uniformly distributed load (UDL) of 21 kN/m and the second loading type is two point loads of 25 kN each. Both the beams were subjected to ASTM E119 standard fire exposure under equal load

ratio of 50% of the flexural capacity at room temperature (70 kNm). Shear force and bending moment diagrams along the span of the beam under both the loading configurations are plotted in Figure 5.31 and Figure 5.32. Pursuant to the loading type in these two beams, the magnitude of peak bending moment is the same at the critical mid-span section, meanwhile, the resulting shear force distribution along the length of the beams is different as illustrated in Figure 5.31 and Figure 5.32. For the two point loading scenario, a pure bending without any shear is generated between the two loading points, while shear force is non-zero along the entire span length under UDL. However, the level of bending moment is 50% of the moment capacity of the beams, whereas shear force is much lower less than 15% of the shear capacity (257 kN). Hence, in this set of analysis, shear effects are minor and flexure dominates the fire behavior and failure of the analyzed beams.

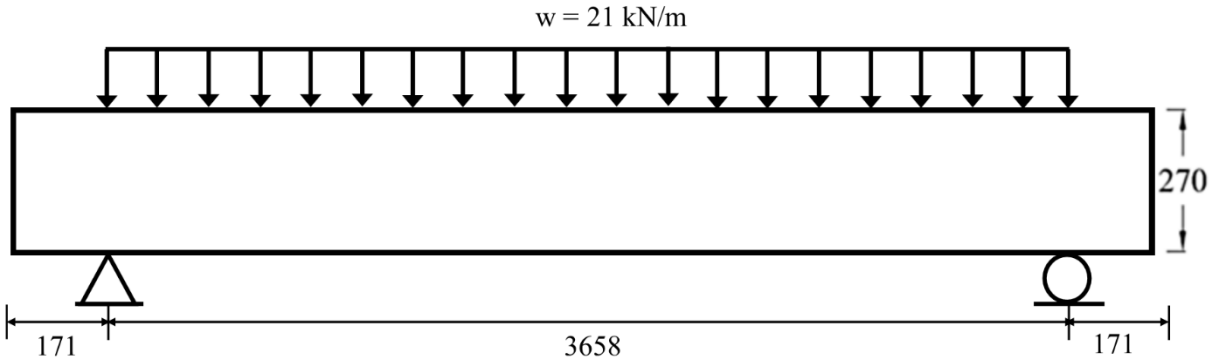

(a) Loading Configuration

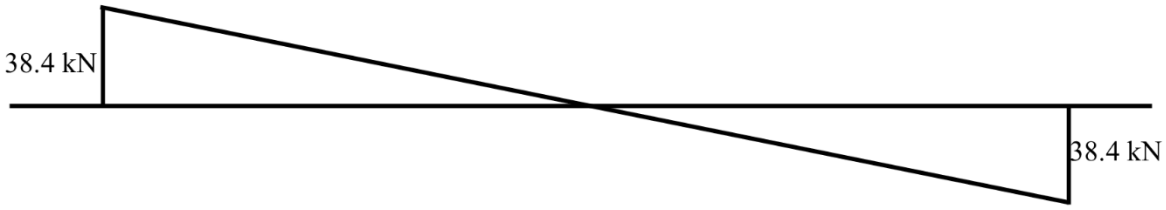

(b) Shear Force Diagram

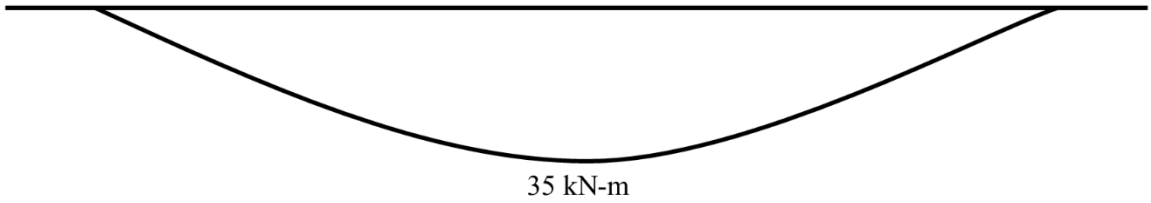

(c) Bending Moment Diagram

Figure 5.31. Uniformly distributed loading on UHPC beam.

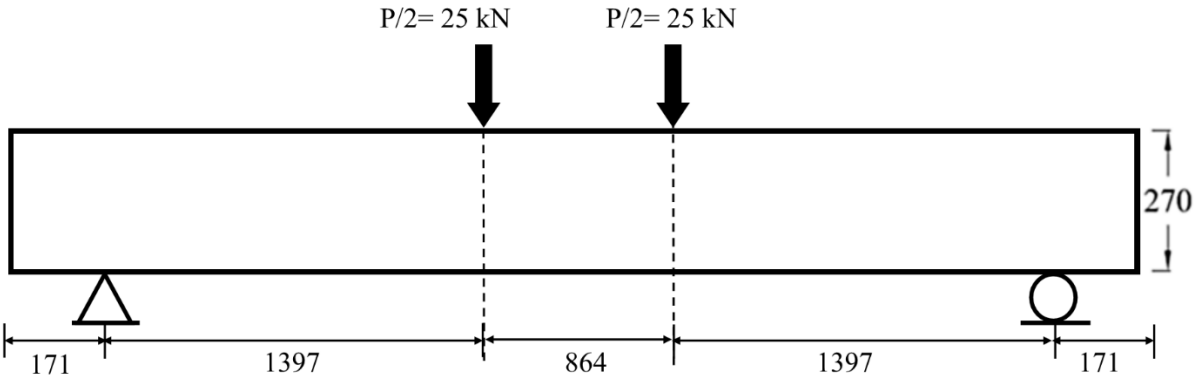

(a) Loading Configuration

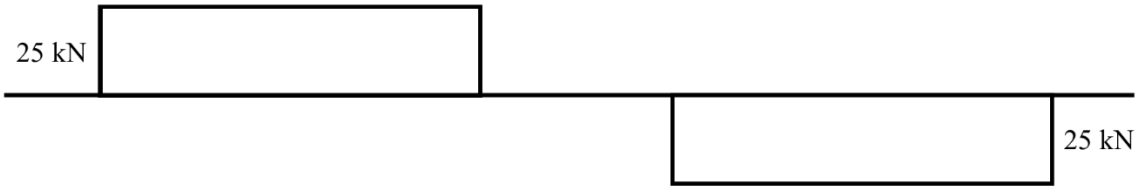

(b) Shear Force Diagram

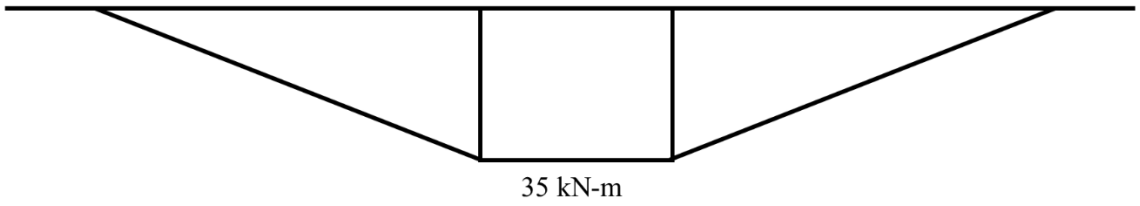

(c) Bending Moment Diagram

Figure 5.32. Two point loading on UHPC beam.

As a result of the same fire exposure, beam dimensions, load ratio, and flexure-dominant loading in the two beams, the temperature gradient, pore pressure, and stresses were similar. Consequently, the thermal response, extent of spalling, deflections, and fire resistance were similar in the analyzed beams. The progression of mid-span deflection of the beams is shown in Figure 5.33. The deflection response of the beam is computed along the length of the beam and is governed by

the level of stresses due to the bending moment in the particular section. For the UHPC beam subjected to UDL, the maximum moment occurs at the mid-span while for the UHPC beam subjected to two point loading, the region between the two point loads experiences maximum levels of bending moment. However, as shown in Figure 5.34, the resulting bending moment from both the loading patterns are similar with minimal differences. This leads to similar mid-span deflections and fire resistance in the analyzed UHPC beams. The response of UHPC beams under shear dominant loading might be different due to variations in developed stresses in the beam, and further studies are required in the future to characterize this behavior.

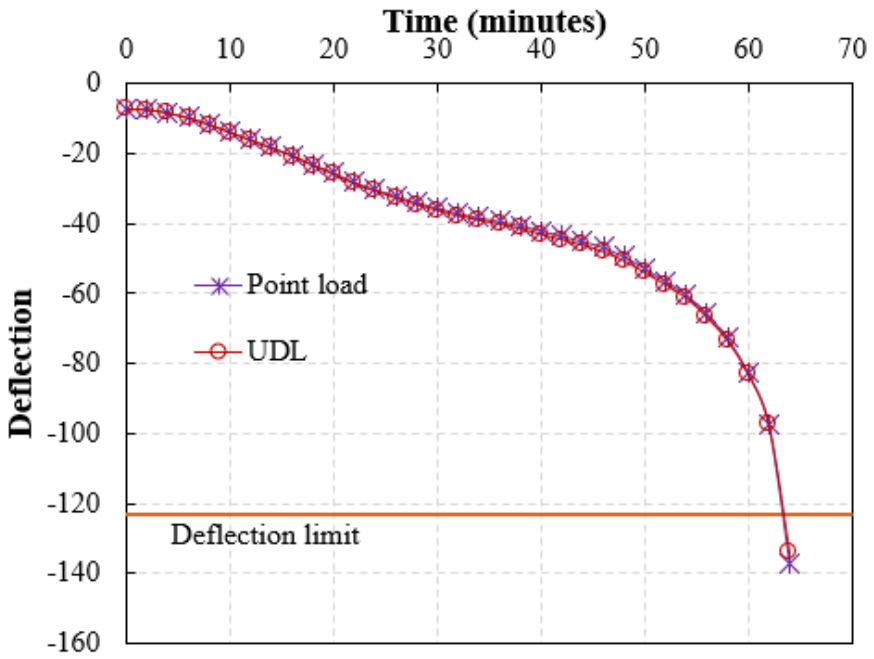

Figure 5.33. Effect of loading type on deflection of UHPC beams.

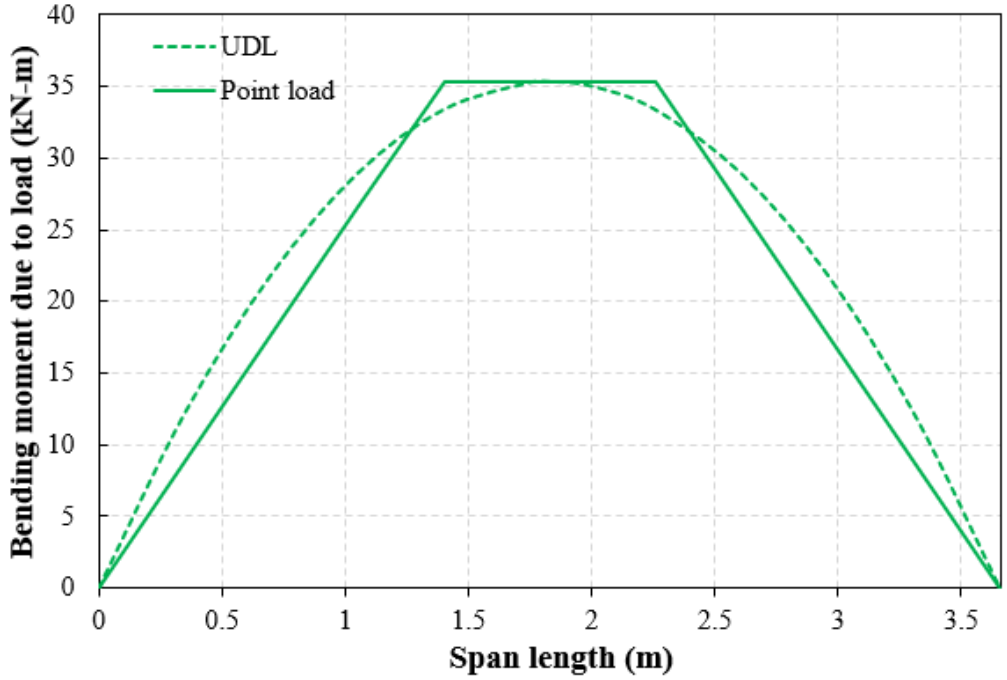

Figure 5.34. Bending moment along span length of UHPC beams under different loading type.

5.3.4.10. Effect of varying dosage of steel fibers

To study the influence of the amount of steel fibers on the fire response of UHPC beams, UHPC with varying dosage of steel fibers of 0.75%, 1.5%, 2.25%, and 3% by volume were utilized. Initial strength properties for UHPC with different volume fractions of steel fibers were incorporated as summarized in Table 5-3, based on room temperature material property tests conducted by Wu et al. [168] which implied that the compressive and tensile strength of UHPC increased with increasing steel fiber dosage. As an illustration, the compressive and tensile strength of UHPC with 0.75% steel fibers are 157 MPa and 5 MPa respectively, whereas for UHPC with 3% steel fibers, compressive strength is 182 MPa and tensile strength is 9.5 MPa. Preliminary studies on high-temperature mechanical properties by Zheng et al. [52] have shown that the rate of relative strength degradation with temperature is not influenced by the dosage of steel fibers. Therefore, the room temperature mechanical properties were extended to high temperature utilizing the empirical relations developed in section 3.5 of this thesis. It should be noted that there is a lack of

data on high-temperature material property variation of UHPC with different amounts of steel fiber.

Table 5-3. Effect of varying content of steel fibers on strength of UHPC.

Case	Beam	Steel fibers content (% by volume)	Room temp. compressive strength f'c (MPa)	Room temp. direct tensile strength f't (MPa)
1	UHPC-B29	0.75	157	5
2	UHPC-B0	1.5	175	6
3	UHPC-B30	2.25	178	7.5
4	UHPC-B31	3	182	9.5

All the UHPC beams were subjected to ASTM E119 standard fire exposure and 50% load ratio of capacity at room temperature. The thermal response of UHPC beams with 0.75%, 1.5%, 2.25%, and 3% of steel fibers by volume, is illustrated in Figure 5.35 by plotting comparative the temperature progression in corner rebar and concrete mid-depth as a function of fire exposure time. The rise in temperatures at mid-depth and rebar occurs at different rates with increasing fire temperatures, with lower temperatures at concrete mid-depth in all the beams than that in the rebar. This is attributed to the lower thermal conductivity of concrete and location of the rebar being closer to the periphery of the fire exposed surface. It can be observed from Figure 5.35 that the rate of rise in temperatures at rebar and mid-depth is slower in the UHPC beam with 3% steel fibers than the other UHPC beams with lower dosage of steel fibers. This can be attributed to the much lower extent of spalling (2.8%) in the UHPC beam with 3% steel fibers as compared to higher amount of spalling (in the range of 5.7-7.8%) in the other UHPC beams. The higher temperatures in other beams with lower dosage of steel fiber resulted from loss of concrete due to fire-induced spalling. Figure 5.36 shows the comparative extent of spalling in the analyzed UHPC beams as a function of fire exposure time. It can be seen from the figure that extent of spalling decreases with increase in volume of steel fibers, and this can be attributed to the improved tensile

strength of UHPC facilitated by the steel fibers. Due to the enhanced tensile strength in UHPC with increasing content of steel fiber, the resistance to the internal tensile stresses developed from pore pressure, thermal gradients, and mechanical loading is improved and in turn, the extent of spalling is minimized.

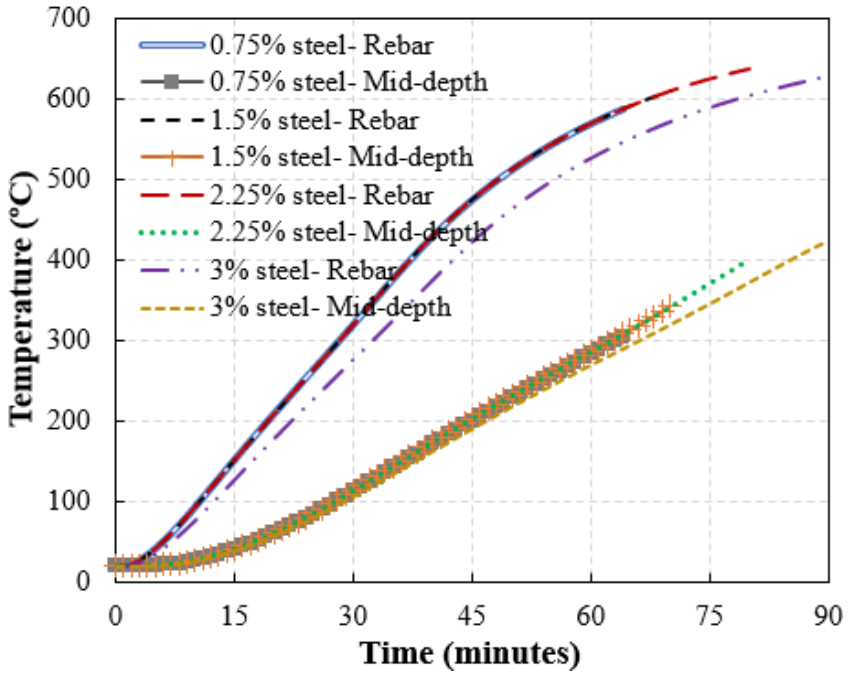

Figure 5.35. Effect of steel fibers on temperature rise at corner rebar and mid-depth of UHPC beams.

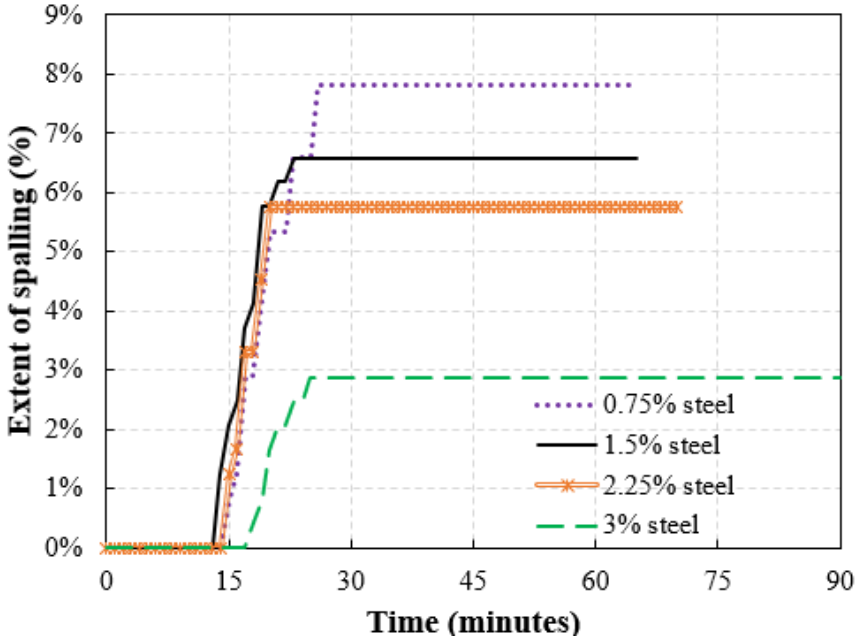

Figure 5.36. Effect of steel fibers on extent of spalling in UHPC beams.

Figure 5.37 shows the comparative variation of mid-span deflection as a function of fire exposure time. In the early stages of fire exposure till 40 min, the response of all the UHPC beams with different dosage of steel fibers is similar due to adequate strength and stiffness in the beams for resisting the applied load level of 50% of their capacity at room temperature. Beyond 45 min into fire exposure, the rate of deflection increase in fire-exposed UHPC beams becomes gradual and slower with increase in steel fiber content. The UHPC beams with higher steel fiber content have higher initial strength than the UHPC beams with lower steel fiber content. Higher initial strength leads to slower degradation of material properties and reduced loss of concrete cross section (due to the lower fire-induced spalling) in these beams with higher amount of steel fibers. Thus, relatively lower deflections and higher fire resistance is experienced by UHPC beams with higher steel fiber content. According to the results of this analysis, the fire resistance of UHPC beams can be increased to 74 min by incorporating 3% by volume steel fibers as compared to fire resistance of 60 min by including 0.75% steel fibers.

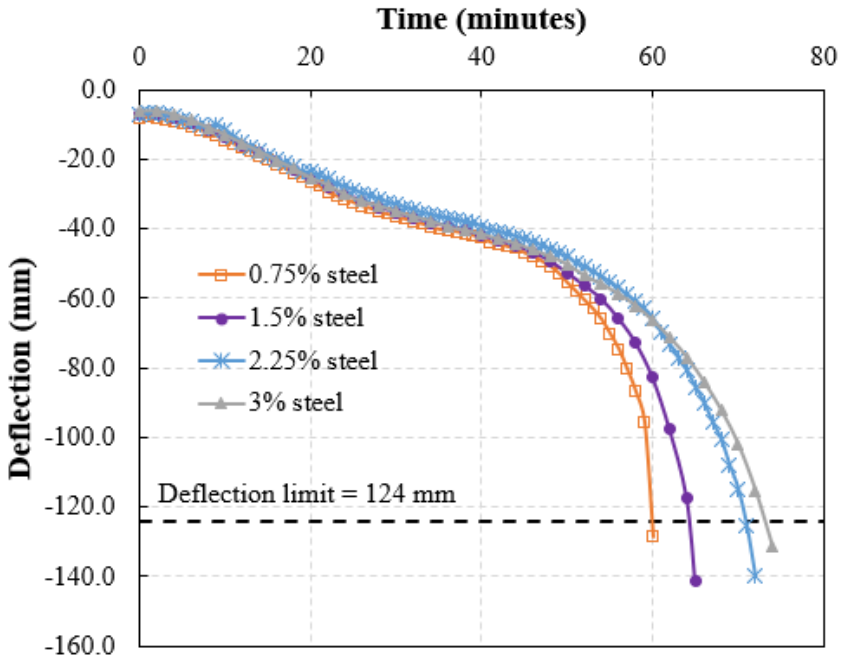

Figure 5.37. Effect of steel fibers on deflection of UHPC beams.

5.3.4.11. Effect of varying dosage of polypropylene (PP) fibers

To evaluate the influence of varying dosage of polypropylene (PP) fibers on the fire response of UHPC beams, four UHPC beams with 0%, 0.1%, 0.2%, and 0.3% by volume PP fiber content were analyzed. All the beams were assumed to contain 1.5% by volume of steel fibers. All four beams were loaded with 50% of their room temperature capacity and exposed to ASTM E119 standard fire exposure. The relative increase in permeability due to the melting of PP fibers at 160℃ is dependent on the fiber dosage amount and is computed in the program according to the fiber percolation theory discussed in section 4.4.2. Additionally, increasing PP fiber dosage results in lower strength (summarized in Table 5-2) due to lower density and introduction of weaker zones in the concrete matrix. The compressive strength of beams with 0%, 0.1%, 0.2%, and 0.3% PP fibers is 175, 162, 151, and 143 MPa. The effect of PP fibers on tensile strength is not significant and ranges from 6 to 5.2 MPa for the considered amounts of PP fiber.

Table 5-4. Effect of varying content of polypropylene fibers on strength of UHPC.

Case	Beam	Polypropylene fibers content (% by volume)	Room temp. compressive strength f'c (MPa)	Room temp. direct tensile strength f't (MPa)
1	UHPC-B0	0	175	6
2	UHPC-B32	0.1	162	5.8
3	UHPC-B33	0.2	151	5.5
4	UHPC-B34	0.3	143	5.2

The thermal response of the four UHPC is compared in Figure 5.38 by plotting corner rebar and concrete mid-depth temperatures as a function of fire exposure time. The temperatures of the beam without any PP fibers increased at a faster rate compared to the other beams and this can be attributed to the highest extent of spalling (6.58%) in this beam, as shown in Figure 5.39. Spalling results in loss of concrete cross-section and higher transmission of heat, resulting in higher temperatures. It can be seen that the steel rebar temperatures in the beams with PP fiber are

identical since spalling was concentrated at upper portions of the beam due to the release of pore pressure through tensile cracking in the region near tensile reinforcement. The effect of varying PP dosage and corresponding spalling on temperatures can be seen at mid-depth wherein the beam with the lowest amount of PP fiber (0.1%) has a higher temperature rise as compared to beams with 0.2% and 0.3% of PP fibers. The temperature rise at mid-depth is similar in beams with 0.2% and 0.3% PP fibers due to a similar extent of spalling (below 1%).

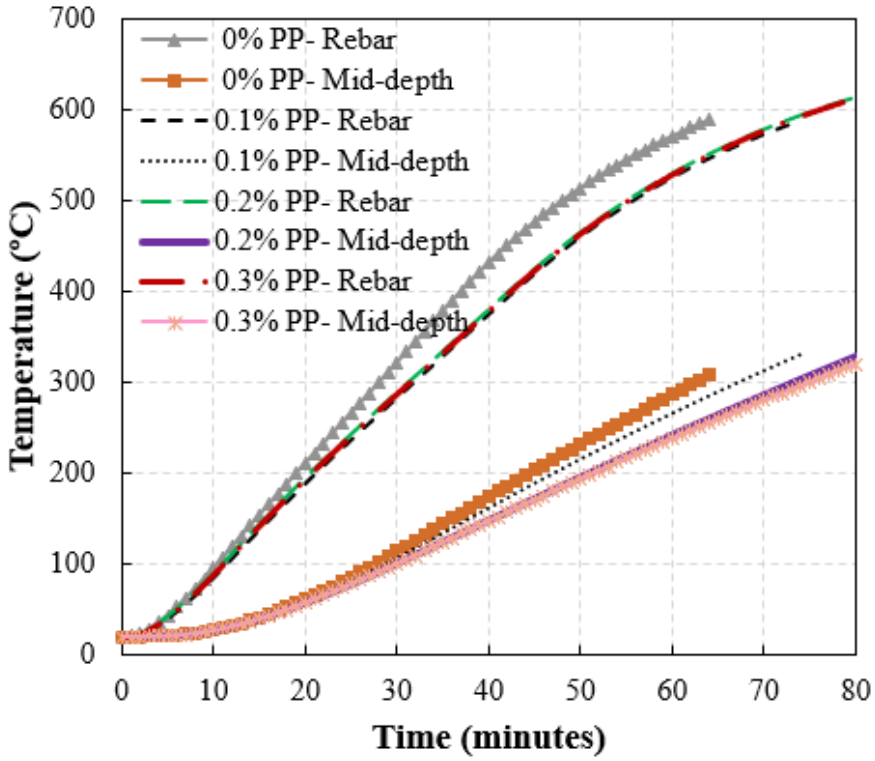

Figure 5.38. Effect of polypropylene fibers on temperature rise at corner rebar and mid-depth of UHPC beams.

The progression of extent of spalling with fire exposure time is plotted in Figure 5.39. It can be seen that the extent of spalling decreases with increase in PP dosage, and even spalling is completely suppressed upon addition of 0.3% PP fiber. The reduction in extent of spalling with increase in amount of PP fibers can be attributed to higher increase in permeability due to well-connected formation of micro-channels upon melting of PP fiber facilitating dissipation of high

pore pressure generated within a concrete member. The variation of pore pressure with fire exposure time for the analyzed beams at 30 mm from the exposed right surface and 60 mm depth from the top surface is plotted in Figure 5.40. It can be observed from Figure 5.40 that a peak pore pressure of 5.8 MPa, 4.2 MPa, 3.4 MPa, and 2.6 MPa develops in UHPC beams with 0%, 0.1%, 0.2%, and 0.3% PP fiber respectively. The peak pore pressure decreases gradually with an increase in the amount of PP fibers in the concrete mix due to the resultant increase in permeability.

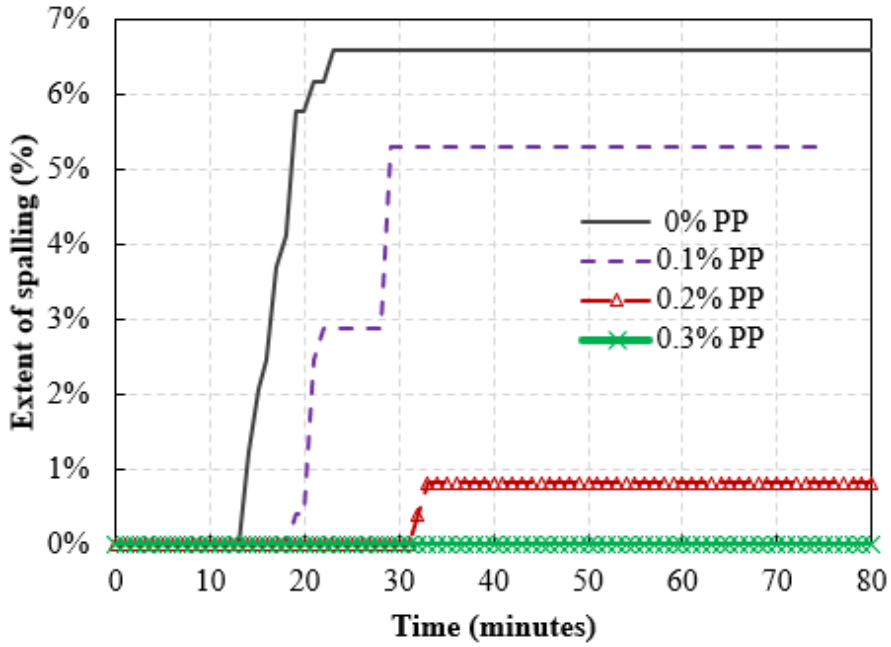

Figure 5.39. Effect of polypropylene fibers on extent of spalling in UHPC beams.

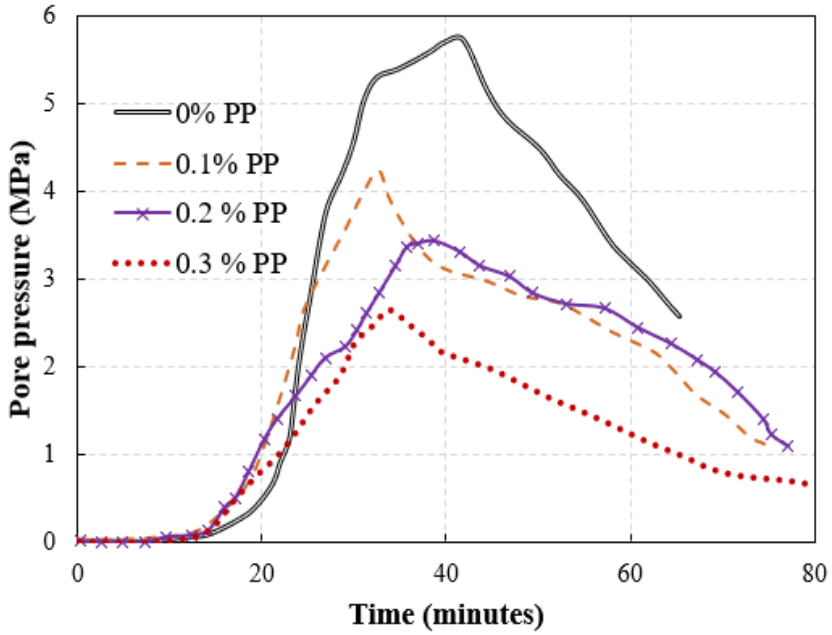

Figure 5.40. Effect of polypropylene fibers on pore pressure in UHPC beams.

The structural response of the four UHPC beams, with varying amount of PP fibers, is compared in Figure 5.41, by plotting the variation in mid-span deflection as a function of fire exposure time. Overall, it can be seen that the beam without PP fibers experienced much larger deflections and failed earlier (at 63 min), than the beams with PP fibers throughout the fire exposure. This can be attributed to faster capacity degradation that resulted from the loss of concrete cross section due to severe spalling in the beam without any PP fibers. The rise in deflections was slower in the beams with PP fibers due to slower degradation of strength and stiffness properties owing to spalling mitigation facilitated by melting of PP fibers. The overall progression of the beams with PP fibers was similar and with the inclusion of 0.1%, 0.2%, and 0.3% of PP fibers, the fire resistance was 73 min, 74 min, and 76 min respectively. The improvement in fire resistance with an increase in fiber dosage was lower in proportion due to a reduction in strength by adding a higher volume of PP fibers.

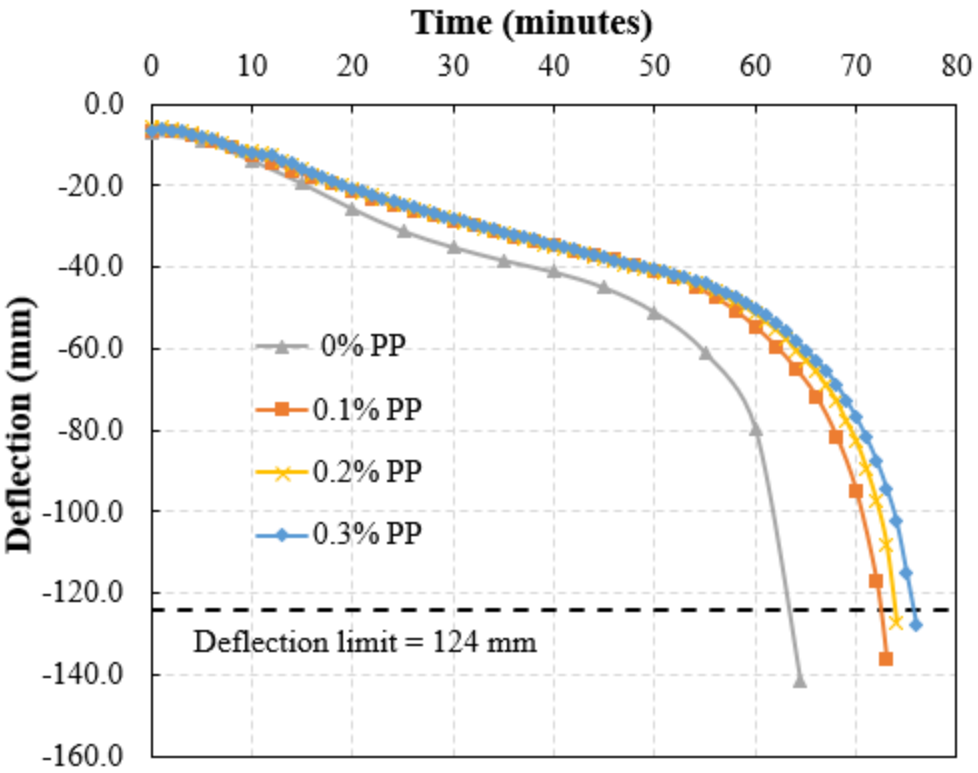

Figure 5.41. Effect of polypropylene fibers on deflection of UHPC beams.

5.3.4.12. Effect of shear reinforcement (and compression bars)

UHPC possesses high compressive and tensile strength, as well as high ultimate tensile strain and ductility, and this can be utilized to realize high shear capacity in UHPC beams. Room temperature studies in the literature have shown that, unlike conventional concrete beams, UHPC beams without shear and compression reinforcement exhibit a similar response as beams with stirrups, without reduction in load carrying capacity and ductility [193–195]. However, the removal of stirrups from beams is not recognized by building design codes (ACI 318 [116]). Moreover, no studies have been undertaken at elevated temperatures to gauge the feasibility of removing stirrups from UHPC members. Under shear dominant loading (as discussed in section 5.3.4.9), the contribution of stirrups and steel fibers in resisting shear forces is critical for determining shear capacity and failure mechanism of UHPC beams.

Due to the lack of fire tests on UHPC beams under shear for model validation, the effect of shear reinforcement cannot be investigated in the current study. In addition, the confinement effect and shear strength provided by stirrups in the beams are not explicitly considered in the developed numerical model. This is because the focus of the thesis is primarily on flexure-dominant loading with no shear between the two point loads utilized in the experimental part of the study. Further studies are needed in the future to specifically study the feasibility of removing shear reinforcement in UHPC beams under fire conditions.

Table 5-5. Summary of varied parameters and results from parametric study.

Varied Parameter	**Beam Designation**	**Parameter Value**	**Fire Resistance (min)**	**Extent of spalling**
Load level	UHPC-B1	Load level-30% of room temperature capacity	87	13.17%
	UHPC-B2	Load level-40% of room temperature capacity	76	8.64%
	UHPC-B0	Load level-50% of room temperature capacity	63	6.58%
	UHPC-B3	Load level-60% of room temperature capacity	55	5.76%
	UHPC-B4	Load level-70% of room temperature capacity	46	5.76%
Fire scenario	UHPC-B0	ASTM E119	63	6.58%
	UHPC-B5	ASTM E1529 (Hydrocarbon)	50	6.17%
	UHPC-B6	Design Fire 1	107	5.35%
	UHPC-B7	Design Fire 2	NF	6.58%
	UHPC-B8	Design Fire 3	50	6.17%
Tensile reinforcement ratio	UHPC-B0	3-D13, ρt=0.9%, Moment capacity-70 kNm	63	6.58%
	UHPC-B9	3-D16, ρt=1.24%, Moment capacity-91 kNm	64	6.58%
	UHPC-B10	4-D13, ρt=1.09%, Moment capacity-84 kNm	62	6.58%
	UHPC-B11	4-D16, ρt=1.65%, Moment capacity-112 kNm	63	6.58%

Table 5-5. (cont'd)

Clear cover thickness	UHPC-B12	Bottom-28 mm, Side- 28 mm	61	6.58%
	UHPC-B13	Bottom-34 mm, Side- 28 mm	63	6.58%
	UHPC-B14	Bottom-44 mm, Side- 28 mm	67	6.58%
	UHPC-B0	Bottom-28 mm, Side- 38 mm	63	6.58%
	UHPC-B15	Bottom-34 mm, Side- 38 mm	67	6.58%
	UHPC-B16	Bottom-44 mm, Side- 38 mm	73	6.58%
Concrete type	UHPC-St-B0	f'c=175 MPa, f't=6 MPa, k0=1.2x10^-18m^2, 1.5% Steel fibers	63	6.58%
	UHPC-StPP-B17	f'c=161 MPa, f't=5.8 MPa, k0=1.2x10^-18m^2, 1.5% Steel and 0.11 %PP fibers	74	5.29%
	NSC-B1	f'c=35 MPa, f't=2.7 MPa, k0=6.5x10^-16m^2, Plain/ no fibers	125	0%
	HSC-B1	f'c=105 MPa, f't=3.6 MPa, k0=2.0x10^-17m^2, Plain/ no fibers	120	4.17%
Specimen shape	UHPC-B18	Rectangular shape	66	5.96%
	UHPC-B19	T shape	55	3.29%
	UHPC-B20	I shape	60	1.88%
Sectional dimensions	UHPC-B21	150mm x 230mm, Moment capacity-41 kNm	53	7.53%
	UHPC-B0	180mm x 270mm, Moment capacity- 70 kNm	63	6.58%
	UHPC-B22	240mm x 360mm, Moment capacity- 129 kNm	74	5.09%
	UHPC-B23	270mm x 410mm, Moment capacity- 165 kNm	80	4.15%
	UHPC-B24	360mm x 540mm, Moment capacity- 379 kNm	96	3.29%
Span length	UHPC-B25	3.66 m	63	6.58%
	UHPC-B26	5 m	62.5	4.31%
	UHPC-B0	6.5 m	62	4.04%
	UHPC-B27	8 m	61	3.92%

Table 5-5. (cont'd)

Loading type	UHPC-B28	Uniformly distributed load; Load level-50%	63	6.58%
	UHPC-B0	Two-point load; Load level-50%	63	6.58%
Steel vol. fraction	UHPC-B29	0.75% vol., f'c=157 MPa, f't=5 MPa	60	7.82%
	UHPC-B0	1.5% vol., f'c=175 MPa, f't=6 MPa	63	6.58%
	UHPC-B30	2.25% vol., f'c=178 MPa, f't=7.5 MPa	71	5.76%
	UHPC-B31	3% vol., f'c=182 MPa, f't=9.5 MPa	74	2.88%
Polypropylene fiber dosage	UHPC-B0	0 % vol. PP fiber, f'c=175 MPa, f't= 6 MPa	63	6.58%
	UHPC-B32	0.1 % vol. PP fiber, f'c=162 MPa,f't=5.8 MPa	73	5.29%
	UHPC-B33	0.2% vol. PP fiber, f'c=151 MPa,f't=5.5 MPa	74	0.82%
	UHPC-B34	0.3% vol. PP fiber, f'c=143 MPa,f't=5.2 MPa	76	0%

5.3.5. Summary

A macroscopic finite element analysis is applied to quantify the influence of critical factors on the fire response of UHPC beams. Based on the results presented in this chapter, the following observations can be drawn on the performance of fire exposed UHPC beams:

- Fire intensity, load level, cross-sectional dimensions, cover thickness, specimen shape, presence, and dosage of steel and polypropylene fibers have a significant influence on the fire performance of the UHPC beams, whereas the tensile reinforcement ratio, span length, and type of flexural loading have a minor or no impact on the fire performance of the UHPC beams.
- Load level has a significant effect on the response of UHPC beams under fire conditions. The fire resistance of UHPC beams can double by reducing the load ratio from 70% to 30% of the room temperature capacity of the beam. However, the extent of spalling in UHPC

beams under higher load levels is lower due to the escape of pore pressure resulting from higher cracking in the tensile zone of the beam.

- Fire severity has a significant effect on the fire behavior of UHPC beams, wherein a higher intensity fire results in lower fire resistance. Extent of spalling is maximum under moderate fire intensity as lower heating results in slow drying of concrete and higher heating results in the release of pore pressure through thermal cracking.
- Cross-sectional dimensions have a significant influence on the response of fire exposed UHPC beams; with larger beam cross-section (higher thermal mass) leading to higher fire resistance and lower extent of spalling.
- Increasing cover to tensile reinforcement has a beneficial effect on the fire resistance of UHPC beams. The fire resistance of a UHPC beam can improve by 20% upon increasing bottom cover thickness from 28 mm to 44 mm and lateral cover thickness from 28 mm to 38 mm.
- The sectional shape has a significant effect on the response of UHPC beams under fire conditions, wherein the sections with thinner web (I-section, T-section) exhibit lower fire resistance than rectangular sections.
- The addition of 1.5-3 % by volume of steel fibers enhances fire resistance of UHPC beams and mitigates fire-induced spalling through slower degradation of tensile strength in UHPC. Incorporating polypropylene fibers using a dosage in the range of 0.1-0.3% by volume to UHPC significantly reduces the extent of fire-induced spalling in UHPC beams and thereby, enhances fire resistance of the beam.

CHAPTER 6

6. Design Recommendations

6.1. General

Ultra-high performance concrete (UHPC) is designed to outperform conventional normal strength concrete (NSC) and high strength concrete (HSC), and is therefore optimized to achieve higher strength (dense and compact microstructure) and enhanced durability (i.e. low permeability to decrease corrosion of steel reinforcement) characteristics. Despite outstanding performance at room temperature, studies clearly indicate that UHPC exhibits lower performance under fire conditions, as compared to NSC and HSC. To attain the dense microstructure of UHPC, admixtures, fillers, and additives are added, which contribute to rapid degradation of strength properties at elevated temperatures. In addition, UHPC is highly prone to fire-induced spalling, which leads to the reduction of concrete cross-section, further accelerating the rate of strength and modulus degradation and causing a loss in load bearing capacity. Spalling not only reduces the fire resistance of concrete members, but also complicates fire resistance assessment, making the prediction of thermal response, structural response, and fire resistance of UHPC difficult. Furthermore, fire-induced spalling is affected by several factors and is interdependent on a number of parameters. Despite the adverse effects of fire-induced spalling on the fire response of concrete members, very limited guidelines and recommendations are available on the treatment of spalling in evaluating fire resistance of concrete members.

The current provisions in codes and standards typically assign fire resistance ratings to concrete members as a function of minimum required dimension (width) and concrete cover thickness to steel reinforcement. Moreover, there are no specific guidelines in codes and standards for the fire resistance design of UHPC structural members. This is mainly owing to the lack of information

on fire resistance of UHPC members due to only limited data from few fire tests and numerical studies on UHPC members. Likewise, it is not reasonable to develop simplified design methodologies or expressions for evaluating the fire resistance of UHPC members based on the limited amount of available experimental data. Nonetheless, based on the available information from the undertaken research, broad guidelines are recommended in this study for minimizing spalling and increasing the fire resistance of UHPC beams.

6.2. Critical factors governing fire performance of UHPC beams

The fire performance of reinforced concrete (RC) members is broadly influenced by concrete cover thickness, specimen dimensions, applied load level, fire scenario compressive strength of concrete, transverse reinforcement, presence of fibers, and aggregate type. These factors were identified and widely studied through fire tests and numerical studies in the literature, extensively carried out on beams and columns made of normal strength concrete (NSC) and high strength concrete (HSC). Contrarily, ultra-high performance concrete (UHPC) being a new class of cementitious material, there have been no studies on the quantification of the critical factors influencing the fire performance of UHPC members. Moreover, the fire behavior of UHPC members is different from that of NSC and HSC members due to the following reasons: (i) slender sections are possible for UHPC members due to high tensile strength of UHPC, which results in reduced thermal mass; (ii) lower cover thickness is needed for prevention against corrosion in UHPC members due to high durability characteristics of UHPC, resulting in lower insulation from fire; (iii) densely packed microstructure of UHPC increases the tendency of UHPC members to spall; (iv) faster degradation of mechanical properties with temperature in UHPC as compared to NSC and HSC. These unique characteristics of UHPC members have not been accounted for in previous studies and therefore, the same level of quantification of the influencing parameters on the fire performance of RC

members made of NSC and HSC cannot be directly applied for UHPC members. Hence, detailed experimental and analytical studies were undertaken in this thesis. Data from the fire tests, numerical model, and parametric studies presented in this thesis show that the fire performance of UHPC, in general, and spalling, in particular, is complex and is dependent on a number of factors. The key factors that influence the occurrence of spalling and eventually fire resistance of UHPC beams are discussed here.

Fire scenario

Fire severity measured in terms of heating rate, intensity (peak temperatures), and duration of fire, significantly influences the fire resistance of RC beams [3,72,73]. A severe fire scenario leads to higher peak temperatures in the member cross-section, resulting in higher degradation of strength in concrete and steel rebars, which in turn decreases fire resistance of the member. UHPC beams are designed to have smaller cross-sections than NSC and HSC beams due to their high strength. As a result of the smaller size of UHPC beams, rise in sectional temperatures are faster, resulting in poorer fire resistance than conventional NSC and HSC beams. In addition, fire scenarios with faster heating rate can induce spalling in concrete members due to the development of high sectional temperature gradients, that generate high thermal stresses and pore pressure in concrete, which can lead to spalling and consequently, reduce fire resistance in concrete members. This effect is more pronounced in beams made of UHPC due to its high susceptibility to spalling as a result of low permeability and dense microstructure of UHPC, as compared to NSC and HSC.

The existing fire provisions in codes and standards are based on standard fire scenarios, which reflect typical building fires. Currently, UHPC finds increasing applications in parking structures and bridges, wherein fires tend to be much more rapid, than building fires. Fires in parking structures and bridges are characterized by fast heating rates or high fire intensities and such fire exposures can lead to higher spalling and consequently, lower fire resistance of UHPC beams.

Therefore, the fire resistance of UHPC beams, based on standard fire exposure, may not be a realistic indication of fire performance.

Specimen dimensions

Published literature shows that fire resistance of RC beams increases by enlarging the cross-sectional dimensions. This is because members with larger sectional size experience slower temperature rise owing to larger thermal mass, which slows down the rise in sectional temperatures resulting in slower degradation in sectional capacity [73,83,196]. As compared to NSC and HSC beams, UHPC beams are typically leaner due to their higher load carrying capacity, as a result of high compressive and tensile strength of UHPC. Thus, due to smaller size and lower thermal mass of UHPC beams, higher temperatures develop across the cross-section, resulting in lower fire resistance of UHPC beams as compared to conventional NSC and HSC beams. Increasing the cross-section of UHPC beam decreases the extent of spalling and improves the fire resistance of that beam, due to lower sectional temperatures through greater mass of concrete.

Previous studies have indicated that increasing the sectional dimensions, specifically of HSC members, might increase the risk of spalling as the specimen size is directly related to the amount of moisture it can contain [73,138,197]. Since the size of UHPC members are smaller than HSC and NSC members, the concern of increase in spalling with increase in size of the member is not envisaged. Further, upon incorporation of appropriate spalling mitigation measures, the risk of spalling lowers and the fire resistance improves with the increasing size of the RC members.

Cover thickness

Current fire design codes and standards assign fire resistance ratings to concrete beams (mainly made of NSC) by prescribing a minimum cover thickness to steel reinforcement and a minimum required width [16,134]. The cover thickness specifications for fire resistance are primarily determined based on corrosion control requirements. Although the design codes do not provide

specific concrete cover thickness requirements for fire ratings of HSC beams, previous studies recommend specifying similar cover thickness to reinforcement for HSC beams, as in the case of NSC beams based on corrosion control requirements [73]. In comparison to NSC and HSC, UHPC has significantly improved durability and crack-control properties which provide higher resistance to corrosion. Therefore, the minimum concrete cover thickness required for corrosion control in UHPC beams may be much lower than NSC and HSC beams, and can be inadequate for satisfying fire resistance requirements in UHPC beams.

The fire resistance of RC beams can be improved by increasing the concrete cover thickness to the tensile steel reinforcement [189]. This is because the temperature rise in steel rebars slows down as the concrete cover thickness increases, which delays the temperature-induced strength deterioration in reinforcement and improves fire resistance of the beam. However, as the thickness of the concrete cover increases, its effect on the rise in rebar temperatures and improvement in fire resistance is somewhat limited. The moment capacity of an RC beam at room temperature depends on the effective depth which is a function of bottom concrete cover thickness. As a result, increasing the bottom concrete cover thickness reduces the flexural capacity of the beam. Further, increasing bottom cover thickness can also widen the tensile cracks in concrete, which can lead to an increase in heat propagation to rebars and decrease fire resistance. Consequently, it is not practical to excessively increase the concrete cover thickness without limitation to improve the fire resistance of RC beams [198].

Load level

Load level has a significant influence on fire-induced spalling and the resulting fire resistance of RC beams [73,75]. Higher load levels reduce the fire resistance of RC beams by inducing early weakening and softening of the constituent materials, resulting in a faster decrease of strength and stiffness of the beam. This effect is more pronounced in UHPC beams since the temperature-

induced strength degradation is greater in UHPC as compared to that in NSC and HSC. Further, previous studies on NSC and HSC beams show that higher applied loading generates higher mechanical stresses, in addition to stresses arising from thermal gradients and pore pressure, and can exacerbate the extent of spalling in the beam [11,91,197]. However, unlike NSC and HSC beams, the extent of spalling in UHPC beams is mostly lower under higher load levels. This is mainly due to the alleviation of pore pressure resulting from increased concrete permeability and cracking in the tension zone of the beam under higher loads [79,96].

Sectional shape

The different cross-sectional shapes, namely, rectangular, T-shape, I-shape, etc. can influence the fire resistance of RC beams. Typically, the beams with non-rectangular sectional shapes experience faster transmission of heat in the thinner portions due to reduced thermal mass, which leads to faster degradation in mechanical properties of the constituent materials and consequently, decreases fire resistance of the beam [199]. Further, the occurrence of even low levels of spalling in a beam section with slender stems can have a detrimental impact on the fire resistance of that member [3]. The negative impact on fire resistance is even more severe for UHPC beams with thinner stems due to further reduction in sectional size (lower thermal mass) of the beam as compared to non-rectangular shape beams made using NSC or HSC.

Fiber reinforcement

The addition of polypropylene or steel fibers minimizes fire-induced spalling and increases the fire resistance of RC members. The polypropylene fibers present in a concrete member melt around 160°C leading to increased permeability in a concrete section, which in turn facilitates the dissipation of fire-induced vapor pressure [10,69,83]. The release of pore pressure helps mitigate fire-induced spalling in concrete members. Addition of steel fibers to concrete mix helps minimize the extent of spalling by improving tensile strength of concrete, as well as slowing down the rate

of degradation in tensile strength with temperature [10,73,75]. Since spalling is not a concern in NSC members, majority of previous studies on strategies for mitigation of spalling were mainly focused on HSC members. Previous research also suggests the incorporation of hybrid fibers, comprising of both steel and steel fibers, for mitigation of fire-induced spalling in HSC members [125,200]. The increased tensile strength, together with higher permeability, resulting from the presence of hybrid fibers reduces fire-induced spalling in an HSC member.

It is critical to incorporate an optimal amount of steel and polypropylene fibers in the concrete mix to favorably minimize spalling and enhance fire resistance of the member. For instance, addition of a lesser amount of steel fibers results in lower tensile strength, which could be inadequate to resist tensile stresses for minimizing spalling. On the other hand, overly increasing the amount of steel fibers does not exhibit any considerable increase in tensile strength and can result in fiber balling and non-uniformity in the concrete mix. Similarly, lower content of polypropylene fiber limits the connectivity of micro-channels after melting of polypropylene fibers, in turn lowering the increase in permeability, and restricting the release of pore pressure for mitigating spalling. Conversely, the addition of higher volumes of polypropylene fibers to the concrete mix leads to a substantial reduction in the strength and workability of the mix.

In contrast to NSC and HSC, UHPC mixes are typically designed to contain steel fibers for attaining their high tensile strength and ductility. Based on past studies, the recommended fiber content for minimizing spalling in HSC members is 0.15% of mix volume in the case of polypropylene fibers, and 0.5% of mix volume in the case of steel fibers, [3,73,125]. Based on the results presented in this thesis, the optimum fiber content for minimizing spalling in UHPC beams is proposed as 0.2% to 0.3% in the case of polypropylene fibers, and about 1.5% to 3% in the case of steel fibers. The optimum dosage of steel and polypropylene fibers for UHPC was found to be

much different and higher than that for HSC owing to differences in their respective microstructure and characteristic properties.

Shear reinforcement

Previous high temperature studies on NSC and HSC members, especially columns, have shown a positive influence on fire resistance by reducing spacing in lateral reinforcement and modifying tie configuration in columns. Further, a reduction in the extent of late-stage spalling has been reported through improved lateral reinforcement configuration in columns due to the contribution of ties holding the longitudinal rebar in place under fire conditions [201–203]. However, there is a lack of such comparative data on the fire response of UHPC members with and without lateral reinforcement.

Typically, the shear capacity of UHPC beams is high owing to the higher tensile strength of UHPC due to the presence of steel fibers. Recent studies at room temperature have indicated the feasibility of removing shear reinforcement from UHPC beams [113,193,194]. However, the reduced shear capacity by removing stirrups can adversely impact the fire resistance of UHPC beams under certain loading conditions, such as shear-dominant loading. Further studies are needed for quantifying the contribution of shear reinforcement in influencing the fire resistance of fire-exposed UHPC beams. In the meantime, it is conservatively recommended to incorporate shear reinforcement in UHPC beams for applications in built infrastructure.

Batch mix proportions

Two types of aggregates are commonly utilized in conventional concrete batch mixes; carbonate aggregate (predominantly consisting of limestone) and siliceous aggregate (largely comprising quartz). Among these two aggregate types, carbonate aggregate provides higher fire resistance and better spalling resistance than siliceous aggregate in concrete members. This can be attributed to an endothermic reaction occurring at around 700°C which lowers the rate of heat increase and

delays the deterioration of strength in concrete. In general, the fire resistance of HSC columns made with carbonate aggregate concrete is about 10% higher than HSC columns made with siliceous aggregate concrete [10,201]. Usually, to attain its dense microstructure, UHPC batch mixes comprise of only fine aggregates (no coarse aggregates) or a controlled amount of coarse aggregates. However, when coarse aggregates are incorporated, it is advantageous to use carbonate aggregate instead of siliceous aggregate based on previous studies.

Concrete type (strength and permeability)

The type of concrete, in terms of the magnitude of its compressive strength and permeability, can significantly influence fire-induced spalling and consequently, fire resistance of reinforced concrete (RC) structural members. The concretes utilized currently for construction can be broadly grouped under normal strength concrete (NSC), high strength concrete (HSC), and ultra-high performance concrete (UHPC) based on compressive strength range. Generally, concrete below a compressive strength of 70 MPa is referred to as NSC, concrete with compressive strength in the range of 70 to 150 MPa is classified as HSC, while concrete with compressive strength above 150 MPa is designated as UHPC [3,17]. However, the definitions for classifying concrete into different categories vary in different codes and standards, such as ACI 216.1 classifies concrete as HSC when the compressive strength is above 83 MPa [134].

Higher strength in concretes (above 70 MPa) is attained through the addition of supplementary cementitious materials and fillers such as silica fume and fly ash to the batch mix. The addition of such fillers reduces interstitial voids and lowers the permeability of concrete. The permeability of UHPC, HSC, and NSC is in the order of 10^{-18}, 10^{-17}, and 10^{-16} m^2 respectively [67,175]. The low permeability in concrete hinders the release of pore pressure and leads to fire-induced spalling. The higher the strength, or the associated lower permeability, the higher is the probability of spalling [203]. Further, the loss of strength with temperature is higher for UHPC as compared to

NSC and HSC. Results from this thesis have shown that UHPC beams exhibit higher spalling levels and significantly lower fire resistance, than NSC and HSC beams [186].

6.3. Current provisions for fire design of NSC and HSC beams

Provisions for evaluating the fire resistance of reinforced concrete (RC) beams are specified in design codes and standards, namely, ACI 216.1 [98] and Eurocode 2 [16]. The design codes and standards follow a prescriptive approach by specifying the minimum sectional dimensions and concrete cover thickness for a concrete member to attain a required fire rating. In some cases, limited consideration is given to aggregate type, density, and support (restraint) conditions of a member. The prescriptive provisions are based on standard fire tests, without taking into account critical parameters such as realistic fire scenarios, loading level, and extent of spalling. Moreover, failure is determined based on the temperature attained in the steel reinforcement, without any consideration to realistic failure criteria based on strength or deflection limits.

For instance, ACI 216.1 provides tables for evaluating fire resistance rating for RC beams and columns made of normal strength concrete (NSC) with a compressive strength lower than 83 MPa. Fire rating listings tabulated in ACI 216.1 for NSC beams are shown in Table 6-1. However, ACI 216.1 does not specify any guidelines for beams made using new types of concrete such as HSC or UHPC. Current prescriptive methods cannot be directly applied for these newer concrete types due to problems such as fire-induced spalling and difference in microstructures. ACI 216.1 only provides some guidelines for mitigating spalling in HSC columns (with compressive strength greater than 83 MPa), through the provision of ties (lateral reinforcement) with 135° bends back into the core of the column, instead of the regular 90° bends in columns.

Table 6-1. Minimum width and cover thickness requirements of unrestrained RC beam for achieving fire resistance adopted from ACI 216.1 [98]

Minimum width (mm)	Minimum cover (mm)				
	1 hour	1.5 hours	2 hours	3 hours	4 hours
127	19	25	32	-	-
178	19	19	19	44	76
254	19	19	19	25	44

Eurocode 2 [16] provides a choice of tabulated data, simplified, or advanced methods for determining the fire resistance of concrete beams. The data in tabulated format provides minimum dimensions and cover thickness to attain desired fire ratings for concrete members based on standard fire tests. For RC beams, the tabulated data is applicable to NSC made with siliceous aggregates. The same tabular data can be used for carbonate aggregate concrete and HSC by altering the required minimum sectional dimensions through specified modification factors. The prescriptive tabulated data only accounts for a limited number of factors influencing fire performance, without any consideration to a number of critical factors such as realistic fire scenarios, loading, spalling, and restraint. The simplified method in Eurocode 2 is based on evaluating reduced sectional capacity at a critical section, considering temperature-induced strength reduction factors to evaluate the reduction in capacity of a structural member at a given fire exposure time. When the decreasing sectional moment capacity reaches below the moment due to applied loading, failure is said to occur. However, the simplified rational design approaches do not fully account for spalling and various failure modes, encountered by structural members under fire conditions. The advanced method in Eurocode 2 involves comprehensive thermal and structural analyses and requires the use of specialized numerical models. Even through advanced methods for evaluating fire resistance, Eurocode 2 does not provide specific guidelines for accounting fire-induced spalling in the analysis.

For addressing spalling, Eurocode 2 states that spalling is unlikely to occur when the moisture content in concrete is lower than 3%. In addition, Eurocode 2 provides some general provisions for mitigating spalling in concrete: (i) use of secondary reinforcement mesh with a nominal cover of 15 mm; (ii) use of concrete that does not tend to spall; (iii) limit the maximum content of silica fume to less than 6% by weight of cement; (iv) use protective thermal layers; and (v) addition of at least 2kg/m^3 polypropylene fibers in the concrete batch mix. The guidelines in Eurocode 2 are qualitative and do not take into account the critical factors that influence spalling phenomenon, such as permeability and tensile strength of concrete, heating conditions, and level of loading.

While fire-induced spalling might occur in all concrete types, UHPC is more susceptible than NSC or HSC, due to its extremely low permeability. The current fire design codes do not provide any design recommendations for UHPC beams under fire conditions. Further, the current fire design provisions in codes of practice for NSC and HSC beams cannot be directly used for UHPC beams as they do not rationally account for fire-induced spalling and temperature-induced strength degradation specific to UHPC. Moreover, these provisions are not applicable for estimating fire resistance under realistic fire scenarios and load conditions. For realistic fire resistance evaluation of UHPC beams, fire tests and numerical studies were undertaken in this thesis. Based on the test data and results from numerical analyses, along with the literature review conducted in Chapter 2, a set of preliminary design guidelines are proposed for mitigating spalling and enhancing the fire performance of UHPC beams.

6.4. Design recommendations for UHPC beams

UHPC is highly susceptible to fire-induced spalling due to its lower permeability and dense microstructure. Spalling reduces the overall concrete cross-sectional area and increases heat transmission from fire to steel reinforcement and inner concrete layers, thereby accelerating the

rate of strength and modulus deterioration causing additional losses in member capacity. The degradation in mechanical properties in concrete and steel reinforcement, combined with loss of concrete cross section due to spalling, can considerably lower the fire resistance of UHPC beam. Based on experimental and numerical studies carried out in this thesis, as well as reported studies in the literature, the following preliminary guidelines and recommendations for enhancing fire resistance and minimizing spalling are proposed.

6.4.1. Guidelines for enhancing the fire resistance of UHPC beams

UHPC is a high-performing construction material that offers a number of advantages. However, there are no specific guidelines in codes and standards for the fire resistance design of the UHPC beams. Based on the detailed studies undertaken in this thesis and in the literature, the following are some of the preliminary guidelines that can be implemented for enhancing fire performance of UHPC beams:

- Although there have been recent studies exploring the feasibility of UHPC beams without stirrups, no data on their fire performance is currently available. Therefore, stirrups must be provided to improve the fire resistance of UHPC beams through increased levels of confinement, and the spacing of the stirrups should not be lower than those for the conventional reinforced concrete beams.
- Spalling in UHPC beams tends to be more severe in fire scenarios characterized by rapid heating rates or high fire intensities. When UHPC is to be used in structural applications where severe fire conditions (e.g. hydrocarbon fire) is likely to occur, such as parking garages, bridges, etc., the fire resistance of UHPC beams should be evaluated by taking into consideration the loss of cross-section due to spalling through advanced analysis approaches.

- The minimum cross-sectional width and cover thickness for attaining the fire resistance ratings (under standard fire exposure) in UHPC beams, with and without polypropylene (PP) fibers are listed in Table 6-2.

  The recommended cover thickness for UHPC beam is higher than the currently required cover thickness for NSC beam, as per ACI 216.1. There is no guidance for fire ratings of HSC beams in ACI 216.1. As an illustration, to attain a fire rating of 1.5 hours, the minimum width required for UHPC beam without polypropylene fibers is 240 mm with a cover of 44 mm, and for UHPC beam with polypropylene fibers is 180 mm with a cover of 44 mm, whereas the minimum width required for NSC beams is 127 mm with a 25 mm cover.

Table 6-2. Minimum width and cover thickness of UHPC beam for achieving fire resistance.

Minimum width (mm)	**Minimum clear cover (mm)**							
	1 hour		**1.5 hours**		**2 hours**		**3 hours**	
	Steel fibers	**Steel and PP fiber**	**Steel fibers**	**Steel and PP fiber**	**Steel fibers**	**Steel and PP fiber**	**Steel fibers**	**Steel and PP fiber**
180	30	30	-	45	-	-	-	-
240	30	30	45	40	65	50	-	-
270	30	30	40	30	45	45	-	75
360	30	30	30	30	40	30	65	55

- Incorporation of alternate solutions such as the application of available commercial insulations will enhance the fire resistance of UHPC beams by providing thermal insulation and delaying the rise in sectional temperatures.

6.4.2. Guidelines for minimizing spalling

UHPC is highly susceptible to fire-induced spalling because of its very low permeability and extremely dense microstructure. By adopting the following broad design guidelines from research carried out in this thesis and past studies, spalling in UHPC beams can be minimized to a significant extent:

- Addition of polypropylene fibers, about 0.2% to 0.3% by volume, to UHPC batch mix will reduce spalling in UHPC beams.
- Steel fibers are typically present in UHPC, and the recommended content of steel fibers by volume for reducing the level of spalling in UHPC beams is 1.5% to 3%.
- The use of carbonate aggregate, instead of siliceous aggregate in UHPC batch mix will reduce the extent of spalling in UHPC beams.

6.4.3. Guidance for advanced analysis

The design recommendations are given for the analyzed beam sizes subjected to 50% load level and ASTM E119 standard fire exposure. However, UHPC beams are prone to spalling which is a complex phenomenon and is influenced by numerous parameters. Hence, it is not possible to account for all the influencing parameters through guidelines or simplified approaches. To account for different critical parameters in evaluating fire resistance, advanced analysis approaches can be applied. Advanced analysis procedures require significant experience, and results are highly contingent on the level of complexity adopted in the analysis.

Advanced analysis can be carried out using a macroscopic finite element approach at incrementing time steps as discussed in Chapter 4 or through the use of commercial finite element (FE) programs such as ANSYS, ABAQUS, etc. The analysis involves the idealization of a UHPC beam into segments and further discretization of the mid-section of each segment into a number of elements. Cross-sectional temperature rise in each segment is calculated through heat balance equations. Temperature-dependent thermal properties of concrete, as discussed in section 4.4.2. form the input of this analysis.

Following temperature calculations, pore pressure is calculated in each element by utilizing principles of mechanics and thermodynamics, including the conservation of the mass of liquid

water and water vapor. Utilizing the sectional temperatures, thermal stress is evaluated based on the temperature-dependent thermal expansion coefficient of concrete and thermal gradients. Also, load-induced (mechanical) stress arising from the applied load present on the beam is evaluated through stress-strain relationships as discussed in section 4.4.2. At each time step, the extent of fire-induced spalling is calculated by taking into consideration the hydro-thermo-mechanical stresses generated due to pore pressure, thermal strains, and structural loading.

Spalling in concrete elements is evaluated based on a two-step mechanism. As per the first step, the spalling of concrete boundary elements (the first layer of a discretized concrete section close to the fire-exposed surface) will occur if the resulting tensile stress due to pore pressure build-up exceeds the decreasing tensile strength due to the increase in sectional temperature. As per the second step, when tensile strength is exceeded by pore pressure in any interior element (elements located in layers beneath the first fire-exposed layer i.e. in second, third, fourth layer, and so on), and the resultant tensile stress due to thermal gradient, load and pore pressure in the elements in front of the interior element is higher than the thermally degraded tensile strength, spalling occurs in those interior and boundary elements. Once spalling occurs in an element, that element is removed from the cross-section, and the reduced cross-section with updated boundary conditions is considered for the subsequent time-step.

The cross-sectional temperatures from the thermal analysis, together with the updated geometry of the beam from the spalling analysis, are used to evaluate the structural response of the UHPC beams. Time-dependent sectional moment-curvature relations are generated at each beam segment utilizing the temperature-dependent degradation in mechanical properties of concrete and reinforcement. These moment-curvature relations form the basis to trace the response of the UHPC beam in the entire range of loading till collapse under fire conditions. A flowchart showing the

steps associated with the fire resistance evaluation of UHPC beam through advanced analysis is presented in Figure 4.1. The analysis is carried out in incrementing time steps until the failure of the beam. A number of response parameters, namely, temperatures, pore pressure, strains, stresses, deflections, and moment capacities, can be generated at each fire exposure time. At each time step, the computed capacity at each segment and deflection in the beam are used to check for failure against predetermined strength and deflection failure limits. The duration to reach the time-step preceding failure is taken as the fire resistance of the beam. The application of an advanced analysis approach for evaluating the fire performance of a typical UHPC beam is illustrated in Appendix C.

6.5. Limitations

Although the presented approach can be applied to evaluate the fire resistance of a range of UHPC beams, there are certain inherent limitations of the approach, as listed below:

- The proposed guidelines are for UHPC beams subjected to flexure dominant loading and may not be applicable for beams under shear dominant loading.
- The proposed guidelines for mitigating spalling and improving fire resistance of UHPC beams is only applicable over a certain range of parameters, shown in Table 6-3.

Table 6-3. Range of limits for applicability of proposed guidelines.

Parameter	**Range**
Load ratio	0.5
Fire scenario	ASTM E119 standard
Beam width (mm)	180-360
Beam width to depth ratio	1.5
Concrete cover thickness (mm)	28-76
Concrete aggregate type	Limestone/carbonate

- The proposed guidelines are applicable to simply supported UHPC beams only, since there is not sufficient data on the effect of fire-induced restraint resulting on fire performance.

6.6. Summary

This chapter presents guidelines for the fire design of UHPC beams based on results from the parametric studies. The following conclusions can be drawn based on the information presented in this chapter:

- The fire severity, load level, cover thickness, specimen shape, sectional dimensions, and dosage of steel and polypropylene fibers have a major influence on the fire performance (both spalling and fire resistance) of UHPC beams, while the tensile reinforcement ratio, span length, and type of flexural loading have a marginal impact on the fire performance of UHPC beams.
- Design recommendations are proposed to attain practical fire resistance ratings in UHPC beams, upto 3 hours under standard fire exposure.
- By incorporating proper measures, both at material and structural levels, spalling in UHPC beams can be minimized to a significant extent and fire resistance can be enhanced.
- Advanced analysis procedure is recommended for evaluating fire resistance of UHPC beams, specifically in case of non-conventional slender UHPC sections such as I-beam, T-beam, etc. Through advanced analysis, the behavior of UHPC beams can be simulated with higher accuracy by incorporating influencing factors, such as fire-induced spalling, specific high-temperature properties of concrete and rebars.

CHAPTER 7

7. Conclusions

7.1. General

Ultra-high performance concrete (UHPC) is an advanced cementitious material possessing high compressive and tensile strength, improved ductility, and excellent durability characteristics [101,114,204]. These enhanced properties of UHPC result through optimization of the granular mixture with a low water-to binder ratio, high fineness admixtures, and steel fibers [111]. As a result of these improved properties, UHPC can be attractive for building more economic, aesthetic, and long-lasting structures than conventional concrete structures. Thus, UHPC is finding increasing applications in high-rise buildings, large-span bridges, and special structures. Although, UHPC possesses superior mechanical properties than normal strength concrete (NSC) and high strength concrete (HSC), UHPC may not exhibit the same level of performance as NSC under fire conditions.

Limited studies exist on the response of UHPC members under fire conditions. In addition, there is a lack of data on high-temperature properties specific to different types of UHPC (with and without polypropylene fibers). Also, there is no numerical methodology to predict fire-induced spalling in UHPC members. To overcome these knowledge gaps, this dissertation presents a comprehensive study on the behavior of UHPC beams under fire conditions. Both experimental and numerical studies were carried out to evaluate the fire resistance of UHPC beams and to quantify the influence of critical factors influencing the fire response. As part of experimental studies, a series of property tests were carried out to generate data on the variation of thermal and mechanical properties of UHPC as a function of temperature. Data from these tests were utilized to formulate empirical property relations for UHPC over 20-750°C temperature range. In addition,

full-scale fire resistance tests were carried out on four UHPC beams. Data from fire tests were utilized to gauge the effect of load level, fire scenario, and presence of polypropylene fibers on the extent of spalling and fire resistance of UHPC beams.

As part of numerical studies, a numerical model, previously developed for normal strength concrete (NSC) and high strength concrete (HSC) beams, was extended to model the response of UHPC beams under realistic fire and loading conditions. This model is based on a macroscopic finite element approach and utilizes time-dependent moment-curvature relationships to trace the response of UHPC beam from pre-loading to failure under fire conditions. The model accounts for high-temperature properties of constituent materials, various strain components, and fire-induced spalling. Spalling was evaluated by taking into account the stresses generated due to pore pressure, thermal gradients, and structural loading under fire conditions. The validity of the model was established by comparing predicted response parameters with measured data from fire resistance tests carried out as part of the experimental program. The validated numerical model was further applied to conduct a set of parametric studies to quantify the influence of critical factors on the fire response of UHPC beams. Results generated from parametric studies were utilized to develop general design guidelines for mitigating spalling and increasing fire resistance in UHPC beams.

7.2. Key Findings

The following key conclusions can be drawn based on information generated as part of this thesis:

1) Mechanical and spalling-related properties of UHPC at elevated temperatures vary quite differently from that of normal and high strength concrete. Therefore, prescriptive-based specifications for normal strength concrete (NSC) and high strength concrete (HSC) beams cannot be directly applied to UHPC beams.

2) The variation of thermal properties with temperature, for plain UHPC, UHPC with only steel fibers, and UHPC with both steel and polypropylene fibers are very much in the same pattern. The thermal conductivity of UHPC decreases in the 20°C-400°C range and increases in the 400°C-750°C range. The specific heat of UHPC remains almost constant up to about 400°C, and then increases up to 600°C followed by a constant trend in the 600°C-750°C range. UHPC experiences an overall mass loss of about 7% in the 20°C-750°C range. The thermal expansion of UHPC increases in the 20°C-900°C range, with the exception of thermal shrinkage taking place in the 700°C-800°C range. Thermal conductivity and thermal expansion are slightly higher in UHPC, whereas specific heat and mass loss are moderately lower in UHPC at elevated temperatures as compared to those in NSC and HSC.
3) The mechanical properties of the two types of UHPC, i.e. UHPC with only steel fibers, and UHPC with both steel and polypropylene fibers exhibit the same trend in mechanical properties throughout the 20°C-750°C temperature range. The compressive strength and tensile strength of UHPC degrade at a gradual rate with temperature, retaining about 20% of room temperature compressive and tensile strengths at 750°C. The elastic modulus of UHPC rapidly degrades till 600°C and then, the rate of loss in elastic modulus slows down in 600-750°C, retaining only 5% of the room temperature elastic modulus at 750°C. The degradation of relative strength and modulus properties with temperature is higher in UHPC and HSC, as compared to NSC, due to the higher cement to aggregate ratio in higher strength concretes, resulting in thermal incompatibilities. Lastly, there is no significant influence of heating rate on mechanical property degradation in UHPC according to the two heating rates adopted in the study i.e. 0.5°C/min and 2°C/min.

4) UHPC beams with only steel fibers (no polypropylene fibers) are highly susceptible to fire-induced spalling due to their dense microstructure, and lower permeability and exhibits lower fire resistance. Fire-induced spalling in UHPC beams mainly occurs in the upper portion (compression zone) resulting in faster temperature rise in the inner compressive layers of concrete. Addition of polypropylene fibers (along with steel fibers) in UHPC significantly reduces the extent of fire-induced spalling in these beams and this, in turn, enhances the fire resistance of the beam. The extent of spalling is less severe in UHPC beams (with only steel fibers, and with both steel and polypropylene fibers) under higher load levels due to alleviation of pore pressure resulting from increased cracking in the tension zone of the beam.

5) The proposed macroscopic finite element based model is capable of tracing the response of UHPC beams from pre-cracking stage to collapse under ambient and fire conditions. The model can account for fire-induced spalling, concrete permeability variations with temperature, different strain components, high-temperature material properties of concrete and steel reinforcement, and realistic failure criteria. Spalling is modeled through the stresses arising due to combined effects of thermal gradients, structural loading, and pore pressure generated in concrete section. In the boundary elements, stresses arising from pore pressure can cause spalling, individually. However, in the interior elements, stresses due to pore pressure, together with tensile stresses induced in the transverse direction by thermal and mechanical loading, cause spalling. The level of spalling significantly influences the fire resistance of UHPC beams, and neglecting spalling can lead to un-conservative fire resistance predictions in certain scenarios.

6) The critical factors that have an influence on the fire performance of UHPC beams are load level, fire scenario, cover thickness, specimen shape, sectional dimensions, and dosage of steel and polypropylene fibers. Other factors such as tensile reinforcement ratio, span length, and type of flexural loading have a moderate influence on the fire resistance of UHPC beams. Further, among beams of different concrete types, the fire resistance of UHPC beams was significantly lower due to higher spalling levels resulting from their lower permeability, than NSC and HSC beams, where permeability is relatively higher.
7) The proposed preliminary guidelines, which include, the addition of polypropylene fibers and increasing cover thickness and sectional dimensions, are effective in minimizing spalling and improving fire resistance of UHPC beams, in lieu of specific guidelines in codes and standards for fire design of UHPC beams.

7.3. Research impact

Ultra-high performance concrete is an emerging construction material and exhibits excellent strength and durability characteristics, over conventional concrete. The information developed as part of this research will have a significant impact on the use of UHPC in building applications. For use in building applications, UHPC members need to satisfy required fire ratings to adhere to building codes. Limited research has shown that UHPC exhibits poor fire performance with faster degradation of properties at elevated temperatures and is highly prone to fire-induced spalling. At present, the required fire resistance ratings of members specified in building codes are assessed through prescriptive rules wherein, fire resistance is determined based on member thickness and concrete cover thickness to reinforcement. These prescriptive rules were developed based on data from standard fire tests on mostly NSC members and do not account for loading, fire, and spalling

effects. Thus, the current design guidelines may not yield realistic fire performance of UHPC members.

The studies presented in this thesis have contributed to the fundamental understanding of the behavior of UHPC beams under fire conditions. The effects of critical influencing factors, such as load level, fire scenario, presence of polypropylene fibers, and influence of spalling are quantified through experimental and numerical studies. Moreover, the numerical model presented in this study provides an effective alternative to fire resistance tests for evaluating the fire response of UHPC beams. This model can predict spalling at a member level incorporating hydro-thermo-mechanical stresses, and accounts for all critical factors that affect the behavior of UHPC beams under fire conditions, namely, temperature-induced property degradation of specific to concrete type, permeability variations due to cracking in concrete, and different failure limit states. The numerical model is used for undertaking parametric studies to quantify the effects of critical influencing factors on the fire resistance of UHPC beams. Further, data from the numerical studies was utilized to develop general design recommendations for improving fire resistance and mitigating fire-induced spalling in UHPC beams. The information developed as part of this research can promote the use of UHPC in structural applications.

7.4. Recommendations for Future Research

This thesis has advanced the state-of-the-art with respect to the fire response of UHPC beams by generating comprehensive data from experiments as well as results from numerical modeling on the behavior of UHPC beams. However, there is additional scope for further research in this area, and the following are a few of the key recommendations for future research:

- Further experimental and numerical studies are needed to develop data on fire response of UHPC beams with different configurations, including cross-sectional shape, shear reinforcement ratio, volume fraction and types of fibers, and loading configurations.
- Spalling-related properties of UHPC can be refined by measuring permeability, pore pressure, porosity, etc. as a function of temperature in UHPC specimens under different heating, loading, and specimen conditions. Such information on spalling-related properties will help to enhance the capability and confidence level in model predictions.
- The numerical approach developed in this study for evaluating the fire response of UHPC beams was through macroscopic finite element method. For ease of use in design practice, future studies demonstrating the implementation of the numerical model using commercial software packages such as ABAQUS, ANSYS, etc. are needed.
- The proposed fire design guidelines, for UHPC beams in this study, are preliminary and formulated mainly by undertaking parametric studies. Additional fire tests on a variety of parameters are needed to validate the numerical studies and establish codal provisions for UHPC beams.

APPENDICES

APPENDIX A. Design calculations for UHPC test beams

This appendix summarizes the room temperature design calculations carried out for the UHPC beams tested in this study [205]. ACI 544 [206] provisions for fiber-reinforced concrete members were followed for the design calculations. The cross-sectional details and loading configurations of the UHPC beams are shown in Figure A.1. The shear force and bending moment diagrams for the beams tested under two-point flexural loading are shown schematically in Figure A.2.

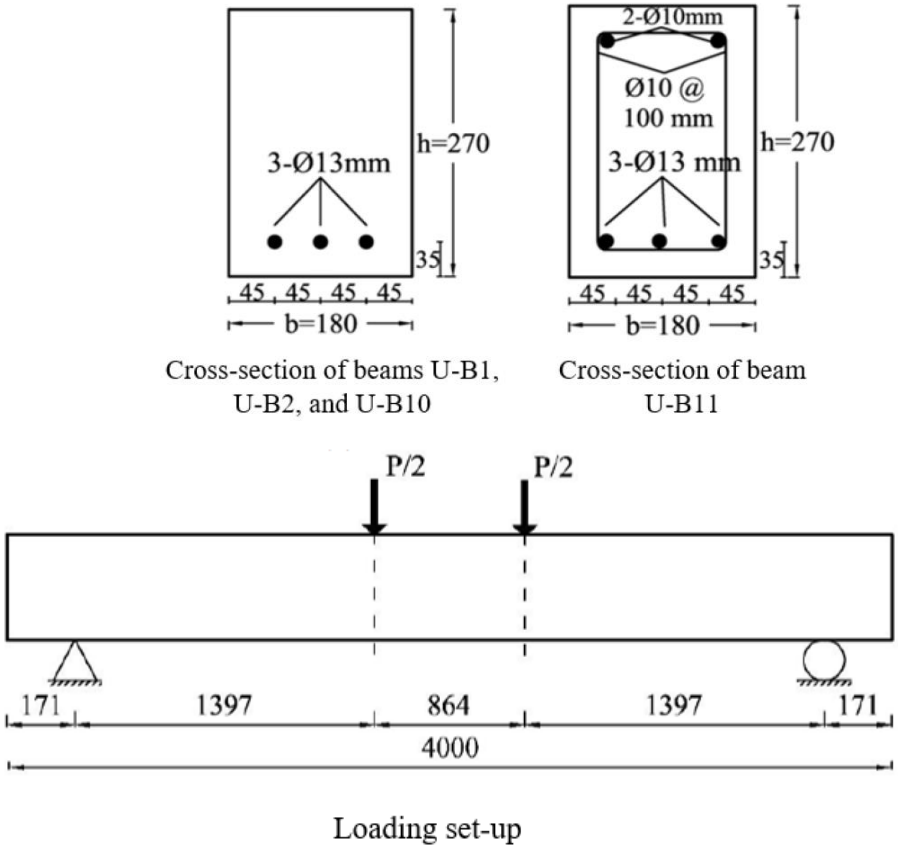

Figure A. 1. Cross section and loading set up of UHPC beams (All dimensions are in mm).

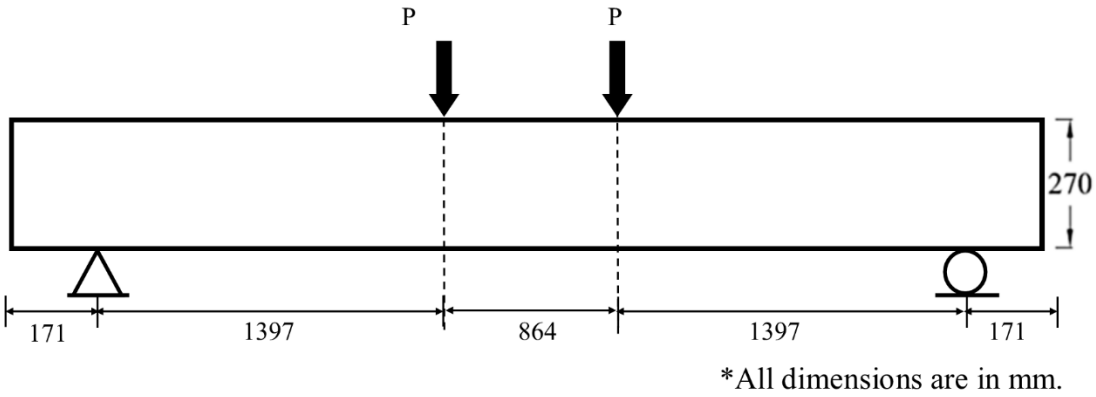

(a) Loading Configuration

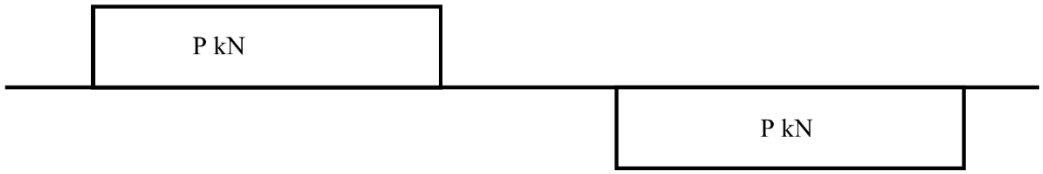

(b) Shear Force Diagram

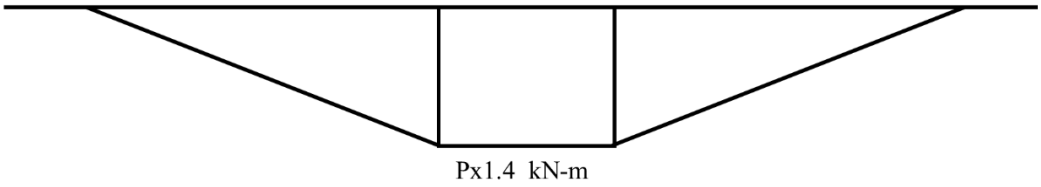

(c) Bending Moment Diagram

Figure A. 2. Schematic of shear force and bending moment diagram for tested UHPC beams.

Compressive strength (f'_c) and elastic modulus (E_c) of UHPC were considered to be 160 MPa and 41 GPa , respectively, and yield strength (f_y) and elastic modulus (E_s) of steel reinforcement were considered to be 400 MPa, and 200,000 MPa, respectively. The UHPC mix used in this study comprises 1.5% (by volume) steel fibers with length (l_f) of 13 mm and diameter (d_f) of 0.2 mm. The nominal concrete cover to the center of the steel rebar is 35 mm in all the beams.

According to ACI 544, the flexural capacity of a steel fiber reinforced concrete (FRC) section is calculated by design assumptions for equivalent stress block diagrams as shown in Figure A.3. Utilizing the equivalent stress blocks for the compressive and tensile regions, the flexural capacity (M_n) of a steel fiber reinforced concrete section with a rectangular cross-section is calculated by the following equation:

$$M_n = A_s f_y \left(d - \frac{a}{2}\right) + \sigma_t b(h-e)\left(\frac{h}{2} + \frac{e}{2} - \frac{a}{2}\right)$$

where A_s = cross-sectional area of tensile reinforcement; f_y = yield strength of steel reinforcement; d=effective depth; h= height of the beam; b= width of the beam; a= depth of equivalent compressive stress block; c= neutral axis depth; e= distance between the extreme concrete compression fiber to the top of the tensile stress block of fibrous concrete; and σ_t = the tensile strength of fibrous concrete.

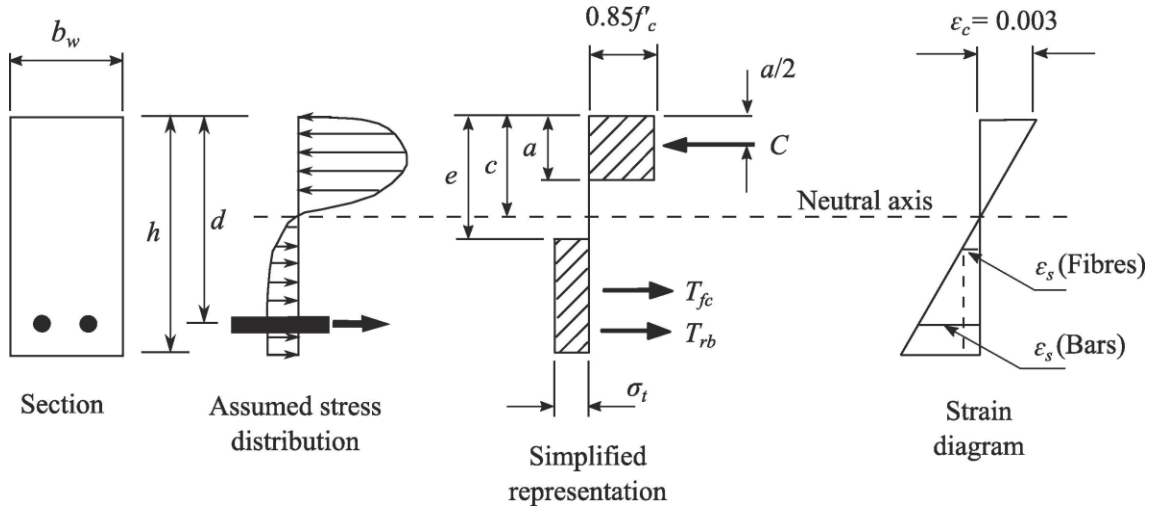

Figure A. 3. Design assumptions for analysis of reinforced concrete beams with steel fibers.

Although, the tensile stress (strength) of concrete is neglected in plain normal strength concrete (NSC), the tensile stress of the concrete of UHPC members (with steel fibers) is accounted for in the design calculation. The tensile stress of fibrous concrete, σ_t (MPa) is calculated by:

$$\sigma_t = 0.00772 \left(\frac{l_f}{d_f}\right) V_f F_{be} = 0.065 \times \frac{13}{0.2} \times 1.5 \times 1.2 = 7.6 \text{ MPa}$$

where l_f = length of steel fiber; d_f = diameter of steel fiber; V_f = percent by volume of steel fiber; and F_{be} = bond efficiency factor which varies from 1.0 to 1.2 depending upon fiber characteristics. F_{be} of 1.2 was used in the present study. The tensile stress of fibrous concrete, σ_t dictates the tensile stress block which is located at distance e from the extreme compression fiber and can be calculated as:

$$e = [\varepsilon_s\ (fibers) + 0.0035] \left(\frac{c}{0.0035}\right)$$

where ε_s (fibers) = the maximum tensile strain in the fibers and c = the depth of the neutral axis. The maximum strain value in the outermost compression fiber of concrete (ε_c) is 0.0035 as per design code ACI 544 [206]. The tensile stress in steel fibers, σ_{sf} (MPa) is given by:

$$\sigma_{sf} = \frac{\tau_f \pi d_f l_f/2}{\frac{\pi}{4} d_f^2} = \frac{10.26 \times \pi \times 0.2 \times 13/2}{\frac{\pi}{4} \times 0.2^2} = 1333.8 \text{ MPa}$$

where τ_f = the average bond strength of fibers, for 1.5% volume fraction of fibers is considered to be 10.26 according to test results from Yoo et al. [111]. The ε_s (fibers) is calculated as:

$$\varepsilon_s\ (fibers) = \frac{\sigma_{sf}}{E_{sf}} = \frac{1333.8}{200000} = 0.00667$$

where E_{sf} = elastic modulus of the steel fibers. The depth of the neutral axis (c) is calculated by tensile and compressive force equilibrium equation of the section, which can be written as:

$$C = T_{rb} + T_{fc}$$

where $C = 0.85 f'_c ab$, wherein f'_c=compressive strength of UHPC; a=effective depth of the compression stress block; and b= width of the beam. The tensile force is computed by accounting for tensile stresses in steel rebar (T_{rb}) and in steel fiber reinforced UHPC (T_{fc}):

$$T_{rb} = A_s f_y$$

$$T_{fc} = \sigma_t b(h - e)$$

C= 0.85 $f'_c\, a\, b$ = 0.85 × 160 × 0.65 × c × 180

$T = A_s f_y + \sigma_t\, b\, (h - e)$

$T = A_s f_y + \sigma_t\, b\, (h - (\frac{(\varepsilon s,\text{fibers} + 0.0035)}{0.0035})\, c)$

T = 3 × ($\frac{\pi}{4}$× 12.7^2) × 400 + 7.6 × 180 × (270 − $\frac{(0.00667 + 0.0035)}{0.0035}\, c$)

Solving $T = C$; we get c = 26.23 mm

Strain in tensile steel can be calculated by interpolation as follows:

$\varepsilon_s = (\frac{d-c}{c})\times 0.0035 = (\frac{235-26.23}{26.23})\times 0.0035 = 0.028 > \varepsilon_y$ (i.e. 0.005)

Therefore, the assumption of rebar yielding is valid.

$e = \frac{0.00667 + 0.0035}{0.0035}$ × 26.23 = 76.22 mm

$$M_n = A_s f_y \left(d - \frac{a}{2}\right) + \sigma_t b(h-e)\left(\frac{h}{2} + \frac{e}{2} - \frac{a}{2}\right)$$

$$M_n = 3 \times \left(\frac{\pi}{4} \times 12.72\right) \times 400 \left(235 - \frac{0.65 \times 26.23}{2}\right)$$

$$+7.6 \times 180 \times (270 - 76.22)\left(\frac{270}{2} + \frac{76.22}{2} - \frac{0.65 \times 26.23}{2}\right) = 78.1\ kNm$$

The longitudinal steel reinforcement spacing, arrangement, and cover were designed as per ACI-318 requirements for conventional beams [116]. Minimum clear spacing between longitudinal bars is the greatest of 25 mm, diameter of bars, and 4⁄3 times the maximum diameter of aggregate. UHPC beam U-B11 was provided with minimum shear reinforcement as per ACI-318 requirement.

$V_{s,min} = \max\begin{Bmatrix} 0.344\, b_w\, d \\ 0.062\sqrt{f'c}\, b_w\, d \end{Bmatrix}$ = 33.17 kN

$A_{v,min} = 0.062\sqrt{f'c}\, \frac{b_w S}{f_y} > 0.344\, \frac{b_w S}{f_y}$

Using # 3 stirrups, S for providing minimum shear reinforcement:

$$S = \frac{A_v f_y}{0.062\sqrt{f'c}\, b_w} \leq \frac{A_v f_y}{0.344\, b_w}$$

$$S = \frac{2 \times \frac{\pi}{4} \times 9.525^2 \times 400}{0.062\sqrt{160}\, \times 180} = 403.8\, mm \leq \frac{A_v f_y}{0.344\, b_w}$$

Also, spacing of stirrups, $S \leq \frac{d}{2} \leq 600$ mm

$$S \leq \frac{d}{2}; S \leq \frac{235}{2} = 117.5 \text{ mm}$$

Therefore, stirrups spacing of 100 mm was selected for beam U-B11.

AFGC [2] recommends expressions for calculating shear capacity of UHPC beams, which consider the shear resistance provided by concrete (V_{conc}), fibers (V_f), and shear reinforcement (V_s). Since in the designed beams, either stirrups were not provided or the contribution of stirrups to shear capacity was not accounted for in the design, only the contribution of concrete ($V_{UHPC} + V_f$) is calculated.

$$V_{UHPC} = V_{\text{conc}} + V_f$$

$$V_{\text{conc}} = \frac{0.21}{\gamma_E \gamma_b}\sqrt{f_c'}\, b\, d = \frac{0.21}{1.5}\sqrt{160}\, \times 180 \times\, 235 =\, 74.9 \text{ kN}$$

where b = the width of the beam, d = the effective depth of the beam, $f'c$=compressive strength of UHPC, $\gamma_E \gamma_b$ is the strength reduction factor = 1.5 (for reinforced beams).

$$V_f = \frac{0.9bd\sigma_p}{\gamma_{bf}\, tan\beta_u}$$

$$\sigma_p = \frac{1}{K}\, \frac{1}{w_{lim}}\, \int_0^{w_{lim}} \sigma(w)dw;\; w_{lim} = \max(w_u, 0.3mm)$$

where β_u is the inclination angle between a diagonal crack and longitudinal direction of the beam (a minimum value of 30º is recommended), K is the orientation coefficient for general effects,

$\sigma(w)$ is the experimental characteristic post-cracking stress for a crack width of w, w_u is ultimate crack width. $\int_0^{w_{lim}} \sigma(w)dw$ is adopted from tests conducted by Yoo et al. [111].

$$\sigma_p = \frac{1}{1.25 \times 6\,mm} \times 27\left(\frac{N}{mm}\right) = 3.6\frac{N}{mm^2}$$

$$V_f = \frac{0.9 \times 180 \times 235 \times 3.6}{1.3 \times tan30^\circ} = 186.2 \text{ KN}$$

$$V_{UHPC} = 74.9 + 186.2 = 257.5 \text{ kN}$$

APPENDIX B. Illustration of condition of beams during fire tests

A significant amount of data and a series of pictures and videos were recorded during the fire tests of the UHPC beams. Few additional images of the tested beams taken through the furnace viewport at key time intervals are provided in this appendix.

Figure B. 1. Typical UHPC beam just prior to fire exposure.

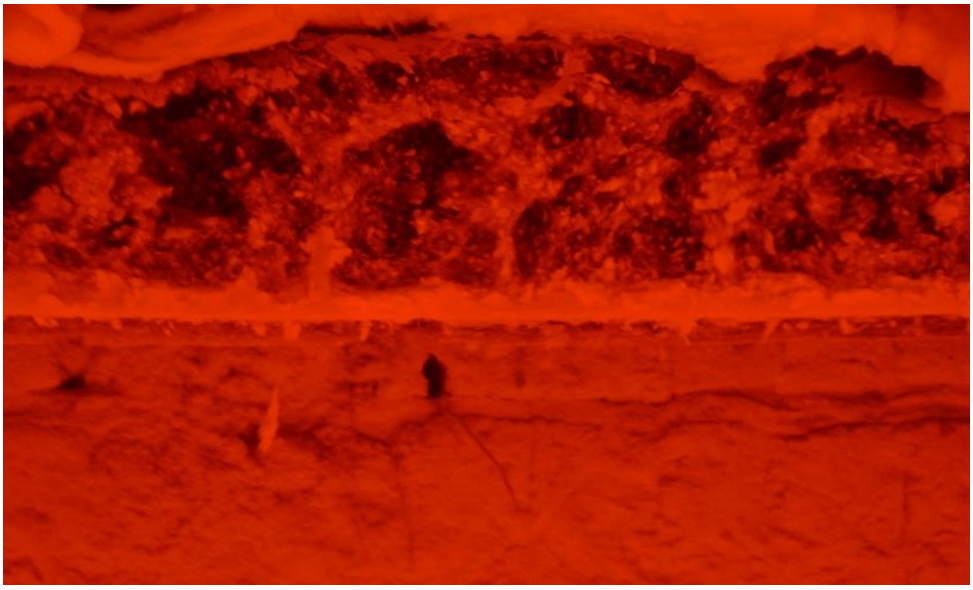

Figure B. 2. UHPC beam U-B1 with only steel fibers (no polypropylene fibers) after 40 minutes into fire exposure.

Figure B. 3. UHPC beam U-B11 with both steel and polypropylene fibers after 40 minutes into fire exposure.

APPENDIX C. Evaluation of fire performance of a UHPC beam through advanced analysis – numerical example

This appendix provides a worked example illustrating the application of advanced analysis for evaluating the fire response of a typical UHPC beam. The UHPC beam in this example, has a width of 180 mm, depth of 270 mm, and span length of 6000 mm. The cross-section and elevation of the UHPC beam are shown in Figure C.1. The compressive strength, direct tensile strength, elastic modulus, and permeability of UHPC are 175 MPa, 6 MPa, 43000 MPa, and $1.2x10^{-18}m^2$, respectively. The tensile reinforcement had a yield strength of 436 MPa, consisting of 3 rebars of 16 mm diameter providing a reinforcement ratio (ρ_t) of 1.24%. The nominal concrete cover to the middle of steel reinforcement is 35 mm. The beam is loaded with a uniformly distributed load of 10 kN/m and subjected to ASTM E119 standard fire scenario.

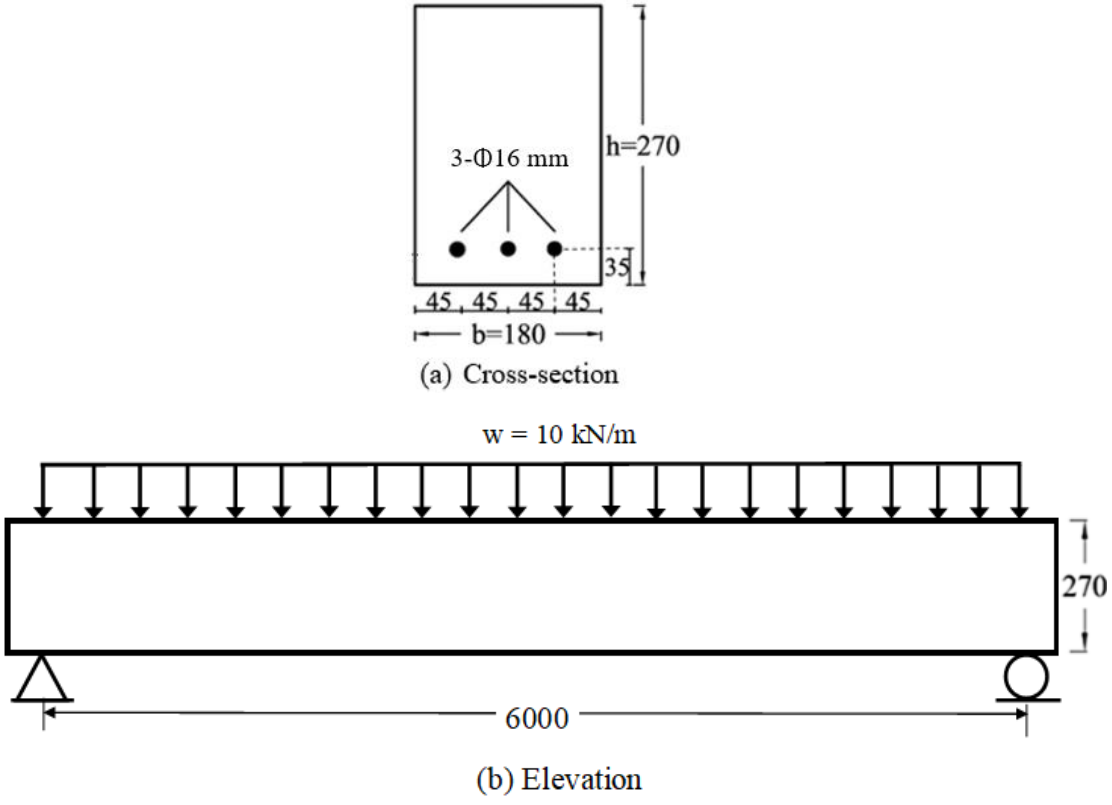

Figure C. 1. Cross-section and elevation of UHPC beam used in the illustration for advanced analysis (All dimensions are in mm).

Step 1: Discretization of the beam

The beam is divided into a number of segments along the length and the mid-section of each beam segment is further discretized into a mesh of two-dimensional rectangular elements as shown in Figure C.2.

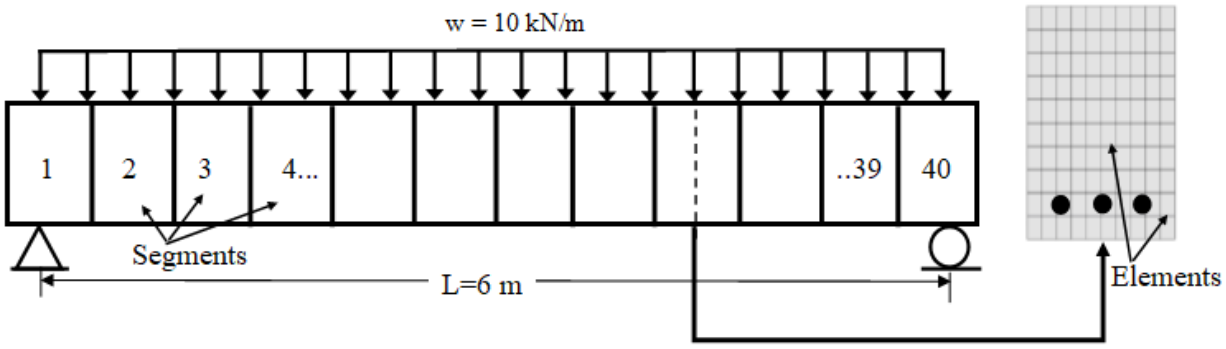

Figure C. 2. Discretization of beam into segments along length and discretization of cross-section into elements.

Step 2: Evaluation of fire temperatures

At each time-step, the temperatures due to fire exposure are established from the ASTM E119 standard fire time-temperature relationship, which is plotted in Figure C.3.

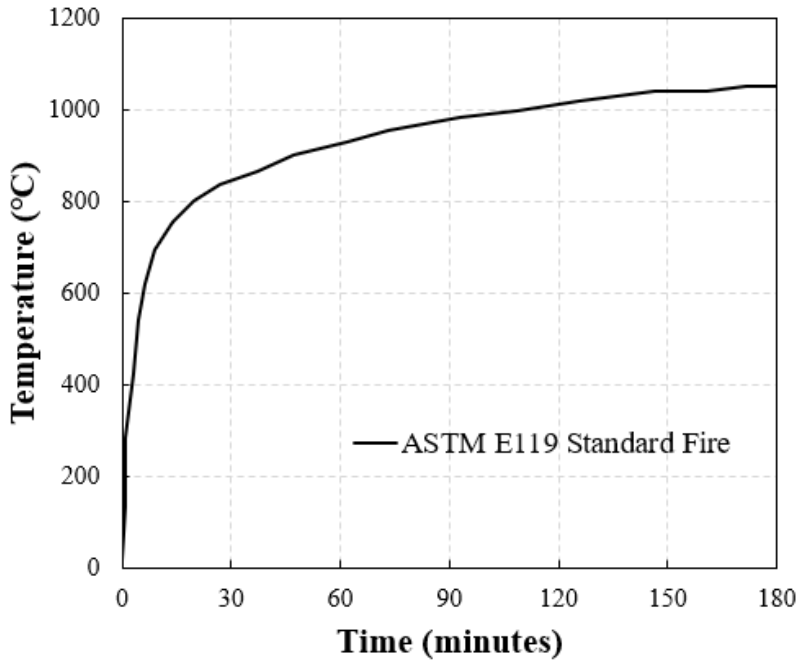

Figure C. 3. Time-temperature curve for standard fire scenario used in the analysis.

Step 3: Evaluation of sectional temperatures

The three sides of the beam (bottom surface and two sides) are assumed to be exposed to fire temperatures as determined from the previous step, while ambient conditions prevail on the top surface to simulate the presence of a slab. Cross-sectional temperatures are evaluated through thermal analysis by establishing heat balance for each element in mid-section of each segment along the beam. The predicted temperatures at corner rebar, middle rebar, and mid-depth as a function of time are shown in Figure C.4. The calculated sectional temperature contours at mid-span after 10 minutes into fire exposure are shown in Figure C.5.

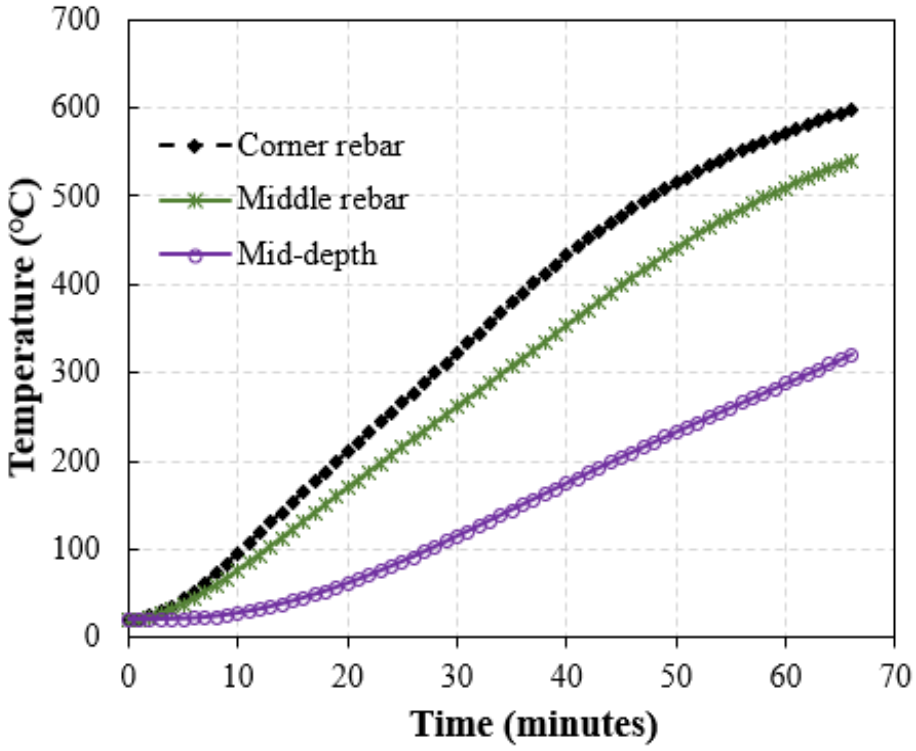

Figure C. 4. Cross-sectional temperatures as a function of time in the analyzed UHPC beam.

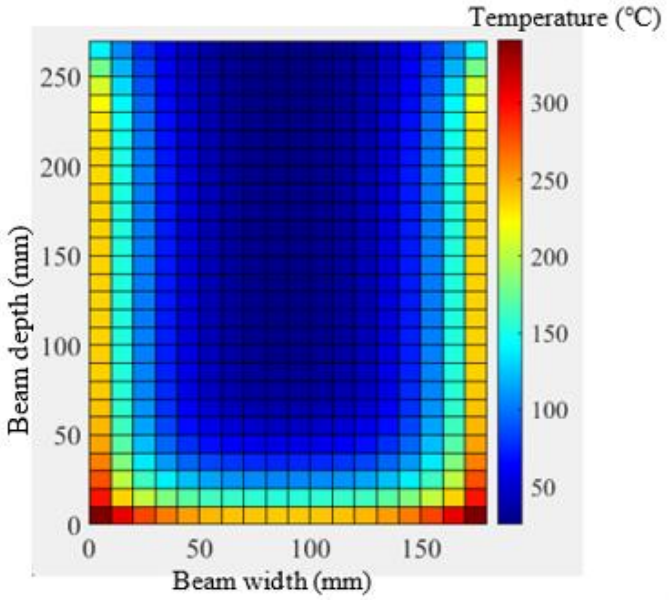

Figure C. 5. Cross-sectional temperature contours at mid-span in the analyzed UHPC beam after 10 minutes into fire exposure.

Step 4: Evaluation of fire-induced spalling

The evaluation of fire-induced spalling is based on two-step mechanism and involves calculation of pore pressure stress (σ_p), thermal stress (σ_{th}), and mechanical stress (σ_{me}). The pore pressure in each element is evaluated by applying mass balance equations, along with the principles of thermodynamics, including the conservation of mass of liquid water and water vapor. The pore pressure distribution at mid-span after 10 minutes into fire exposure is shown in Figure C.6. The thermal stress is evaluated utilizing the thermal gradients developed within the cross-section and temperature-dependent thermal expansion coefficient of concrete. The thermal gradients induced transverse thermal stress distribution at mid-span after 10 minutes into fire exposure is shown in Figure C.7. The mechanical stresses in each element are obtained by utilizing the temperature-dependent stress-strain relations of concrete corresponding to the mechanical strain computed from the moment-curvature analysis. The mechanical stress distribution in the transverse direction at mid-span after 10 minutes into fire exposure is shown in Figure C.8.

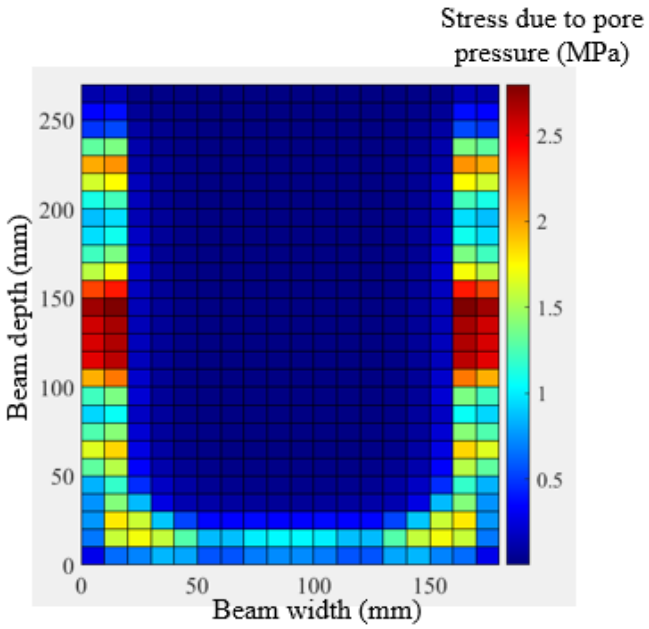

Figure C. 6. Pore pressure distribution at mid-span in the analyzed UHPC beam after 10 minutes into fire exposure.

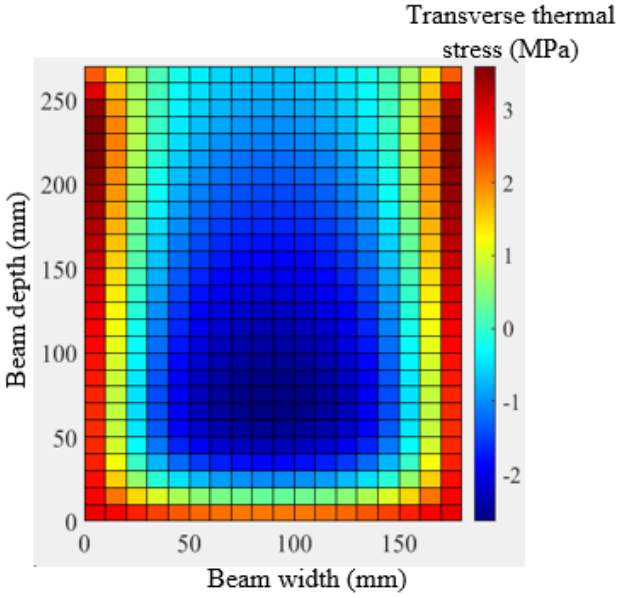

Figure C. 7. Cross-sectional thermal stress contours at mid-span in the analyzed UHPC beam after 10 minutes into fire exposure.

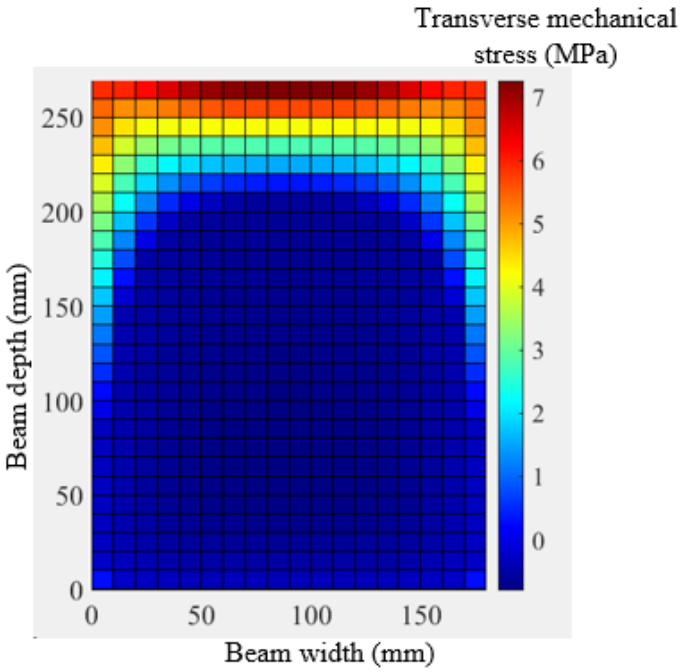

Figure C. 8. Cross-sectional mechanical stress contours at mid-span in the analyzed UHPC beam after 10 minutes into fire exposure.

As per the first step of the spalling mechanism, the concrete boundary elements (located in the first layer of a discretized concrete section close to the fire-exposed surface) will spall if the resulting tensile stress due to pore pressure build-up exceeds the decreasing tensile strength due to the rise in sectional temperature. As per the second step of the mechanism, when tensile strength is exceeded by pore pressure in any interior element (located in layers beneath the first layer closest to the fire i.e. second, third, fourth layer, and so on), and the resultant tensile stress due to thermal gradient, load and pore pressure in the elements in front of the interior element is higher than the thermally degraded tensile strength, spalling occurs in those interior and boundary elements. At each time increment, based on the spalling mechanism, the spalled elements (area) are removed from the cross-section, and the remaining cross-section. The evaluated extent of spalling as a function of fire exposure time for the analyzed UHPC beams is shown in Figure C.9.

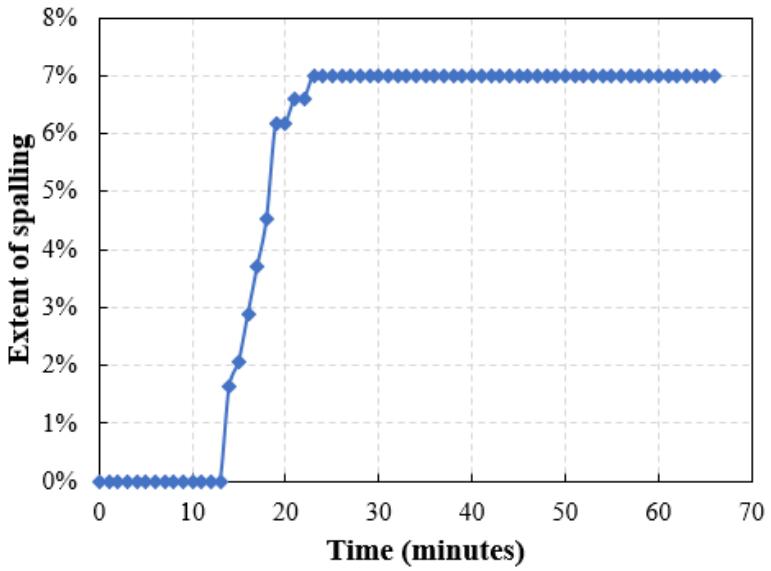

Figure C. 9. Extent of spalling as a function of time in the analyzed UHPC beam.

Step 5: Calculation of moment-curvature relations

Using the temperature-dependent mechanical properties of constituent materials, namely, concrete and steel reinforcement, a moment-curvature relation is generated, through an iterative process, for each segment at various time steps. The calculated moment-curvature curves for the mid-span of the analyzed UHPC beam are shown in Figure C.10 at various time steps.

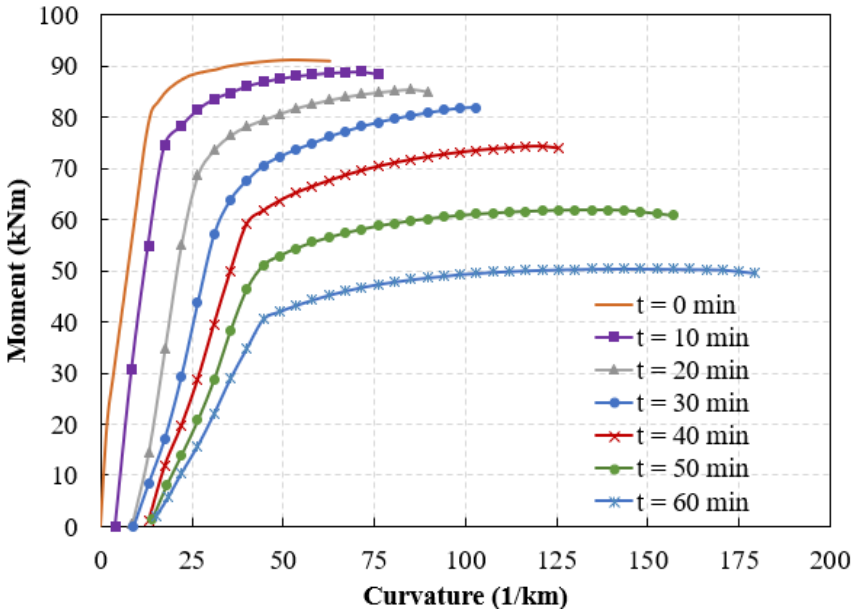

Figure C. 10. Moment–curvature curves at various fire exposure times for the analyzed UHPC beam.

Step 6: Calculation of moment capacity and deflection of the beam

The maximum value of the moment in the moment-curvature relations determines the moment capacity of each segment of the beam at each time step, as shown in Figure C.11. The mid-span deflection of the beam is calculated using the moment-area method and is plotted in Figure C.12 as a function of fire exposure time.

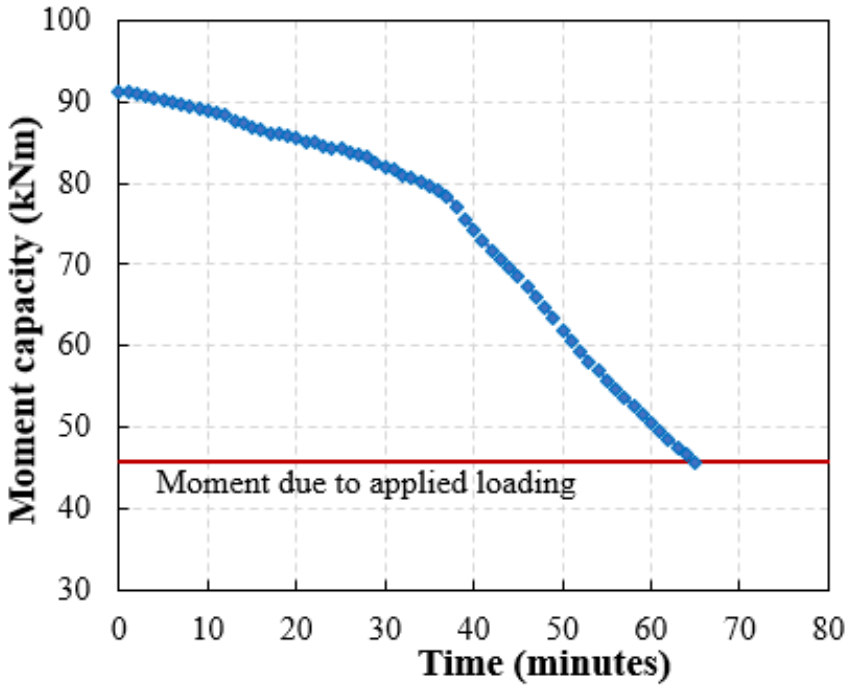

Figure C. 11. Variation of moment capacity for the analyzed UHPC beam as a function of fire exposure time.

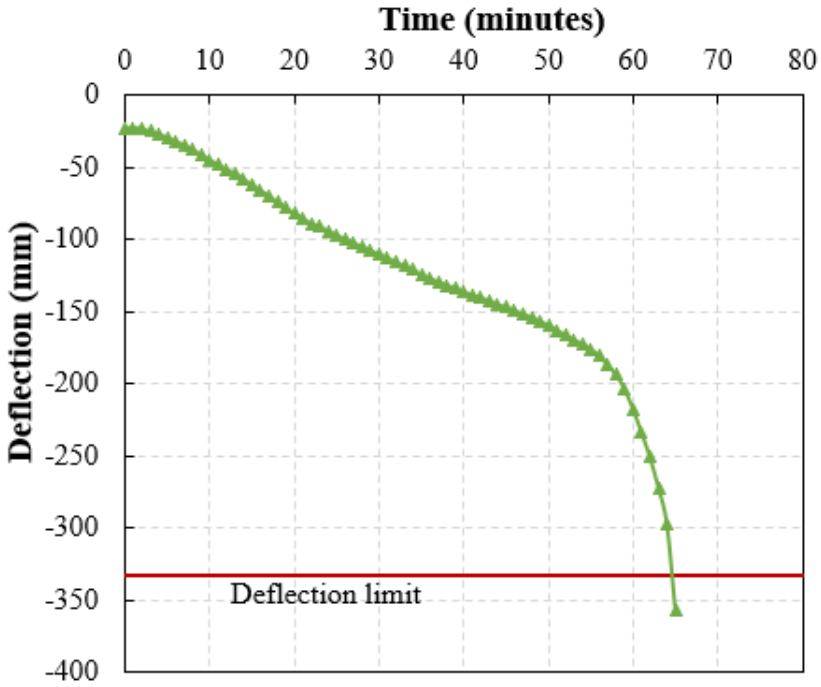

Figure C. 12. Variation of deflection for the analyzed UHPC beam as a function of fire exposure time.

Step 7: Calculation of fire resistance of the beam

The moment capacity and deflection of the UHPC beam computed in the previous step are utilized to check the failure of the beam. At each time increment, each segment of the beam is checked to see if the moment capacity or deflection has exceeded the limiting criterion. The analyzed UHPC beam failed at 65 minutes according to both the strength and deflection criteria.

APPENDIX D. Material properties at elevated temperatures

This appendix provides a summary of high temperature material property relationships used in the numerical model and parametric studies for concrete (normal strength concrete (NSC), high strength concrete (HSC), and ultra-high performance concrete (UHPC)) and steel reinforcement.

D.1. Normal Strength Concrete

The equations presented in this section have been reproduced from ASCE manual [22].

D.1.1. Thermal Capacity

For carbonate aggregate concrete,

$$\rho_{cT} = \begin{cases} 2.566 \times 10^6 & 20℃ \le T \le 400℃ \\ (0.1765T - 68.034) \times 10^6 & 400℃ \le T \le 410℃ \\ (-0.05043T + 25.00671) \times 10^6 & 410℃ \le T \le 445℃ \\ 2.566 \times 10^6 & 445℃ \le T \le 500℃ \\ (0.01603T - 5.44881) \times 10^6 & 500℃ \le T \le 635℃ \\ (0.005T - 100.90225) \times 10^6 & 635℃ \le T \le 715℃ \\ (-0.22103T - 176.07343) \times 10^6 & 715℃ \le T \le 785℃ \\ 2.566 \times 10^6 & T \ge 785℃ \end{cases}$$

D.1.2. Thermal Conductivity

For carbonate aggregate concrete,

$$k_{cT} = \begin{cases} 1.355 & 20℃ \le T \le 293℃ \\ -0.001241T + 1.7162 & T \ge 293℃ \end{cases}$$

D.1.3. Thermal Strain

$$\varepsilon_{th} = [\, 0.004\,(T^2 - 400) + 6\,(T - 20)\,] \times 10^{-6}$$

D.1.4. Stress-strain Relationships

$$\sigma_c = \begin{cases} f'_{c,T}\left[1-\left(\dfrac{\varepsilon-\varepsilon_{max,T}}{\varepsilon_{max,T}}\right)^2\right] & \varepsilon \le \varepsilon_{max,T} \\ f'_{c,T}\left[1-\left(\dfrac{\varepsilon_{max,T}-\varepsilon}{3\,\varepsilon_{max,T}}\right)^2\right] & \varepsilon > \varepsilon_{max,T} \end{cases}$$

$$f'_{c,T} = \begin{cases} f'_c & 20℃ \le T \le 450℃ \\ f'_c\left[2.011-2.353\left(\dfrac{T-20}{1000}\right)\right] & 450℃ \le T \le 874℃ \\ 0 & T > 874℃ \end{cases}$$

$$\varepsilon_{max,T} = 0.0025 + (6.0T + 0.04T^2) \times 10^{-6}$$

D.2. High Strength Concrete

The equations presented in this section have been reproduced from Kodur et al. [41].

D.2.1. Thermal Capacity

For carbonate aggregate concrete,

$$\rho_{cT} = \begin{cases} 2.45 \text{ x } 10^6 & 20℃ \le T \le 400℃ \\ (0.026T - 12.85) \text{ x } 10^6 & 400℃ \le T \le 475℃ \\ (0.0143T\text{-}6.295) \text{ x } 10^6 & 475℃ \le T \le 650℃ \\ (0.1894T - 120.11) \text{ x } 10^6 & 650℃ \le T \le 735℃ \\ (\text{-}0.263 - 212.4) \text{ x } 10^6 & 735℃ \le T \le 800℃ \\ 2\text{x } 10^6 & 800℃ \le T \le 1000℃ \end{cases}$$

D.2.2. Thermal Conductivity

For carbonate aggregate concrete,

$$k_{cT} = \begin{cases} 0.85(2\text{-}0.0013T) & 20℃ \le T \le 300℃ \\ 0.85(2.21\text{-}0.002T) & T \ge 300℃ \end{cases}$$

D.2.3. Thermal Strain

$$\varepsilon_{th} = [\ 0.004\ (T^2 - 400) + 6\ (T - 20)\ ] \text{ x } 10^{-6}$$

D.2.4. Stress-strain Relationships

$$\sigma_c = \begin{cases} f'_{c,T}\left[1-\left(\dfrac{\varepsilon_{max,T}-\varepsilon}{\varepsilon_{max,T}}\right)^{H}\right] & \varepsilon \le \varepsilon_{max,T} \\ f'_{c,T}\left[1-\left(\dfrac{30\,(\varepsilon-\varepsilon_{max,T})}{(130-f'_c)\,\varepsilon_{max,T}}\right)^{2}\right] & \varepsilon > \varepsilon_{max,T} \end{cases}$$

$$f'_{c,T} = \begin{cases} f'_c[1.0-0.003125(T-20)] & \mathrm{T} \le 100℃ \\ 0.75f'_c & 100℃ \le \mathrm{T} \le 400℃ \\ f'_c[1.33-0.00145T] & \mathrm{T} > 400℃ \end{cases}$$

$$\varepsilon_{max,T} = 0.0018 + \left(6.7f'_c + 6.0T + 0.03T^2\right) \times 10^{-6}$$

$$H = 2.28 - 0.012f'_c$$

D.3. Ultra High Performance Concrete

The equations presented in this section are based on experiments carried out in this thesis. The thermal properties are proposed by Kodur et al. [118] and the mechanical properties are proposed by Banerji and Kodur [165].

D.3.1. Specific Heat

ρ_{cT} =

$2\text{x}10^{-6}\,\text{T}^2 + 0.0013\text{T} + 1.6918$	20°C ≤ *T* ≤ 300°C
-0.0046T+3.6677	300°C ≤ *T* ≤ 400°C
0.0054T-0.3217	400°C ≤ *T* ≤ 600°C
0.0006T+2.5588	600°C ≤ *T* ≤ 700°C

D.3.2. Thermal Conductivity

k_{cT} =

-0.0092T+3.1136	20°C ≤ *T* ≤ 100°C
-0.0035T+2.5802	100°C ≤ *T* ≤ 400°C
0.0021T+0.3481	400°C ≤ *T* ≤ 500°C
$-10^{-5}\,\text{T}^2 + 0.0111\text{T} - 1.6565$	500°C ≤ *T* ≤ 700°C

D.3.3. Thermal Strain

$$\varepsilon_{th} = \begin{cases} 2\text{x}10^{-6}\text{T}^2 + 0.0002\text{T} + 0.0014 & 20°\text{C} \le T \le 600°\text{C} \\ -1.443\text{x}10^{-5}\text{T}^2 + 0.0188\text{T} - 5.2031 & 600°\text{C} \le T \le 800°\text{C} \\ 0.0037\text{T} - 2.342 & 800°\text{C} \le T \le 900°\text{C} \end{cases}$$

D.3.4. Strength Degradation

The following equations provide reduction factors of compressive strength, elastic modulus, tensile strength and peak strain at elevated temperatures.

$$\alpha_{T,compression} = -1.02*10^{-3}*\text{T} + 1.02$$

$$\alpha_{T,modulus} = 1.42*10^{-6}*\text{T}^2 - 2.4*10^{-3}*\text{T} + 1.05$$

$$\alpha_{max,T} = 2.7*10^{-8}*\text{T}^3 - 2*10^{-5}*\text{T}^2 + 8.1*10^{-3}*\text{T} + 0.85$$

$$\alpha_{T,tensile} = \begin{cases} 2\text{x}10^{-6}\text{T}^2 + 0.0002\text{T} + 0.0014 & 20°\text{C} \le T \le 600°\text{C} \\ -1.443\text{x}10^{-5}\text{T}^2 + 0.0188\text{T} - 5.2031 & 600°\text{C} \le T \le 800°\text{C} \\ 0.0037\text{T} - 2.342 & 800°\text{C} \le T \le 900°\text{C} \end{cases}$$

D.3.5. Stress-strain Relationships

$$\sigma_c = \begin{cases} f'_{c,T}\left[\dfrac{k_1\,\beta\,(\frac{\varepsilon}{\varepsilon'_{cT}})}{k_1\,\beta - 1 + (\frac{\varepsilon}{\varepsilon'_{cT}})^{k_1\,\beta}}\right] & \varepsilon \le \varepsilon_{max,T} \\ f'_{c,T}\left[\dfrac{k_2\,\beta\,(\frac{\varepsilon}{\varepsilon'_{cT}})}{k_2\,\beta - 1 + (\frac{\varepsilon}{\varepsilon'_{cT}})^{k_2\,\beta}}\right] & \varepsilon > \varepsilon_{max,T} \end{cases}$$

$$\beta = \frac{1}{1 - \dfrac{f'_{cT}}{\varepsilon'_{cT} E_{cT}}}$$

$$k_1 = 4.11 * 10^{-8} * \text{T}^3 - 4.19 * 10^{-5} * \text{T}^2 + 0.017 * \text{T} + 0.038$$

$$k_2 = 3.24 * 10^{-8} * \text{T}^3 - 3.67 * 10^{-5} * \text{T}^2 + 0.013 * \text{T} + 0.48$$

D.4. Reinforcing Steel

D.4.1. Thermal strain

The equations presented in this section have been reproduced from Eurocode 2 [16].

$$\varepsilon_{ths} = \begin{cases} 1.2\text{x}10^{-5}\text{T} + 0.4\text{x}10^{-8}\text{T}^2 - 2.416\text{x}10^{-4} & 20℃ \leq \text{T} \leq 750℃ \\ 1.1 \text{ x } 10^{-2} & 750℃ \leq \text{T} \leq 860℃ \\ 2\text{x}10^{-5}\text{T} - 6.2\text{x}10^{-3} & 860℃ \leq \text{T} \leq 1200℃ \end{cases}$$

D.4.2. Stress-strain relationship

The stress-strain relationships have been adopted from Shakya and Kodur [162]. The strength and modulus degradation have been reproduced from Eurocode 2 [16].

$$\sigma_s = \begin{cases} \varepsilon_s E_{s,T} & \varepsilon_s \leq \varepsilon_{sy,T} \\ f_{sy,T} & \varepsilon_{sy,T} \leq \varepsilon \leq \varepsilon_{sp,T} \\ f_{sy,T} \times \left[\dfrac{ft1}{f_{sy,T}} - \left(\dfrac{ft1}{f_{sy,T}} - 1\right)\left(\dfrac{0.12 - \varepsilon}{0.12 - \varepsilon_{sp,T}}\right)^4\right] & \varepsilon_{sp,T} \leq \varepsilon \leq 0.12 \\ ft1 + \dfrac{\left(f_{u,T} - ft1\right)}{(0.15 - 0.12)}(\varepsilon - 0.12) & 0.12 \leq \varepsilon \leq 0.15 \end{cases}$$

$$\varepsilon_{sy,T} = \frac{f_{sy,T}}{E_{s,T}};\ \varepsilon_{sp,T} = 2.75 \times \varepsilon_{sy,T};\ f_{u,T} = 0.05 f_{sy,T}$$

$$ft1 = \begin{cases} 1.33 \times f_{sy,T} & T \leq 300℃ \\ 0.000004\text{T}^2 - 0.0047T + 2.36 & T > 300℃ \end{cases}$$

Table D- 1. Values for the Main Parameters of the Stress-strain Relationships of Reinforcing Steel at Elevated Temperatures (Eurocode 2).

Steel Temperature T (°C)	f_{yT} / f_y	EsT / Es
20	1	1
100	1	1
200	1	0.9
300	1	0.8
400	1	0.7
500	0.78	0.6
600	0.47	0.31
700	0.23	0.13
800	0.11	0.09
900	0.06	0.0675
1000	0.04	0.045
1100	0.02	0.0225
1200	0	0

fy and *Es* are yield strength and modulus of elasticity at room temperature

REFERENCES

REFERENCES

[1] JSCE. Recommendations for design and construction of ultra-high strength fiber reinforced concrete structures 2004.

[2] AFGC/SETRA. Ultra high performance fibre-reinforced concretes. French Civil Engineering Association, Bagneux, France n.d.;2002.

[3] Kodur V, Naser M. Structural fire engineering. McGraw Hill Professional London; 2020.

[4] Harmathy TZ. Fire safety design and concrete. Harlow, U.K.: Longman; 1993.

[5] Bazant ZP, Thonguthai W. Pore pressure and drying of concrete at high temperature. ASCE J Eng Mech Div 1978;104:1059–79.

[6] Peng SW, Qin QH, Cheng SM, Chen GQ. Exact solution of coupled heat and mass transfer with double moving interfaces in a porous half-space. Part 2: Mass transfer controlled by the fick and darcy laws. International Journal of Energy Research 1992;16:401–11. https://doi.org/10.1002/er.4440160507.

[7] Bazant ZP. Analysis of Pore Pressure, Thermal Stress and Fracture in Rapidly Heated Concrete. International Workshop on Fire Performance of High-Strength Concrete. Proceedings. Appendix B: Workshop Papers. B10, Gaithersburg, MD: NIST; 1997, p. 155–64.

[8] Anderberg Y. Spalling phenomenon of HPC and OC. NIST SP 919, Gaithersburg, MD: NIST; 1997, p. 69–75.

[9] Ulm F-J, Coussy O, Bažant ZP. The "Chunnel" fire. I: Chemoplastic softening in rapidly heated concrete. Journal of Engineering Mechanics 1999;125:272–82. https://doi.org/10.1061/(ASCE)0733-9399(1999)125:3(272).

[10] Kodur V. K. R., Cheng Fu-Ping, Wang Tien-Chih, Sultan M. A. Effect of Strength and Fiber Reinforcement on Fire Resistance of High-Strength Concrete Columns. Journal of Structural Engineering 2003;129:253–9. https://doi.org/10.1061/(ASCE)0733-9445(2003)129:2(253).

[11] Dwaikat MB, Kodur VKR. Response of restrained concrete beams under design fire exposure. Journal of Structural Engineering 2009;135:1408–17. https://doi.org/10.1061/(ASCE)ST.1943-541X.0000058.

[12] Phan LT, Carino NJ. Fire performance of high strength concrete: research needs. Advanced Technology in Structural Engineering, 2000, p. 1–8.

[13] Kodur VKR, Wang TC, Cheng FP. Predicting the fire resistance behaviour of high strength concrete columns. Cement and Concrete Composites 2004;26:141–53. https://doi.org/10.1016/S0958-9465(03)00089-1.

[14] Felicetti R, Gambarova PG, Meda A. Residual behavior of steel rebars and R/C sections after a fire. Construction and Building Materials 2009;23:3546–55. https://doi.org/10.1016/j.conbuildmat.2009.06.050.

[15] LaMalva KJ. Structural fire engineering, American Society of Civil Engineers; 2018.

[16] EN 1992-1-2. Eurocode 2: Design of concrete structures-Part 1-2: General rules-structural fire design. CEN, Brussels: 2004.

[17] Kodur V. Properties of Concrete at Elevated Temperatures. ISRN Civil Engineering 2014. https://doi.org/10.1155/2014/468510.

[18] Khaliq W, Kodur V. High Temperature Mechanical Properties of High-Strength Fly Ash Concrete with and without Fibers. ACI Materials Journal 2012;109.

[19] Shin K-Y, Kim S-B, Kim J-H, Chung M, Jung P-S. Thermo-physical properties and transient heat transfer of concrete at elevated temperatures. Nuclear Engineering and Design 2002;212:233–41.

[20] Kodur VKR, Sultan MA. Effect of temperature on thermal properties of high-strength concrete. Journal of Materials in Civil Engineering 2003;15:101–7.

[21] Kodur V, Khaliq W. Effect of temperature on thermal properties of different types of high-strength concrete. Journal of Materials in Civil Engineering 2011;23:793–801.

[22] Lie TT. Structural fire protection, American Society of Civil Engineers; 1992.

[23] Kodur VKR, Harmathy TZ. SFPE Handbook of Fire Protection Engineering. Properties of Building Materials, Section 1 2002.

[24] Felicetti R, Gambarova PG, Bamonte P. Thermal and mechanical properties of light-weight concrete exposed to high temperature. Fire and Materials 2013;37:200–16.

[25] Kodur VK, Banerji S, Solhmirzaei R. Test methods for characterizing concrete properties at elevated temperature. Fire and Materials 2020;44:381–95.

[26] ASTM C177-19: Standard test method for steady-state heat flux measurements and thermal transmission properties by means of the guarded-hot-plate apparatus. ASTM International, West Conshohocken, PA n.d.;2019.

[27] ASTM C1363-19: Standard test method for thermal performance of building materials and envelope assemblies by means of a hot box apparatus. ASTM International, West Conshohocken, PA n.d.;2019.

[28] ISO 8302: 1991-Thermal insulation — Determination of steady-state thermal resistance and related properties — Guarded hot plate apparatus. Switzerland, Geneva 1991.

[29] ISO - ISO 22007-2:2015 - Plastics — Determination of thermal conductivity and thermal diffusivity — Part 2: Transient plane heat source (hot disc) method n.d. https://www.iso.org/standard/61190.html (accessed June 15, 2020).

[30] ASTM E1269 - 11(2018): Standard test method for determining specific heat capacity by differential scanning calorimetry. ASTM International, West Conshohocken, PA n.d.;2018.

[31] ISO 11357-4:2014- Plastics — Differential scanning calorimetry (DSC) — Part 4: Determination of specific heat capacity. Switzerland, Geneva n.d.;2014.

[32] ASTM E831. Standard Test Method for Linear Thermal Expansion of Solid Materials by Thermomechanical Analysis. West Conshohocken, PA: ASTM International; 2014. https://doi.org/10.1520/E0831-14.

[33] ISO 11359-2:1999-Plastics — Thermomechanical analysis (TMA) — Part 2: Determination of coefficient of linear thermal expansion and glass transition temperature. Switzerland, Geneva n.d.;1999.

[34] ASTM E1131-20, Standard test method for compositional analysis by thermogravimetry. ASTM International, West Conshohocken, PA n.d.;2020.

[35] ISO 11358-1:2014-Plastics — Thermogravimetry (TG) of polymers — Part 1: General principles. Switzerland, Geneva n.d.;2014.

[36] Kodur VKR, Dwaikat MMS, Dwaikat MB. High-Temperature Properties of Concrete for Fire Resistance Modeling of Structures. MJ 2008;105:517–27. https://doi.org/10.14359/19982.

[37] Ju Y, Liu H, Liu J, Tian K, Wei S, Hao S. Investigation on thermophysical properties of reactive powder concrete. Science China Technological Sciences 2011;54:3382–403.

[38] Zheng W, Luo B, Wang Y. Stress–strain relationship of steel-fibre reinforced reactive powder concrete at elevated temperatures. Mater Struct 2015;48:2299–314. https://doi.org/10.1617/s11527-014-0312-9.

[39] Sanchayan S, Foster SJ. High temperature behaviour of hybrid steel–PVA fibre reinforced reactive powder concrete. Mater Struct 2016;49:769–82. https://doi.org/10.1617/s11527-015-0537-2.

[40] AFGC/SETRA. Ultra high performance fibre-reinforced concretes 2002.

[41] Cheng F-P, Kodur VKR, Wang T-C. Stress-Strain Curves for High Strength Concrete at Elevated Temperatures. J Mater Civ Eng 2004;16:84–90. https://doi.org/10.1061/(ASCE)0899-1561(2004)16:1(84).

[42] Khaliq W, Kodur VKR. Effect of High Temperature on Tensile Strength of Different Types of High-Strength Concrete. ACI Materials Journal 2011;108.

[43] ASTM C39/C39M-18: Standard test method for compressive strength of cylindrical concrete specimens. ASTM International, West Conshohocken, PA n.d.;2018.

[44] ASTM C496/C496M-17: Standard test method for splitting tensile strength of cylindrical concrete specimens. ASTM International, West Conshohocken, PA n.d.;2017.

[45] RILEM TC 129 MHT. Test methods for mechanical properties of concrete at high temperatures n.d.;1995.

[46] ASTM C469: Standard test method for static modulus of elasticity and poisson's ratio of concrete in compression. ASTM International, West Conshohocken, PA n.d.;2014.

[47] ASTM C78 / C78M - 18: Standard Test Method for Flexural Strength of Concrete (Using Simple Beam with Third-Point Loading). ASTM International, West Conshohocken, PA n.d.;2018.

[48] ASTM C1583 / C1583M - 20: Standard Test Method for Tensile Strength of Concrete Surfaces and the Bond Strength or Tensile Strength of Concrete Repair and Overlay Materials by Direct Tension (Pull-off Method). ASTM International, West Conshohocken, PA n.d.;2020.

[49] Tai Y-S, Pan H-H, Kung Y-N. Mechanical properties of steel fiber reinforced reactive powder concrete following exposure to high temperature reaching 800 C. Nuclear Engineering and Design 2011;241:2416–24.

[50] Zheng W, Luo B, Wang Y. Compressive and tensile properties of reactive powder concrete with steel fibres at elevated temperatures. Construction and Building Materials 2013;41:844–51. https://doi.org/10.1016/j.conbuildmat.2012.12.066.

[51] Zheng W, Li H, Wang Y. Compressive behaviour of hybrid fiber-reinforced reactive powder concrete after high temperature. Materials & Design 2012;41:403–9. https://doi.org/10.1016/j.matdes.2012.05.026.

[52] Zheng W, Li H, Wang Y. Compressive stress–strain relationship of steel fiber-reinforced reactive powder concrete after exposure to elevated temperatures. Construction and Building Materials 2012;35:931–40. https://doi.org/10.1016/j.conbuildmat.2012.05.031.

[53] Li H, Liu G. Tensile Properties of Hybrid Fiber-Reinforced Reactive Powder Concrete After Exposure to Elevated Temperatures. Int J Concr Struct Mater 2016;10:29–37. https://doi.org/10.1007/s40069-016-0125-z.

[54] Abid M, Hou X, Zheng W, Hussain RR. Effect of Fibers on High-Temperature Mechanical Behavior and Microstructure of Reactive Powder Concrete. Materials 2019;12:329. https://doi.org/10.3390/ma12020329.

[55] Zeiml M, Lackner R, Leithner D, Eberhardsteiner J. Identification of residual gas-transport properties of concrete subjected to high temperatures. Cement and Concrete Research 2008;38:699–716. https://doi.org/10.1016/j.cemconres.2008.01.005.

[56] Noumowe AN, Siddique R, Debicki G. Permeability of high-performance concrete subjected to elevated temperature (600°C). Construction and Building Materials 2009;23:1855–61. https://doi.org/10.1016/j.conbuildmat.2008.09.023.

[57] Kalifa P, Chene G, Galle C. High-temperature behaviour of HPC with polypropylene fibres From spalling to microstructure. Cement and Concrete Research 2001:13.

[58] Liu X, Ye G, De Schutter G, Yuan Y, Taerwe L. On the mechanism of polypropylene fibres in preventing fire spalling in self-compacting and high-performance cement paste. Cement and Concrete Research 2008;38:487–99. https://doi.org/10.1016/j.cemconres.2007.11.010.

[59] Bošnjak J, Ožbolt J, Hahn R. Permeability measurement on high strength concrete without and with polypropylene fibers at elevated temperatures using a new test setup. Cement and Concrete Research 2013;53:104–11. https://doi.org/10.1016/j.cemconres.2013.06.005.

[60] ASTM C1202 - 19: Standard Test Method for Electrical Indication of Concrete's Ability to Resist Chloride Ion Penetration. ASTM International, West Conshohocken, PA n.d.;2019.

[61] Kim H, Lee C-J, Shon C-S, Moon H, Chung C-W. Mechanical performance and chloride ion penetration of polyolefin fiber reinforced concrete designed for shotcreting at marine environment. Journal of Structural Integrity and Maintenance 2020;5:8–17. https://doi.org/10.1080/24705314.2019.1692164.

[62] ASTM C1585 - 20: Standard Test Method for Measurement of Rate of Absorption of Water by Hydraulic-Cement Concretes. ASTM International, West Conshohocken, PA n.d.;2020.

[63] RILEM TC 116-PCD. Permeability of Concrete as a Criterion of its Durability. Recommendations 2009.

[64] Klinkenberg LJ. The permeability of porous media to liquids and gases. Drilling and production practice, American Petroleum Institute; 1941.

[65] ASTM C642 - 13: Standard Test Method for Density, Absorption, and Voids in Hardened Concrete. ASTM International, West Conshohocken, PA n.d.;2013.

[66] RILEM 049-TFR. Testing methods for fibre reinforced cement-based composites 1984.

[67] Li Y, Tan KH, Yang E-H. Influence of aggregate size and inclusion of polypropylene and steel fibers on the hot permeability of ultra-high performance concrete (UHPC) at elevated temperature. Construction and Building Materials 2018;169:629–37. https://doi.org/10.1016/j.conbuildmat.2018.01.105.

[68] Poon C-S, Azhar S, Anson M, Wong Y-L. Comparison of the strength and durability performance of normal- and high-strength pozzolanic concretes at elevated temperatures. Cement and Concrete Research 2001;31:1291–300. https://doi.org/10.1016/S0008-8846(01)00580-4.

[69] Yermak N, Pliya P, Beaucour A-L, Simon A, Noumowé A. Influence of steel and/or polypropylene fibres on the behaviour of concrete at high temperature: Spalling, transfer and mechanical properties. Construction and Building Materials 2017;132:240–50. https://doi.org/10.1016/j.conbuildmat.2016.11.120.

[70] Li Y, Pimienta P, Pinoteau N, Tan KH. Effect of aggregate size and inclusion of polypropylene and steel fibers on explosive spalling and pore pressure in ultra-high-performance concrete (UHPC) at elevated temperature. Cement and Concrete Composites 2019;99:62–71. https://doi.org/10.1016/j.cemconcomp.2019.02.016.

[71] Felicetti R, Lo Monte F, Pimienta P. A new test method to study the influence of pore pressure on fracture behaviour of concrete during heating. Cement and Concrete Research 2017;94:13–23. https://doi.org/10.1016/j.cemconres.2017.01.002.

[72] Kodur VKR. Guidelines for fire resistance design of high-strength concrete columns. Journal of Fire Protection Engineering 2005;15:93–106. https://doi.org/10.1177/1042391505047740.

[73] Kodur VK. Innovative strategies for enhancing fire performance of high-strength concrete structures. Advances in Structural Engineering 2018;21:1723–32. https://doi.org/10.1177/1369433218754335.

[74] Shah AH, Sharma UK. Fire resistance and spalling performance of confined concrete columns. Construction and Building Materials 2017;156:161–74. https://doi.org/10.1016/j.conbuildmat.2017.08.167.

[75] Ali F, Nadjai A, Silcock G, Abu-Tair A. Outcomes of a major research on fire resistance of concrete columns. Fire Safety Journal 2004;39:433–45.

[76] Franssen J-M, Dotreppe J-C. Fire Tests and Calculation Methods for Circular Concrete Columns. Fire Technology 2003;39:89–97. https://doi.org/10.1023/A:1021783311892.

[77] Choi EG, Shin YS. The structural behavior and simplified thermal analysis of normal-strength and high-strength concrete beams under fire. Engineering Structures 2011;33:1123–32.

[78] Lee J-H, Sohn Y-S, Lee S-H. Fire resistance of hybrid fibre-reinforced, ultra-high-strength concrete columns with compressive strength from 120 to 200 MPa. Magazine of Concrete Research 2012;64:539–50.

[79] Kahanji C, Ali F, Nadjai A. Explosive spalling of ultra-high performance fibre reinforced concrete beams under fire. Journal of Structural Fire Engineering 2016;7:328–48.

[80] Hou X, Ren P, Rong Q, Zheng W, Zhan Y. Effect of fire insulation on fire resistance of hybrid-fiber reinforced reactive powder concrete beams. Composite Structures 2019;209:219–32. https://doi.org/10.1016/j.compstruct.2018.10.073.

[81] Mai V-C, Nguyen T-C, Dao C-B. Numerical simulation of ultra-high-performance fiber-reinforced concrete frame structure under fire action. Asian J Civ Eng 2020;21:797–804. https://doi.org/10.1007/s42107-020-00240-4.

[82] Ren P, Hou X, Rong Q, Zheng W. Quantifying Fire Insulation Effects on the Fire Response of Hybrid-Fiber Reinforced Reactive Powder Concrete Beams. Fire Technol 2019. https://doi.org/10.1007/s10694-019-00937-2.

[83] Kodur VKR. Spalling in high strength concrete exposed to fire: concerns, causes, critical parameters and cures. Advanced Technology in Structural Engineering, Philadelphia, Pennsylvania, United States: ASCE; 2000, p. 1–9. https://doi.org/10.1061/40492(2000)180.

[84] Dwaikat MB, Kodur VKR. Hydrothermal model for predicting fire-induced spalling in concrete structural systems. Fire Safety Journal 2009;44:425–34. https://doi.org/10.1016/j.firesaf.2008.09.001.

[85] Ichikawa Y, England GL. Prediction of moisture migration and pore pressure build-up in concrete at high temperatures. Nuclear Engineering and Design 2004;228:245–59. https://doi.org/10.1016/j.nucengdes.2003.06.011.

[86] Msaad Y, Bonnet G. Analyses of heated concrete spalling due to restrained thermal dilation: Application to the “chunnel” fire. Journal of Engineering Mechanics 2006;132:1124–32. https://doi.org/10.1061/(ASCE)0733-9399(2006)132:10(1124).

[87] Gawin D, Pesavento F, Schrefler BA. Towards prediction of the thermal spalling risk through a multi-phase porous media model of concrete. Computer Methods in Applied Mechanics and Engineering 2006;195:5707–29. https://doi.org/10.1016/j.cma.2005.10.021.

[88] Zhang HL, Davie CT. A numerical investigation of the influence of pore pressures and thermally induced stresses for spalling of concrete exposed to elevated temperatures. Fire Safety Journal 2013;59:102–10.

[89] Zhao J, Zheng J, Peng G, van Breugel K. A meso-level investigation into the explosive spalling mechanism of high-performance concrete under fire exposure. Cement and Concrete Research 2014;65:64–75.

[90] Tenchev R, Purnell P. An application of a damage constitutive model to concrete at high temperature and prediction of spalling. International Journal of Solids and Structures 2005;42:6550–65. https://doi.org/10.1016/j.ijsolstr.2005.06.016.

[91] Dwaikat MB, Kodur VKR. Fire induced spalling in high strength concrete beams. Fire Technology 2010;46:251. https://doi.org/10.1007/s10694-009-0088-6.

[92] Kodur V, Dwaikat M. Fire-induced spalling in reinforced concrete beams. Proceedings of the Institution of Civil Engineers - Structures and Buildings 2012;165:347–59. https://doi.org/10.1680/stbu.11.00013.

[93] Gawin D, Pesavento F, Schrefler BA. Modelling of hygro-thermal behaviour of concrete at high temperature with thermo-chemical and mechanical material degradation. Computer Methods in Applied Mechanics and Engineering 2003;192:1731–71. https://doi.org/10.1016/S0045-7825(03)00200-7.

[94] Gawin D, Pesavento F, Castells AG. On reliable predicting risk and nature of thermal spalling in heated concrete. Archives of Civil and Mechanical Engineering 2018;18:1219–27. https://doi.org/10.1016/j.acme.2018.01.013.

[95] Shen L, Li W, Zhou X, Feng J, Di Luzio G, Ren Q, et al. Multiphysics Lattice Discrete Particle Model for the simulation of concrete thermal spalling. Cement and Concrete Composites 2020;106:103457. https://doi.org/10.1016/j.cemconcomp.2019.103457.

[96] Banerji S, Kodur V, Solhmirzaei R. Experimental behavior of ultra high performance fiber reinforced concrete beams under fire conditions. Engineering Structures 2020;208:110316. https://doi.org/10.1016/j.engstruct.2020.110316.

[97] Zeiml M, Lackner R, Mang HA. Experimental insight into spalling behavior of concrete tunnel linings under fire loading. Acta Geotechnica 2008;3:295–308. https://doi.org/10.1007/s11440-008-0069-9.

[98] ACI A. 216.1 M-07: Standard Method for Determining Fire Resistance of Concrete and Masonry Construction Assemblies. Detroit, USA: American Concrete Institute 2007.

[99] ASTM E119-19. Standard Test Methods for Fire Tests of Building Construction and Materials. West Conshohocken, PA: American Society of Testing Materials; 2019.

[100] ISO 834-1:1999. Fire Resistance Tests – Elements of Building Construction-Part 1: General Requirements. Switzerland, Geneva: 1999.

[101] Russell HG, Graybeal BA, Russell HG. Ultra-high performance concrete: A state-of-the-art report for the bridge community. United States. Federal Highway Administration. Office of Infrastructure; 2013.

[102] KCI. Design recommendations for ultra-high performance concrete K-UHPC 2012.

[103] Wille K, Boisvert-Cotulio C. Material efficiency in the design of ultra-high performance concrete. Construction and Building Materials 2015;86:33–43. https://doi.org/10.1016/j.conbuildmat.2015.03.087.

[104] Wang J, Liu J, Wang Z, Liu T, Liu J, Zhang J. Cost-Effective UHPC for Accelerated Bridge Construction: Material Properties, Structural Elements, and Structural Applications. Journal of Bridge Engineering 2021;26. https://doi.org/10.1061/(ASCE)BE.1943-5592.0001660.

[105] Sbia LA, Peyvandi A, Lu J, Abideen S, Weerasiri RR, Balachandra AM, et al. Production methods for reliable construction of ultra-high-performance concrete (UHPC) structures. Materials and Structures 2017;50:7.

[106] Dong Y. Performance assessment and design of ultra-high performance concrete (UHPC) structures incorporating life-cycle cost and environmental impacts. Construction and Building Materials 2018;167:414–25.

[107] Racky P. Cost-effectiveness and sustainability of UHPC. Proceedings of the International Symposium on Ultra High Performance Concrete, Kassel, Germany, 2004, p. 797–805.

[108] Kodur V, Solhmirzaei R, Agrawal A, Aziz EM, Soroushian P. Analysis of flexural and shear resistance of ultra high performance fiber reinforced concrete beams without stirrups. Engineering Structures 2018;174:873–84.

[109] Chen Y, Matalkah F, Yu Y, Rankothge W, Balachandra A, Soroushian P. Experimental Investigations of the Dimensional Stability and Durability of Ultra-High-Performance Concrete. Advances in Materials Science 2017;6:1–8.

[110] Yoo D-Y, Yoon Y-S. Structural performance of ultra-high-performance concrete beams with different steel fibers. Engineering Structures 2015;102:409–23.

[111] Yoo D-Y, Lee J-H, Yoon Y-S. Effect of fiber content on mechanical and fracture properties of ultra high performance fiber reinforced cementitious composites. Composite Structures 2013;106:742–53.

[112] Khoury GA. Effect of fire on concrete and concrete structures. Progress in Structural Engineering and Materials 2000;2:429–47. https://doi.org/10.1002/pse.51.

[113] Yang IH, Joh C, Kim B-S. Structural behavior of ultra high performance concrete beams subjected to bending. Engineering Structures 2010;32:3478–87.

[114] Yoo D-Y, Banthia N, Yoon Y-S. Experimental and numerical study on flexural behavior of ultra-high-performance fiber-reinforced concrete beams with low reinforcement ratios. Canadian Journal of Civil Engineering 2017;44:18–28.

[115] Yoo D-Y, Yoon Y-S. A review on structural behavior, design, and application of ultra-high-performance fiber-reinforced concrete. International Journal of Concrete Structures and Materials 2016;10:125–42.

[116] Committee ACI. Building code requirements for structural concrete (ACI 318-19) and commentary (ACI 318R-19), Farmington Hills, MI: American Concrete Institute; 2019.

[117] Chen T, Gao X, Ren M. Effects of autoclave curing and fly ash on mechanical properties of ultra-high performance concrete. Construction and Building Materials 2018;158:864–72.

[118] Kodur V, Banerji S, Solhmirzaei R. Effect of Temperature on Thermal Properties of Ultrahigh-Performance Concrete. J Mater Civ Eng 2020;32:04020210. https://doi.org/10.1061/(ASCE)MT.1943-5533.0003286.

[119] Shin K-Y, Kim S-B, Kim J-H, Chung M, Jung P-S. Thermo-physical properties and transient heat transfer of concrete at elevated temperatures. Nuclear Engineering and Design 2002;212:233–41. https://doi.org/10.1016/S0029-5493(01)00487-3.

[120] Lie TT, Kodur VKR. Thermal and mechanical properties of steel-fibre-reinforced concrete at elevated temperatures. Canadian Journal of Civil Engineering 1996;23:511–7.

[121] Kodur VKR, Sultan MA. Structural behaviour of high strength concrete columns exposed to fire 1998.

[122] Abdallah S, Fan M, Rees DWA. Effect of elevated temperature on pull-out behaviour of 4DH/5DH hooked end steel fibres. Composite Structures 2017;165:180–91. https://doi.org/10.1016/j.compstruct.2017.01.005.

[123] Khaliq W, Kodur V. Thermal and mechanical properties of fiber reinforced high performance self-consolidating concrete at elevated temperatures. Cement and Concrete Research 2011;41:1112–22.

[124] Richardson AE. Compressive strength of concrete with polypropylene fibre additions. Structural Survey n.d.;2006.

[125] Khaliq W, Kodur V. Effectiveness of polypropylene and steel fibers in enhancing fire resistance of high-strength concrete columns. Journal of Structural Engineering 2018;144:04017224. https://doi.org/10.1061/(ASCE)ST.1943-541X.0001981.

[126] Kadleček V, Modrý S. Size effect of test specimens on tensile splitting strength of concrete: general relation. Materials and Structures 2002;35:28.

[127] Khaliq W, Taimur. Mechanical and physical response of recycled aggregates high-strength concrete at elevated temperatures. Fire Safety Journal 2018;96:203–14. https://doi.org/10.1016/j.firesaf.2018.01.009.

[128] Peng G-F, Huang Z-S. Change in microstructure of hardened cement paste subjected to elevated temperatures. Construction and Building Materials 2008;22:593–9.

[129] Giaccio GM. Mechanical behaviour of thermally damaged high-strength steel fibre reinforced concrete. Mater Struct 2005;38:335–42. https://doi.org/10.1617/14175.

[130] Li Y, Zhang Y, Yang E-H, Tan KH. Effects of geometry and fraction of polypropylene fibers on permeability of ultra-high performance concrete after heat exposure. Cement and Concrete Research 2019;116:168–78. https://doi.org/10.1016/j.cemconres.2018.11.009.

[131] Carreira DJ, Chu K-H. Stress-Strain Relationship for Plain Concrete in Compression. ACI Journal n.d.;1985:797–804.

[132] Wu Z, Shi C, He W, Wang D. Uniaxial compression behavior of ultra-high performance concrete with hybrid steel fiber. Journal of Materials in Civil Engineering 2016;28:06016017.

[133] Hurley MJ, Gottuk DT, Hall Jr JR, Harada K, Kuligowski ED, Puchovsky M, et al. SFPE handbook of fire protection engineering. Springer; 2015.

[134] ACI 216.1. Code requirements for determing fire resistance of concrete and masonry construction assemblies. Farmington Hills, MI, USA.: American Concrete Inst; 2014.

[135] Castillo C. Effect of transient high temperature on high-strength concrete. PhD Thesis, Rice University n.d.;1987.

[136] Williams B, Kodur V, Green MF, Bisby L. Fire endurance of fiber-reinforced polymer strengthened concrete T-beams. ACI Structural Journal 2008;105:60.

[137] Agrawal A, Kodur V. Residual response of fire-damaged high-strength concrete beams. Fire and Materials 2019;43:310–22.

[138] Hertz KD. Limits of spalling of fire-exposed concrete. Fire Safety Journal 2003;38:103–16.

[139] Yoo D-Y, Banthia N, Yoon Y-S. Flexural behavior of ultra-high-performance fiber-reinforced concrete beams reinforced with GFRP and steel rebars. Engineering Structures 2016;111:246–62.

[140] Gao WY, Dai J-G, Teng JG, Chen GM. Finite element modeling of reinforced concrete beams exposed to fire. Engineering Structures 2013;52:488–501. https://doi.org/10.1016/j.engstruct.2013.03.017.

[141] Schrefler BA, Majorana CE, Khoury GA, Gawin D. Thermo-hydro-mechanical modelling of high performance concrete at high temperatures. Engineering Computations 2002. https://doi.org/10.1108/02644400210444320.

[142] Davie CT, Pearce CJ, Bićanić N. A fully generalised, coupled, multi-phase, hygro-thermo-mechanical model for concrete. Materials and Structures 2010;43:13–33. https://doi.org/10.1617/s11527-010-9591-y.

[143] EN 1991-1-2. Eurocode 1 – Actions on Structures. Part 1–2: General Actions – Actions on Structures Exposed to Fire. CEN, Brussels 2002.

[144] Lie TT, Erwin RJ. Method to calculate the fire resistance of reinforced concrete columns with rectangular cross section. ACI Structural Journal 1993;90:52–60.

[145] Kalifa P, Menneteau F-D, Quenard D. Spalling and pore pressure in HPC at high temperatures. Cement and Concrete Research 2000;30:1915–27. https://doi.org/10.1016/S0008-8846(00)00384-7.

[146] Ortiz M. A constitutive theory for the inelastic behavior of concrete. Mechanics of Materials 1985;4:67–93. https://doi.org/10.1016/0167-6636(85)90007-9.

[147] Kodur VKR, Dwaikat M. A numerical model for predicting the fire resistance of reinforced concrete beams. Cement and Concrete Composites 2008;30:431–43. https://doi.org/10.1016/j.cemconcomp.2007.08.012.

[148] Anderberg Y, Thelandersson S. Stress and deformation characteristics of concrete at high temperatures: experimental investigation and material behaviour model. Lund Institute of Technology Lund, Sweden; 1976.

[149] Harmathy TZ. A comprehensive creep model 1967.

[150] Hibbeler RC. Structural analysis. 8th ed. Upper Saddle River, NJ: Pearson Education Inc.; 2014.

[151] Yazdani S, Schreyer HL. An anisotropic damage model with dilatation for concrete. Mechanics of Materials 1988;7:231–44. https://doi.org/10.1016/0167-6636(88)90022-1.

[152] Voyiadjis GZ, Abu-Lebdeh TM. Damage Model for Concrete Using Bounding Surface Concept. Journal of Engineering Mechanics 1993;119:1865–85. https://doi.org/10.1061/(ASCE)0733-9399(1993)119:9(1865).

[153] Kodur V, Banerji S. Modeling the fire-induced spalling in concrete structures incorporating hydro-thermo-mechanical stresses. Cement and Concrete Composites 2021;117:103902. https://doi.org/10.1016/j.cemconcomp.2020.103902.

[154] Gernay T, Millard A, Franssen J-M. A multiaxial constitutive model for concrete in the fire situation: Theoretical formulation. International Journal of Solids and Structures 2013;50:3659–73. https://doi.org/10.1016/j.ijsolstr.2013.07.013.

[155] Tenchev RT, Li LY, Purkiss JA. Finite element analysis of coupled heat and moisture transfer in concrete subjected to fire. Numerical Heat Transfer: Part A: Applications 2001;39:685–710. https://doi.org/10.1080/10407780119853.

[156] Shi H, Xu B, Zhou X. Influence of mineral admixtures on compressive strength, gas permeability and carbonation of high performance concrete. Construction and Building Materials 2009;23:1980–5. https://doi.org/10.1016/j.conbuildmat.2008.08.021.

[157] Boel V, Audenaert K, De Schutter G. Gas permeability and capillary porosity of self-compacting concrete. Materials and Structures 2008;41:1283–90. https://doi.org/10.1617/s11527-007-9326-x.

[158] Kollek JJ. The determination of the permeability of concrete to oxygen by the Cembureau method—a recommendation. Materials and Structures 1989;22:225–30.

[159] Pijaudier-Cabot G, Dufour F, Choinska M. Permeability due to the Increase of Damage in Concrete: From Diffuse to Localized Damage Distributions. J Eng Mech 2009;135:1022–8. https://doi.org/10.1061/(ASCE)EM.1943-7889.0000016.

[160] Nguyen D-L, Thai D-K, Kim D-J. Direct tension-dependent flexural behavior of ultra-high-performance fiber-reinforced concretes. The Journal of Strain Analysis for Engineering Design 2017;52:121–34. https://doi.org/10.1177/0309324716689625.

[161] Massicotte B, Elwi AE, MacGregor JG. Tension-Stiffening Model for Planar Reinforced Concrete Members. Journal of Structural Engineering 1990;116:3039–58. https://doi.org/10.1061/(ASCE)0733-9445(1990)116:11(3039).

[162] Shakya AM, Kodur VKR. Effect of temperature on the mechanical properties of low relaxation seven-wire prestressing strand. Construction and Building Materials 2016;124:74–84. https://doi.org/10.1016/j.conbuildmat.2016.07.080.

[163] Tao Z, Wang X-Q, Uy B. Stress-Strain Curves of Structural and Reinforcing Steels after Exposure to Elevated Temperatures. J Mater Civ Eng 2013;25:1306–16. https://doi.org/10.1061/(ASCE)MT.1943-5533.0000676.

[164] Garcia MA. Sedimentation Engineering: ASCE Manuals and Reports on Engineering Practice No. 110. American Society of Civil Engineers, New York 2008.

[165] Banerji S, Kodur V. Effect of Temperature on Mechanical Properties of Ultra-High Performance Concrete. Fire and Materials 2021.

[166] Youssef MA, Moftah M. General stress–strain relationship for concrete at elevated temperatures. Engineering Structures 2007;29:2618–34. https://doi.org/10.1016/j.engstruct.2007.01.002.

[167] Felicetti R, Gambarova PG, Sora MN, Khoury GA. Mechanical behaviour of HPC and UHPC in direct tension at high temperature and after cooling. Fifth RILEM symposium on fibre-reinforced concretes, Lyon, France: 2000, p. 749–58.

[168] Wu Z, Shi C, He W, Wu L. Effects of steel fiber content and shape on mechanical properties of ultra high performance concrete. Construction and Building Materials 2016;103:8–14.

[169] Rasul M, Ahmad S, Adekunle SK, Al-Dulaijan SU, Maslehuddin M, Ali SI. Evaluation of the Effect of Exposure Duration and Fiber Content on the Mechanical Properties of Polypropylene Fiber-Reinforced UHPC Exposed to Sustained Elevated Temperature. JTE 2019;48:4355–69. https://doi.org/10.1520/JTE20180687.

[170] Bentz DP. Fibers, percolation, and spalling of high-performance concrete. Materials Journal 2000;97:351–9.

[171] Shi C, Wu Z, Xiao J, Wang D, Huang Z, Fang Z. A review on ultra high performance concrete: Part I. Raw materials and mixture design. Construction and Building Materials 2015;101:741–51.

[172] Wang C, Yang C, Liu F, Wan C, Pu X. Preparation of ultra-high performance concrete with common technology and materials. Cement and Concrete Composites 2012;34:538–44.

[173] Liu X, Ye G, De Schutter G, Yuan Y, Taerwe L. On the mechanism of polypropylene fibres in preventing fire spalling in self-compacting and high-performance cement paste. Cement and Concrete Research 2008;38:487–99.

[174] Wu Z, Wong HS, Buenfeld NR. Influence of drying-induced microcracking and related size effects on mass transport properties of concrete. Cement and Concrete Research 2015;68:35–48.

[175] Bošnjak J, Ožbolt J, Hahn R. Permeability measurement on high strength concrete without and with polypropylene fibers at elevated temperatures using a new test setup. Cement and Concrete Research 2013;53:104–11.

[176] Tran VH, Meftah F, Izoret L, Behloul M. On explicit modeling of polypropylene fiber effects on hydro-thermal behavior of heated concrete. MATEC Web of Conferences 2013;6:05007. https://doi.org/10.1051/matecconf/20130605007.

[177] Progelhof RC, Throne JL, Ruetsch RR. Methods for predicting the thermal conductivity of composite systems: a review. Polymer Engineering & Science 1976;16:615–25.

[178] Kumlutaş D, Tavman IH, Çoban MT. Thermal conductivity of particle filled polyethylene composite materials. Composites Science and Technology 2003;63:113–7.

[179] Kaviany M. Principles of heat transfer in porous media. Springer Science & Business Media; 2012.

[180] Hill AA, Straughan B. Poiseuille flow in a fluid overlying a porous medium. Journal of Fluid Mechanics 2008;603:137–49.

[181] Gernay T. Fire resistance and burnout resistance of reinforced concrete columns. Fire Safety Journal 2019;104:67–78. https://doi.org/10.1016/j.firesaf.2019.01.007.

[182] Neves IC, Rodrigues JPC, Loureiro A de P. Mechanical Properties of Reinforcing and Prestressing Steels after Heating. Journal of Materials in Civil Engineering 1996;8:189–94. https://doi.org/10.1061/(ASCE)0899-1561(1996)8:4(189).

[183] EN 1994-1-2. Eurocode 4 – Design of Composite Steel and Concrete Structures. Part 1–2: General Rules – Structural Fire Design. Brussels 2005;Commission of European Communities.

[184] Franssen JM. Thermal elongation of concrete during heating up to 700 C and cooling. University of Liege, Available at: Http://Hdl Handle Net/2268/531 1993.

[185] Schneider U. Concrete at high temperatures—a general review. Fire Safety Journal 1988;13:55–68.

[186] Kodur V, Banerji S. Comparative fire behavior of reinforced concrete beams made of different concrete strengths. 2020. https://doi.org/10.14264/bd10594.

[187] Connolly RJ. The spalling of concrete in fires. Ph.D. Thesis. Aston University, United Kingdom, 1998.

[188] Banerji S, Kodur VKR, Solhmirzaei R. Fire response of ultra high performance concrete beams. International Interactive Symposium on Ultra-High Performance Concrete, vol. 2(1), Albany, New York, USA: Iowa State University Digital Press; 2019.

[189] Kodur VKR, Dwaikat M. Performance-based Fire Safety Design of Reinforced Concrete Beams. Journal of Fire Protection Engineering 2007;17:293–320. https://doi.org/10.1177/1042391507077198.

[190] ASTM. ASTM E1529-14a: . Standard test methods for determining effects of large hydrocarbon pool fires on structural members and assemblies. West Conshohocken, PA, USA 2014.

[191] Sritharan S. Design of uhpc structural members: Lessons learned and astm test requirements. Advances in Civil Engineering Materials 2015;4:113–31.

[192] Hasgul U, Yavas A, Birol T, Turker K. Steel fiber use as shear reinforcement on I-shaped UHP-FRC beams. Applied Sciences 2019;9:5526.

[193] Solhmirzaei R, Kodur VKR, Banerji S. Shear Behavior of Ultra High Performance Concrete Beams without Stirrups. International Interactive Symposium on Ultra-High Performance Concrete, vol. 2, Iowa State University Digital Press; 2019.

[194] Voo YL, Poon WK, Foster SJ. Shear Strength of Steel Fiber-Reinforced Ultrahigh-Performance Concrete Beams without Stirrups. Journal of Structural Engineering 2010;136:1393–400. https://doi.org/10.1061/(ASCE)ST.1943-541X.0000234.

[195] Lantsoght EO. How do steel fibers improve the shear capacity of reinforced concrete beams without stirrups? Composites Part B: Engineering 2019;175:107079.

[196] Majorana CE, Salomoni VA, Mazzucco G, Khoury GA. An approach for modelling concrete spalling in finite strains. Mathematics and Computers in Simulation 2010;80:1694–712.

[197] Naser MZ. Heuristic machine cognition to predict fire-induced spalling and fire resistance of concrete structures. Automation in Construction 2019;106:102916. https://doi.org/10.1016/j.autcon.2019.102916.

[198] Shi X, Tan T-H, Tan K-H, Guo Z. Influence of concrete cover on fire resistance of reinforced concrete flexural members. Journal of Structural Engineering 2004;130:1225–32.

[199] Khoury GA. Effect of fire on concrete and concrete structures. Progress in Structural Engineering and Materials 2000;2:429–47. https://doi.org/10.1002/pse.51.

[200] Ali F, Nadjai A. Fire resistance of concrete columns containing polypropylene and steel fibers. Special Publication 2008;255:199–216.

[201] Kodur V, Mcgrath R. Fire endurance of high strength concrete columns. Fire Technology 2003;39:73–87.

[202] Kodur VK, McGrath R. Effect of silica fume and lateral confinement on fire endurance of high strength concrete columns. Canadian Journal of Civil Engineering 2006;33:93–102.

[203] Kodur VKR, Phan L. Critical factors governing the fire performance of high strength concrete systems. Fire Safety Journal 2007;42:482–8. https://doi.org/10.1016/j.firesaf.2006.10.006.

[204] Shafieifar M, Farzad M, Azizinamini A. Experimental and numerical study on mechanical properties of Ultra High Performance Concrete (UHPC). Construction and Building Materials 2017;156:402–11. https://doi.org/10.1016/j.conbuildmat.2017.08.170.

[205] Solhmirzaei R. Response of Ultra High Performance Fiber Reinforced Concrete Beams under Flexure and Shear. vol. Ph.D. Thesis. Michigan State University; 2021.

[206] Committee 544 ACI. Design considerations for steel fiber reinforced concrete, American Concrete Institute; 2009.